Doctoral Dissertation
Doctoral program in Bioengineering and Medical-Surgical Sciences

Design of medical devices and multifunctional biomaterials for tailored tissue engineering

Elisa Fiume

* * * * * *

Supervisors
Prof. Enrica Verné, Supervisor
Prof. Cristina Bignardi, Supervisor
Prof. Francesco Baino, Supervisor

Doctoral Examination Committee

Prof. Alessandra Bianco, Università degli Studi di Roma Tor Vergata
Prof. Pasquale Vena, Politecnico di Milano
Prof. Gigliola Lusvardi, Università di Modena e Reggio Emilia

Politecnico di Torino
June 2021

I hereby declare that, the contents and organisation of this dissertation constitute my own original work and does not compromise in any way the rights of third parties, including those relating to the security of personal data.

……..

Elisa Fiume

Turin, April 29th 2021

Summary

Finding an effective strategy for the clinical treatment of bone defects can be considered a real surgical priority of our time.

Considering the level of technological progress achieved in biomedical field, engineering and materials processing, the inherent limitations resulting from the use of autologous grafts, still considered the golden standard in bone transplantation, cannot and must no longer be ignored.

Among the various materials proposed over time, particular attention goes to bioactive glasses (BGs), invented at the end of the 1960s by Professor Larry Hench.

The incredible potential of these materials was recognized right away thanks both to their capability to establish a chemical bond in contact with biological tissues and stimulate beneficial cellular pathways, thus promoting the integration of the graft and considerably shortening the healing time of the bone defect.

As a result, starting from the latest 90s', researchers focused on the development of suitable processing techniques aimed at the production of BG-based porous scaffolds, i.e. three-dimensional bone substitutes to be used in place of auto-, allo- and xeno-grafts, able to support cell migration and tissue ingrowth over time.

Nevertheless, although undeniable progress has been made, there has not yet been a complete transfer of this technology from laboratories to clinical practice, actually imputable to various causes, related both to material's properties and some relevant and still unsolved regulatory issues.

This Ph.D research work aimed at providing a contribution in shortening the gap between experimentation and clinical application of BG-based scaffolds for the management of bone defects.

New synthesis methods and strategies for the production and processing of bioactive glasses and scaffolds have been introduced, together with novel characterization tools and devices for the advanced characterization of BG-based grafts.

More specifically, four scaffold types were produced by different manufacturing processes, ranging from traditional methods (foam replication and glass foaming), to more advanced ones, based on additive manufacturing technologies (robocasting).

All the scaffolds were characterized by relating chemical/structural properties to bioactivity/biological response and, for each device, processing parameters were optimized to guarantee adequate porosity features, mechanical properties and bioactive behaviour in relation to minimal requirements identified for BTE applications.

Direct comparison between the scaffolds was legitimated by the use of the same basic material in all the processes, i.e. a silicate bioactive glass named 47.5B, based on the composition 47.5 SiO_2-2.5P_2O_5-20CaO-10MgO-10Na_2O-10K_2O (mol. %), produced both by traditional melt-quenching and chemical sol-gel synthesis.

Within the present activity, a great significance has been attributed to mathematical and physical modelling as reliable supporting tools for scaffolds characterization. Besides, considerable efforts were addressed to the design and development of a custom-made cellular bioreactor for cell seeding and dynamic perfusion, able to simulate the *in-vivo* like environment, providing a more realistic forecast of scaffold's performances after implantation.

It is strongly believed, indeed, that mathematical modelling, physical simulations and, in general, *in silico* models, could provide a decisive contribution to a clearer definition of validation protocols for BG-based scaffolds, currently based on costly *trial-and-error* approaches.

The overall study here reported demonstrates the exceptional versatility of the selected BG system and its adaptability to different processing approaches. In fact, 47.5B glass proved to be an excellent candidate as implantable material, as no cytotoxicity and inflammatory response were observed both *in vitro* and *in vivo*. Moreover, its exceptional physic-chemical properties revealed an enormous potential in the production of highly-porous vitreous and glass-ceramic sintered products with proper micro- and macrostructural properties for BTE applications.

External collaborations

I. Characterization of glass and glass ceramics

- **In vitro cellular tests:** Department of Health Sciences - Università degli Studi del Piemonte Orientale, Novara, Italy (reference persons: Prof. Lia Rimondini and Dr. Andrea Cochis);
- **In vivo studies:** Interinstitutional Research Center, Tashkent Medical Academy, Uzbekistan and Faculty of Prosthetic Dentistry, Tashkent State Dental Institute, Uzbekistan (Reference persons: Prof. Dilshat Tulyaganov and Dr. Avzal Akbarov).

II. Production and characterization of glass and glass ceramic scaffolds

- **Production of dolomite-foamed scaffolds:** Department of Natural-Mathematical Sciences of the Turin Polytechnic University in Tashkent, Tashkent, Uzbekistan (Reference person: Prof. Dilshat Tulyaganov);
- **Robocasting of melt-derived and sol-gel materials:** Faculty of Medicine and Health Technology of the University of Tampere, Tampere, Finland (Reference person: Prof. Jonathan Massera, 3-months visiting period);
- **Micro Computed Tomography measurements for pores analysis:** Department of Materials, Biotechnology and Energy of the Innovation Center Iceland (ICI), Reykjavik, Iceland (Reference person: Dr. Gyssur Örlygsson);
- **Permeability measurements:** Applied Metrology and Engineering Division of the National Institute of Metrological Research (INRiM), Turin, Italy (Reference persons: Dr. Alessandro Schiavi)

III. Design and optimization of a multifunctional perfusion bioreactor for bone tissue engineering

- **Activity coordination, design and optimization of the bioreactor system and physical simulations:** Department of Mechanical and Aerospace Engineering - Politecnico di Torino, Italy (Reference person: Prof. Diana Massai).
- **Fabrication of the bioreactor by additive manufacturing technology and optimization of the electrical stimulation system:** Department of Electronics and Telecommunications - Politecnico di Torino, Italy
- **Biological tests**: Department of Health Sciences - Università degli Studi del Piemonte Orientale, Novara, Italy (Reference person: Prof. Lia Rimondini and Dr. Andrea Cochis)

Acknowledgements

I am first grateful to Prof. Francesco Baino, who followed my steps since our first meeting in 2016, when I was still a simple master student. To him I owe patience, dedication and perseverance, as well as the humility that only a great teacher like him can demonstrate. Thank you for every opportunity to better myself, your constant support and for being a true a mentor and example to follow, not only in the academic field.

I also wish to thank my supervisors, Prof. Enrica Verné and Prof. Cristina Bignardi, for their endless availability and enthusiasm shown during these three years. I really hope, one day, to realize my dream of becoming a faculty member involved and passionate in experimental research, just like you.

I must also thank Fondazione Compagnia di San Paolo, for funding my doctoral fellowship.

I would also like to thank Prof. Jonathan Massera, for welcoming me to his research group at the Tampere University of Technology. My Finnish visiting period was at the same time one of the most difficult and exciting moments of my Ph.D. Nevertheless, I can only remember with pleasure every Sunday spent in the laboratory and the long discussions below freezing, as well as the help and support received in integrating into a reality so distant from what is familiar to me.

I must also thank the Solid and Fluid Biomechanics Group of the Department of Mechanical and Aerospace Engineering and, in particular, Dr. Diana Massai, for giving me the opportunity to test myself in a new research field. Working on the development of a cellular bioreactor was a precious experience of personal and professional growth that I will treasure in future years.

A proper thank goes to the research group of the Applied Metrology and Engineering Division of the National Institute of Metrological Research (INRiM) in Turin and, in particular, a huge thanks to Dr. Alessandro Schiavi for providing the equipment for permeability measures and introducing me to the fascinating world of metrology. Your professional collaboration certainly made a decisive contribution to my work. I sincerely hope to have the opportunity to work with you again in the future.

A sincere thanks also to Dr. Gyssur Örlygsson, for performing micro-CT analyses at the Innovation Center Iceland (ICI), necessary for the implementation of the mathematical model used for scaffolds characterization.

I also thank Andrea Cochis and Prof. Lia Rimondini for performing the *in vitro* biocompatibility tests and Prof. Dilshat Tulyaganov for doing the *in vivo* characterization and providing dolomite-foamed scaffolds necessary for the study.

I must also thank all those who contributed to my research activity with technical assistance, too many to be able to thank you all individually, but your every single contribution has been fundamental for the finalization of this work. In particular extra thanks to Mauro Raimondo, Salvatore Guastella, Daniele D'ambrosio, Gianpaolo Serino and Antonio Favero for morphological/compositional analyses, XRD characterization and mechanical tests.

The Glance Group, coordinated by Prof. Monica Ferraris, has been certainly a great team to work with. Thank you so much for every single day, coffee breaks, emotional support, endless patience and good mood. In particular, let me thank Alessandro and Fred, for the closeness and support shown in this last difficult period.

Special thanks to Remo, Rosalba, Andrea and Elena, simply for being here all this time, and to my little nephew Elia, for moments of leisure between chapters of the thesis, jumping on the bed like funny hens.

A special "four-legged" thank to Tequila Cat and Tequila Dog, the true partners in this endless smart-working period. You only lack the ability to speak, but your purring and wagging tail is more eloquent than any word.

I will always be grateful to my super family, because only with super powers it is possible to close the distance. Your love is rooted in my heart, always with me. Thank you for believing in me from the first moment. Thank you for not letting me fall apart during the last, difficult months. Thank you for being my courage.

Finally, let me address my greatest thanks to Lorenzo, the one who really has had first-hand experience, together with me, of this big adventure. A man with such big shoulders that he can handle anything. Considering all the things we have managed to do together during the last three years, I have no doubt: I can't wait to marry you!

To my father

Contents

List of Tables

Chapter 1

Chapter 2

Chapter 3

Chapter 4

Chapter 5

Chapter 6

Chapter 7

List of Figures

Chapter 1

Chapter 2

Chapter 3

Chapter 4

Chapter 5

Chapter 6

Chapter 7

Chapter 1

Inside the World of Bone Regeneration: Biological Properties, Clinical Needs and Perspectives for the Future

1.1 Introduction

Nowadays, bone grafting procedures for the management of medium-to-critical size bone defects are considered the order of the day, with more than two million surgeries performed every year all over the world.

In the last decades, the scientific community has been involved into an active and fruitful research activity for the development of novel bone substitutes to be used in Bone Tissue Engineering (BTE), with the ambitious aim of pushing the boundaries of the current therapies, mainly based on autologous and allogenic transplantation.

Nevertheless, regenerating bone is still considered a real clinical challenge requiring a complex and synergic multidisciplinary approach, as well as considerable economic, academic and human resources.

As a result, despite the latest technological advances in medicine, engineering and materials science, autologous bone is still considered the golden standard in grafting

surgeries. However, drawbacks deriving from its clinical usage are undisputable, thus creating a pressing need for prompt and effective solutions.

Therefore, specific questions must be considered:

Why is regenerating bone so difficult?

Which are the clinical requirements that still remain to be satisfied and which are the most relevant issues to be addressed in order to improve current manufacturing processes?

Which are the real causes that continue to hamper the complete technological transfer of synthetic bone grafts to clinical practice? Are they based just on regulatory issues or is there any need to explore new technologies?

1.2 Bone regeneration: general aspects

The skeletal system of humans and vertebrates is composed of bone, a dense and mineralized connective tissue responsible for important metabolic, physiological and structural functions [1].
Due to its peculiar composition, given by the combination of an organic and inorganic mineral part, bone is able to absorb high energy before breaking [2], [3], thus being particularly suitable as protective structure for vital organs and mechanically performant in load bearing anatomical sites [4].
Differently from most of the other biological tissues, bone is characterized by the peculiar capability of self-repairing and remodeling under the action of external forces of different nature, including mechanical [5]–[7], electrical [8] and magnetic ones [9], [10].
More specifically, there is experimental evidence of the capability of bone cells to modulate a specific response by transducing mechanical stresses into biochemical signals [11], while collagen fibrils confer on bone piezoelectric properties [12].
Bone structural adaptation to external stimuli was first observed in 1892 and officially formalized in the Wolff's Law, according to which:

"Every change in the form and function of bones or of their function alone is followed by certain definite changes in their internal architecture, and equally definite alteration in their external conformation, in accordance with mathematical laws [13]*"*

As a direct consequence, bone is continuously subjected to structural, morphological and even compositional changes, which depend not only on age, life style and general health conditions of each individual, but also on the specific anatomical site considered, according to the physiological function.
The difficult task of controlling and regulating bone remodeling over the whole life time is entrusted to the simultaneous action of different specialized cellular species, whose combined metabolic activity aims at maintaining the physiological homeostasis conditions [14], [15].

In particular, bone tissue is composed of four cell types: osteoblast, bone lining cells and osteoclasts, located on the bone surface, and osteocytes, located in the bone inner part [16].
It is not by chance that the most diffused bone diseases are the result of severe cellular metabolic decompensation, with remarkable effects on the overall bone properties from the nano- to the macro-scale [17], [18].
The physiological healing process of a traumatic fracture is maybe the most striking proof of the exceptional adaptivity and dynamism of bone tissue and, when the defect size is restrained, complete bone healing occurs within an average time of 6-8 weeks [19], following the process described in **Figure 1.1** [20].

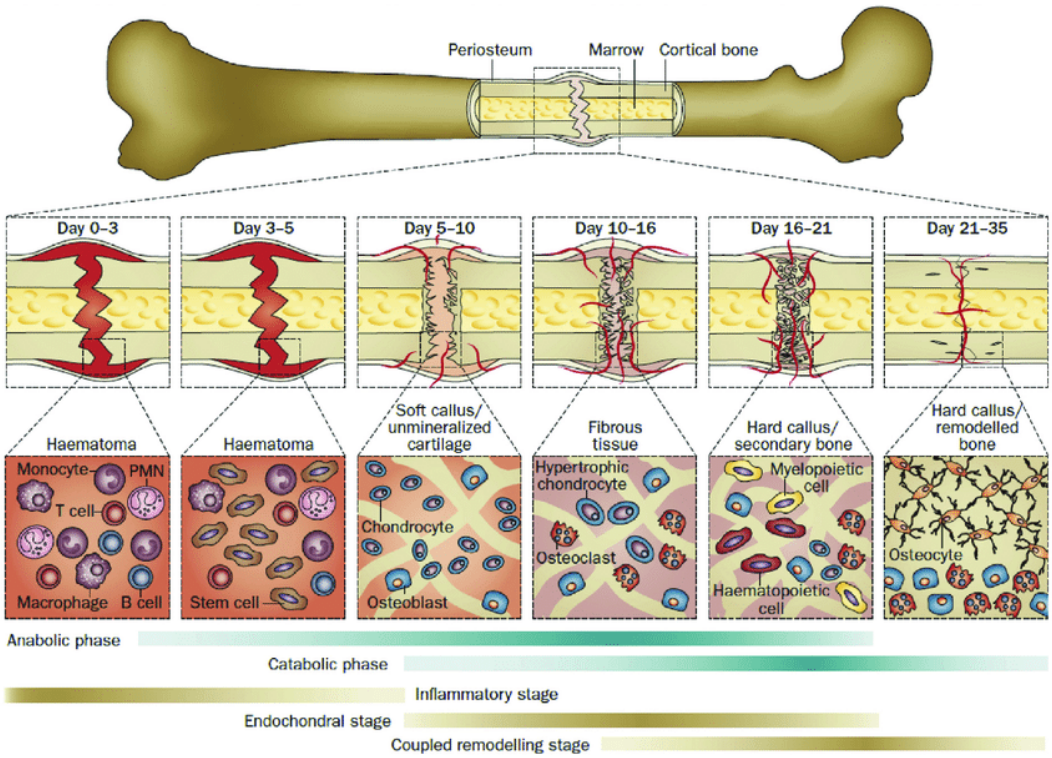

Figure 1. 1. Physiological healing process of a typical bone fracture. Figure reproduced from Wang and Yeung [20] under the Creative Commons Attribution-NonCommercial-NoDerivatives 4.0 International.

While minor bone defects are usually rapidly repaired, the management of critically-sized bone defects deriving from congenital diseases, surgical tumors removal and serious traumatic events is still considered one of the major clinical challenges of our times [21].
In all these cases, the usage of implantable bone substitutes at the defect site is highly recommended to guide, support and improve tissue growth, leading to complete regeneration in a shorter time, with great benefits both to the patient and the sanitary system [22], [23].
Bone grafts of natural origin (bone transplants) are currently the most widely used in surgical procedures, due to their intrinsic biocompatibility, as well as their biological and morphological similarity to the native tissue [24].

However, despite undisputable strengths, biological grafts suffer for important limitations, such as donor site morbidity and limited tissue availability [24].
In this perspective, synthetic bone substitutes, also named *scaffold*s, represent today a high-value asset to be used in combination with cells and growth factor therapy to restore the original functionality of the native tissue (**Figure 1.2**) [25].
This novel approach is known by the name of Bone Tissue Engineering (BTE) and is based on the development of biocompatible tissue substitutes able to promote new tissue growth by mimicking the native extracellular matrix (ECM) [26].

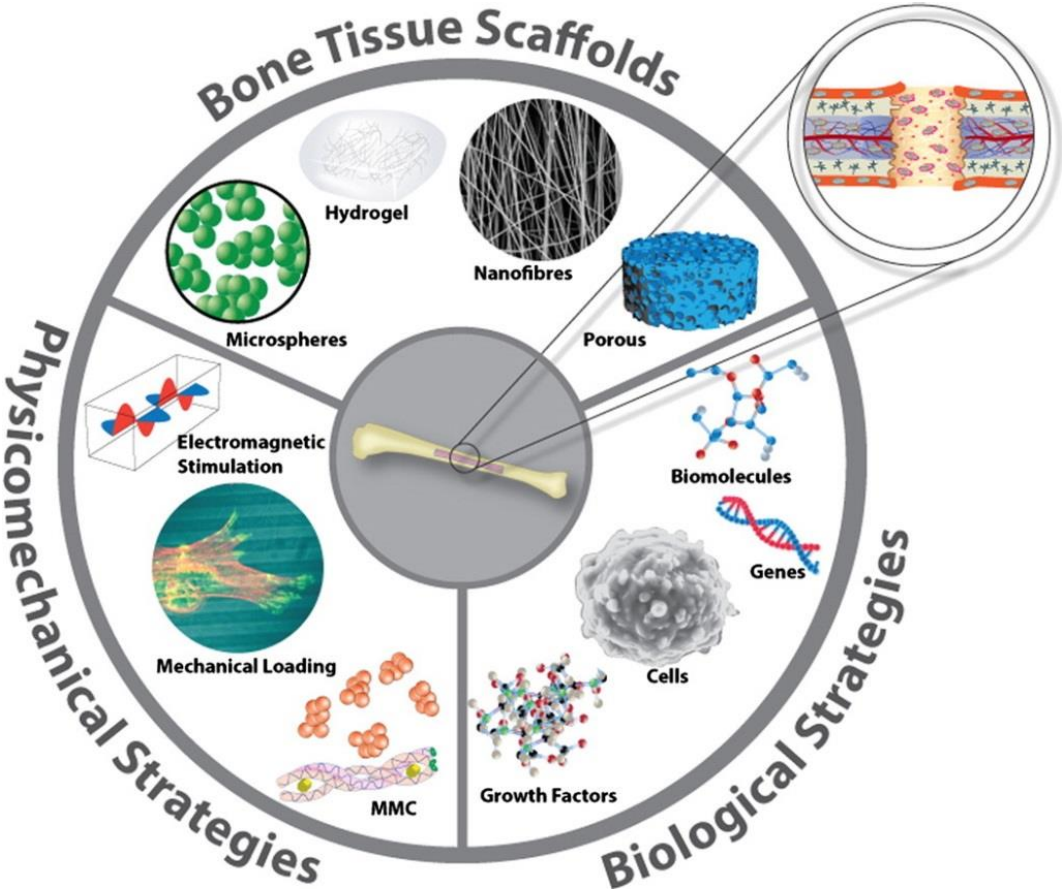

Figure 1. 2. Overview on BTE approaches combining different types of biocompatible scaffolds with biological and physic-mechanical strategies for the treatment of medium-to-critical sized bone tissue defects. Figure reproduced with permission from Fernandez-Yague et al. [27].

The main advantage of a BTE approach lies in the possibility to by-pass organ and tissue transplantation, which may be followed by rejection and transmission of pathologies and is commonly associated to very long waiting lists deriving from the lack in organs and tissues available for the transplant [28].
The pressing need for synthetic bone substitutes is the main driving force which guides BTE research through the development of new-generation engineered bone grafts and, over the last years, several materials have been proposed for bone regeneration (i.e. metals, ceramics, polymers and composites), in combination both with traditional processing techniques and the latest additive manufacturing technologies [29].

The right coupling between material and manufacturing strategy for the production of scaffolds is maybe the most relevant factor to be considered in order to obtain reliable three-dimensional (3D) architectures, which is a not-always easily achievable goal.
The choice of the processing technique, in fact, has to be properly evaluated in order to preserve or even improve the original characteristics of the selected biomaterial. The three pillars on which the selection of a material for bone regeneration is based are undoubtedly biocompatibility, bioactivity and degradability, where the degradation rate has to be tuned according to the physiological healing time of bone in order to preserve an adequate mechanical integrity over the whole duration of the treatment.
Concerning mechanical behavior, it is besides advisable to avoid bone resorption and stress shielding phenomena, resulting from a mismatch in mechanical properties between the tissue and the implant [29].
For all these reasons, optimizing the design of the porous architecture plays a pivotal role in order to:

i) Provide adequate mechanical support and mass transport properties, by the right combination of materials, 3D structure and manufacturing process;
ii) Promote the interaction between cells and the implant by providing topographical and biochemical cues, by mean of an opportune selection/processing of the basic material.

In the last decade, the importance of supplying a suitable growth environment able to reproduce specific *in vivo*-like exercise conditions given by the combination of mechanical, electrical and biological stimuli has been demonstrated, leading to an improvement of the overall quality of the newly-formed tissue by restoring its original function more efficiently and in a shorter time [30].
When dealing with porous scaffolds, in fact, dynamic 3D culture conditions have to be preferred in order to ensure adequate nutrient/oxygen supply and catabolites elimination, as well as a more faithful reproduction of the dynamic biological environment [31].
In this regard, bioreactor-based systems represent today key components for the development of advanced engineered grafts thanks to the optimization of mass-transport phenomena, stimulation, monitoring and control protocols, thus overcoming the current limitations of traditional cell cultures [30].
Despite all the efforts, BTE has not yet achieved a complete translation into clinical practice: the high technological costs deriving from the necessity to use high-quality and pure materials and the lack of well-defined international norms are just two of the main causes that currently hinder the spreading of reproducible and standardize manufacturing processes for the production of synthetic bone substitutes [32].

In the present chapter, the attention will be focused on bone tissue, with the aim of shedding light on the main critical aspects related to the development of therapeutically effective BTE strategies to be implemented in clinical practice.

First, a summary description of bone as biological tissue will be provided, with an emphasis on structure, composition and physical properties.
Then, the current therapeutic approaches for the management of medium-to critical size bone defects will be described in detail, discussing the characteristic that an ideal synthetic graft for bone regeneration should exhibit.
Finally, a brief overview on bioreactor systems for 3D dynamic cell cultures will be presented, putting an accent on perfusion and shear stress systems combining multiple stimulation strategies.

1.3 The bone tissues

Bone is a dynamic and highly adaptive connective tissue responsible for important metabolic and structural functions for the human body, such as minerals storage (mainly calcium and phosphorus), hematopoiesis, structural support to the body and locomotion.
Classification of bones can be carried out on several fronts, on the basis of geometrical, morphological and structural features.
The basic unit of bone tissue is the mineralized collagen fibril, hierarchically organized from the macro- to the nano-scale; as a direct result, at each level of the hierarchical organization, bone exhibits peculiar physical and mechanical properties, which vary according both to its compositional and structural arrangement.

1.3.1 Composition and hierarchical organization of bone

From a materials science point of view, bone can be assumed as a hierarchical nanocomposite material consisting of an organic (30-35 wt.%) and an inorganic mineral component (65-70 wt.%).

Apart from bone cells, which will be illustrated later in the chapter, the remaining organic phase of bone, constituting part of the ECM, is mainly composed of proteins, divided in:

i) structural proteins: collagen (Type I) and fibronectin;
ii) proteins with specialized functions, including signaling molecules, growth factors and enzymes [33].

The mineral phase of the ECM is predominantly composed of calcium phosphates, but also calcium carbonates, fluorides and magnesium phosphates can be found.
Calcium phosphates are mainly in the form of apatite crystals [$(Ca_{10}(PO_4)_6)^{2+}$], where the two positive charges are usually balanced by hydroxyl ions (OH^-), forming *hydroxyapatite* (HA) ($Ca_{10}(PO_4)_6(OH)_2$) [1], [34].

The *mineralized collagen fibril*, constituting the basic unit of bone tissue, derives from the permeation and the progressive growth of nanometric needle-like crystals of HA within the empty spaces existing between collagen microfibrils.

The chemical composition of bone tissue is detailed in **Table 1.1** [1], [34].

Table 1. 1. Chemical compositional features of human bone [1], [34].

	Phase		Chemical composition (wt.%)		Function
Bone Tissue	Organic ~ 30-35		Bone cells ~ 2	Osteocytes Osteoblasts Osteoclasts Lining cells	Maintenance of bone homeostasis conditions (see **Table 1.2**)
		Bone Matrix	Proteins ~ 98	Collagen ~ 20 Non-collagen ~ 3 (osteocalcin, osteonectin, osteopontin, thrombospondin, morphogenetic proteins, sialoprotein, serum protein	Mechanical strength under tensile/flexural stresses
			Trace elements	Polysaccharides, lipids and cytokines	
	Inorganic ~ 65-70		Phosphates	Hydroxyapatite ($Ca_{10}(PO_4)_6(OH)_2$) ~ 60 Magnesium phosphates	Mechanical strength under compressive stresses; Mineral storage (99% Ca, 85% P, 40-60% Na and K in the body
			Carbonates ~ 4	Calcium carbonates	
			Citrates ~ 0.9	Sodium, calcium and potassium citrates	
			H_2O ~ 9		
			Ions	Na^+ (~ 0.7), Mg^{2+} (~ 0.5), Cl^- (~ 0.13) Others: K^+, F^-, Zn^{2+}, Fe^{2+}, Cu^{2+}, Sr^{2+}, Pb^{2+}	

Generally speaking, there are two structural types of bone, *woven* and *lamellar*.

In physiological conditions, the *woven bone* is a transitional tissue, in fact, it can be found both in the development stage and in the fracture healing process; it is composed of mineralized collagen fibril bundles with neither discernable orientation nor structural organization at higher level.

On the other hand, in *lamellar bone* the basic unit arranges into well-ordered structures, providing very peculiar characteristics at different magnitude scales [35].

Hence, different levels and structures can be identified [36] :

i) the macrostructure: *cancellous* and *cortical* bone;
ii) the microstructure (from 10 to 500 μm): *Haversian systems*, *osteons*, *single trabeculae*;
iii) the sub-microstructure (1–10 μm): *lamellae*;
iv) the nanostructure (from a few hundred nanometers to 1 μm): *fibrillar collagen* and *embedded mineral*;

v) the sub-nanostructure (below a few hundred nanometers): molecular structure of constituent elements, such as mineral, collagen, and non-collagenous organic proteins.

The hierarchical organization typical of lamellar bone is schematically illustrated in **Figure 1.3** [37].

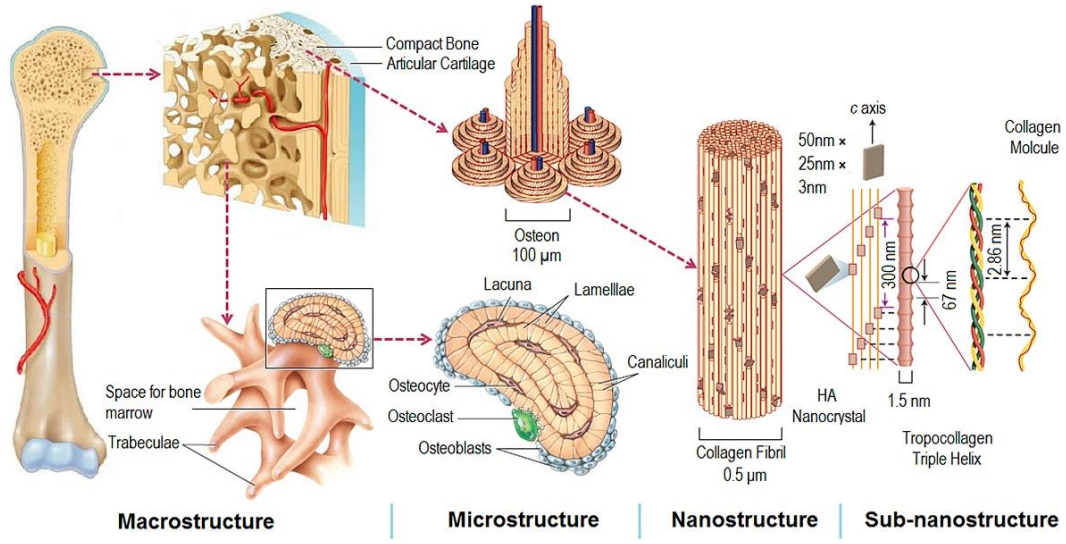

Figure 1. 3. Hierarchical structure of human bone. Image reproduced with permission from Wang et al. [37]

At the *macroscale*, bone can be classified into *cortical* (or *compact*) and *cancellous* (also *trabecular* or *spongy*) bone, on the basis of the tissue density, morphological, metabolic and structural features [1].

Despite they both are made of *lamellar bone*, the mechanical performances, as well as their mass transport properties are deeply different. For this reason, their distribution within the human body is efficiently managed according to the anatomical position, on the basis of the loading conditions and the specific functions to be performed.

The 80 wt.% of the human skeleton is composed of cortical bone, and the 20 wt.% of trabecular one. While the high density, proper of cortical bone, provides good mechanical resistance under compression, torsion and tensile stresses, the high porosity levels observed in the open-cell architecture of trabecular bone, typically between 50 and 90 vol.%, reflect into a better vascularization of the tissue and take part into cell migration, nutrients/oxygen supply and elimination of metabolic wastes [1].

At the *microscale level*, the structural arrangement depends on the macrostructure considered.

In cortical bone, the structural unit is represented by the *osteons (or Haversian Systems)*, arranged around a central canal, called *Haversian canal*, containing both small blood vessels and nerves, tightly packed together to form a solid mass.

Around the canal, the bone matrix is concentrically arranged into rings of tubular *lamellae*, connected by small channels (*canaliculi*) containing gap junctions, fundamental for osteocytes communication.

In cancellous bone, the structural unit is the *trabecula*, which arranges in the 3D space to form an open-cell architecture composed of bars, plates and roads with a mean diameter ranging from 50 to 300 μm [36].
At the *nanoscale*, bone is characterized by the presence of collagen fibrils, arranged into a triple helix, and hydroxyapatite crystals, deposited within specific holes and pore regions of the collagen fibrils during the mineralization and bone remodeling, thus filling all the available empty spaces [36].

1.3.2 Bone cells and bone remodeling

Bone cells constitute about the 2 % by weight of the organic component of the ECM and are divided into four different phenotypes: osteocytes, osteoblasts, osteoclasts and bone lining cells, concisely described in **Table 1.2**.

Table 1. 2. Chemical compositional features of human bone [1], [34].

Cell type	Morphological features	Origin	Function
Osteoblasts	Cuboidal cells Abundant rough endoplasmic reticulum Prominent Golgi apparatus Secretory vesicles	Mesenchymal stem cells (MSC)	Bone matrix deposition Osteoclastogenesis Metabolic functions
Osteoclasts	Terminally differentiated multinucleated giant cells	Mononuclear cells of the hematopoietic stem cell lineage	Bone matrix resorption Cytokines source May be involved in: osteoblast differentiation, immune system activation, proliferation of tumoral cells
Lining cells	Quiescent flat-shaped osteoblasts Thin and flat nuclear profile	Mesenchymal stem cells (MSC)	Gatekeeper function Communication with osteocytes
Osteocytes	Rounded or elongated shape in trabecular and cortical bone, respectively	Mesenchymal stem cells (MSC)	Mechano-transduction Modulation of the mechanism of bone resorption Metabolic function

The combined action of these cellular species is fundamental to correctly manage bone turnover and remodeling over the entire life time, in order to:

i) Adapt bone architectural features in response to external forces and stimuli;
ii) Spontaneously repair microfractures within the bone matrix;
iii) Prevent the accumulation of old bone;
iv) Maintain the shape, the quality and the size of the skeleton.

In this regard, achieving the right balance between osteoclasts resorption activity and new bone matrix deposition is crucial; this is possible due to the capability of osteoblasts to express a double phenotype: on one side, the osteogenic phenotype is responsible for the secretion of bone matrix and, on the other, the osteoclastogenic phenotype promotes the differentiation to osteoclasts in the old bone area [14].
During bone remodeling, osteoblasts and osteoclasts arrange in what is called Basic Multicellular Unit (BMU), exhibiting different characteristics according to the considered macrostructure (trabecular or cortical bone).
Specifically, it is possible to identify three different stages within the remodeling cycle:

i) *Resorption stage*: partially differentiated mononuclear preosteoclasts migrate to the bone surface and form multinucleated osteoclasts (osteoclastic resorption)
ii) *Reversal stage*: as soon as the osteoclastic resorptive cycle is completed, mononuclear cells appear on the bone surface and prepare the surface for osteoblasts differentiation and migration, secreting specific proteins which act as substrate for osteoblasts attachment, in order to begin new bone synthesis
iii) *Formation stage*: synthesis of new bone matrix by osteoblasts until all the resorbed bone is replaced by newly formed tissue. At the end of this phase, the surface is covered by bone lining cells. Thus, a prolonged resting period begins, lasting until the next remodeling cycle [11], [38].

Although bone is physiologically programmed to self-repair, in some cases this important process can be delayed or even hindered due to multiple factors, e.g. hormonal changes, ageing, changes in physical activity, use of drugs or secondary diseases, which may result in severe disorders of bone metabolic activity [39].
In some conditions, such as post-menopausal osteoporosis, arthritis and periodontal diseases, a net loss of bone tissue can be observed due to an acceleration of the bone resorptive cycle resulting from an over-formation of BMU, which determines a delay in new bone synthesis compared to the high resorption rates [40].
These mechanisms have been also associated to an enhanced expression of inflammatory cytokines and RANKL[40], which promotes the differentiation to an osteoclastic phenotype [41], as well as increased expression of factors that inhibit Wnt signaling [40], fundamental to allow the formation of new bone [42].

1.3.3 Mechanical properties of bone

Bones are essential to the skeleton-muscle system, as they contribute to the development of motion, together with muscles, cartilage and tendons. Due to their high mineralization level, bones are the main load bearing components of this apparatus and their mechanical response is properly modulated according to the anatomical site and the specific physiological function (e.g. locomotion, mastication, structural support or protection to organs).

An accurate and detailed review describing bone mechanical behavior both in healthy and diseased conditions has been recently published by Morgan and coworkers [43]. The review systematically discusses the most relevant factors affecting the mechanical response of bones, operating a distinction between cortical and trabecular tissue and analyzing their selective contribution to the overall structural properties of the whole bone.

Determining bone mechanical properties can be a true challenge as the result of mechanical tests can be significantly affected both by biological and non-biological factors, including testing conditions, moisture content and storage conditions of the biological specimens [44]. Moreover, there is experimental evidence of the influence of bone hierarchy on the mechanical response of the tissue at different magnitude scales [36].

As described in *Paragraph 1.2.1*, bone is characterized by a well-organized hierarchical structure constituted by various components irregularly oriented in the 3D space. Consequently, bone behaves as an anisotropic material, which means that its mechanical response is highly dependent on the considered direction. Thus, when analyzing bone mechanical properties, longitudinal and radial responses with respect to the shaft of the bone have to be considered equally significant [44].

From a biological point of view, the mechanical behavior of bone is the direct result of the combination of multiple factors, some of which, in turn, may be subjected to enormous changes according to ageing, sex and presence of comorbidities.

As an example, it is possible to consider the enormous variation in mechanical properties at different stages of the human body development: children's bones are in fact characterized by a lower elastic modulus and bending strength compared to adults, resulting in a higher absorbed energy and deflection capability before reaching fracture [45].

Due to the composite nature of bone tissue, its mechanical properties are, in fact, affected by the relative proportion between the various components of the ECM: on one side the organic component, mainly represented by type I collagen fibrils, confers tensile strength, while the inorganic mineral part provide mechanical strength under compression loading conditions (**Table 1.1**) [1], [34].

Hence, the mineralization level, e.g. the amount of ash masses within the tissue, represents one of the key points having a major effect on the mechanical behavior of bone.

In physiological conditions, depending on the specific anatomical site, the mineralization of cortical bone can vary within a very wide range (typically 45-85 wt.%), resulting, in turn, in a great variation in elastic modulus, bending strength and fracture toughness, according to an adaptive mode able to regulate cellular mechanisms [46].

On the contrary, in trabecular bone, comparable values of elastic modulus have been calculated for different anatomical sites, but a very high inter-subject differentiation is appreciable, as well as a great variation along the bone length and around the periphery [47].

In cortical bone, one of the major effects of ageing is represented by hyper mineralization and increased bone porosity, which determines a progressive decrease in fracture toughness. As a result, falls in the elderly are commonly associated with fractures and several weeks of hospitalization [48].
Analogous structural changes can be observed also in trabecular bone: with ageing trabeculae progressively become thinner and connectivity and volume fraction decrease, with a consequent decrease in stiffness and strength [49].

Table 1.3 provides a comparison between mechanical properties of bone in relation to typical porosity ranges observed in human cortical and trabecular bone.

Table 1. 3. Mechanical properties of trabecular and cortical bone (physiological ranges) [50].

Bone type	Total Porosity ε_0/ Vol.%	Compressive strength σ_c/ MPa	Elastic modulus E/ GPa	Tensile strength σ_t/ MPa	Fracture toughness K_c/ MPa·m$^{1/2}$
Cortical	5-15	130-200	7-30	50-151	2-12
Trabecular	40-95	0.1-16	0.05-0.5	n.a.	n.a.

While the mechanical properties of cortical bone are mainly affected by the mineralization level of the tissue and the organization of the solid matrix, the overall mechanical properties of trabecular bone are the result of two different contributions [36]:

i) Structural properties, given by the 3D arrangement of trabecular in the space, considered in global stress analysis;
ii) Material properties, defined as the intrinsic properties of each single trabecular strut, providing information about bone health status and its adaptive potential to external stimuli.

Some authors sustain that the different mechanical behavior observed in cortical and trabecular bone has to be attributed exclusively to the different density level, as they are actually composed of the same material, i.e. *lamellar bone* [51]–[53].
However, considering bone metabolism, this assumption seems to be quite weak, as the activity levels of trabecular bone are remarkably higher than those observed in cortical one due to the larger surface area exposed to marrow by trabecular bone. As bone turnover mechanism occurs at the surface, trabecular bone is on average remarkably younger than cortical one [4]. According to this, denying the contribution made by the process of maturation of the tissue over time would be definitely too superficial and misleading [54], [55].
Shifting to the microscale, the mechanical properties of Haversian systems have been determined for the first time by Ascenzi and coworkers, who collected the main results in several research papers describing the behavior of each single osteon under compression [56], tension [57], bending [58] and torsion [59] testing modes. A comprehensive analysis would suggest a strong dependence of the mechanical properties from the orientation of the *lamellae*, where a longitudinal orientation improves mechanical response under tension, torsion and even bending stresses,

while the mechanical performances under compression seem to be improved by an alternated orientation.
Even for cancellous bone, the mechanical properties of a single trabecula have been object of study of several research groups [54], [55], [60], [61], albeit with some ambiguity.
In particular, this last point is still an area of great scientific interest when dealing with the development of regenerative medicine approaches for the management of bone defects. An accurate determination of the mechanical properties of a single trabecula, in fact, would allow a deeper knowledge on the overall bone conditions both in the presence of metabolic diseases and at the interface with implant biomaterials. In fact, compared to cortical bone, trabecular one is more inclined to evolve toward a pathological state and, for this reason, most of the research studies aimed at the design and optimization of BTE scaffolds refer to the physiological ranges reported for trabecular bone, rather than those typical of cortical one.

1.3.4 Electrical properties of bone

In bone tissue, the electrical forces at atomic level are considered fundamental for the maintenance of bone structural integrity and simultaneously determine peculiar biological, chemical and physical properties [62].
Piezoelectricity, or *piezoelectric effect*, is a typical property of many crystalline solids related to the distortion of chemical bonds under loading conditions, which leads to the production of an alternating current (AC) in response to the mechanical stress.
The piezoelectric effect in human bone was reported for the first time in 1955, when Fukada and Yasuda demonstrated the existence of an electrical polarization in dry bone specimens as a result of the application of a mechanical load [63].
After having excluded the involvement of the cellular component, a preliminary hypothesis attributed the piezoelectric response of bone to the slipping of collagen fibers, both in bending and in compression mode [64], but only a few years later, in 1971, this theory was confirmed by Marino and Becker, who rigorously proved the involvement of the organic component of bone matrix [65].
Nevertheless, the study did not exclude the possibility of further contributions, suggesting a plausible effect of the application of shear forces at the collagen-mineral interface resulting in the movement of the mineral crystals along the fibers [65].
For many years, bone piezoelectricity and pyroelectricity have been exclusively attributed to the peculiar molecular structure of collagen, characterized by an asymmetric structural point group [66], assuming no contribution from the mineral part (HA). In fact, the mechanical distortion of chemical bonds in HA crystals would not be able to induce a significant polarization due to the presence of a centrosymmetric group in the hexagonal system [67], [68].
However, more recent computational studies reported a lack of an inversion center in HA that could theoretically confer a piezoelectric behavior on the crystal [69], [70].

In **Figure 1.4**, the piezo response of a collagen fibril (Figure 1.4 a-b) and nanocrystalline HA (Figure 1.4 c-d), potentially involved in the development of the overall piezoelectric response of bone tissue (Figure 4 d-e-f), are represented.

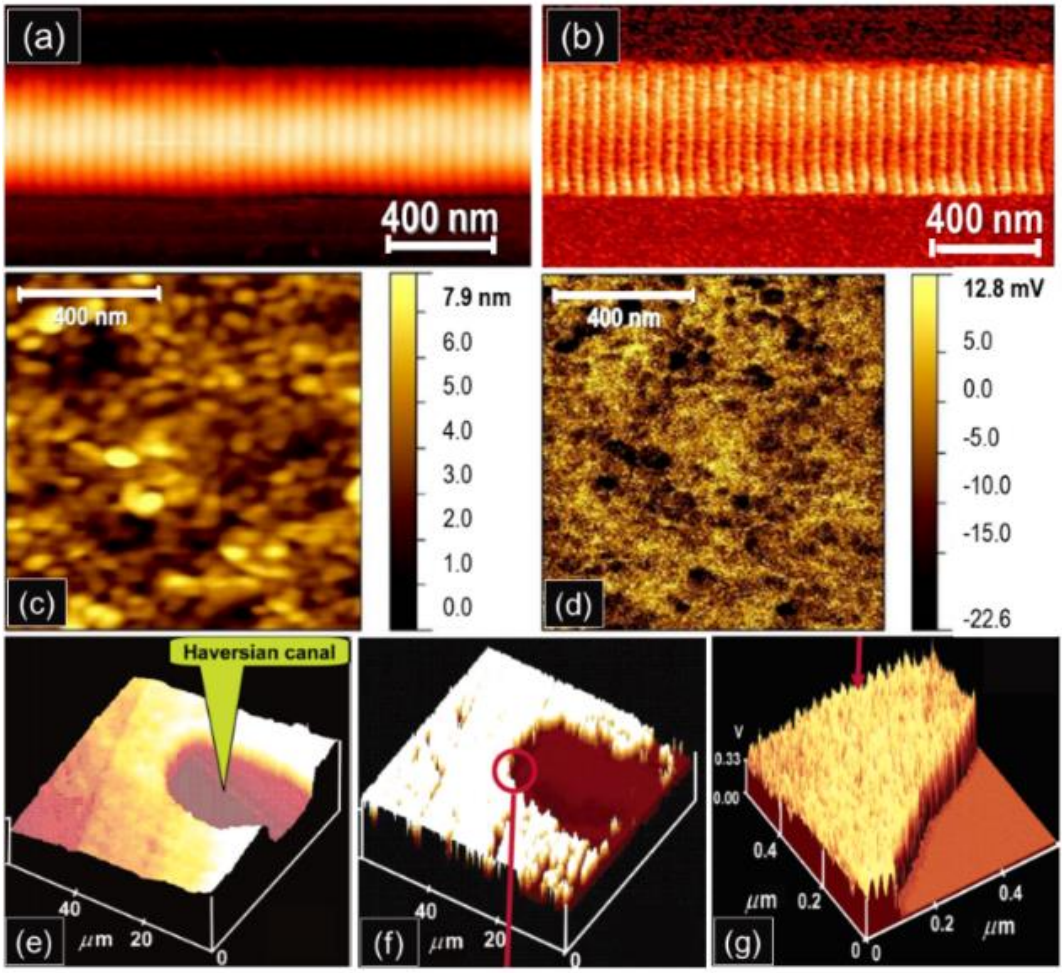

Figure 1. 4. Atomic Force Microscopy (AFM) image of a single collagen fibril (a) and Piezoresponse Force Microscopy (PFM) image (b) showing the amplitude of its shear piezoelectric response [71]; AFM topography (c) and PFM measurements (d) of a nanocrystalline HA sample [69]; PFM image of cross section of a sample from mature cortical bone (tibial shaft): (e) topography, (f) piezo response in proximity of the haversian canal and (g) nanoscale resolution piezo response image in proximity of the haversian canal [72]. Images reproduced with permissions. Figure c-d reproduced under a Creative Commons Attribution-NonCommercial-NoDerivs 3.0 Unported License.

The discovery of bone piezoelectricity opened up new interesting possibilities in bone regenerative strategies. It has been demonstrated, indeed, that in areas subjected to compression, the surface of the tissue was electronegative, inducing bone resorption while, in areas subjected to tensile stresses, bone was electropositive and new tissue synthesis was favored [8].

As a result, in recent years, many literature studies focused on the application of electromagnetic fields and the development of piezoelectric biomaterials to improve bone regeneration in tissue engineering strategies.

At the cellular level, the influence of electrical stimulation on bone remodeling, as well as the possibility to enhance bone healing mechanisms was successfully proved both *in vivo* and *in vitro*, with strong evidences of improved osteogenetic activity.

In 2001, Wiesman and coworkers [73] observed enhanced mineral formation *in vitro* in cultures stimulated by pulsed electrical fields (PEF) compared to the non-stimulated controls, observing nodules and mineralized globules under the action of capacitively coupled electric fields. In a more recent study, the beneficial effect of electrostatic field on both bone mineralization and cell differentiation capacity was reported; interestingly, a dependence between initial cell density and cell response has been observed and ECM synthesis and cell differentiation were favored at high and low initial cellular density, respectively [74].
Beside the beneficial effects given by the exposure of bone cells to electric fields, latest advances in BTE propose the use of piezoelectric materials for the manufacturing of mechanoelectrical-transduction scaffolds able to generate and allow the transfer of bioelectric signals analogously to native bone. It has been demonstrated, indeed, that piezoelectric materials can provide beneficial effects on cellular signaling pathways, enhancing tissue regeneration at the defect site [75].

1.4 Bone regeneration and tissue engineering: from biological grafts to synthetic scaffolds

With more than two million surgeries performed every year all over the world, bone is currently the second most frequently transplanted biological tissue after blood [20]. Despite that, the clinical treatment of bone defects continues to be a controversial matter due to a persistent lack of consensus around definitions, robust models and best practices for their surgical management.
The origin of bone defects is quite various: high energy traumas, infections, tumors resection and congenital pathologies are just few examples of causes that could determine an extended bone loss, known under the name of *critically-sized bone defect*.
Given that bone is capable of self-renewal, in first approximation, it can be assumed that a bone defect becomes pathological when the physiological self-healing capability is seriously compromised, thus requiring an external action. The relative size of the defect compared to the absolute bone size, anatomical variations, the physiological environment surrounding the defect, the age of the patient, as well as the presence of comorbidities and/or chronical diseases are relevant additional factors to be considered for the global evaluation of the defect size [21].
Whenever the physiological self-healing capability of bone is compromised, the use of bone grafts is considered fundamental to support the regeneration of the tissue, thus restoring its physiological function [22], [24], [25], [28], [76].

1.4.1 Biomaterials and scaffolds for bone tissue engineering

The implantation of biomaterials for improving and restoring the original function of damaged organs and tissues is a quite ancient strategy. Today, the set of these medical practices answers to the name of Tissue Engineering (TE), officially defined in 1988 at the National Science Foundation Workshop as:

"*the application of principles and methods of engineering and life sciences toward the fundamental understanding of structure-function relationship in normal and*

pathological mammalian tissues and the development of biological substitutes to restore maintain or improve tissue function [77]*."*

TE is thus an advanced multidisciplinary field based on the cooperation of experts with different technological and scientific backgrounds to regenerate damaged tissues by the synergic combination of cells, responsible for the synthesis of new tissue, biochemical/physical stimuli, for inducing specific cellular response, and implanted 3D biomaterial scaffolds, acting as templates for supporting and guiding new tissue ingrowth and regeneration, according to the general operative cycle depicted in **Figure 1.5**.

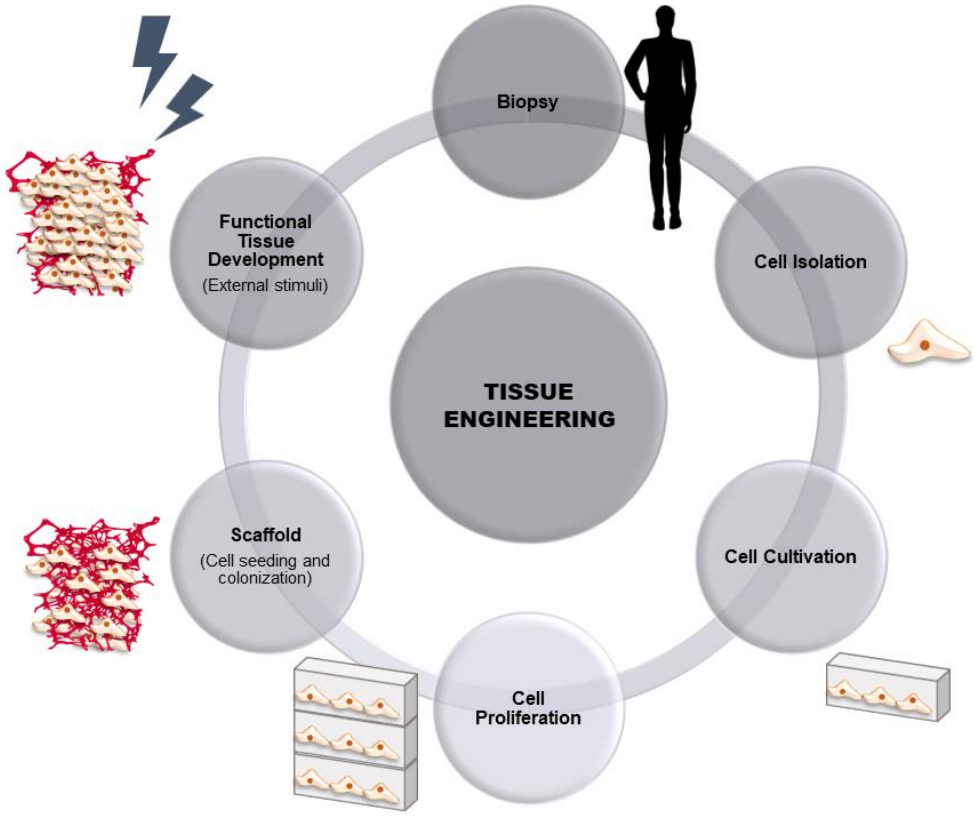

Figure 1. 5. Schematic representation *of a tissue engineering cycle.*

The suitability of a biomaterial for use as bone graft mainly relies on four important properties, described by Albrektsson et al. [78]:

i) *Osteoconduction*, which is the capability to induce cell attachment and allow osteoblasts and osteoprogenitor stem cells to migrate within the 3D volume of the graft;
ii) *Osteoinduction*, which is the capability to induce the differentiation of pluripotent stem cells to bone-forming cell-lineage, which, in turn, induce osteogenesis;
iii) *Osteogenesis*, which is the capability to promote new bone formation by donor cells derived from either the host or graft.
iv) *Osteointegration*, which is the capability of the implant to establish a stable chemical interface with the host tissue, without triggering any foreign body

reaction, which might compromise the right interaction between the material and the native bone.

Current clinical practice for the management of extended bone defects is mainly based on the transplantation of autologous bone, due to its ability to support tissue regeneration without triggering any adverse reaction. It is easy to see that the main strength which makes autologous bone still the golden standard among bone substitutes, is its obvious similarity to the native tissue thus meeting both mechanical and biological requirements. This allows easily avoiding any immunogenic response and rejection problems, as well as the risks of pathologies transmission, as the donor is the patient himself.
However, some drawbacks deserve to be mentioned, such as limited tissue availability, the presence of a second surgical site, and other severe complications, including chronic pain, dysesthesia and risk of infections. Moreover, the need to remove bone from the donor site makes it necessary to perform the surgery under general anesthesia, carrying additional risks to the patient [79].
The first alternatives to autologous bone transplantation are allotransplants and xeno-transplants, based respectively on the use of bone grafts from genetically different donors of the same species (cadavers) or other species (animals or vegetables); although these approaches partially solve the issue of tissue availability and donor site morbidity, as the source is external, they introduce the great problem of disease transmission and development of a severe immune response, thus making it mandatory the administration of anti-rejection therapies. Another great limit related to the use of allograft and xenografts, lies in the high costs of sterilization and storage, not necessary for autologous bone [80].

1.4.2 Looking for the ideal bone graft: general guidelines for scaffold design and manufacturing

In the last decades, the need for synthetic bone grafts remarkably increased due to both the growing ageing population and the increasing rate of occurrence of invalidating diseases such as tumors and obesity, which made it urgent to find effective alternatives to meet the growing demand.
In recent years, new classes of materials and innovative manufacturing techniques have been introduced, bringing great new opportunities in biomedical field. In this regard, for example, the introduction of additive manufacturing technologies (AMTs) has represented a big step forward in achieving high level of reproducibility and standardization of manufacturing processes, with the possibility to obtain patient-specific products as undisputable added value [81].
However, despite latest advances in material sciences and manufacturing technologies, the ideal scaffold for bone tissue engineering is still far from a concrete realization: considering the minimal requirements that an ideal bone graft should exhibit, reported in **Table 1.4**, bone is in fact a challenging tissue in many respects.

Table 1. 4. List of the minimum requirement that a bone scaffold should match in order to be used in a Tissue Engineering approach.

Biocompatibility	- Promote cell adhesion and proliferation - Promote cell differentiation and migration - Promote ECM synthesis - Induce minimal immune response - Avoid releasing toxic degradation products
Bioactivity	- Create a stable bonding interface with the host tissue - Promote bone cell activity and osteogenesis
Biodegradability	- Match the physiological healing time of the tissue
Mechanical properties	- Share mechanical load with the host bone - Maintain mechanical integrity during degradation and tissue remodeling
3D-structure	- Open-cell architecture - Promote mass transport - Support cell migration, vascularization and bone ingrowth
Manufacturing technology	- Cost effectiveness - Scalability - Repeatability/reliability - Sterilization, delivery and storage of the final product

Apparently, biocompatibility and bioactivity requirements seem to be the easiest ones to be satisfied, in fact, many different biomaterials are now available for bone tissue engineering applications [82].
In general, the choice for the realization of bone grafts falls on metals, bioactive ceramics, bioactive glasses, natural or synthetic polymers or composites of these [82].
However, the most important aspect concerns materials degradability in contact with body fluids [83]. In fact, in a typical tissue engineering approach, the scaffold is not prosthetic and has not to be intended as a permanent implant. This means that the scaffold should gradually degrade in order to be replaced by and in tune with the body own's newly generated biological tissue.
According to what said up to now, bone healing rate is not a simple aspect to manage as it is function of multiple variables, including first subject characteristics (age, sex and general health conditions) and then anatomical factors (interested site, type of bone).
It is known, for example, that in young individuals, fractures normally heal to the point of weight-bearing in about six weeks, with complete mechanical integrity not returning until approximately one year after fracture, but in the elderly the rate of repair slows down [84].
This means that, in first approximation, the use of the same material in different clinical cases could not be equally performant.
Another critical aspect to be considered when designing scaffolds intended for bone regeneration is the achievement of a right balance between mechanical properties and 3D porous structure, both fundamental to induce the physiological growth of new bone.

The relation between mechanical properties and porosity features imposes that as the porosity and the mean pore size of the scaffolds increase, the mechanical strength is dramatically affected: in this regard, it is necessary to find a compromise between good mechanical resistance and suitable microporous features to provide adequate mechanical integrity while favoring tissue ingrowth and vascularization of the bone substitute.

From a mechanical point of view, one of the most critical aspects, especially in load bearing applications, is the achievement of a suitable primary stability of the implant as soon as possible after the surgery. It is thus important to have a good matching between the mechanical properties of the scaffold and the surrounding tissue to satisfy the physiological demand of native bone without inducing tissue resorption; as previously mentioned, in fact, bone cells act as mechano-transductor, modulating their metabolism as a consequence of the stimuli that are received. It has been reported indeed that the stimuli derived from scaffold deformation are able to highly influence osteo inductive phenomena and this is the reason why mechano-transduction strategies are widely used to allow osteoinductive fluid flow within the scaffolds [85].

3D scaffolds have to be characterized by a highly interconnected porous structure opportunely designed to promote cell penetration and guarantee suitable mass transport properties. An open cell-architecture is not only fundamental to allow oxygen supply and nutrients exchange but also for a proper elimination of the waste products from the core of the scaffold to the peripheral areas. Moreover, the mean pore size of the scaffold should be carefully considered as pores need to be large enough to allow cell migration in the scaffold but small enough to have a sufficiently high specific surface to reach a critical cellular density on the surface of the scaffold. As a result, for each specific application it is possible to define a critical range depending on the cell phenotype.

Studies suggested that a bimodal pore distribution is beneficial for the development of functional bone: pores below 100 μm have been reported to favor cell attachment on the surface of the scaffold, while a pore size from 100 to 500 μm promote cell migration, proliferation and differentiation through the entire 3D volume, favor neovascularization and improve mass transport of oxygen and nutrient [86].

In this regard, another key parameter is represented by the intrinsic permeability, usually determined by combining 3D imaging, flow mathematical and physical modeling and numerical simulations of the scaffold physical properties. It has been demonstrated that a minimum value of $3 \cdot 10^{-11}$ m^2 is the permeability threshold to ensure scaffold vascularization and proper mineralization of the newly formed tissue [86].

Last, but not least, the manufacturing technology used to produce the scaffold has to be cost effective and repeatable in order to scale up the production while containing costs and guaranteeing high quality levels of the final products. It is fundamental to develop manufacturing processes responding to good manufacturing practice standards to favor the spread of tissue engineering in clinical practice. Among the other factors, delivery and storage of the final products have to be well defined in order to preserve its integrity and thus, its functionality.

1.5 Bone regeneration and tissue engineering: from static cell cultures to multifunctional bioreactors

Static *in vitro* cultures for small cellular constructs and cell monolayers have been employed for a long time with enthusiastic results in several medical fields, particularly in urology [87] and dermal regeneration [88].
These cultures techniques are able to provide suitable nutrient and oxygen supply to cells and tissues relying mainly on diffusive and convective mechanisms, which however become definitely less efficient when dealing with bigger cellular constructs, characterized by comparable dimensions in all the directions of the 3D space [89].
This aspect can be easily explained by considering the mathematical expressions of the two physical laws governing mass transport phenomena in static cell cultures: the Fick's first law of diffusion (**Equation 1.1**) and the Stokes-Einstein equation (**Equation 1.2**) [90]:

$$J = -D\frac{d\varphi}{dx} \quad \textbf{1.1}$$

$$D = \frac{kT}{6\pi R} \quad \textbf{1.2}$$

According to the Fick's first diffusion law (**Equation 1.1**), the mass flux is related to the gradient eventually generated at the medium/cells interface, where J is the diffusive flux (mol m^{-2} s^{-1}), D is the diffusion coefficient (m^2/s), φ is the concentration in ideal mixtures (mol/m^3) and x is the position (m).
The Stokes-Einstein equation (**Equation 1.2**), instead, puts in relation the radius of the diffusing particle R (m) and the temperature T (°C) to the diffusion coefficient D (m^2/s) through the Boltzmann constant k. As the volume of a sphere is proportional to the cube of the radius, it results that the diffusion coefficient D is inversely proportional to the cube root of molecular weight [90].
It is thus clear how increasing the number of cells and, even more so, using 3D-porous substrates for cell attachment and proliferation, might dramatically affect nutrient/oxygen supply and catabolites elimination if proper strategies for medium refresh and fluids recirculation are not adopted [91].
The main effects resulting from the application of static cultures to 3D constructs are [90], [92]:

- Poor homogenization of the newly formed tissue
- Development of a necrotic center
- Gradient formation
- Limited tissue size
- Static environment

As a result, the introduction of 3D-porous scaffolds as support to the regenerative process of organs and tissues opens up new issues and challenges in cell culture

strategies, imposing a shift from conventional static cultures to 3D dynamic conditions able to reproduce as closely as possible the physiological environment.
Due to the increasing complexity of 3D dynamic cell culture systems, operating an accurate control and monitoring of all the parameters is becomes a fundamental and sometimes complicated task not to be underestimated as it may affect cell viability and thus the whole outcome of the culture. Some of the crucial parameters to be continuously monitored and controlled to ensure a correct development of the tissue include physical stimulation of the constructs, pH, temperature and humidity conditions, as well as the presence of signaling molecules and growth factors in the culture environment [89].

Bioreactors are considered smart devices intrinsically able to reproduce the *in vivo* environment under controlled and strictly monitored conditions.
These devices are in fact able to supply multiple stress regimes and signals of different nature (i.e. compressive, shear and rotational forces, as well as electrical stimulation) following standardized and optimized protocols.
This actually represents an added value to BTE strategies, since the newly formed tissue will be able to growth as similar as possible to the physiologic bone in all its features, both functional and morphological ones.
Moreover, the possibility of scale-up and standardize the culture procedure and thus the production of engineered bone grafts represents an attractive opportunity to allow an actual clinical usage of this technology [89].

In the following section additional details on bioreactor systems for bone regeneration will be provided, paying particular attention to the general minimal requirements, the currently available designs and the most important and influencing aspects to be considered in order to obtain a functional engineered bone substitutes ready for implantation.

1.5.1 TE bioreactors: general project requirements

BTE bioreactors have been introduced to overcome the limits related to the application of static cell culture conditions to 3D scaffolds in tissue engineering applications.
Even though the design of a bioreactor has to be optimized according to the type of the tissue and specific clinical application, there are some common crucial points to be always considered when developing a TE bioreactor.
Some of these are closely related to biological aspects: last generation bioreactors for TE, in fact, should be able to control and improve cell growth and new tissue formation, guarantee uniform cell distribution, provide and maintain a controlled physiological environment where cells and tissue can grow under the action of *in vivo*-like stimuli, improve mass transport mechanisms by implementing optimized mixing strategies and enable reproducibility, control and automation of the whole process.
Some other aspects, instead, are more related to practical issues and consider the ease of use and the compatibility of the device with the common laboratory practices. As a result, bioreactors should be thought to be constituted of modulable

components, to be quickly and easily assembled, small in dimension, sterilizable and reusable. Moreover, when graphical interfaces are necessary for monitoring culture parameters, they should be intuitive and user-friendly in order to reduce the possibility of errors by different operators.

Figure 1.6 summarizes the main functions that a generic bioreactor system for TE applications should carry out during the development of functional biological tissues. All these functions have to be carefully considered when designing a new device, in order to adapt the culture conditions to the specific cellular construct and, thus, to the final clinical application.

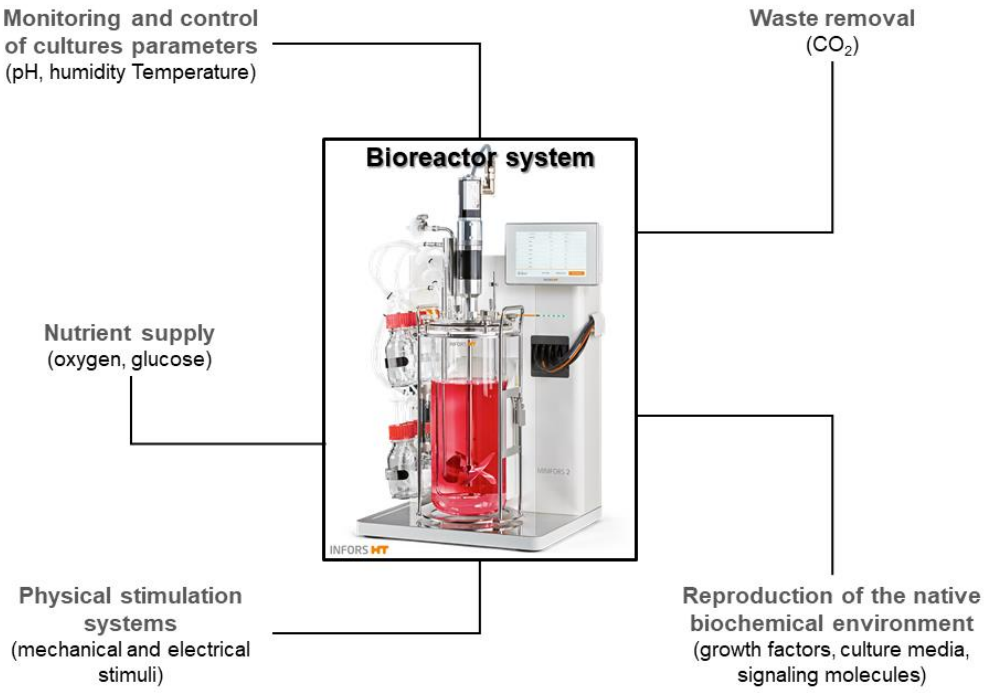

Figure 1. 6. Schematic of the most relevant aspect to be considered in the design of a bioreactor system for 3D dynamic cell cultures. In the picture, by way of illustration, INFORS HT Minifors 2 bench-top bioreactor system.

Another important aspect to be considered is the cost effectiveness related to the realization and the use of these systems: limiting the costs of both the manufacturing processes and the actual implementation of dynamic cell cultures, in fact, has to be considered the real key to make bioreactors available in clinics, thus closing the gap between research achievements and the final applications [30], [89], [90], [92].

1.5.2 BTE bioreactors type: a brief overview

At this point of the dissertation, it should be clear that the main advantage related to the implementation of dynamic cell cultures in bioreactors is given by the possibility to mimic the physiological conditions in a highly controlled and monitored environment, reducing operator-dependent variability and improving the reproducibility and the standardization of cell seeding, expansion and differentiation protocols.

Over the last decades, several type of bioreactors for bone tissue have been designed and developed (**Figure 1.7**), each one exhibiting both advantages and disadvantages, where the main differences are based on operating principle, ease of use, cost/effectiveness, osteogenic stimuli, as well as control and monitoring units integrated within the system, as summarized in **Table 1.5**.

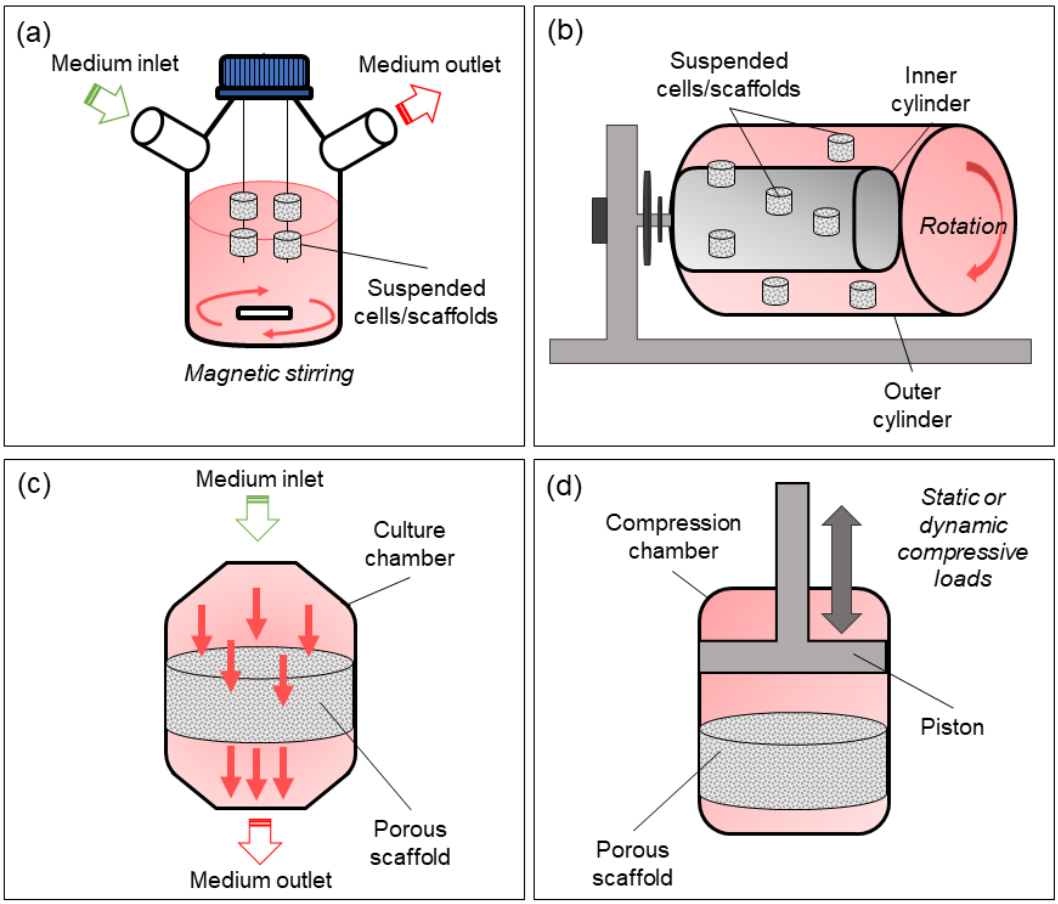

Figure 1. 7. Types of bioreactors optimized for bone tissue engineering applications: a) spinner flask; b) rotating wall vessel; c) perfusion; d) compression.

Table 1. 5. Bioreactor-based systems for bone tissue engineering strategies.

Bioreactor type	Characteristic	Function	Advantages	Disadvantages
Spinner flasks bioreactor (SF)	Cylindrical container with side arms (inlet + outlet) and a mixing element. Scaffolds are in fixed position	The mixing element generates a convective flow and hydrodynamic forces which support mass transport	- hMSCs differentiation into osteoblasts - Improved mass transport	- ECM formation limited to the scaffold's surface - Turbulent shear at the surface
Rotating wall vessel bioreactor (RWV)	Two concentric cylinders: the outer one is the culture chamber filled with the medium and contains scaffolds and microcarriers, while the inner cylinder is static and allows gas exchange.	The outer cylinder rotates generating gravitational forces that acts on cell constructs while accelerating the culture media	- Low turbulence - Different possible configurations	- Lower expression of osteoblastic markers compared to SF - Cell growth and mineralization limited to the scaffold surface - Collisions with the walls and subsequent cell damage
Perfusion bioreactor (P)	Hydraulic circuit composed of a culture chamber, a reservoir and a pump. Direct and indirect perfusion configurations available	The culture medium is forced through the chamber and the scaffold by the presence of a pump system which produces a continuous or not continuous fluid flow	- More uniform mixing of the medium compared to sf and RWV - Better environmental control and physical stimulation of cells in larger constructs - ALP activity and osteopontin secretion	- Indirect perfusion configuration may lead to the development of gradients
Compression bioreactors (C)	System composed of a compression chamber, the cell/scaffold construct and a piston	The piston applies static or dynamic compressive loads directly to the constructs.	- Mechanical loading promotes functional osteogenic differentiation	- Lack of *in vivo* studies - No univocal stimulation protocols identified

Spinner flasks

Among BTE bioreactors, spinner flasks (SFs) represent the simpler design (Figure 7 a). They consist of a bottle with two side arms (medium inlet and outlet) filled with culture medium, in which scaffolds and cellular construct are suspended in fixed position by mean of vertical needles. The agitation of the medium is

guaranteed by a stirrer plate acting on a magnetic bar, which generates convective forces able to mitigate the formation of nutrient gradients [93].

Thanks to the possibility to accommodate a large number of scaffolds, SFs have the potentiality to be used for the production of clinically relevant volumes of engineered bone substitutes. However, the continuous mixing of the culture media usually generates high shear stress values and turbulent flow, which limits the new tissue growth to the surface of the scaffolds, thus making SF bioreactors almost unsuitable for the optimization of large cellular constructs [94]. For this reason, their use is currently dedicated to preliminary cell seeding [92].

Rotating wall vessel bioreactor

The rotating wall vessel (RWV) bioreactor, schematically depicted in Figure 7 b, was developed at NASA's Johnson Space Center with the goal of reducing the shear stresses generated during the operations of launch and landing of the space shuttles but, after testing the device on earth, it was observed that cells aggregated to form structures similar to tissues.
The RWV system was originally based on:

i) A solid body rotation, a vessel which rotates horizontally around its axed, filled with culture media.
ii) Silicon rubber membrane for oxygenation

RWV bioreactors generate a low turbulence culture environment which favors the formation of large cellular aggregates under microgravity conditions.
However, just like SFs, they are also are limited to small-sized constructs due to insufficient mass transport inside the scaffolds. In addition, several studies reported poor osteogenic differentiation due to an inadequate stimulation given by the low shear stress [30], [92], [93].

Perfusion systems

Bioreactors based on flow perfusion have been developed with the aim of exceeding the limits of the systems described above.
Perfusion bioreactors (P), in fact are characterized by more homogeneous mixing conditions and a better control on the culture environment, as the culture media is directly perfused through the scaffolds in a continuous or non-continuous flowing mode by the action of a pumping system.
Given the scientific relevance of such devices in the development of engineered bone grafts, it was decided to deepen the most relevant aspects concerning their design, operating principle and applications in a dedicated section (*Paragraph 1.4.3*) [94].

Compression systems

In vivo, bone is physiologically subjected to the combination of different mechanical loads under compression, tension, bending, shear and torsion conditions.
Compression bioreactors (C) were developed with the aim of reproducing more faithfully the physical stimulation of bone in the biological environment by

applying hydrodynamic mechanical forces by mean of a piston/compression system moving under the action of a motor [30], [92], [93].
Compression bioreactors have been coupled with perfusion systems to enhance mass transport and nutrient supply, with promising results in long-term cultures of large cell/scaffold constructs [95].

1.5.3 Bioreactor systems for bone tissue: a focus on perfusion devices as multifunctional systems for advanced BTE applications

In vivo, bone is continuously subjected to the application of cyclic loads which influence fluid flow through the tissue and produce shear forces which influence the metabolic activity of osteoblast and osteocytes.
Hence, load bearing is a major requirement characterizing the tissue original function, which requires the development of strategies optimizing simultaneously mass transfer and physical stimulation in order to provide physiologically relevant loads, in accordance to the specific clinical needs [30].
As a result, perfusion and shear stress are the two important pillars on which the design of a bioreactor intended for bone tissue engineering should be based.

In these regards, flow-perfusion cultures present several advantages.
First of all, compared to SF and RWV systems, as the fluid flow is forced through the scaffold directly inside the pores, these bioreactors are able to successfully overcome external and internal diffusional limitations thus mitigating the risk of formation of a necrotic center and inducing the mineralization of the ECM over the entire volume of the 3D strut.
Moreover, the extreme versatility of these devices, given by the possibility to adapt the circuit to multiple purposes, makes it possible to shift from seeding conditions to culture ones and vice versa by simply optimizing perfusion parameters.
It is sufficient, in fact, to equip the basic tubing system with an additional seeding loop, injection points and valves to inoculate cells and isolate the main circuit during the procedure [94].
Apart from these valuable opportunities, of course the undisputable added value of these devices is the great opportunity to exploit the perfusion circuit to simultaneously apply mechanical stresses to the cultured cells, while providing a uniform mixing of the media under optimized flowing conditions.
This is possible thanks to the action of hydrodynamic forces generated by the movement of the culture media upstream and downstream the porous scaffolds [96].

Over the years, several perfusion bioreactors have been optimized by different research groups, most of them presenting similar features in the design of the basic perfusion system, schematically depicted in **Figure 1.8**.

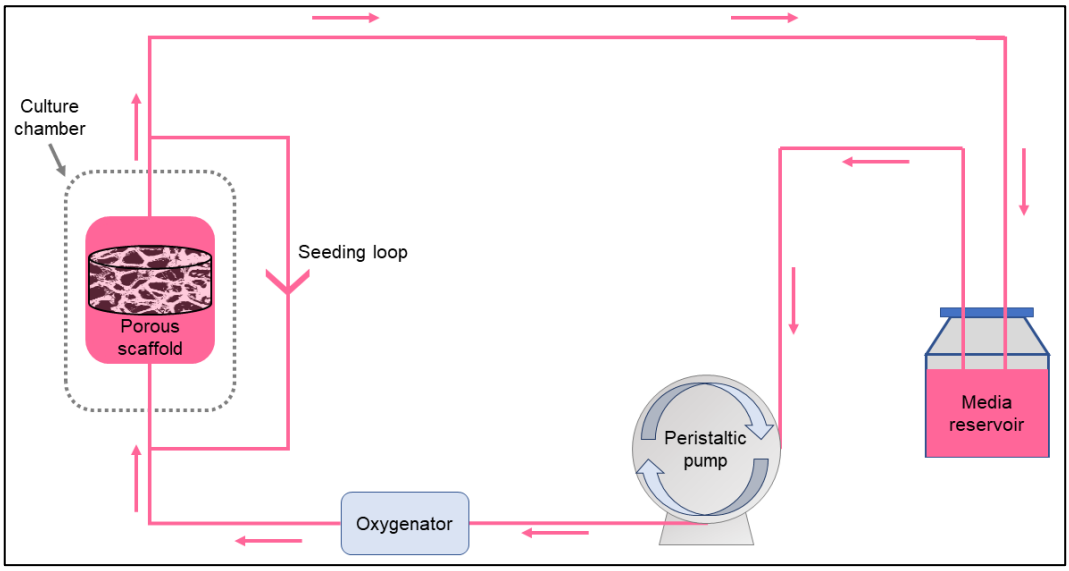

Figure 1. 8. Schematic of a typical perfusion system equipped with media oxygenator (optional).

One of the most important parameters to be optimized when designing a perfusion system is the shear rate to apply to cellular constructs, which has to be adapted according to the operating conditions of the perfusion systems.
Different values, indeed, have to be set depending on whether the bioreactor is used under cell seeding, expansion or differentiation conditions.
In addition, shear rate has to be optimized according to the features of the scaffold, including both material properties (i.e. material compliance) and porosity levels. Minimal porosity requirements, in fact, have to be satisfied in order to avoid an uncontrolled increase of pressure inside the culture chamber, resulting in the application of high shear stresses to cells and constructs.
Thus, for a given material, lower shear rates have to be applied for less porous scaffold, in order to facilitate direct perfusion.
Given the number of parameters involved, defining a unique range for shear rate is still today considered a controversial matter. In this regard it is believed that computational fluid dynamic (CFD) would play an essential role to facilitate the determination of scaffold-dependent flow rates for bone tissue engineering experiments in laboratory practice to avoid or minimize the traditional trial and error approaches, which are time-consuming and expensive.

Zhao and coworkers [97] recently combined computational fluid dynamics (CFD) and mechano-regulation theory to optimize flow rates of a perfusion bioreactor according to various scaffold's geometries, including in the study pore shape, porosity and average pores dimension with the aim of maximizing ECM mineralization induced by shear stress.
Optimal flow rates were identified in the range 0.5-5 mL/min, corresponding to a fluid velocity of 0.166-1.66 mm/s, as indicated in **Table 1.6** [97].

Table 1. 6. Recommended fluid velocity ranges to maximize ECM mineralization according to scaffold's porosity features [97]

Porosity features of scaffolds		Fluid velocity/ mm/s								
		0.03	0.07	0.17	0.33	0.66	1.00	1.66	2.66	3.98
Pore shape	Spherical									
	Rectangular									
Pore diameter	0.2									
d_p/	0.3									
mm	0.5									
Total Porosity	50									
ε_0/	70									
vol.%	90									

However, in a previous study, a shear rate equal to 4 mL/min was found not to produce great benefit compared to static culture conditions [98].
In a review by Gaspar et al. [94], the optimal range for ECM mineralization was identified on the basis of previous literature analysis between 0.2 and 1 ml/min, where higher values lead to enhanced matrix deposition, while very low flow rates facilitate cell attachment and improve cell viability.
Optimizing fluid flow dynamics is of primary importance as it affects the mechanical stimulation of cells inside the device and depends both on the bioreactor's inlet flow rate and 3D-scaffold architecture.
In a very recent study, Saatchi et al. used CFD simulations to assess fluid dynamic in 3D-printed scaffolds with different angular orientations between strands in each layer inside a perfusion bioreactor at different inlet flow rates.
The study revealed the existence of a linear relationship between the bioreactor inlet flow rate and the average fluid velocity, average fluid shear stress and average wall share stress inside the scaffolds; in particular, by decreasing the angular orientation between strands in each layer and increasing the inlet flow rate, the magnitude and distribution of fluid velocity, fluid shear stress, and wall shear stress inside the scaffold increased [99].
In another computational study, finite element method was used to investigate the effect of hydrodynamic of fluid flow inside a novel bioreactor combining perfusion with rotating forces to enhance cell growth and osteogenic differentiation.

Velocity values and shear stress were calculated implementing Navier–Stokes and Brinkman equations. The enhanced cell proliferation and higher ALP activity observed in the analyzed system suggested the possibility to successfully combine multiple stimulation strategies such as rotation and perfusion to provide the correct environment for bone tissue engineering applications [100].

Prototypes of perfusion bioreactor and perfusion + rotation combined systems developed by Nokhbatolfoghahaei and coworkers [100] are depicted in **Figure 1.9**.

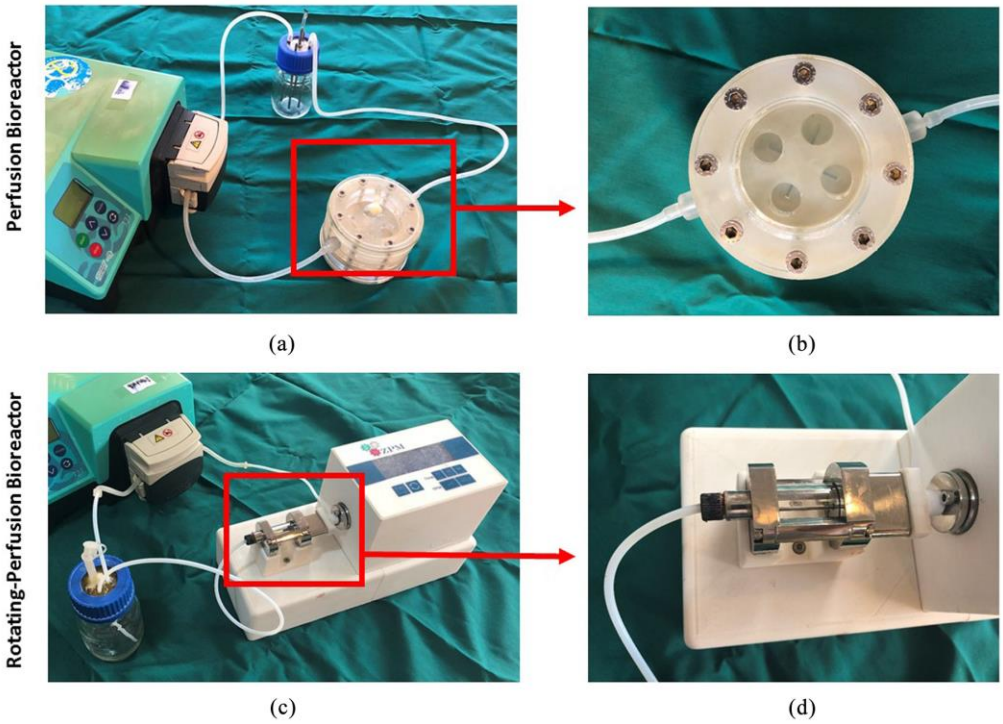

Figure 1. 9. Prototype model of perfusion (a) and rotating + perfusion (b) bioreactors and the respective culture chambers (b and d) designed by Nokhbatolfoghahaei and coworkers. Image reproduced with permission from [100].

Among the various available designs for perfusion systems, the culture chamber represents one of the most common differentiating elements.

A unique design for the culture chamber, in fact, is almost impossible, as it has to be necessarily optimized according to:

i) the features of the scaffold (geometrical shape and material's properties)
ii) the specific function to be carried out (cell seeding, differentiation or both)

In all these cases, the main objective is to optimize the design in order to facilitate direct perfusion of the porous scaffold, avoiding the formation of gradients inside the culture chamber. Moreover, the presence of sharp edges has to be avoided to facilitate cleaning procedures and minimize the formation of stagnation areas and vortexes, potentially able to trigger metabolic pathways leading to cellular death.

In this regard, Bhaskar and colleagues [101] recently developed a modular, autoclavable and cost-effective bioreactor system suitable for large scaffolds with different shape and size. The system, optimized for long term cell culture under dynamic flow conditions, was able to successfully support the osteogenic differentiation of human embryonic stem cell-derived mesenchymal progenitors (hES-MP cells) cultured on large polyurethane (PU) scaffolds (30 mm diameter × 5 mm thickness) in osteogenesis induction media (OIM).
The design of the culture chamber developed by Bhaskar et al. [101] is described in **Figure 1.10**.

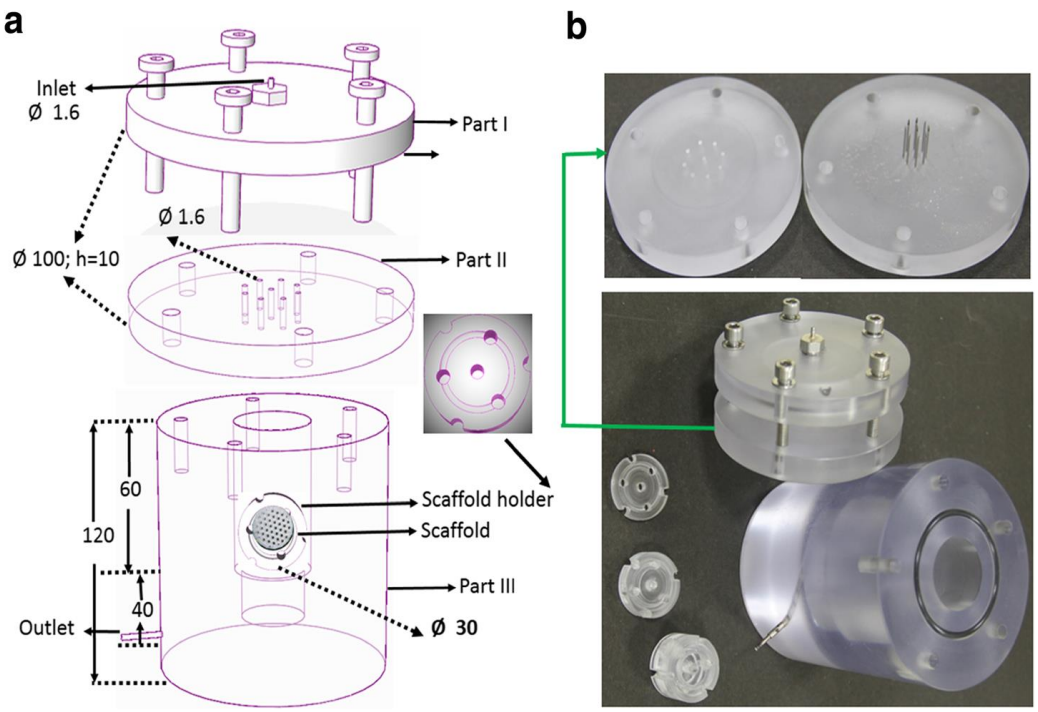

Figure 1. 10. Design of the perfusion bioreactor: (a) Computer Aided Design (CAD) 3D-model and (b) photographs of the various components: Part I – sealing component with a single inlet connection; Part II – interchangeable multichannel circular disk or multi hypodermic needle disc, providing inlet channels for the culture media; Part III - chamber containing the scaffold. All the units are represented in mm. Image reproduced with permission from Bhaskar et al. [101].

Most of the perfusion systems described in literature support steady perfusion, i.e. are based on a continuous flow through the scaffolds. However, there is the possibility to incorporate oscillatory or pulsatile flow, which seems to improve the quality of the tissue.
In this regard, Stavenschi et al. [102] carried out a systematic analysis of oscillatory fluid flow (OFF) parameters to investigate the MSCs osteogenic responses and late stage lineage commitment. Cells were exposed to different OFF (1-5 Pa; 0.5-2 Hz) up to 4h stimulation. The study demonstrated the positive effect of OFF on the osteogenic response of MSCs in a shear stress magnitude, frequency, and duration dependent manner that is gene specific.

Undoubtedly, perfusion bioreactor systems represent more complex devices requiring the optimization of multiple parameters to support the formation of functional bone tissue.
However, concerning osteogenic differentiation and mineralization, significantly better results have been reported compared to SF an RWV devices, but additional efforts are still required to promote the use of these promising systems in clinical practice for the production of customized ready to use bone substitute.

It is strongly believed that great advantages can be established by substituting current therapies with engineered bone grafts, mainly deriving from the possibility to use autologous cells for the development of clinically safe and highly reliable patient-specific bone substitutes.

In this regard the open challenges to be faced in the future by the global research community are:

i) the identification of univocal flow-rate ranges, optimized according to the in vivo-like conditions and definition of globally recognized guidelines for the setting of operating conditions.
ii) the development of multifunctional systems able to support both cell culture and dynamic cell seeding, which would remarkably improve the clinical relevance of bioreactor-based system
iii) the development of highly reproducible and reliable protocols aimed at improving the automatization of processes, thus allowing to scale-up the use of such devices from laboratories to industrial scale.
iv) The integration of additional controlled systems for the physical stimulation of constructs.

Chapter 2

Bioactive glasses: Properties and applications in bone tissue engineering

2.1 Introduction to bioactive glasses

The invention of bioactive glasses (BGs) represented a true revolution in materials science and biomedicine, continuing, still today, to inspire numerous generations of young researchers all over the world [103].

The reason for such a keen scientific interest lies in the combination of bioactive properties with the amorphous nature typical of glassy materials, determining a clear distinction between BG-based implants and first/second-generation biomaterials, widely used in the past. At the beginning, indeed, biocompatible implants were intended to be completely inert in contact with the biological environment, i.e. they preferably had not to induce any reaction within the body [104].

On the contrary, the term "*bioactive"* refers to the peculiar capability to establish a stable bond with biological tissues, resulting from the chemical interaction between the material surface and the physiological environment and leading, in a very short time, to the complete integration of the implant.

In BGs, this process is associated to the progressive conversion of the material into hydroxyapatite (HA) resulting from a continuous ion-exchange mechanisms at the material/fluid interface, which is furthermore responsible for the upregulated expression of osteogenetic factors [105]–[107].

Basing on the level of interaction with the physiological environment, i.e. the ability of the material to provide a controlled and continuous supply of chemical cues able to stimulate cell metabolic activity, bioactive materials can be classified into [108]:

i) *Class A bioactive materials*, exhibiting both osteoconductive and osteinductive properties (as defined in **Chapter 1**), favor cell colonization by osteogenic stem cells, thus determining both an extracellular and intracellular response given by the interaction with ions released from the material's surface.
ii) *Class B bioactive materials*, exhibiting only osteconductive properties determined by extracellular factors.

Among bioactive ceramics, both calcium phosphates and BGs have been successfully used in orthopedics and dentistry for the regeneration of bone defects. However, compared to BGs, calcium phosphate ceramics, such as stoichiometric hydroxyapatite, are characterized by higher chemical stability in physiological environment and are classified as *class B* bioactive materials. On the other hand, the disrupted silicate structure, characterizing most of BG-based systems, exhibits faster bone bonding kinetics due to the presence of a highly reactive amorphous phase in contact with body fluids.

The first BG-based system, known by the name of 45S5 Bioglass® (commercially available since 1984), was developed in 1969 by Larry L. Hench on the basis of the Na_2O-CaO-SiO_2 ternary state diagram (**Figure 2.1**), with the aim to optimize a new-generation biocompatible materials able to survive the exposure to the aggressive physiological environment [109].

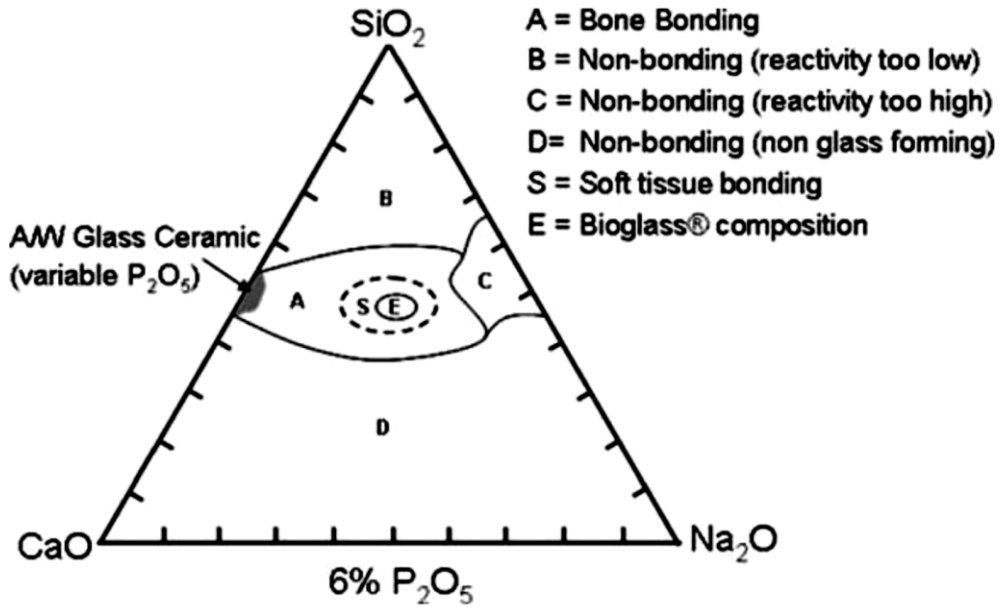

Figure 2. 1. Compositional diagram for bone bonding. Image reproduced with permission from Hench et al. [109].

Specifically, 45S5 bioactive system is based on a quaternary oxide composition (45S5, 45SiO_2- 6P_2O_5- 24.5Na_2O- 24.5CaO, wt.%) [109], where silica (SiO_2) is the

glass forming oxide and SiO_4 tetrahedron is the basic unit of the network, sharing up to four oxygen atoms and creating –Si–O–Si– bridging oxygen bonds, which stabilize the network. On the other hand, both calcium and sodium, acting as modifier oxides, disrupt the glass structure by creating non-bridging oxygen bonds. The relatively low silica content (≤ 60 mol.%), as well as the high number of modifiers, make this glass highly reactive in contact with body fluids, leading to a rapid conversion to HA and inducing the differentiation of osteoprogenitor stem cell to an osteoblastic phenotype, responsible for the production of a well-mineralized bone matrix.

Since the discovery of the first bioactive composition, many other bioactive systems with analogous or even improved characteristics have been developed.
In particular, beside common silicate glasses, often characterized by too long conversion times compared to the healing rate of biological tissues, B_2O_3 [110] and P_2O_5 [111] have been also proposed as alternative network forming oxides in all those applications requiring enhanced reactivity and faster HA deposition kinetics, with promising results in soft tissue repair (wound healing, dermal repair) [112] and muscles, tendons and ligaments regeneration [113], respectively.

Consequently, the high versatility of BG-based systems both in terms of compositional features and processing strategies, makes them widely appreciated in different medical fields, shifting from hard [114] to soft tissue regenerative approaches [115] (**Figure 2.2**).

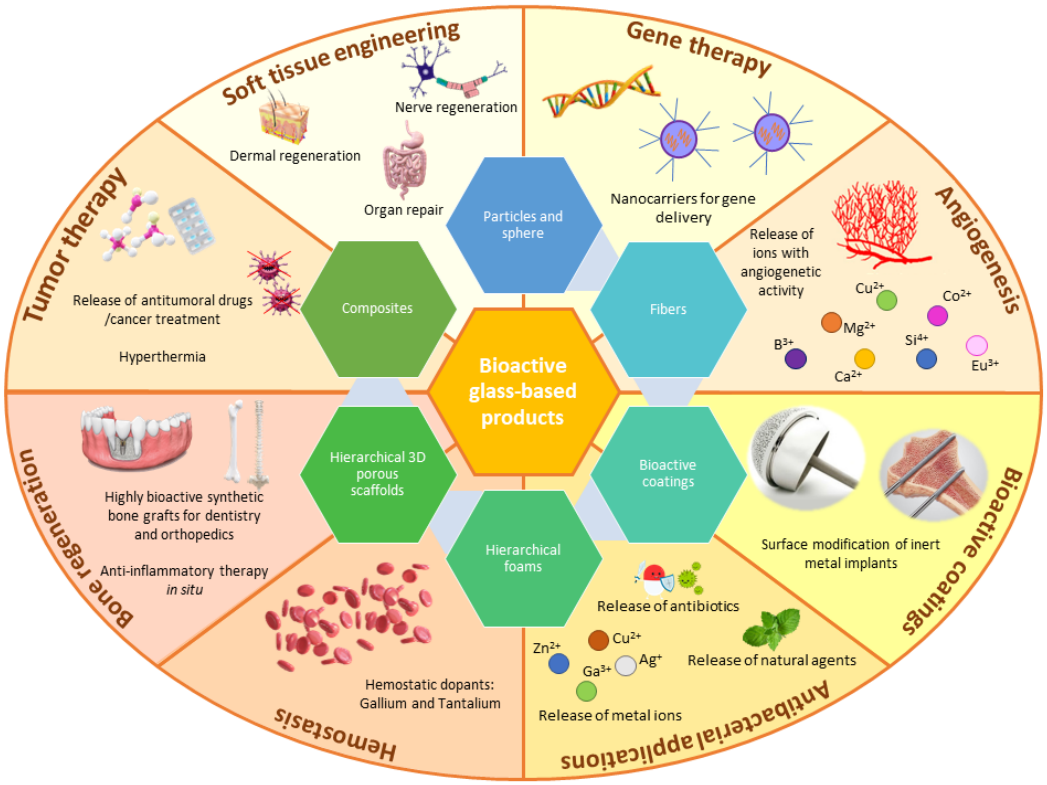

Figure 2. 2. Overview of clinical applications of BG-based systems.

Although the high therapeutic efficacy of BGs has been successfully demonstrated in very different applications (e.g. tumor treatment [116], [117], drug delivery

[118], burns management [119] and nerve regeneration [120]), their capability to be gradually osteo-integrated while stimulating specific osteogenetic pathways, make them materials of choice primarily in bone defect management.
As a direct consequence, the possibility to use BGs as basic material for the realization of synthetic bone grafts, i.e. three-dimensional (3D) porous scaffolds, was soon explored by numerous research groups and, over time, several manufacturing strategies have been optimized for obtaining 3D bone-like architectures able to support tissue ingrowth and regeneration [121], [122]. Nevertheless, in the light of the observation made in **Chapter 1**, there is still a long road ahead before BG-based scaffolds will be fully-fledge available in clinical practice.

Although fifty years have passed since the revolutionary discovery of BGs, this fascinating world has not yet reached saturation and there is still considerable room for improvement concerning a number of different aspects, from the synthesis of raw materials, to the optimization of scaffold manufacturing procedures. This is the reason why BGs and derived products continues to exert a powerful influence on applied academic research, from traditional bone engineering applications to latest-introduced research fields, such as tumor therapy and interfacial TE applications.

Within the present Chapter a general overview on BGs features is provided, including processing methods currently available for their synthesis. Then, the attention will be focused on BG-based porous scaffolds manufacturing processes. Three dedicated sections will delve into foam replica method (FRM), foaming strategies (FS) and robocasting (RC), constituting the manufacturing processes implemented within the present comparative research study, with the aim of outlining the most relevant processing parameters and criticisms able to exert a major effect on the final features of the scaffolds produced.

2.2 Mechanism of bioactivity and bone bonding

The bioactivity mechanism, first proposed by Hench [107], [109], is still accepted for silicate bioactive glasses and it is based on two main events:

i) The formation of an hydroxycarbonate apatite (HCA) layer on the surface of the material, culminating in the crystallization of the amorphous calcium phosphate layer;
ii) The dissolution of ionic products from the surface of bioactive glasses and the activation of osteogenetic pathways leading to the mineralization of the extracellular matrix.

As soon as the material comes in contact with physiological fluids, Ca^{2+} and Na^{+} are released from the surface of the material and replaced by H^{+} and H_3O^{+} coming from the surrounding environment. Si-OH silanol bonds are thus established on the surface of the material. At this stage, the pH of the interfacial solution markedly increases and a silica-rich layer forms on the surface of the glass (**Equation 2.1)**.

$$Si - O - Na^+ + H^+ + OH^- \rightarrow SiOH^+ + Na^+(aq) + OH^- \qquad \textbf{2.1}$$

During this stage, cations depletion within the material results in a net negative charge on the surface of the glass. The enhanced release of Na^+ species from the BG surface depends on the high ionic character of the Na-O bond compared to the Si-O one, exhibiting, on the other hand, a high covalent component.

The alkaline pH environment determines the breaking O–Si–O bonds by OH^- groups, disrupting the silica network.
Soluble silica is released in the form of $Si(OH)_4$ and silanol groups are exposed on the surface of the material, in direct contact with the solution (**Equation 2.2**).

$$Si - O - Si + H_2O \rightarrow Si - OH + OH - Si \qquad \textbf{2.2}$$

Then, the silica-rich layer, poor in Na^+ and Ca^{2+} ions is subjected to competitive condensation and re-polymerization reactions.

The micro-porosity of this intermediate reaction layer, from 30 to 50 Å, allows calcium and phosphate ions to migrate across the layer from the solution to the surface of the material and *vice versa.*

In the end, hydroxyl and carbonated groups are incorporated from the solution while the glass continues to dissolve. The calcium phosphate layer, initially amorphous, gradually crystallizes, becoming very similar to the nano-crystalline mineral phase observed in physiological bone, thus establishing a direct anchoring to the native tissue.

It was demonstrated that the presence of the HCA reaction layer promotes protein absorption onto the surface of the material, essential to induce the attachment and proliferation of osteoprogenitor stem cells and their subsequent differentiation to an osteoblastic phenotype, in charge of the synthesis of a well-mineralized bone matrix, which typically occurs within 6-12 days from the implant [123].

The bone bonding ability characterizing BGs is the direct effect of the rapid conversion of the material into HA upon contact with body fluids, according to the reaction mechanism described above.

Chemical composition, crystalline structure, and processing parameters of bioactive materials are all factors potentially able to significantly affect the reaction kinetics of the material in the physiological environment and thus, its therapeutic efficacy.

It has been demonstrated, indeed, that the bioactivity class of the material and the healing rate of bone tissue upon exposure are intimately linked. In particular, biomaterials belonging to *class A* are able to induce better and faster tissue healing compared to those belonging to *class B.*

This aspect is directly related to the mechanism of ion dissolution, which in turn relies upon the microstructural nature of the material, i.e. crystalline, semi-crystalline or amorphous.

In fact, ion release phenomena from the surface, responsible for the precipitation of the HA reaction layer, are mainly related to the amorphous phase, while crystalline ones improve the overall chemical stability of the system.
As a result, HA and calcium phosphates materials, belonging to *class B*, exhibit lower dissolution rates in contact with body fluids compared to BG fully-amorphous systems.
Compositional features of the material are also relevant. As an example, it was demonstrated that calcium deficient hydroxyapatite exhibits higher reactivity compared to stoichiometric one [124].
On the other hand, dealing with silica-based glasses, the bioactivity of the material is strictly related to the silica content, where a dramatical reduction in the bioactive potential has been observed for systems having a silica content higher than 60 mol.% [125]. In fact, glasses with lower silica content, are characterized by a less interconnected silica network resulting in a lower chemical stability.
Among the other strategies commonly implemented to modify the connectivity of glass silica network, the introduction of proper modifiers, able to improve or eventually decrease the reactivity of the glass, is one of the most effective, resulting in a wide variety of different bioactive compositions reported in literature.

Last but not least, synthesis and post-processing of BGs can induce important modifications in HA deposition kinetics and bone bonding ability, as it will be shown shortly.

2.3 Synthesis routes for making BGs

Nowadays, BGs can be produced both by traditional melt-quenching route and sol-gel chemical synthesis. Although most of the times these processes are put in competition, it should be simply noted that they actually offer different, both valuable, possibilities, to be properly considered according to the desired final outcome.

2.3.1 Melt-quenching route

Melt-quenching process is undoubtedly the most common and traditional way to obtain glass materials by melting of specific reactants, acting as oxides precursors. Actually, the production of BGs by melt-quenching route is not different from the procedures followed for obtaining conventional soda-lime glasses, with a greater attention to the purity of starting materials and equipment-contamination issues, aimed at guaranteeing high-quality and standardized medical products.
In a typical process, powdered rough reagents, typically carbonates and phosphates, are mixed in proper amounts, transferred into a dedicated crucible – made of platinum or alumina, properly selected to avoid contamination induced by diffusive phenomena - and heated up to the melting point.
In general, high melting temperatures are required for highly stable aluminosilicate compositions (T~1500-1600 °C), while the melting of borate and phosphate systems is usually carried out at lower temperatures, typically between 1200-1300°C.

According to the final application, it is possible to obtain products characterized by different shapes. Specifically, direct forming via casting into moulds leads to the production of dense monoliths, while water quenching leads to the production of a glass frit by sudden cooling. In general, glass frits are produced as intermediate step for obtaining fine glass powders with controlled grain size, as they can be easily mechanically grinded.
Sometimes, powders can be subsequently pressed to form compact pellets which are then sintered to achieve higher densification, or can be used as basic material for the production of scaffolds by different manufacturing strategies [126].

2.3.2 Sol-gel process

Compared to melt-quenching process, sol-gel synthesis is a relatively young technology introduced at the end of the 19th century and used for the first time in bioactive glass manufacturing only in 1991 [127].
In sol-gel process, silica nanoparticles form and assembly at room temperature thanks to hydrolysis and poly-condensation reactions catalyzed by proper chemical agents [128]. The glassy material is produced upon calcination treatments, performed at lower temperatures compared to the ones used for melting [129].

Within a typical sol-gel synthesis it is possible to identify three main phases:

i) preparation of a colloidal particle suspension, the sol;
ii) gelation of the sol, resulting in a more rigid and interconnected network in which pores and chains are usually immersed into a liquid phase;
iii) removal of the solvent by low-temperature thermal treatments which include ageing, drying and calcination.

Sol gel glasses for biomedical applications are usually obtained from the reaction of hydrolysis and polycondensation of alkoxides, such as tetraethyl orthosilicate (TEOS) and tetramethyl orthosilicate (TMOS).

The sol is prepared by mixing alkoxides and/or organometallic reagents in a wet environment (usually water and ethanol are used as solvents) in the presence of a catalyst, either acids or bases. The role of the catalyst is to lower the activation energy of hydrolysis (**Equation 2.3**) and polycondensation (**Equation 2.4 a** and **b**) reactions, which, at this stage, are competitive and proceed simultaneously.

$$\equiv Si - OR + H_2O \leftrightarrow \equiv Si - OH + ROH \qquad \textbf{2.3}$$

Hydrolysis

$$\equiv Si - OR + OH - Si \equiv \leftrightarrow \equiv Si - O - Si \equiv + ROH \ (2) \qquad \textbf{2.4 a}$$

Condensation with alcohol elimination

$$\equiv Si - OH + OH - Si \equiv \leftrightarrow \equiv Si - O - Si \equiv + H_2O \ (3) \qquad \textbf{2.4 b}$$

Condensation with water elimination

Where the R group indicates an alkyl functional group in the form C_xH_{2x+1} [130].

In sol-gel synthesis, achieving an accurate control on all the variables involved in the process is fundamental. In fact, even small changes related to temperature/pH conditions, oxides precursors, catalyst type or amount could affect the properties of the final product.

As an example, the kinetics of hydrolysis and polycondensation reactions have an influence on the gel structure. When an acidic catalyst is used, the first step of hydrolysis is the fastest one and the rate of reaction progressively decreases over time. This determines the formation of a weakly branched sol and the resulting gel is constituted by a fine network of linear chains which form well-ordered, hexagonal mesopores in the structure. Gels derived from acidic catalysis are highly reactive at the chain ends, conferring to the glass network the ability to easily deform plastically [131]–[133]. Moreover, it was observed that an increase in water content could led to a decrease in the mechanical strength of the gel, characterized by lower density, elastic, shear and bulk moduli.

Another factor influencing the hydrolysis reaction of TEOS is the H_2O: TEOS or EtOH: TEOS molar ratio, as well as the solvent concentration. In particular, by increasing the H_2O: TEOS ratio the solvent polarity increases, thus favouring the formation of bigger silica primary particles [133].

2.3.3 Melt-quenching and sol-gel process: comparison of techniques

Both the methods described above are potentially suitable for obtaining bioactive amorphous materials. However, none of these could be actually defined better than the other one. For this reason, the final choice must be weighted on the basis of each specific application, in the light of composition-related requirements, textural properties and degradation rates of the material.

Considering compositional features, for example, sol-gel route may offer some advantages compared to traditional melt-quenching.

The composition of melt-derived glasses, indeed, has to be properly adjusted on the basis of both technological and bioactivity requirements. As a result, very often specific oxides have to be introduced in order to facilitate melting and casting procedures, as well as to properly fulfil reaction criteria in contact with biological fluids.

As an example, referring to the ternary state diagram depicted in **Figure 2.1**, in silica-based BGs, the bioactive potential is deeply influenced by the SiO_2 content. High amounts of SiO_2 (>60 wt.%), in fact, make the glass network very stable upon dissolution, thus limiting ionic release end exposure of functional –OH groups at the interface with biological fluids [134].

On the contrary, in sol-gel glasses, the specific surface area (SSA), and thus the number of reaction sites available for ion exchange, are maximized by the presence of pores at the meso-scale, which confer to the material superior textural properties,

intrinsic in the process itself. As a consequence, sol-gel glasses show bioactivity in a wider compositional range, preserving their HA forming ability up to 90 mol.% of SiO_2 [135].
In addition, using sol-gel technology could be helpful in overcoming some typical processing limitations of melt-derived glasses, such as the presence of metallic ions eventually forming unwanted alloys with the platinum crucible. In fact, sol-gel glasses can be easily doped at room temperature by the introduction of proper precursors, representing a relevant plus when dealing with metal oxides.

Nevertheless, when dealing with sol-gel synthesis, an accurate control on environmental variables and chemical interactions between reagents is strictly required to properly predict the outcome of the process and guarantee high reproducibility and reliability of results. Even small variations related to one of the synthesis parameters, in fact, are able to induce relevant changes within in the gel properties. Beside the presence of multiple synthesis parameters, the long waiting times between subsequent phases of the process lead inevitably to a higher complexity of the chemical synthesis route compared to the faster (and easier) melt-quenching one.

Moreover, it should be considered that the presence of a disorganized mesoporous texture in sol-gel glass (2-50 nm) [136] is the primary factor affecting the mechanical behavior of sol-gel derived products, limiting their use in load bearing applications.

Recently, mesoporous materials, and particularly mesoporous bioactive glasses (MBGs), have caught the attention of the scientific community. These materials are characterized by a very high surface area and a well-organized mesoporous texture given by the use of proper structure directing agents within the synthesis, which make them potentially able to provide a double action, i.e. supporting bone tissue ingrowth and regeneration and providing a direct treatment to diseased bone by a controlled release of therapeutic agents housed inside the mesopores [137], [138].

2.3.4 Bioactive glass-ceramic (BGC) materials

Mechanical brittleness is an intrinsic limit of all glassy materials, regardless of the synthesis route.
One of the most common and easiest strategies to improve the mechanical performances of BG-based products is based on high temperature treatments to induce the nucleation of crystalline phases within the material, thus leading to the production of glass-ceramics with improved mechanical properties [139].
Polycrystalline materials are obtained from the controlled heating treatment at high temperature of a base glass with the aim of inducing the nucleation and growth of specific crystalline phases within the material [140], whose features are intimately linked to the composition of the starting glass. As a result, glass ceramics are characterized by the presence of one or more crystalline phases embedded into a residual amorphous matrix, with a crystalline degree usually ranging between 30 and 70% [141].

Although it was demonstrated that the nucleation of crystalline phases is potentially able to drastically reduce the reactivity of the material in aqueous environment (i.e. glass bioactivity in contact with body fluids) [142], the available manufacturing technologies offer the possibility to opportunely control and tailor the nucleation and growth of crystalline phases by properly setting heating conditions and temperature treatment [143].
In particular, there are two methods used for controlling the nucleation of crystalline phases [140]:

i) Controlled internal (or bulk) crystallization within the base glass, performed into two different subsequent phases: a) nucleation of crystallites at low temperature (slightly above the T_g) and b) crystals growth and join at grain boundaries, performed at higher temperatures.
ii) Controlled crystallization on the surface of the base glass, in which the nucleation of crystals can be induced directly on the surface of the material. In this case, glass is crushed into fine particles and the surface of the of the glass powders grains is activated to produce crystals, which proceed to grow inwards from the surface of the glass powders.

It is possible to produce glass-ceramic materials starting either from melt-derived or sol-gel glasses, according to the schematic provided in **Figure 2.3**.

However, dealing with sol -gel process, an additional issue must be carefully evaluated, i.e. the decrease in the SSA of sol-gel bioactive foams with the increase of the calcination temperature [144].

Thus, the calcination treatment has to be design in order to preserve the intrinsic nanotexture proper of sol-gel systems, forecasting a certain decrease of the SSA and, consequently, a further slowing down of the HA deposition rates.

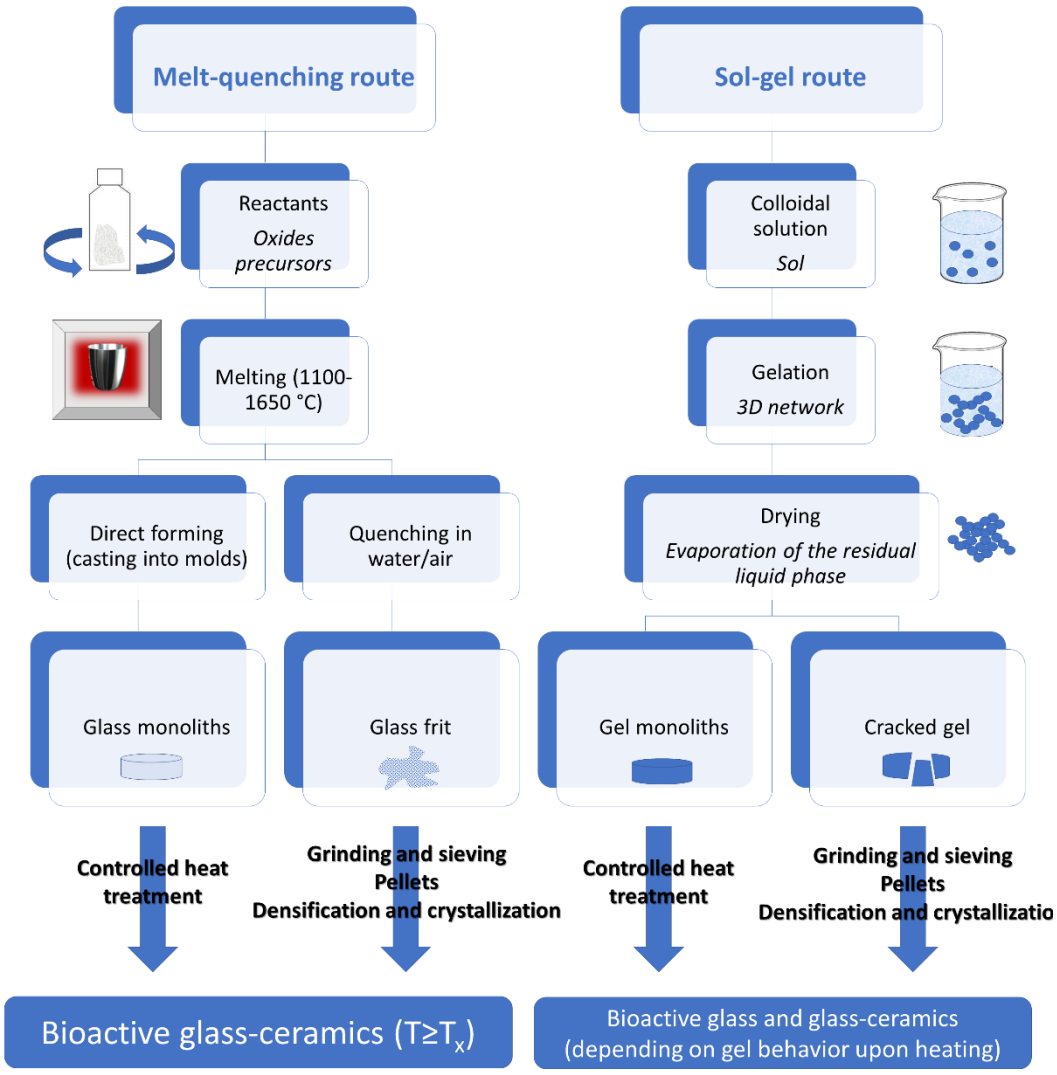

Figure 2. 3. Schematic of processing methods for making BGs and BGCs.

2.4 BG-based scaffolds for tissue engineering applications

The production and optimization of TE scaffolds based on BGs and BGCs is, still today, a very current research topic. Indeed, the enormous potential of these materials for the production of synthetic bone grafts is undisputable and actively inspire researchers towards the optimization and the validation of these devices.

Scaffold manufacturing strategies described in literature differ for architectural features, i.e. pore size distribution, pore shape and interconnectivity, mechanical properties, manufacturing costs and reliability/repeatability of the manufacturing process. In particular, the last two aspects deserve special attention as they define the possibility to scale-up the production of TE scaffolds, thus facilitating the complete translation of scaffold-assisted regenerative strategies from concept to clinic.

Most of the available technologies for the production of BG-based 3D porous structures are, in fact, affected by poor reproducibility and standardization levels. The only exception is represented by solid free-form fabrication (SFF) strategies, which, starting from ‘80s, have gradually begun to invade almost every daily-life

field. However, their spread in biomedicine is clearly lagging behind other industrial fields due to the high technological costs required for the processing of high-quality raw materials under strictly-controlled environmental conditions.

As a first approximation, it is possible to divide scaffold manufacturing technologies in three different macro-groups, as described below:

i) Particles sintering around a template
ii) Foaming strategies
iii) Solid free-form fabrication technologies

2.4.1 Particle sintering around a template

This technique is essentially based on the sintering of glass and glass-ceramic powders around a sacrificial template acting as porogen agent [145].
In this process, the thermal treatment plays a double role: on one side, it allows to obtain highly densified struts by particles sintering and, on the other, it induces the thermal degradation of the organic template.
The thermal treatment is usually carried out above the temperature of glass transition T_g of the material. For $T \geq T_g$, indeed, the viscosity of glass and glass ceramics decreases with increasing temperatures, following an exponential trend, thus allowing the viscous flow of the particles on the others and the consequent formation of sintering necks. This process, known by the name of sintering by viscous flow, occurs in two different phases, i.e. densification and pores occlusion. However, the closure of interstitial pores is a very slow process, partially hindered by the presence of gases within the pores and this makes it very difficult to obtain fully densified sintered products [146].
In these regards, the use of small particles size is usually preferred to maximize contact points and allow the production of closely packed structures showing superior mechanical properties.
However, when amorphous particles are used as starting materials, decreasing particles size could dramatically enhance devitrification phenomena, as a consequence of the higher exposed surface area, according to the mechanisms described above.

The use of various porogen agents, both of synthetic and natural origin, has been already reported in literature, including polymers of various shape, i.e polyethylene (PE) granules and polyurethane (PU) foams, ice crystals and corn-, rice- or potato-derived starch granules [147]–[150].

Although scaffolds produced by space-holder methods, based on the use of organic particles with suitable size for TE strategies, are usually characterized by superior mechanical properties, they are affected by important drawbacks, including low and uncontrolled pore size and distribution and poorly interconnected porous network, as well as total porosity below the lower reference value acceptable for human trabecular bone (**Figure 2.4**), making them almost unsuitable for promoting tissue ingrowth and vascularization within the 3D volume of the graft.

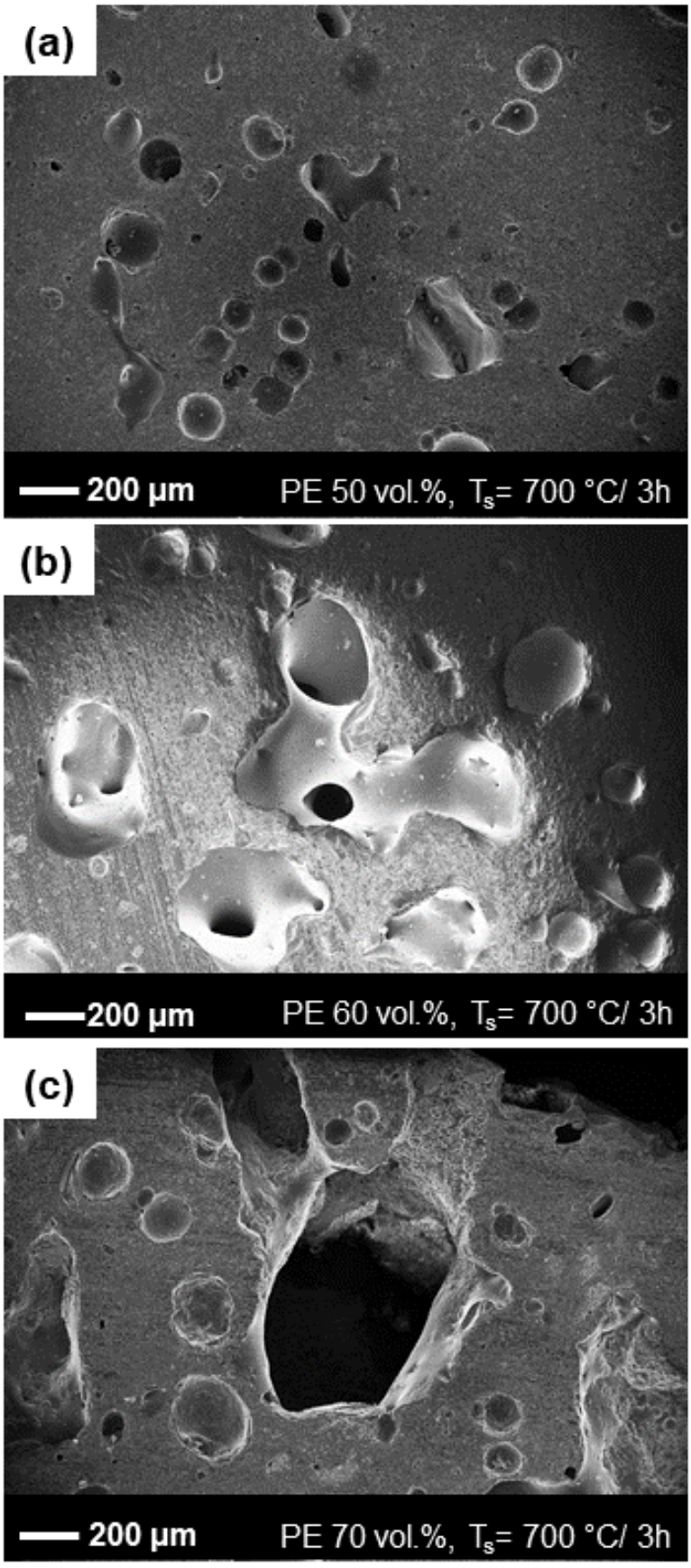

Figure 2. 4. BG-based scaffolds obtained by thermal consolidation of particles around a sacrificial template (PE granules). The figure shows how, despite pore size was in the typical reference range of trabecular bone and the overall porosity of the scaffolds increases by increasing the volumetric content of sacrificial particles, pores remain almost isolated, with few inter-pore windows.

A focus on foam replica method

Foam replica method can be certainly considered a subcategory of this group, but reveals interesting advantages compared to traditional space-holder methods.

The technique, in fact, allows to obtain highly interconnected porous structures showing architectural features very similar to that of natural spongy bone, with open and interconnected porosity in the range of 40–95 vol.%, depending on the type of sacrificial template used[121], [145].

The foam replica method was developed by Schwartzwalder and Somers in 1963 [151], but its use for the production of bone tissue engineering scaffolds was independently pioneered by Chen et al. [150] and Park et al. [152] only in 2006, representing a great opportunity for the development of bone-like BG-based scaffolds.

Since that moment, in fact, foam replica method has been extensively used in combination with melt-derived, sol-gel and MBGs, with promising results both *in vitro* and *in vivo*.

The process is essentially based on the replication of the porous structure of a sacrificial template, which could be both of natural and synthetic origin, in order to obtain its positive replica made of glass or glass-ceramic particles sintered around the organic template.

Within a typical process, a foamy 3D structure is repeatedly dipped in a glass particles suspension (slurry) obtained by mixing glass powder within a binder solution, opportunely selected to favour the attachment of glass particles to the template. As an example, for polyurethane (PU) sponges, which are actually the most popular template for the implementation of the technique, PVA is used as binding agent.

In this way, a consistent coating can be obtained on the foam struts, where the thickness is adjustable on the number of consecutive immersions or the solid load contained within the slurry formulation. afterwards, the excess slurry is removed by simply squeezing the foams, which are then left to dry in order to obtain the so-called green bodies, which are then subjected to high temperature thermal treatments to remove the organic template and densify the structure upon sintering. Frequently, the foam burning out and the glass sintering are combined in a single treatment, carried out by maintaining a very low heating rate in order to burn out the foam preserving the integrity of the bioactive coating [150].

Nowadays, foam replica method is widely implemented in laboratory practice both in its traditional version and in new and sometimes very creative reinterpretations. Silicate, borate and phosphate scaffolds showing trabecular-like architecture have been characterized in terms of microporous architecture, compositional, microstructural, mechanical and biological properties by numerous research groups.

Foam replica method was also successfully used in combination with evaporation-induced self-assembly (EISA) [153] to fabricate hierarchical porous BG (HPBG) scaffolds, where a polyurethane foam and a surfactant are used as co-templates for

scaffold macro-pores and mesopores, respectively [154], [155]. A similar procedure was carried out by Wu et al. [156], who obtained hierarchical Fe-doped scaffolds with suitable magnetic behaviour to be used in tumour therapy by hyperthermia approach.

In recent years, much attention has been addressed to the use of natural templates, due to their easy availability and low-cost, thus leading to the possibility of obtaining diverse and environment-friendly structures with even superior mechanical properties [157].
As an example, the use of marine sponges led to a great improvement in the compressive strength of foam replicated scaffolds, provided by the lower total porosity of marine sponges compared to PU ones. In this regard, Boccardi et al. [158] reported the preparation of scaffolds replicating the morphology of two different type of marine sponges. Interestingly, even if a reduction in total porosity was observed (68-76 vol.%), the scaffolds exhibited a considerable microporosity, inherited from the template, which was almost totally absent in scaffolds derived from PU foams.

Other groups reported the use of corn stalks [157], cattail stalks [159] and mushroom stalks [160] as macroporous templates, obtaining good results in terms of replica fidelity.

A different approach was proposed by Xia et al. [161], who used demineralized bone matrix as sacrificial template to develop a biomorphic bioactive glass-gelatin composite scaffold having both structure and mechanical behaviour similar to cancellous bone.

Some examples of different morphologies obtained by the replication of various porous template are collected in **Figure 2.5**.

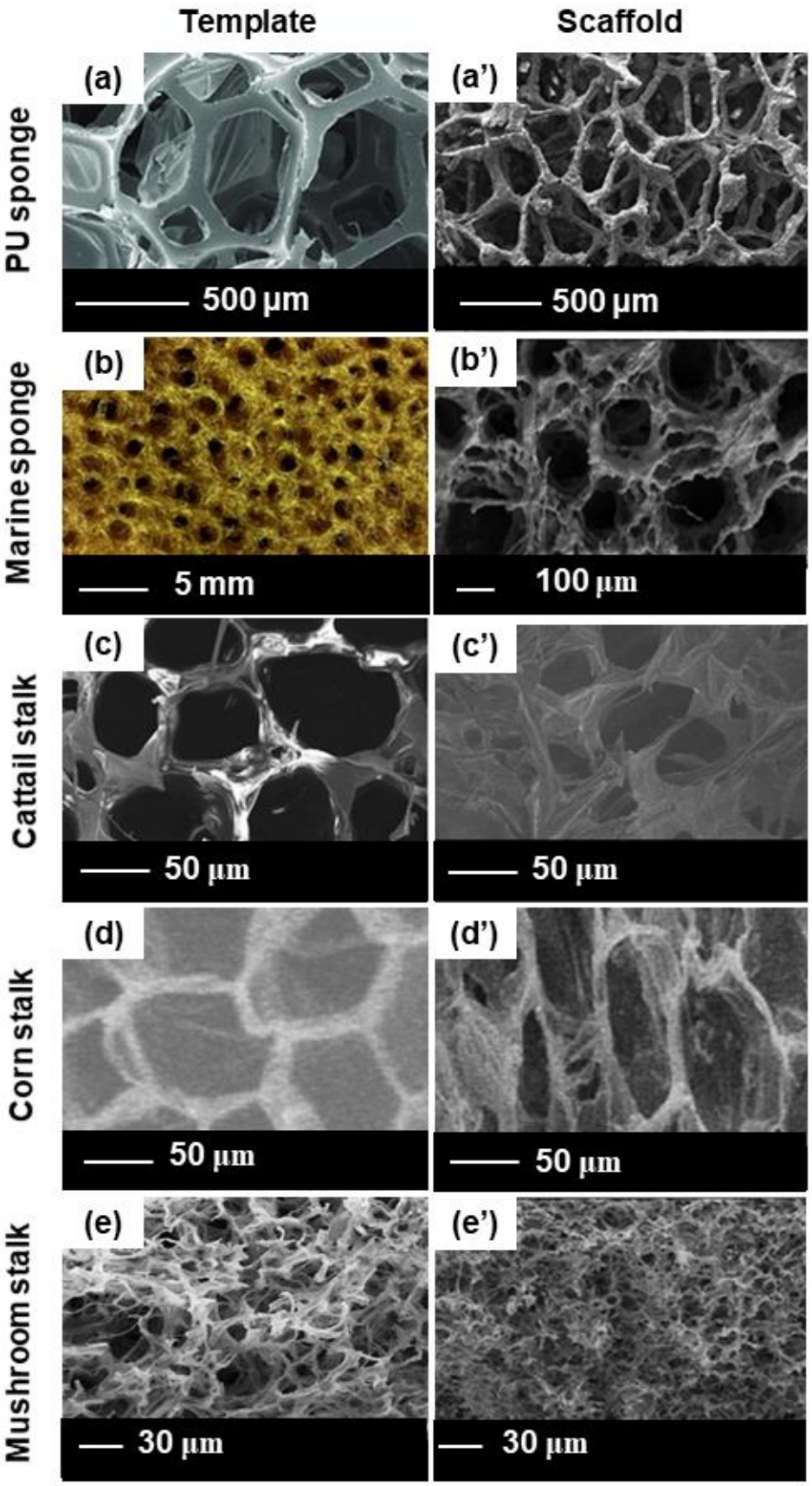

Figure 2. 5. Foam replica method: SEM morphological images of different templates and related 3D porous scaffold. Figure a-a', c-c', d-d', e-e' adapted respectively from Chen et al. [150], Ma et al. [159], Jiang et al. [157]and Han et al. [160], with permission. Images b-b' reproduced from Boccardi et al. [158] under the terms of the Creative Commons Attribution License.

One of the major drawbacks concerning scaffolds produced by foam replication technique is related to the mechanical properties of the final structures.
As can be seen in **Table 2.1**, a part few exceptions, most of the scaffolds described in literature exhibit mechanical properties very close to the lower limit reported for human trabecular bone.

Table 2. 1. Structural properties of BG-based scaffolds produced by replication of different porous templates.

Glass System	Template	Pore Size/ µm	Total Porosity/ vol.%	Compressive Strength/ MPa	Ref.
45S5 Bioglass®	PU	510-720	~90	0.3–0.4	[162]
45S5 Bioglass®	Spongia Aagaricina (marine sponge)	0–600	68±0.2	1.8±0.3	[158]
45S5 Bioglass®	Spongia Llamella (marine sponge)	0–900	76±2	4±0.4	[158]
CEL2 $45SiO_2$-$3P_2O_5$-26CaO-7MgO-$15Na_2O$-$4K_2O$ mol%	PU	100-600	66.4±2	4.5±0.9	[163]
SCNA $57SiO_2$–34CaO–$6Na_2O$–$3Al_2O_3$ mol%	PU	~240	56±6	18±5	[164]
58S $58SiO_2$-33CaO-$9P_2O_5$ wt%	DBM	300–700	89.3±2.0	0.16±0.05	[161]
58S-Gelatin $58SiO_2$-33CaO-$9P_2O_5$ wt%, gelatin > 10 wt%	DBM	300–700	87.7±1.1	4.9±0.2	[161]
5.0Silk–MBG SiO2–CaO–P2O5	PU	200–400	~94	~0.25	[165]

This can be certainly attributed both to the high porosity levels achievable by the process and to the brittle nature typical of glass materials, but not only.
The process, indeed, is characterized by some intrinsic issues related to the practical execution, which make it highly operator-dependent and poorly reproducible, thu affecting the mechanical properties of the graft.
It is sufficient to consider, as an example, the dipping-squeezing phase. This apparently simple task, in fact could determines important modifications in the mechanical performance of the scaffolds as it defines the distribution of the slurry

within the 3D volume and the homogeneity of the porous architecture. Other relevant factors concern the mixing and the drying phase, potentially associated to the formation of concentration gradients within the slurry and its accumulation by gravity at the bottom of the sponges, respectively, thus determining, in both cases an uneven distribution of the material within the porous structure.

2.4.2 Foaming strategies

Foaming techniques rely on the use of proper foaming agents to be added either to melt-derived glass powders or sol-gel process, in order to create air bubbles acting as templates for macroporosity generation.
When melt-derived glasses are foamed, the surfactant is usually added to a glass slurry, i.e. a suspension of glass powders into a fluid media, while, in sol-gel synthesis, the surfactant is added to the sol just before gelation. However, when foams are produced by thermal decomposition of specific chemicals, glass powders and foaming agent can be also dry-mixed until a homogeneous powder batch is obtained.

Foaming techniques can be further divided into different categories, basing on the operating principle. The extreme versatility of glasses extended to very different applications, even beyond medical ones, allowed to inherit some of these processes directly from the industrial field, simply changing the composition of the staring glass and paying particular attention to the potential toxicity of all the elements and co-products taking part in the process.

The first BG-based scaffold was developed by sol-gel foaming in 2002 [166], using Teepol as surfactant to stabilize air bubbles produced upon vigorous agitation and HF as gelation catalyst. The use of a surfactant is required to reduce the surface tension at the gas–liquid interface, but its action is limited over time. For this reason, the use of a gelation catalyst is recommended to fix the desired structure before thermal treatment.
Most of sol-gel foams are characterized by a hierarchical porous architecture, with a bubble- like porosity at the macroscale (10-500 μm) and mesopores, intrinsic in the chemical synthesis, within 2-50 nm [121]. This hierarchical organization is highly beneficial as it enhances cellular interaction with the device, resembling the multi-scale architecture of biological bone.
Due to the presence of mesopores, scaffolds produced by sol-gel foaming exhibit a very high SSA (100–200 m^2/g) which improves the chemical reactivity of the surface in contact with the physiological environment, leading to a faster conversion to HA and a better biological interaction.
The major drawback affecting hierarchical sol-gel foams concerns their mechanical properties. In particular, their low compressive strength (0.3–2.3 MPa), makes their usage in load bearing applications not properly advisable.

Melt-derived glasses are usually foamed by gel-cast foaming. In a typical process, glass powder is added to a solution of organic monomers (usually acrylates) to produce a slurry. Then, the slurry is foamed under vigorous agitation to induce *in*

situ polymerization in the presence of a surfactant, which stabilize air bubbles, and a catalyst, to lower the energy of activation of the polymerization reaction. As the polymerization progresses, the viscosity increases and, just prior to gelation, the foams are poured into moulds, dried, and sintered at high temperature to remove the polymeric organic phase and densify the strut [167].
It is possible to adjust the scaffold porosity by regulating the idle time, i.e. the time interval between the addition of the polymerization initiator and the catalyst and the beginning of the polymerization reaction [145].
Just like sol-gel foaming, identifying the right pouring window is crucial for the final outcome of the process, in fact, if the foam is poured too soon, it will collapse under its own weight, destroying the porous architecture.
Water is highly appreciated as solvent, because it can be easily eliminated by drying processes slightly above 100 °C [145]. However, the exposure of BGs to an aqueous environment during the manufacturing could led to an early reaction of the material even for very short time windows, depending on the glass composition.
Although scaffolds produced by gel casting are generally characterized by proper features for bone regenerative approaches, there is little chance of scalability of the process to industrial level.

Another group of foaming strategies is based on the gas generation upon thermal decomposition of chemical compounds, such as peroxide and carbonates.

Peroxide (H_2O_2) foaming allows the production of porous scaffold by heating a peroxide solution up to 60 °C, to allow the release of water vapor and oxygen, which act as foaming agents producing bubbles during the reaction.
Navarro et al. [168] mixed powders of phosphate glass with different amounts of H_2O_2 solution. The resulting slurry was poured into a mould, foamed at 60 °C, and subjected to drying and sintering. Reasonably, the study revealed a great dependence between the H_2O_2 amount and the porosity level of the scaffolds, with voids percentage increasing with increasing volumes of foaming agent.

Given the high reactivity of BGs in aqueous environment, which could lead to important modification in glass structure before implantation, compromising the bone healing potential of the material, alternative strategies based on dry-mixing could represent a valuable alternative to preserve the original properties of the glass. In this regard, within the present research project, a novel foaming strategy is proposed for the first time in scaffolds manufacturing for bone regenerative applications, as it will be described in **Chapter 4**.

Some examples of different morphologies obtained by various foaming strategies are depicted in **Figure 2.6**.

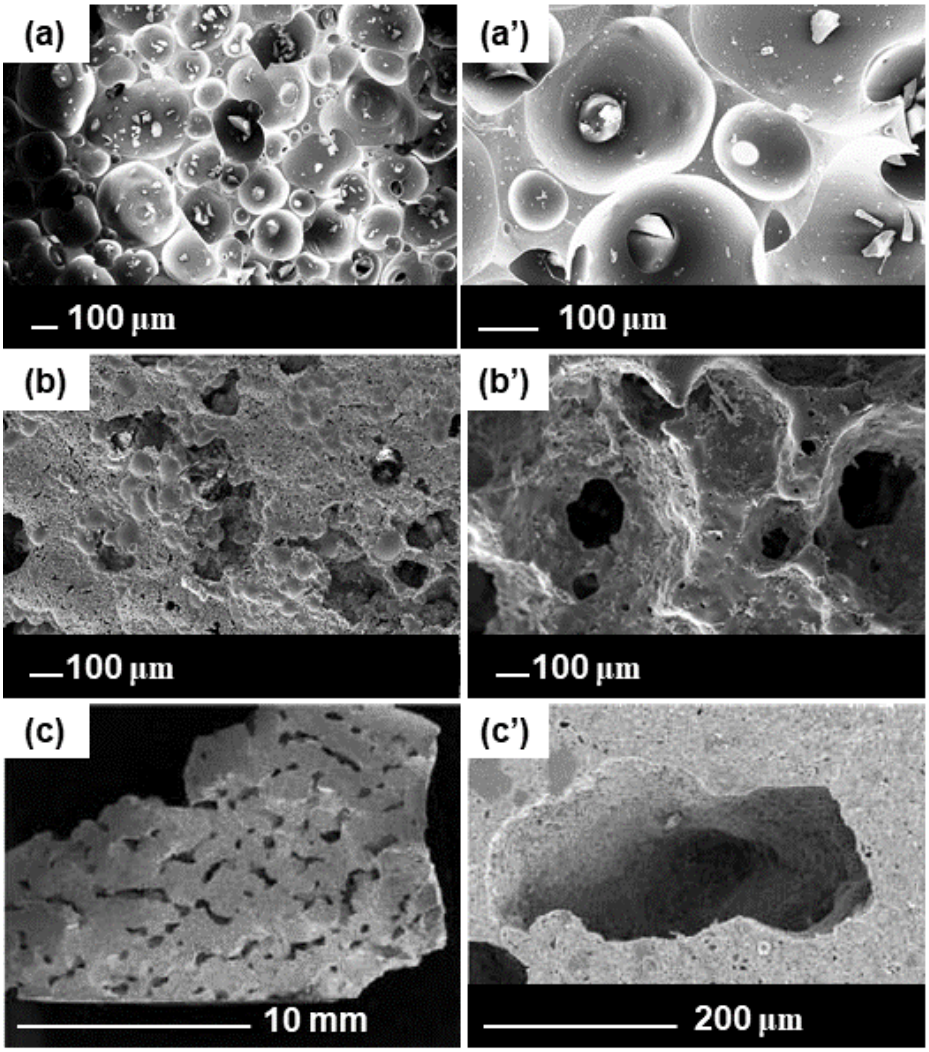

Figure 2. 6. Glass Foaming: SEM morphological analysis of BG-based scaffolds obtained by sol-gel foaming (a), gel-cast foaming (b) and H_2O_2 foaming (c). Images b-b' and c-c' adapted respectively from Wu et al. [169] and Navarro et al. [168], with permission.

2.4.3 Solid Free-Form Fabrication Technologies

Since 1980s, Solid Free-Form Fabrication technologies, also known by the name of additive manufacturing technologies (AMTs), radically changed the world of materials processing in multiple industrial fields [170].

While in traditional manufacturing methods, the final product is obtained by a progressive removal of material (top-down approach), in AMTs the object is built following a bottom-up approach, based on the continuous addition of material until the creation of the 3D object.

Apart from this substantial difference, the most appealing feature of AMTs is the possibility to accurately reproduce specific features basing on previously defined models [171], resulting in an intrinsic high reproducibility and reliability of the overall manufacturing process.

In these regards, compared to other technological fields, the use of AMTs in biomedicine and health science can truly make a significant difference, associated to the possibility to obtain patient-specific devices on the basis of anthropomorphic models derived from clinical imaging techniques, such as computed tomography

(CT) and magnetic resonance (MR). However, the possibility to customize 3D-printed devices inevitably introduces new issues and challenges when drafting a design control model for FDA consideration of market approval, due to the necessity to meet regulatory standards related to the manufacturing quality assurance [172].
For this reason, the use of AMTs in clinical practice is still almost confined to surgical planning and few other secondary applications mostly limited to the laboratory scale and research field [173]–[175].

Despite this, over the last years, many efforts have been made to define reproducible protocols aimed at the production of synthetic bone grafts with tailored structural and mechanical features for bone tissue engineering (BTE) applications [176], [177].

It is possible to divide SFF techniques into direct SFF and indirect SFF. Direct SFF involves the direct building of the scaffold from the biomaterial, while, in indirect SFF, the biomaterial is cast into moulds that are subsequently removed by using an opportune solvent.
Direct SFF techniques, involving the direct building of the scaffold from the biomaterial, present the great advantage of being highly reproducible thanks to the intrinsic automation, but are of difficult implementation due to the required high compatibility between equipment and biomaterials; as an example, a typical problem occurring during glass and glass-ceramic processing by extrusion-based strategies is the risk of nozzle occlusion in the printing head.

In general, a scaffold manufacturing process based on AMTs can be divided into four different phases [178]:

i) Production of a computer-generated model describing the 3D architecture of the final device by using a CAD software or a text script;
ii) Segmentation of the model by dividing the 3D structure into subsequent cross-sections;
iii) Data implementation;
iv) Production of the physical model

Over time, several SFF techniques have been used for BTE scaffold fabrication, including 3D printing (3DP), fused deposition modelling (FDM), ink-jet printing, stereolithography (SL), and selective laser sintering (SLS) [178]. However, still very little information is available in the literature regarding the BGs processing by AMTs.

A focus on robocasting

Robocasting is currently considered one of the most effective and powerful AMTs for the processing of glass and glass ceramic materials.
The technique is based on the continuous extrusion of a filament through a nozzle onto a flat platform, on which the scaffold is gradually built following a layer-by-layer deposition mode.

A typical equipment for robocasting is composed of a printing head, containing the syringe filled with the ink, and the building platform, on which the ink is deposited. The relative movements between the two components are instructed by a dedicated software, able to elaborate and convert either text or CAD files to .stl files, containing the structural and morphological features of the scaffold, as well as deposition parameters, such as velocity of extrusion, spacing between adjacent layers (z-spacing), number of layers, and so on.

The overall process occurs under controlled pressure conditions which intrinsically regulate, together with nozzle diameter, the dimension of each single strut, and thus they have to be properly set on the basis of the rheological behaviour of the ink to be extruded.
The printing ink is usually a slurry, obtained by mixing glass or glass ceramic powder with a polymer-based binder solution. Pluronic F-127 is one of the most commonly used binders for robocasting in bone applications [179]–[181], together with ethyl cellulose/polyethylene glycol and carboxymethyl cellulose [182]–[185]. The optimization of the rheological behaviour of the slurry is crucial to the final outcome of the overall printing process. As a matter of fact, most of the issues related to robocasting procedures, in fact, depends on the extrusion process and on the quality of the ink.

In particular, the slurry should be [186]:

i) Pseudoplastic, in order to properly flow through a small-diameter nozzle without applying high air pressure.
ii) Non-flowable, to preserve the shape after deposition.
iii) Highly strong, to bear the weight of the overlying structures

One of the key aspects characterizing robocasting technology is related to the capability of the printing ink to change its rheological properties basing, as an example, on temperature variations [180], [187].
The ink delivery can take place either by controlling the displacement of the plunger inside the syringe, tuning the pressure in order to maintain a constant displacement over time, or by maintaining a constant pressure inside the syringe. Some printing set-up offer the possibility to adjust extrusion parameters according to the flowing resistance opposed by the ink as a result of its rheological response to variable external conditions, in order to deliver a constant quantity of ink [188].

The two factors that usually control the quantity of deposited material are i) the velocity of displacement of the printing head in the xy (horizontal) plane and ii) the dispensing pressure, while the z-spacing affects the adhesion between adjacent layers and has to be adjusted according to the mean thickness of the rods and the diameter of the nozzle selected for printing.
Scaffolds obtained by robocasting are usually affected by inhomogeneous drying over the entire volume, mainly determined by the presence of the printing substrate (usually acetate sheets) which partially hinder air circulation, resulting in a faster drying of the scaffold top compared to the bottom.

According to the dimensions of the printed scaffold, drying may be operated both at room temperature or in mild-heating conditions. For large volume scaffolds (above 1 # 1 # 1 cm), the usage of preheated ovens may be helpful to avoid drying gradients in the 3D structure, thus preserving its integrity.

Robocast bioceramic scaffolds were produced for the first time by Franco and co-workers in 2010, introducing calcium phosphates (HA and β-TCP) within a hydrogel-based printing ink [180].
Since that moment, various BG-compositions have been used by several research groups, producing different macroporous architectures given by the relative orientation of rods belonging to adjacent layers (**Figure 2.7**).

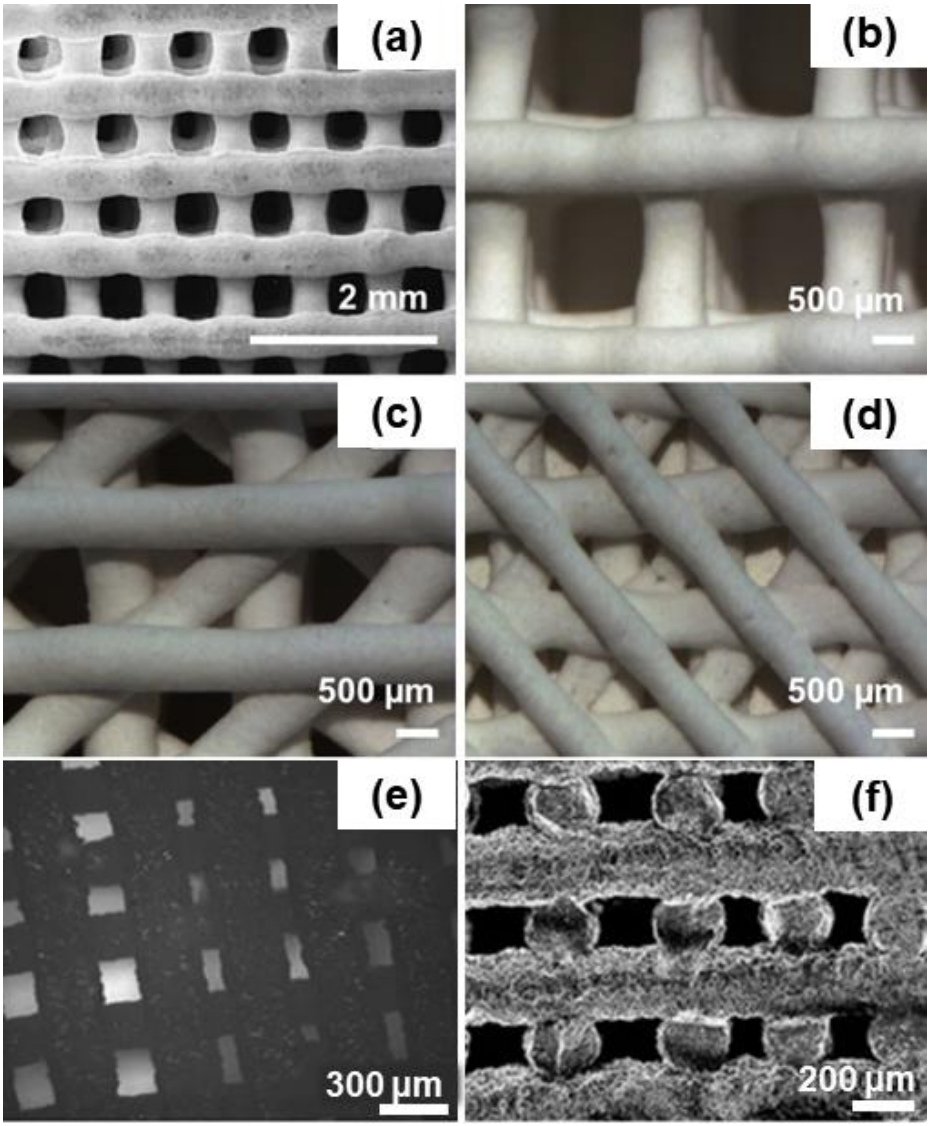

Figure 2. 7. Robocasting: Scanning Electron Microscopy (SEM) morphological images of BG-based scaffolds showing different geometrical arrangement of pores. Figure adapted with permission from ref. [189] (a-b-c-d) and ref. [190] (e-f, reproduced under the Creative Commons Attribution Licens).

A few years after the pioneering study of Franco et al. [180], Liu and co-workers [181] used robotic deposition to produce 13-93 glass-based grid-like scaffolds with 47 vol.% porosity and 300 μm pore width.
Flexural and compressive tests were performed before and after soaking test in SBF and *in vivo* implantation in a murine subcutaneous model, in order to investigate the influence of HA deposition on the mechanical response of the scaffold. Interestingly, a decrease in the compressive strength of the scaffolds was observed both after in vivo implantation and bioactivity tests in SBF, together with a shift from brittle to elastoplastic response, observed after 2- and 4- week implantation *in vivo* and revealing a bone-like behaviour [181].

Probably one of the greatest achievements related to the applications of robocasting technology to the processing of BG-based materials, in particular Bioglass®, was the production of fully vitreous grid-like scaffolds with compressive strength suitable for BTE applications, defined between 2 and 13 MPa and total porosity of 60-80 vol.%, obtained by Eqtesadi and coworkers in 2014 [183].

Robocasting was found to be also suitable for the production of composite scaffolds, as described by Montealleh et al. [184]. In particular, the study focused on the effects of different post-processing thermal treatments on the mechanical response of 45S5 Bioglass®-based scaffolds reinforced by HA/PCL nanocomposite coatings. CAD-derived original architecture was successfully retained upon sintering both in amorphous and highly crystallized scaffolds, and compressive strength values between 2 MPa and 11 MPa were obtained, definitely within the physiological range reported for trabecular bone (**Chapter 1**).

Although robocasting of melt derived glasses has been extensively experimented by several research groups, the processing of sol-gel derived glasses by this technology is still poorly investigated.
This paucity of studies has to be attributed to the different behaviour exhibited by mesoporous material once in contact with a fluid media, compared to dense melt-derived glass, which causes additional issues in the preparation of a printing ink with suitable characteristics for extrusion.
This issue has been addressed in the present research activity, in which multicomponent gel-based inks were successfully obtained by sol-gel process. Further details will be provided in **Chapter 4**.

Chapter 3

Materials and methods – Part 1

3.1 Introduction

Most materials and scaffolds investigated in this PhD thesis are based on an experimental silica-based bioactive glass composition, referred to as 47.5B, which was first developed in 2009 at Politecnico di Torino by Verné and coworkers, in the Department of Applied Science and Technology (DISAT) [191].

This chapter discusses the experimental methods and techniques used to produce and characterize glass and glass-ceramic materials based on the 47.5B compositional system, with a particular emphasis on morphological/compositional features, microstructural/textural properties and bioactive behavior in simulated physiological environment. Both melt-derived and sol-gel materials based on the 47.5Bcomposition were produced, investigated and critically compared, where relevant.

Synthesis and characterization of basic materials used for scaffold manufacturing were entirely carried out in the Department of Applied Science and Technology of Politecnico di Torino, while biological *in vitro* and *in vivo* tests for a preliminary cytocompatibility evaluation were carried out at the University of Piemonte Orientale, Novara, and at the Tashkent Medical Academy and Tashkent State Dental Institute, in Uzbekistan, respectively.

Part of the methods described in the present chapter have been published in:

- *Fiume, E.; Verné, E.; Baino, F. Biomedical Glasses 2019, 5, 46-52.*

- *Fiume, E.; Migneco, C.; Verné, E.; Baino, F. Materials 2020, 13, 540.*
- *Fiume, E.; Serino, G.; Bignardi, C.; Verné, E.; Baino, F. Applied Sciences 2020, 10, 8279.*

3.2 Synthesis of 47.5B-based glasses and glass-ceramics

At the very beginning of their history, BGs were exclusively produced by melt-quenching route, but starting from the '90s, sol-gel process became a very promising technological field for obtaining highly homogeneous and chemically pure materials suitable for medical applications [126].

The main difference between melt-quenching and sol-gel chemistry undoubtedly concerns the textural properties of the final products, influencing both cell/material interactions and degradation kinetics [192]. Despite this, the performances of BGs in contact with body fluids depend on a complex combination of several factors, including the synthesis technology, the compositional system and the final shape (e.g. powders, monoliths, sintered products, fibers, etc.).

As a direct result, the selective determination of the effect of the synthesis process on material's properties could be possible only with all factors equal, including the nominal composition of the materials analyzed.

In the present study, 47.5B glass and glass-ceramic materials were synthetized both by melt-quenching and sol-gel route and used for the production of bioactive scaffolds by various manufacturing strategies, as will be illustrated in detail in **Chapter 4**.

In the first part of this chapter, the melt-quenching and sol-gel synthesis of multicomponent bioactive materials based on the 47.5B composition is described, aiming at directly compare the physical properties of melt-derived and sol-gel materials with same nominal composition.

In the second part of the chapter the attention will be shifted to 47.5B melt-derived products, as promising material for scaffold manufacturing.
In particular, special attention will be payed to the crystallization process of this material, as well as its sintering behavior upon thermal treatment.
Biological response in contact with cells and tissues will be discussed too, supported by preliminary *in vitro* cytocompatibility tests and *in vivo* studies on animal models.

3.2.1 Melt-quenching route

47.5B bioactive glass, belonging to the compositional system SiO_2-P_2O_5-CaO-MgO-K_2O-Na_2O, was produced by traditional melt-quenching route both in form of fine powder and bulk material.

The nominal composition of the glass is reported in **Table 3.1**.

Table 3. 1. Nominal composition of 47.5B bioactive glass.

Oxide	Mol.%	Molecular weight / g/mol	Mass /g	Wt.%
SiO_2	47.5	60.084	28.540	45.336
P_2O_5	2.5	141.945	3.549	5.637
CaO	20	56.079	11.216	17.816
MgO	10	40.304	4.030	6.402
Na_2O	10	61.979	6.198	9.845
K_2O	10	94.196	9.420	14.963

Silica (SiO_2), calcium carbonate ($CaCO_3$), calcium phosphate ($Ca_3(PO_4)_2$), magnesium carbonate hydroxide pentahydrate ($(MgCO_3)_4$ Mg $(OH)_2 \cdot 5H_2O$), sodium carbonate (Na_2CO_3) and potassium carbonate (K_2CO_3) were used, in the right proportion, as precursors of glass oxides.
In particular, the following balanced chemical reactions were considered:

$$SiO_2 \rightarrow SiO_2$$

$$Ca_3(PO_4)_2 \rightarrow \mathbf{3}\ CaO + P_2O_5$$

$$CaCO_3 \rightarrow CaO + CO_2$$

$$(MgCO_3)_4\ Mg\ (OH)_2 \cdot 5H_2O \rightarrow \mathbf{5}\ MgO + \mathbf{4}\ CO_2 + \mathbf{6}\ H_2O$$

$$Na_2CO_3 \rightarrow Na_2O + CO_2$$

$$K_2CO_3 \rightarrow K_2O + CO_2$$

The mass of each reagent was calculated according to **Equation 3.1**:

$$m_{reac} = \frac{m_{glass}}{100} \cdot wt.\%_{ox} \cdot \frac{PM_{react}}{PM_{ox}} \qquad \mathbf{3.1}$$

where m_{reac} is the mass of each reagent, m_{glass} is the mass of glass to be produced, $wt.\%_{ox}$ is the percentage by weight of each oxide, PM_{reac} is the molecular weight of the reagent and PM_{ox} is the molecular weight of the correspondent oxide within the composition.

The masses of reagents required for producing 100 g of material are reported in **Table 3.2**.

Table 3. 2. Masses of reagents required for producing 100 g of 47.5B glass.

Reagent	Chemical formula	Molecular weight PM_{react} / g/mol	Reagent mass m_{react} / g
Silicon Oxide	SiO_2	60.08	45.34
Calcium Phosphate	Ca_3PO_4	310.18	12.32
Calcium Carbonate	$CaCO_3$	100.09	19.87
Magnesium carbonate hydroxide pentahydrate	$(MgCO_3)_4$ Mg $(OH)_2 \cdot 5H_2O$	485.65	15.43
Sodium carbonate	Na_2CO_3	105.99	16.84
Potassium carbonate	K_2CO_3	138.21	21.95

Raw reagents were mixed overnight (t ≥12 h) inside sealed plastic bottles onto rotating rollers, in order to improve the homogeneity of the batch; then, the powder was hand pressed into a platinum crucible by mean of a pestle (**Figure 3.1**, ***Preparation of the crucible***).

Afterwards, a platinum plate was placed on the crucible to prevent the dispersion of volatile species and any possible leakage of material upon heating. The melting was carried out into a high-temperature furnace (Nabertherm 1800 GmbH, Lilienthal, Germany), dividing the heating treatment in two different stages: first, the powder was heated up to 1000 °C with a ramp of 12°C/min to allow the thermal decomposition of carbonates. After a 10 min-dwell, the ramp was changed to 15 °C/min and the temperature was further increased up to 1500 °C. The temperature was maintained constant for a time between 0.5 and 1 h, to improve the homogeneity of the melt and optimize its viscosity, in order to facilitate the casting procedure (**Figure 3.1**, ***Melting and casting***).

According to the desired shape of the final product, the melt was poured under different conditions (**Figure 3.1**, ***Final products***):

i) For the production of BG-powders, a glass frit was produced by quenching in distilled water; then the material was milled (Pulverisette 0, Fritsch, Idar-Oberstein, Germany) and sieved (stainless steel sieve, Giuliani Technology Srl, Turin, Italy) to the desired grain size. In the present study, glass particles with grain size below 25 and 32 μm were produced and named respectively 47.5B-25 and 47.5B-32.

ii) For the production of bulk samples, the melt was poured into a hot brass cylindrical mold with diameter of 10 mm and immediately placed inside a furnace pre-heated at 500 °C to perform a 10 h-annealing treatment, in order to obtain a glass rod with no residual internal stresses.
The annealing treatment was performed slightly below the temperature of glass transition of the material ($T_g \approx 530$ °C), previously assessed by mean of Differential Thermal Analysis (DTA) measurements, as later described in ***Paragraph 3.3*****.**
Before being extracted, the rod was left to slowly cool down at about 20 °C inside the furnace, to prevent the risk of thermal shock. Then, 2 mm-thick glass slices (47.5B-B) were obtained by mean of a tabletop precision saw (Buehler, IsoMet™ High Speed Pro, USA-Illinois).

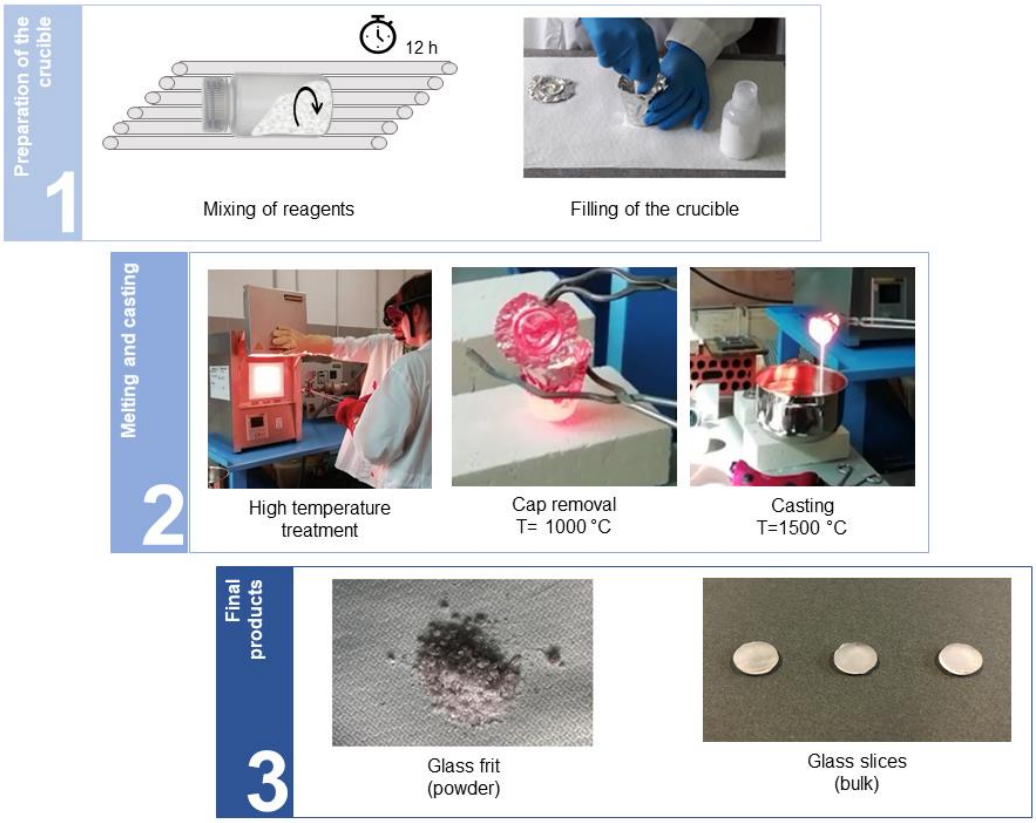

Figure 3. 1. Schematic diagram of the melt-quenching process used for the production of 47.5B-based glass powder and bulk.

3.2.2 Sol-gel process

Multicomponent materials in the complex six-oxide 47.5B system (**Table 3.1**) were produced by sol-gel route.

Tetraethyl orthosilicate (TEOS), tri-ethyl phosphate (TEP), calcium nitrate tetrahydrate ($Ca(NO_3)_2 \cdot 4H_2O$), sodium nitrate ($NaNO_3$), magnesium nitrate hexahydrate ($(MgNO_3)_2 \cdot 6H_2O$) and potassium nitrate (KNO_3) were used as SiO_2, P_2O_5, CaO, Na_2O, MgO and K_2O sources, respectively.

In particular, the following balanced reactions were considered:

$$SiC_8H_{20}O_4 + H_2O \rightarrow SiO_2 + 4\ C_2H_5OH$$

$$72\ HNO_3 + 2\ (C_2H_5O)_3\ PO \rightarrow 51\ H_2O + 12\ CO_2 + P_2O_5 + 72\ NO_2$$

$$Ca(NO_3)_2 \cdot 4H_2O \rightarrow CaO + 2\ HNO_3 + 3\ H_2O$$

$$Mg(NO_3)_2 \cdot 6H_2O \rightarrow MgO + 2\ HNO_3 + 5\ H_2O$$

$$2\ NaNO_3 + H_2O \rightarrow Na_2O + 2\ HNO_3$$

$$2\ KNO_3 + H_2O \rightarrow K_2O + 2\ HNO_3$$

The synthesis was carried out at room temperature (~20 °C) in aqueous acidic environment inside sealed bottles, using HNO_3 (2N) as catalyst for the hydrolysis reaction of TEOS.

HNO_3 (2N) was prepared by dilution of 70 wt.% HNO_3. In particular, for obtaining 50 ml of HNO_3 (2N), 6.4 ml of HNO_3 (70 wt.%) were added to 43.6 ml of bi-distilled H_2O.

During the whole synthesis the sol was gently mixed, with a constant stirring rate of 200 rpm, to avoid the formation turbulent structures.

In **Table 3.3**, the amounts of reagents required, starting from 60 ml of H_2O and 10 ml of HNO_3 (2N), are reported.

Table 3. 3. Masses and volumes of reagents used for producing about 110 ml of 47.5B-based sol.

Reagent	Chemical formula	Molecular weight (g/mol)	Mass or volume (g or ml)
TEOS	$SiC_8H_{20}O_4$	208.33	35.1 ml
TEP	$(C_2H_5O)_3$ PO	182.16	3.7 ml
Calcium Nitrate tetrahydrate	Ca $(NO_3)_2 \cdot 4H_2O$	236.15	15.612 g
Magnesium Nitrate hexahydrate	$(MgNO_3)_2 \cdot 6H2O$	256.41	8.4615 g
Sodium nitrate	$NaNO_3$	84.99	5.6093 g
Potassium nitrate	KNO_3	101.11	6.6733 g

The synthesis took place in three main stages:

Bi-distilled water and HNO_3 (2N) were mixed in a sealed flask up to 5 min using a H_2O: HNO_3 (2N) volumetric ratio of 6;

TEOS was added to the solution in proper amount and mixed under continuous gentle stirring for 15 min, without creating vortexes. An H_2O: TEOS molar ratio of 20 was used, basing on a previous study by Bahniuk et al. [193], who described the synthesis of multicomponent silicate sol-gel materials belonging to the 45S5 compositional system $45SiO_2$,-24.5Na_2O,-24.5CaO-6P_2O_5, wt.%.

All the other reagents were then sequentially added to the batch and the sol was mixed for 45 min more, until the complete dissolution of all the reagents was achieved.

At the end of the synthesis, the sol appeared clear and transparent, without any phase separation.

Gelation process was completed at room temperature for 72 h. After that, samples were aged at 60 °C for 72 h in an oven.

Both the gelation and the ageing treatments were carried out in sealed flasks to prevent the dispersion of organic components. Only for the drying phase, the caps were carefully unscrewed and the temperature was raised up to 120 °C to allow the slow evaporation of the alcoholic liquid phase. After 48 h hours, a dried gel, named DG-120, was obtained.

At this stage, in order to follow the evolution of the material upon heating, part of the DG-120 material was stored for further investigation inside a drier closet, thus mitigating moisture absorption.

Among the characterization analyses performed on DG-120, DTA was carried out to identify the most suitable calcination temperature to obtain a fully-inorganic material, as described in *Subparagraph 3.3.1*.

In the light of DTA results, two different heating programs (**Figure 3.2**) were designed, selecting T_{s1}= 625 °C and T_{s2}= 800 °C as the most suitable calcination temperatures for DG-120, thus obtaining SG-625 and SG-800 samples, respectively. Intermediate dwelling times were also identified on the basis of endothermal/exothermal peaks position in DTA thermograph.

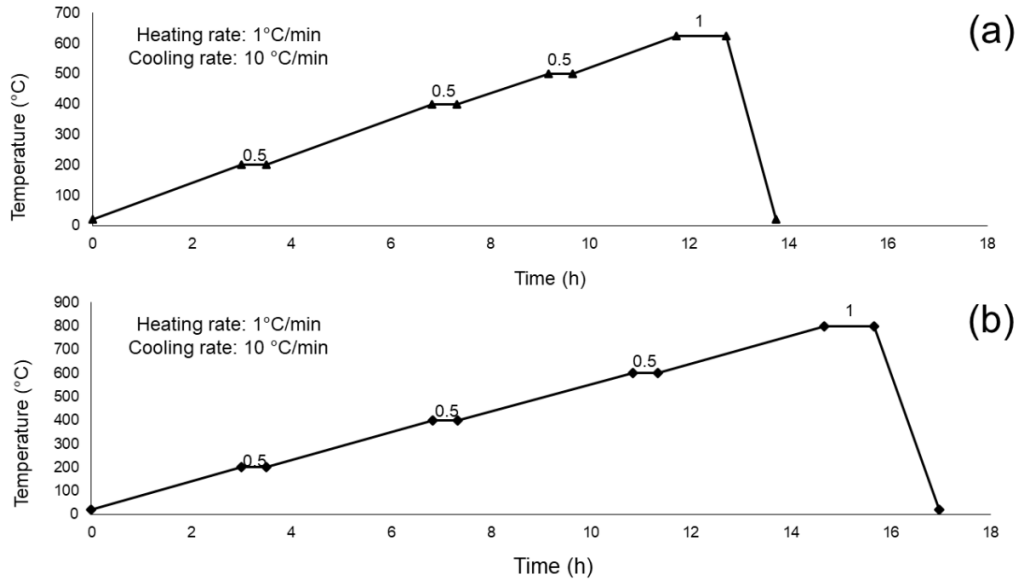

Figure 3. 2. Heating programs used for the calcination of DG-120 at T_{s1} = 625 °C (a) and T_{s2} = 800 °C (b).

The calcined materials SG-625 and SG-800 were then ball milled and sieved below 32 μm, as previously described in *Subparagraph 3.1.1* for 47.B-32 powder.

The overall sol-gel synthesis of 47.5B multicomponent sol-gel materials - SG-625 and SG-800 - is represented in **Figure 3.3**.

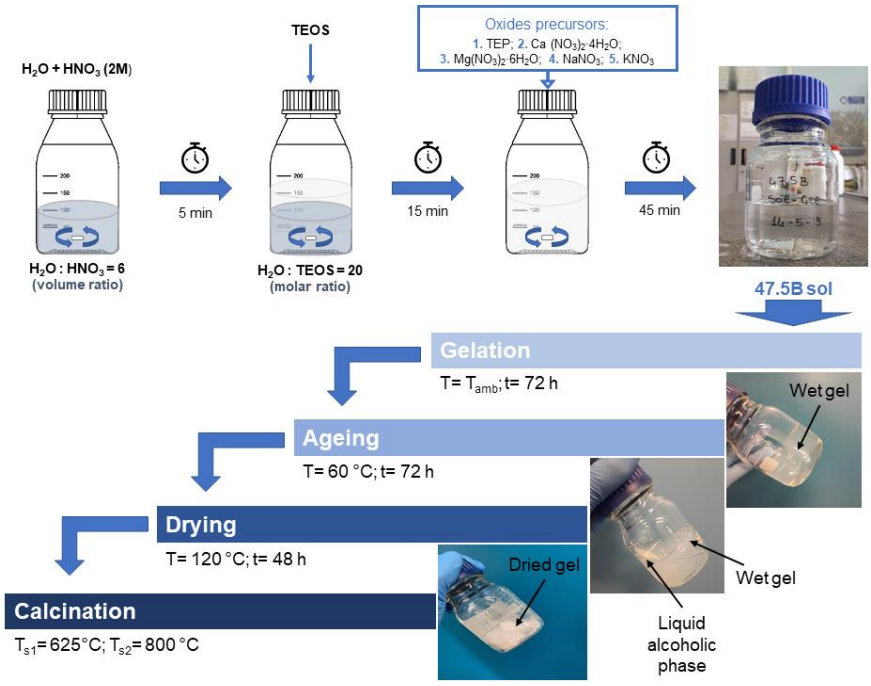

Figure 3. 3. Schematic diagram of the sol-gel synthesis carried out for the production of multicomponent materials based on the 47.5B compositional system.

3.3 Characterization of 47.5B-based glasses and glass-ceramics

Table 3.4 provides an overview of the analysis techniques used to characterize basic glass and glass-ceramic materials.

Table 3. 4. Characterization techniques used for the analysis of glass and glass-ceramic samples.

Characterization technique	Aim of the analysis	Samples analysed
Differential thermal analysis	Non-isothermal: Determination of the characteristic temperatures; analysis of the crystallization behaviour Isothermal: analysis of the sintering behaviour	47.5B-32; DG-120 47.5B-32 47.5B-32
Hot stage microscopy	Isothermal: analysis of the sintering behaviour	47.5B-32
Thermogravimetry	Determination of the mass loss upon heating	DG-120
X-Ray diffraction	Individuation of crystalline phases	47.4B-32; DG-120; SG-625; SG-800; 47.4B-32-based sintered products
Scanning electron microscopy/Energy dispersion spectrometry	Analysis of morphological and compositional features	47.4B-32; DG-120; SG-625; SG-800
Bioactivity tests	Evaluation of the bioactivity and characterization of the HA reaction layer	47.4B-32; SG-625; SG-800
In vitro cellular tests	Preliminary cytocompatibility evaluation	47.5B-B (ceramized at 650°C)
In vivo studies	Biological response in animal model	47.5B-32

3.3.1 Basic characterization analyses performed on 47.5B-32, SG-625 and SG-800

Thermal analyses

Differential Thermal Analysis (DTA; DTA404PC, Netzsch, Selb, Selb, Germany) was performed on 47.5B-32 and DG-120 samples with different aim.

In the first case, the analysis was carried out in order to identify the characteristic temperatures of the material, specifically, glass transition temperature (T_g), crystallization onset temperature (T_x) and maximum rate of crystallization temperature (T_p). In the second case, instead, DTA analysis was useful to identify the most suitable calcination temperature of sol-gel DG-120, to obtain fully inorganic materials.

For the analysis, 47.5B-32 and DG-120 powders (50 mg) were heated up to 1200 °C in platinum crucibles, using a heating rate of 10 °C/min in platinum crucibles. High-purity Al_2O_3 alumina powder was used as inert reference material.

Under the same conditions and using the same equipment, thermogravimetric analysis (TGA) was concurrently performed on DG-120 to quantify the mass loss of the material upon heating.

The analysis of the DTA thermograph was carried out following the criteria listed below:

T_g was identified at the inflection point, as obtained from the first derivative of the plot;

Peaks in the positive verse of the y-axis (local maxima) were associated to exothermal reactions, while peaks in the negative verse of the y-axis (local minima) were attributed to endothermal reactions.

Analysis of the crystalline microstructure

X-ray diffraction analysis (XRD; X'Pert Pro PW3040/60 diffractometer, PANalytical, Eindhoven, Netherlands) was performed on 47.5B-32, DG-120, SG-625 and SG-800 samples to identify the presence of crystalline phases deriving from the thermal treatment and determining the microstructural features of the samples analyzed.

The analysis was performed using a Bragg–Brentano camera geometry with a Cu K incident radiation (wavelength = 0.15405 nm). The 2θ angle varied within 10–70° and the voltage and the current were fixed at 40 kV and 30 mA, respectively. Adata acquisition step counting time of 1 s was used, with a step size of 0.02. Powder size for SG-625 and SG-800 was below 32 μm, to obtain comparable results with 47.5B-32.

The analysis of crystalline phases was carried out by mean of X'Pert HighScore software 2.2b (PANalytical, Eindhoven, The Netherlands), equipped with the PCPDFWIN database.

Bioactivity tests in Simulated Body Fluid (SBF)

The apatite-forming ability of 47.5B-32, SG-625 and SG-800 samples was investigated by soaking the materials powders in a Simulated body Fluid (SBF, pH= 7.40 ± 0.1 at T= 36.5 ± 0.1 °C), prepared according to the protocol described by Kokubo and Takadama in 2006 [194].

A mass-to-volume (powder/SBF) ratio of 1.5 mg/mL was used, according to a previous study reported by the Technical Committee 4 (TC04) of the International Commission on Glass (ICG) [195].

In vitro bioactivity tests were performed at 37° C in an orbital shaker incubator (IKA 3510001 KS 4000 I Control Incubator Shaker, IKA-Werke GmbH & Co. KG, Staufen, Germany), with a constant shaking speed of 100 rpm. The pH was monitored at T= 37 ± 0.1 °C at specific time points (6 h, 24 h, 48 h, 72 h, 168 h and 336 h). In this way it was possible to qualitatively evaluate the ion exchange phenomena between the material surface and the solution on the basis of the pH increase.

At the end of the experiment, the test tubes containing powders and SBF were placed into a centrifuge (Hermle Z306 Universal Certrifuge, Benchmark Scientific Inc., Edison, NJ, USA) to allow powders to decant at the bottom of the tube. Afterward, the SBF was completely removed by a syringe and the powders were rinsed with bi-distilled water. After water removal, the powders were left to dry at 37° C in static conditions for 48 h. Once dried, the powders were stored into sealed plastic tubes (Eppendorf, Hamburg, Germany) before morphological and compositional evaluation.

Pores analysis and textural properties

Nitrogen (N_2) adsorption–desorption porosimetry (ASAP2020 Micromeritics, Norcross, GA, USA) was used to evaluate and compare the textural properties of 47.5B-32, SG-625 and SG-800 materials and to identify possible effects of the synthesis method. The SSA was assessed by applying the Brunauer–Emmett–Teller (BET) theory [196].

Morphological and compositional assessments

The morphology and composition of samples before (DG-120, SG-625 and SG-800) and after in vitro bioactivity tests (MD-47.5B, SG-625 and SG-800) were investigated by scanning electron microscopy (SEM) and energy-dispersive X-ray spectroscopy (EDS) (field-emission SEM equipped with EDS; SupraTM 40, Zeiss, Oberkochen, Germany) in order to evaluate the surface evolution occurring as a result of the reaction process between the material and the solution upon soaking. For the analysis, powders were fixed onto a carbon adhesive tape and sputter-coated with a thin layer of chromium (7 nm). The inspection voltage was set at 15 kV.

3.3.2 Toward scaffold manufacturing: investigating the crystallization and sintering behavior of 47.5B-32 glass

Analysis of the crystallization process

Glass devitrification phenomena, i.e. the nucleation of crystalline phases within the amorphous matrix upon high-temperature treatments, is usually described by two parameters:

i) the Johnson-Mehl-Avrami (JMA) coefficient (n), which depends on the mechanism nucleation and growth of crystals [197], [198];
ii) activation energy for crystallization.

In the present work, the JMA coefficient was calculated by using two independent techniques. The JMA coefficient was quantified by suing two independent techniques. First, it was determined by the Ozawa equation [199]:

First, the Ozawa equation was used (Equation 3.2):

$$n = \frac{d(\ln(-\ln(1-\chi)))}{d(\ln\beta)}\bigg|_T \qquad \textbf{3.2}$$

where χ is the volume fraction of crystallized phase at a fixed temperature T and β is the heating rate.

In order to estimate χ, differential thermal analysis (DTA; DTA404PC, Netzsch, Germany) were performed at various heating rates (β_1= 10, β_2= 20, β_3= 30 and β_4= 40 °C/min). For all the measurements, 50 mg of 47.5B-32 glass was heated up to 1200 °C in a platinum crucible under nitrogen (N_2) flow (inert atmosphere) using the same mass of Al_2O_3 powder as a reference material.

The glass transition temperature T_g and the temperature of maximum crystallization rate (T_p) were determined as described above, respectively at the inflection point of the DTA curve and at the maximum of the exothermic peak (Figure 3.4 a). The accuracy of the measurements was ± 3 °C.

The volume fraction of crystallized phase χ was calculated as the ratio between the partial area under the exothermic peak at a given temperature and the total area under the peak, as depicted in Figure 3.4 b.

It is possible to plot ln (− ln (1 − χ)) as function of ln β, where the slope of the line obtained by linear interpolation of data is n.

Hence, the value of the JMA parameter n was calculated as mean ± standard deviation of the slopes of the plots.

The second method used to estimate the n coefficient the Augis-Bennet method, according to **Equation 3.3** [200]:

$$n = \frac{2.5\, RT_p^2}{\Delta T_{FWHM} E_c} \qquad \textbf{3.3}$$

where ΔT_{FWHM} is the full width of the DTA exothermic peak at the half maximum, as shown in Figure 3.4 c, E_c is the activation energy for crystallization and R= 8.314 J/mol K is the ideal gas constant. In this case, the JMA parameter was calculated as mean ± standard deviation of the n-values determined at each heating rate (β).

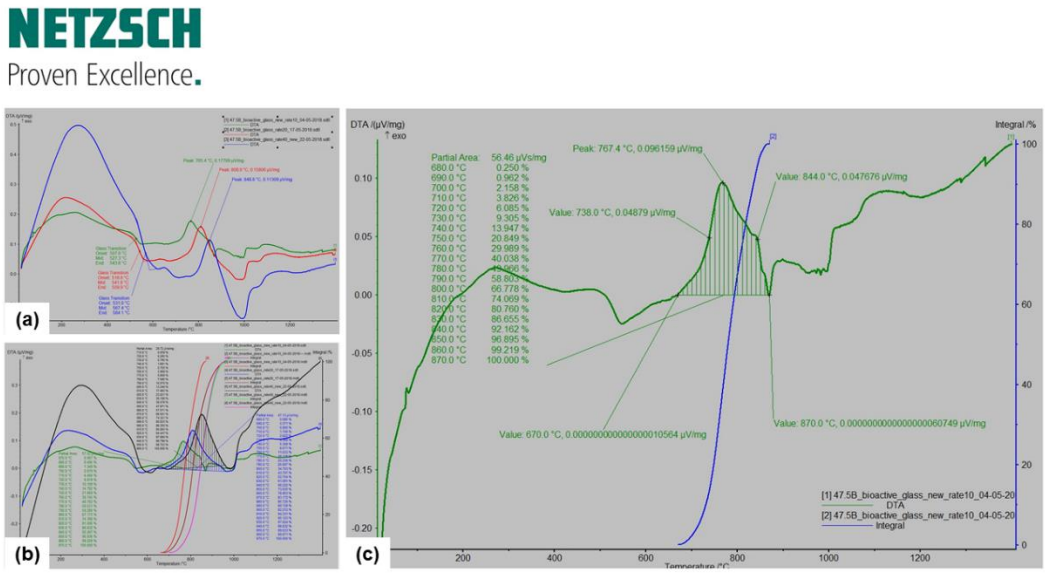

Figure 3. 4. Graphical interface of the DTA software (TA404PC, Netzsch, Germany) used for data analysis.

It is possible to assess E_c from non-isothermal DTA data by applying models which establish a relation between the variation of T_p and the heating rate β. In this regard, a first equation (**Equation 3.4**) was proposed by Kissinger [201]:

$$\ln \frac{\beta}{T_p^2} = -\frac{E_{c,K}}{RT_p} + constant \qquad \textbf{3.4}$$

A plot of $\ln \frac{\beta}{T_p^2}$ vs. $\frac{1}{T_p}$, followed by linear interpolation, gives a straight line of slope $E_{c,K}/R$, from which $E_{c,K}$ can be easily calculated.

However, in another study, Matusita and coworkers [202] demonstrated that Equation 3.4 can be applied only if the crystal growth occurs on a fixed number of nuclei, meaning that the Kissinger model actually yields an underestimated value of the E_c if most nuclei are formed during the DTA measurement, as the number of nuclei may vary with the heating rate β.

As a solution, Matusita and Sakka proposed a more general alternative equation, directly derived from the Kissinger's model (**Equation 3.5**) [203]:

$$\ln\frac{\beta^n}{T_p^2} = -\frac{mE_c}{RT_p} + constant \qquad \textbf{3.5}$$

where E_c is the actual activation energy for crystallization, n is the JMA exponent and m is a numerical factor which varies between 1 and 3 according to the dimensionality of crystal growth: for three-dimensional sphere-like crystallization, m=3, for two-dimensional plate-like crystallization, m= 2 and, for one-dimensional rod-like crystallization, m=1 [204].

From linear interpolation of data obtained by plotting $\ln\frac{\beta^n}{T_p^2}$ as function of $\frac{1}{T_p}$, it results a straight line with slope $\frac{mE_c}{R}$, from which E_c can be easily calculated.

In general, with m=1, surface crystallization is preponderant, while, for m= 3 bulk crystallization predominates, as schematically depicted in **Figure 3.5**

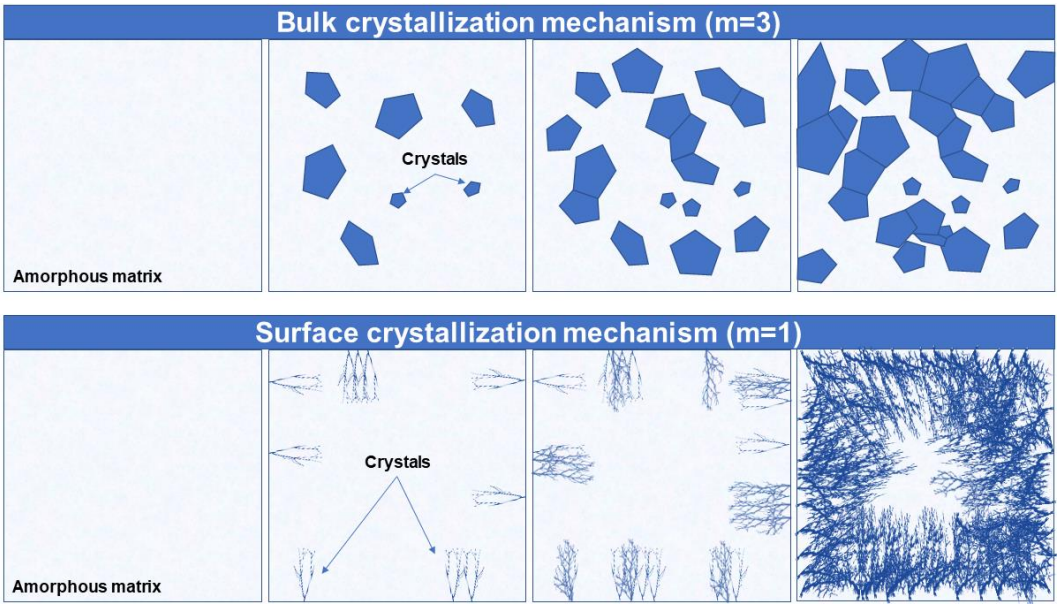

Figure 3. 5. Type of crystallization mechanisms occurring in a glass material upon heating.

When the nucleation of crystals occurs predominantly at a constant heating rate β, during the DTA measurement, it is possible to explicit n as m+1, while, when the nuclei formed in a previous heating treatment (before DTA measurement), it results that n=m. However, if surface crystallization is dominant, m=n=1, regardless of whether nuclei are formed prior to or during thermal analysis: in this case, Matusita-Sakka equation (**Equation 3.5**) essentially reduces to the Kissinger one (**Equation 3.4**), mining that $E_c = E_{c,K}$ [204].

The activation energy for viscous flow (E_{vf}) was estimated according to the model proposed by Francis et al. [205], actually consisting of a Kissinger-type model.

Thus, a plot of $\ln \frac{\beta}{T_g^2}$ vs. $\frac{1}{T_g}$, followed by linear interpolation, gives a straight line of slope $\frac{E_{vf}}{R}$, from which E_{vf} can be easily calculated.

However, the validity of the JMA model is verified under specific conditions. Malek [198] showed that, for the model to be applicable, the crystallization rate $\frac{d\chi}{dt}$ must be only dependent on fraction of crystallized glass and the temperature T, regardless of the thermal history of the material.

This validity test is based on the analysis of a probe function $z(\chi) \propto d\chi/dt$, which, under non-isothermal conditions is defined by **Equation 3.6**:

$$z(\chi) = \Phi T^2 \qquad \textbf{3.6}$$

where Φ is the specific heat flow. According to the **Equation 3.6**, the function z(χ) does not depend on kinetic parameters, and the JMA model is valid if the maximum of z(χ) is located at $\chi = 0.63 \pm 0.02$ [206].

Analysis of the sintering behaviour

The sintering behaviour of 47.5B-32 was investigated by isothermal DTA and Hot Stage Microscopy (HSM) by using a DTA 404 PC instrument (Netzsch, Selb, Germany) and HSM EMI III (Hesse Instruments, Germany), respectively.

The aim was to simulate analogous heating conditions to those required for inducing glass densification in a conventional scaffold manufacturing process based on the thermal consolidation of particles.

In this regard, six different sintering temperatures (T_{s1} = 600, T_{s2} = 650, T_{s3} = 700, T_{s4} = 750, T_{s5} = 800 and T_{s6} = 850, °C) have been identified in the temperature range 600-850 °C, in order to investigate changes occurring in the porous microstructure upon heating.

The lower limit of the range was chosen to be slightly above the T_g of the system, while the upper limit was identified in correspondence to the end of the descending tract of the crystallization peak, accordingly with previous DTA analysis described in *Subparagraph 3.3.1*.

In both cases, the thermal cycle was designed following a multistage program, defined as follow:

- Step 1: from 20 to 400 °C, heating rate 60 °C/min;
- Step 2: from 400 to T_s, heating rate 5°C/min;
- Step 3: 3 h-dwell, T_s.

For DTA measurements, 100 mg of 47.5B glass powders were introduced in Pt-Rh crucibles provided by the manufacturer and high-purity (99%) Al_2O_3 was used in the same amount as a reference material.

For HSM measurements, cylindrical samples of 47.5B-32 pressed powders with diameter 3 mm and height 3 mm were positioned onto a high purity alumina plate

inside the furnace chamber; black and white images showing the silhouettes of the samples were acquired during the whole duration of the test and analyzed by means of a dedicated image analysis software (EMI III- Software für das Erhitzungs mikroskop, Hesse Instruments, Germany). Sample shrinkage was quantified in terms of normalized height (h/h_0) as a function of both time and temperature, where h_0 was the height of cylindrical sample at the beginning of the test (3 mm) and h was the actual height of the sample measured during the analysis.

The analysis of the sintering behavior was completed by XRD surface analysis, performed using the same equipment and operating parameters described in *Subparagraph 3.3.1*.

Six glass tablets of 12 mm diameter and 2 mm height were prepared by pressing 47.5B-32 glass powders using a manual hydraulic press (P400ir Cagimbra, Italy; 1.4 MPa, 15 s). Each tablet was sintered at a different temperature, following the same thermal treatment described above. Before underwent diffractometry measurements, the surface of the sintered tablets was polished using 320–4000 grit SiC papers at 500 rpm. After polishing, samples were immersed in an ultrasonic bath for approximately 5 to 10 min, to remove residual debris.

3.3.3 Biological response of 47.5B glass products

In vitro cellular tests

In vitro cellular tests were carried out at the University of Piemonte Orientale (UPO), Novara, Italy (Prof. Lia Rimondini's team).

Preliminary cytocompatibility tests were performed on 47.5B-B samples ceramized at 650 °C (47.5B-Bc) for 3h (n= 20), using a heating and cooling rate of 5 and 10 °C/min, respectively. Prior to cell exposures, the surfaces of the samples were hand-polished by using 320–4000 grit SiC papers at 500 rpm. After polishing, samples were immersed in an ultrasonic bath for approximately 5 to 10 min, to remove residual debris.

Specimens were heat sterilized at 180°C for 1 h and stored at room temperature prior to be used for biological assessments. Polystyrene was used as substrate for the positive control group and test results where normalized towards it.

Preliminary cytocompatibility of 45.5B-Bc was evaluated on three different cellular phenotypes, used as representative of the tissues potentially in contact with the implant material at the defect site:

- human mature osteoblasts (U2OS, ATCC HTB-96)
- human mesenchymal stem cells (BMSCs, ATCC PCS500012)
- human endothelial cells (EA.hy926, ATCC CRL-2922)

Cells used for experiments were purchased from the American Type Culture Collection (ATCC, Manassas, USA).

BMSCs were cultivated in low-glucose Dulbecco's modified Eagle medium (DMEM, Sigma-Aldrich) supplemented with 15% fetal bovine serum (FBS, Sigma) and 1% antibiotics (penicillin/streptomycin) at 37 °C, 5% CO_2 atmosphere.

U2OS were cultured in high-glucose Dulbecco's modified eagle's medium (DMEM, Sigma-Aldrich) supplemented with 10% fetal bovine serum, 1% antibiotics (penicillin/streptomycin) at 37 °C, 5% CO_2 atmosphere.

EA.hy926 were cultured in high-glucose Dulbecco's modified eagle's medium (DMEM, Sigma-Aldrich) supplemented with 10% fetal bovine serum, 1% antibiotics (penicillin/streptomycin) at 37 °C, 5% CO_2 atmosphere.

Cells were directly seeded onto specimens' surface in a defined concentration (1x104 cells/specimen) and cultivated for 1-2-3 days, up to 80-90 % confluence.

Then, cells were detached by trypsin-EDTA solution, harvested and used for experiments.

At each time points, the viability of the cells in direct contact with specimens was evaluated by the Alamar blue assay (Alamar Blue™, from Life Technologies) following Manufacturer's instructions.

Briefly, supernatant cells were removed from each well-containing cells and replaced with Alamar blue solution (10% v/v in fresh medium). Plates were incubated in the dark for 4 h and then 100 µl were removed, spotted into a new black 96-well plate and fluorescence signals were evaluated with a spectrophotometer (Spark, Tecan Trading AG, CH) using a fluorescence excitation wavelength 570 nm and a fluorescence emission reading 590 nm.

The adhesion spread and morphology of cells cultivated onto specimens' surface was visually checked by digital light microscopy (Invitrogen EVOS Floid, from Thermo Scientific).

In vivo studies

In vivo biocompatibility tests were performed at the Interinstitutional Research Center, Tashkent Medical Academy, Uzbekistan and at the Faculty of Prosthetic Dentistry, Tashkent State Dental Institute, Uzbekistan (Dr. Avzal Akbarov's team).

Before proceeding with the implantation of the material, acute toxicity tests for the determination of the median lethal dose (LD_{50}), i.e the dose required to kill 50% of a test subject population, were performed. The study was carried out following the European Communities Council Directives of 24 November 1986, 86/609/EEC and the national guidelines for research on laboratory animals. Moreover, approval of the Ethical Committee of Uzbekistan under reference no. 9, dated 3.12.2019) was obtained. The animals were quarantined and acclimatized in vivarium conditions for 14 days at 21° C and subjected to 12-h light/dark cycles under a regular diet, according to approved norms.

A preliminary pilot study was performed to identify the dose range to be used in the next stage. More specifically, 30 adult male mice (weight= 20-23 g) were divided into 5 groups and subjected to intraperitoneal injections. The infusion for injection was prepared by vigorously mixing 1 g of 47.5B-32 within 9 ml of physiological solution. The suspension was stored at 37 °C for 24 h and then filtered. Intraperitoneal administration was conducted according to the following dose ranges:

- 500 mg/kg
- 1000 mg/kg
- 1500 mg/kg
- 2000 mg/kg
- 2500 mg/kg

After the injection, animals were individually kept in acrylic boxes, kept under observation for the first four hours, 24 hours and daily for 14 days.

For the determination of actual LD_{50}, 36 mature male rats (weight= 160-188 g) were divided into 6 groups. The testing substance was prepared by suspending 47.5B-32 within distilled water containing potato starch (1g starch/100 g of water). The substance was administered by gavage for 0, 12 and 24 h, as described in ref. [207], [208]. Finally, the LD_{50} was calculated by Probit analysis using StatPlus 2009 Professional, 5.8.4. version software [209], [210]. At the end of 14 days the total number of deaths was recorded.

For *in vivo* tests, 47.5B-32 glass was implanted into healthy and completely matured (1-year old) *Chinchilla* rabbits (weight: 2.8–3.0 kg). Before surgery, animals were identified according to the period and the group (C: control; T: treated), as indicated in **Table 3.5**, and kept in individual cages, following the ethical guidelines and rules of local Governmental bodies.

Table 3. 5. Design of the implantation surgical plan.

Observation stage/ month	T Groups	C Groups	N° of animals per group
1	1, 2, 3	4, 5, 6	3
2	7, 8, 9, 10	11, 12, 13, 14	4
3	15, 16, 17, 18	19, 20, 21, 22	4

All surgical procedures were conducted with the permission of the local ethics committee (the Ethical Committee of Uzbekistan under reference no. 9, dated 3.12.2019) and Ministry of Health of Uzbekistan (the certificate issued to the Interinstitutional research center, Tashkent Medical Academy, Uzbekistan under reference no. 3, dated 13.01.2020).

The intra-operative sequence, represented in **Figure 3.6**, was characterized by the events listed below:

1. The animal was place on the operating table under sedation (Figure 3.6 a);
2. The surgical field was prepared by removing hair with a razor (Figure 3.6 b) to identify the incision site (Figure 3.6 c);
3. Systemic anesthesia was administered (Figure 3.6 d);
4. The skin was cut by mean of a surgical scalpel in order to expose femoral diaphysis region (Figure 3.6 e-f).

5. A bone defect with a 2 mm diameter was created by drilling (Figure 3.6-g);
6. Before implantation, 47.5B-32 glass was heated up 180 °C and sterilized in alcohol (Figure 3.6 h);
7. The glass was placed inside the defect by mean of a surgical spatula (Figure 3.6 i-j-k). Incision without any implantation with drilling a hole of 2 mm diameter and about 10 mm length was performed in the C group.
8. The glass was consolidated inside the defect by pressing (Figure 3.6 l-m);
9. The incision was sewed up (Figure 3.6 n-o).

At the end of each observation stage, rabbits were sacrificed by decapitation.

All femurs were subsequently fixed in 10% phosphate buffered formalin for 72 h for future histological and histo-morphometrical analysis. Then, the femurs were decalcified in 10% formic acid formalin solution for 14 days and sectioned to the longitudinal axis through the anteromedial aspect of the defect.

Finally, the tissue blocks were sectioned and stained with hematoxylin and eosin (H&E) and observed by optical microscopy for histopathological evaluation.

The analysis was carried out paying particular attention to the development of an inflammatory response, new woven bone formation at the margins and in inner part of the defect and woven bone maturation to physiological lamellar bone.

The presence and intensity of bone formation was assessed for statistical analysis [211], [212] through following histological scoring scale:

1: no osteogenesis

2: weak osteogenesis

3: medium-low osteogenesis

4: medium-high osteogenesis

5: good-low osteogenesis

6: good-high osteogenesis

7: perfect osteogenesis

Each slide of histopathological sections was divided into four segments for detailed analysis. Scores mediated on the four quadrants constituted the score of the slide [211].
Wilcoxon-Mann-Whitney test was selected for statistical analysis [211]. This type of test involves the calculation of a statistic named U, whose distribution under the null hypothesis is known [213]. The tests were performed with a level of significance of 5%.

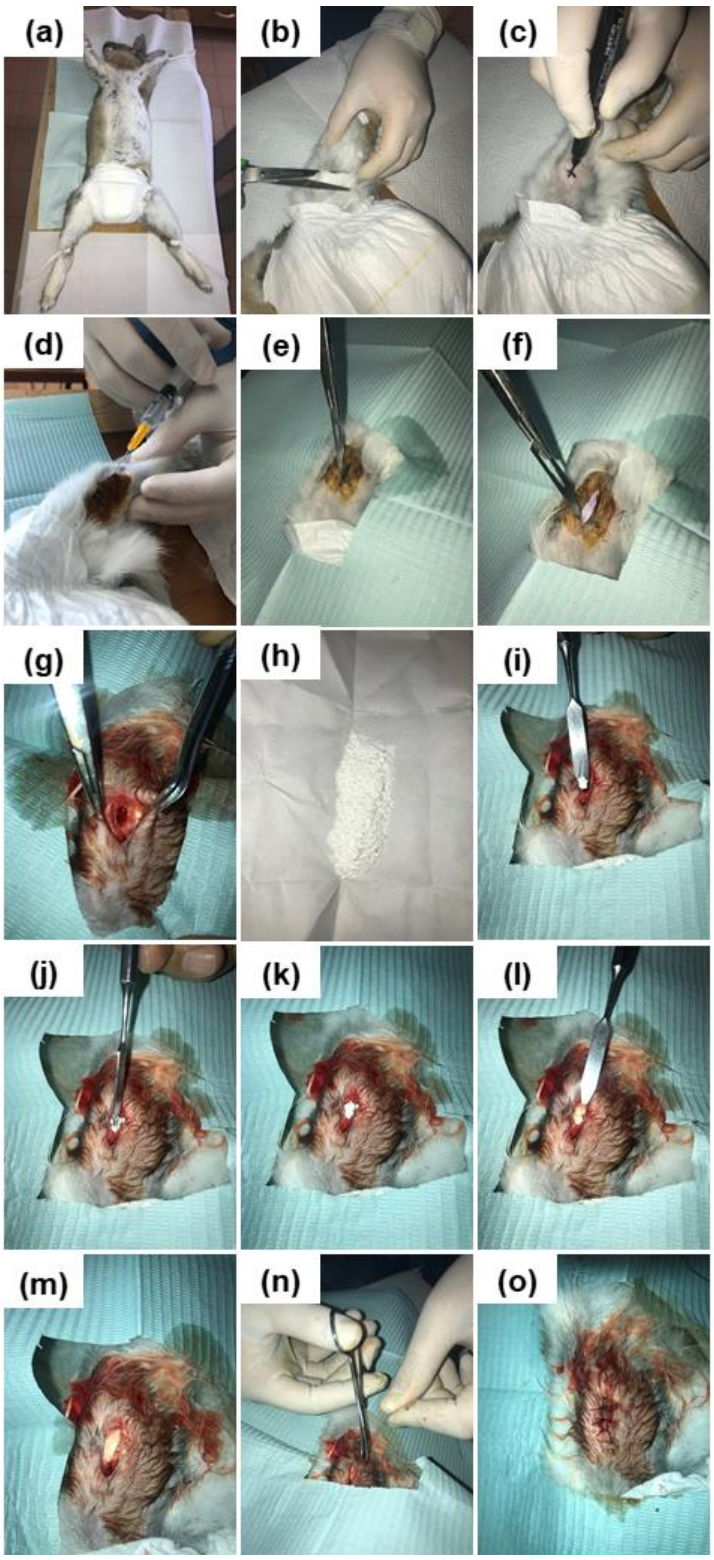

Figure 3. 6. Intra-operatory sequence of pictures showing the surgical procedure implemented for the implantation of 47.5B-32 glass.

Chapter 4

Materials and methods – Part 2

4.1 Introduction

The exceptional thermal behavior upon heating exhibited by 47.5B glass makes it a very promising candidate for the production of mechanically resistant 3D porous scaffolds.
In the present chapter, different manufacturing strategies for obtaining 3D porous scaffolds based on the 47.5B compositional system and morphological, microstructural, mechanical and bioactive characterization performed will be described in detail.
The activities reported in this section were carried out in cooperation with the Department of Natural-Mathematical Sciences of the Turin Polytechnic University in Tashkent (Tashkent, Uzbekistan), the Faculty of Medicine and Health Technology of the University of Tampere (Tampere, Finland), the Department of Materials, Biotechnology and Energy of the Innovation Center Iceland (ICI) (Reykjavik, Iceland) and the Applied Metrology and Engineering Division of the National Institute of Metrological Research (INRiM) (Turin, Italy). This was justified by the high technological and/or novelty level behind the fabrication strategies or characterizations performed.

Part of the research activity introduced in the present chapter has been object of publication in:

- *Fiume, E.; Schiavi, A.; Orlygsson, G.; Bignardi, C.; Verné, E.; Baino, F. Acta Biomaterialia 2021, 119, 405-418.*
- *Fiume, E.; Tulyaganov, D.; Ubertalli, G.; Verné, E.; Baino, F. Materials 2020, 13, 628.*

- *Fiume, E.; Serino, G.; Bignardi, C.; Verné, E.; Baino, F. Applied Sciences 2020, 10, 8279.*
- *Fiume, E.; Serino, G.; Bignardi, C.; Verné, E.; Baino, F. Molecules 24, 2954.*

4.2 Scaffold manufacturing

The backbone of this Ph.D. research was a comparative study between 47.5B-based glass and glass-ceramic scaffolds obtained by different manufacturing processes. Within the study, both "renewed" traditional methods and additive manufacturing technologies were included, aiming at defining new and reliable procedures for the design, fabrication and advanced physical-chemical characterization of BG porous scaffolds to be used in the clinical management of critically-sized bone defects. The activity, schematically organized as represented in **Figure 4.1**, focused on:

i) Foam replica method, implemented both with traditional and alternative sacrificial templates
ii) Glass foaming (dolomite foaming)
iii) Robocasting of melt-derived and sol-gel materials

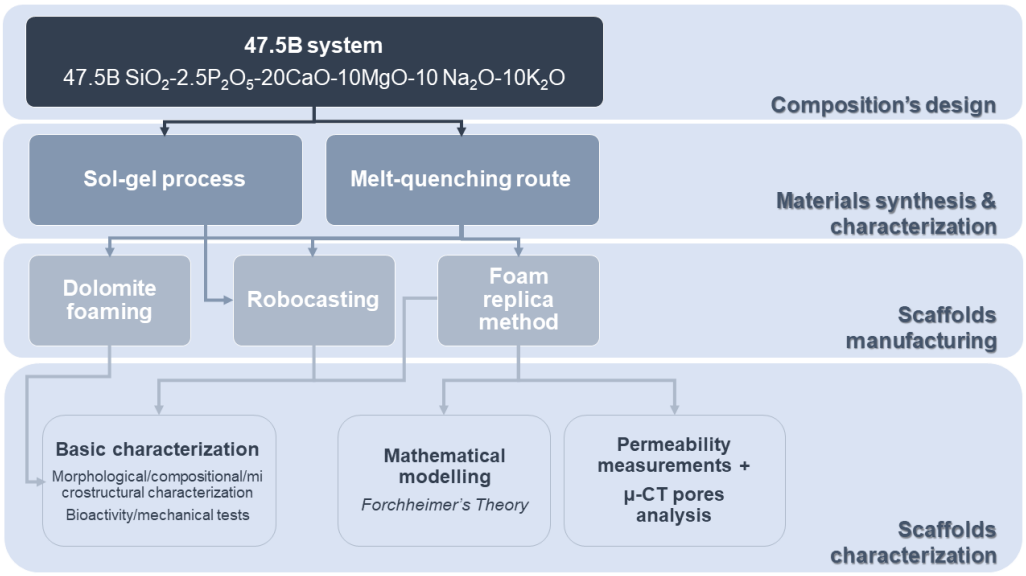

Figure 4. 1. Schematic diagram of the experimental activity showing how materials have been distributed for scaffold manufacturing.

Results will be discussed in **Chapter 6**.

4.2.1 Foam replication technique

The first implemented technique has been the traditional foam replica method, particularly appreciated in the last fifteen years for the possibility to obtain bone-like scaffolds characterized by 3D open-cell architecture able to allow proper cell migration and tissue ingrowth, as deeply discussed in **Chapter 2** [214]–[216].

In the present study, both conventional polyurethane (PU) sponges and novel macroporous sacrificial templates have been used in combination with 47.5B-32 glass powder, with different goals.

In the first case, the choice of PU industrial foams was dictated by the need of counting on a long-established manufacturing technology to focus the study on the effect produced by different sintering treatments on the porous microstructure of the foams, where the sintering range was defined on the basis of the considerations made in **Chapter 3**, *Subparagraph 3.3.2*.
In order to do this, mathematical modelling, supported by micro-computed tomography (μ-CT) imaging and accurate permeability laminar airflow alternating pressure wave drop measurements, was implemented to univocally quantify the effect of different pore features on mass transport properties in the selected temperature range.
Scaffolds characterization was completed by destructive crushing tests in order to evaluate the mechanical performances of the produced foams under compressive loading conditions.

In the second case, animated by the desire to combine biomaterials science and technology with waste management, an innovative and highly sustainable approach was developed.
This activity, inspired by the extreme versatility typical of foam replication technique, was carried out with a dual purpose:

i) explore new possibilities in terms of macroporous templates suitable for BTE approaches;
ii) provide a contribute in saving wastes for the development of highly sustainable and eco-friendly strategies for producing biomedical scaffolds by minimizing costs and environmental impact.

In order to do this, traditional foam replica technique was revised to adapt the process to the use of stale bread derived from industrial wastes, challenging selected as new sacrificial template due to its exceptional similarity to trabecular bone.

Replication of commercia PU sponges

Industrial PU foam sheets, easily available on the market as air and water filters, were selected as sacrificial templates; in particular, PU foams with a 45 ppi porosity and a 10 mm thickness were used.
In order to obtain a cylindrical geometry of the scaffolds, the foams were properly shaped by mean of cutting dies having a diameter of 13 and 16 mm, where sponges with a smaller diameter were used for low-temperature sintering treatments (T_{s1} and T_{s2}), while oversized templates were required approaching the crystallization onset of the material T_x in order to properly consider the higher densification occurring upon heating. This trick allowed to maintain the final diameter of all the sintered samples in the optimal 8-10 mm range for permeability evaluation and compression tests.

Scaffolds were prepared according to the schematic diagram in Figure 4.2 a.
A glass slurry, with composition 64H_2O – 6 polyvinyl alcohol (PVA) – 30 47.5B-32 (wt.%), was prepared by suspending glass powder into a binder solution.

First, PVA granules were dissolved in water at 60 °C under continuous magnetic stirring (200 rpm), until a clear solution was obtained (Figure 4.2 b). After about 30 min, some water was added dropwise to restore the original H_2O/PVA ratio and the solution was left to cool at room temperature.
Then, 47.5B-32 powder was added and mixed up to 10 min with a stirring rate of 300 rpm to achieve a homogeneous dispersion of glass particles (Figure 4.2 c). Subsequently, PU sponges were dipped one-by-one for 15 s into the glass slurry.

In order to remove the excess slurry from the pores, the cylinders were subjected to a properly designed compression protocol, (**Figure 4.3**), aimed at achieving a better control on the slurry distribution, thus improving the reproducibility and the repeatability of the overall manufacturing process.
All the samples underwent three complete immersion-compression cycles: after each immersion, the cylindric sample was placed onto a raised metallic grid and compressed to 2/3 of its diameter by the application of an instantaneous load (F=8.829 N), perpendicular to the grid plane.
In total, each sample underwent four compressions: between a compression and the following one, the cylinder was rotated 90 ° around the rotation axis in order to achieve a homogeneous distribution of the glass slurry within the whole porous volume. In order to avoid the formation of concentration gradients resulting from particles decanting, the slurry was subjected to vigorous agitation between one sample and the next up to availability.

After this stage, the impregnated sponges were placed onto a non-absorbent paper sheet and rotated at regular time intervals of about 5 min for 30 min and of 10-15 min for the subsequent 60 min, until no more slurry traces were visible on the substrate. Hence, drying was completed overnight at room temperature.

After drying, glass-coated foams (*green bodies*), shown in Figure 4.2 d, were thermally treated for 3 h at six different temperatures (T_{s1} = 600, T_{s2} = 650, T_{s3} = 700, T_{s4} = 750, T_{s5} = 800 and T_{s6} = 850, °C), keeping a constant heating and cooling rate of 5 °C/min and 10 °C/min, respectively.

Samples with suitable geometry for permeability assessment and mechanical tests were obtained by rectifying upper and lower surfaces of each scaffold by mean of a metallographic grinding polishing machine (Struers, LaboPol-2, 250-500 rpm). SiC sand papers with a #600 to #800 grit size were used until flat and parallel faces were obtained.
After polishing, scaffolds were immersed in an ultrasonic bath for 5 min to remove polishing debris, rinsed with pure ethanol and left to dry at room temperature overnight. Final dimensions (diameter, D_s and height, L_s) and mass m_s of the scaffolds after polishing were determined by digital caliper and precision scale.

As an example, Figure 4.2 e and Figure 4.2 f show the front view and the top view of scaffolds thermally treated at 650 °C, in which a high reproduction fidelity of the original template, as well as a good reproducibility of the final result at the macroscale is clearly appreciable.

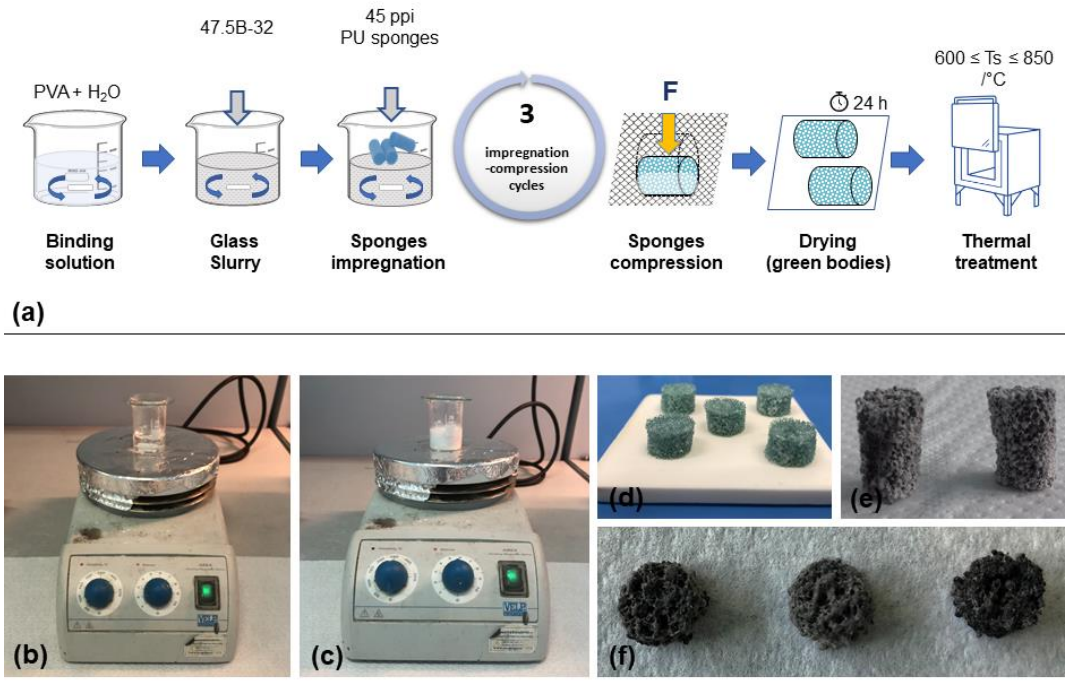

Figure 4. 2. a) Schematic diagram of scaffold manufacturing by foam replication technique; Experimental set up for the preparation of the glass slurry: b) preparation of the PVA-based binding solution, c) addition of47.5B-32 powder. d) cylindrical glass-coated foams before sintering; e) front view and f) top view of 47.5B-32 glass scaffolds sintered at 650°C.

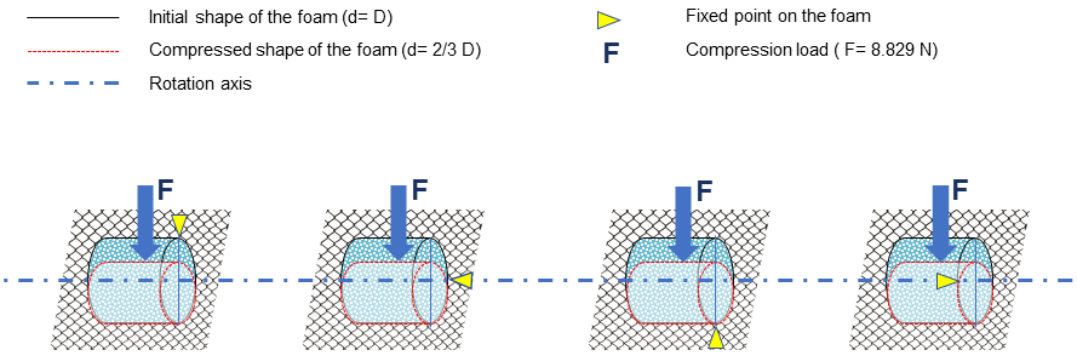

Figure 4. 3. Schematic representation of the compression protocol implemented for scaffold manufacturing. The yellow triangle in the picture indicates the rotation path of the foam cylinder.

In the following discussion, samples produced by foam replication technique will be referred to as FRS-T_{sn}, where the acronym FRS stands for *Foam-Replicated Scaffolds*, while T_{sn} indicates the specific temperature at which the sintering process was carried out.

Replication of stale bread derived from industrial wastes

Bread is worldwide recognized to be a staple food for human consumption, and, as a result, it is available in a wide variety of types at a very low cost.

In particular, in industrialized countries, home of consumerism and convenience food, bread is sold on the market in packaged formats produced by standardized processes that minimize variation among different batches coming from the same company.

In Italy and most of countries worldwide, packaged bread-based products must be sold with an expiry date, after which sale is not allowed anymore and expired bread becomes waste for disposal [217].

In the frame of this Ph.D. research activity, stale bread deriving from industrial wastes was proposed for the first time as a suitable candidate for templating the macroporous structure of glass-based scaffolds produced by a properly revised foam replica method.

Recently expired bread from industrial wastes (Roberto Industria Alimentare S.r.l., Treviso, Italy) was cut into regular stripes (Figure 4.4 a) and dried for 30 min in an oven at 80 °C, in order to remove residual moisture and/or alcoholic substances commonly used as food additives and preservatives. Then, 10×15×10 mm cuboidal samples were obtained by mean of a cutter (Figure 4.4 b).

The use of the new organic template makes it necessary to properly optimize the slurry formulation. In particular, the most crucial aspect of the process was the need to preserve the integrity of bread during the replica procedure while allowing the slurry to penetrate the whole porous volume of the template.

The first test, performed to assess the effective feasibility of the approach, was carried out following the procedure previously described for FRS, keeping the same composition (47.5B-32: PVA: H_2O= 30:6:64, wt.%).
However, in this case the impregnation of the template was inefficient and the formation of an outer shell of glass limiting the penetration of the slurry to the inner core was observed (Figure 4.4 c).

In the attempt to solve this problem, the slurry formulation was opportunely modified following a conventional *trial-and-error* approach.
Specifically, it was decided to test three different slurry compositions, obtained by varying the ratio between the slurry components and the size of the glass particles. In particular, all the tests performed aimed at favoring, following different strategies, the impregnation of the template by:

i) Reducing the PVA content from 6 wt.% to 1 wt.% to mitigate the formation of the transparent film typically formed upon drying, which could be likely responsible for the formation of the outer shell on the external surface of the cuboidal bread sample;
ii) Reducing the viscosity of the slurry by lowering the content of solid particles from 30 to 25 wt.%;
iii) Reducing the viscosity of the slurry by using finer glass particles having a particle size below 25 μm.

The compositions details are summarized in **Table 4.1**, where different samples are referred to as BDS-x, where the acronym BDS stands for *Bread-Derived Scaffolds,* while the letter *x* indicates the specific composition.

Table 4. 1. Slurry compositions tested for the production of BDS.

Sample name	Glass	Glass particle size/ µm	Slurry composition/ wt.%		
			PVA	H_2O	Glass
BDS-0	47.5B-32	≤ 32	6	64	30
BDS-a	47.5B-32	≤ 32	1	69	30
BDS-b	47.5B-32	≤ 32	6	69	25
BDS-c	47.5B-25	≤ 25	6	64	30

In order to preserve the integrity of the sacrificial template, the foam replica process was modified eliminating the impregnation-compression process. The bread blocks were instead soaked, one-by-one, into the slurry, until complete impregnation was achieved, i.e. until the sample had sunk.
Impregnated bread cuboids were left to dry at room temperature for about 48 h onto a raised metallic grid in order to allow the exceeding slurry to drop down by gravity.

An example of BDS_a green body revealing a homogeneous distribution of the slurry is represented in Figure 4.4 d. Compared to un-soaked bread blocks, glass-coated cuboids appeared shrunk, due to the effect of the dried PVA-based solution on the breadcrumbs, as well as a partial collapse of the 3D strut under the weight of the coating material.

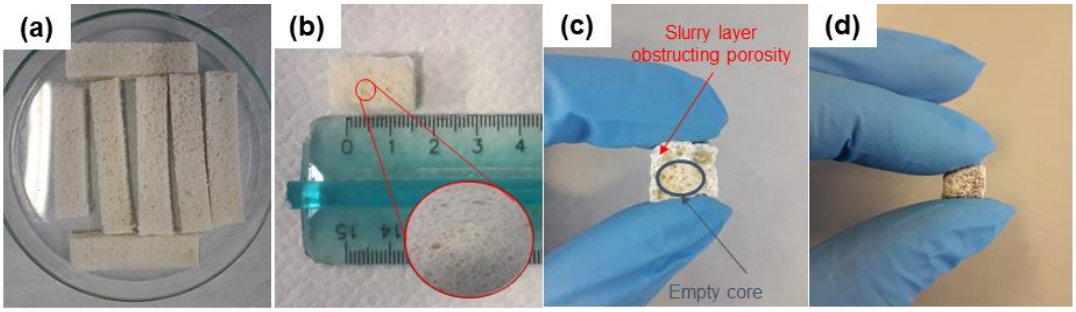

Figure 4. 4. a) Bread stripes before drying; b) bread cuboid before impregnation; c) cross-section of a green body obtained by using BDS_0 slurry composition, revealing an inefficient impregnation of the porous template; d) BDS-a green body before sintering, revealing a homogeneous distribution of the slurry material over the whole 3D volume.

The sintering temperature was selected following preliminary sintering treatments performed at T_s= 700 °C, which revealed an unsatisfactory densification of the scaffolds upon heating. The thus obtained samples, indeed, were hardly manageable and extremely brittle, thus suggesting the need for optimizing the thermal program.

Hence, the sintering temperature was increased and the *green bodies* were finally sintered at 750 °C for 3 h with a heating rate of 5°C/min, thus allowing the organic phase to be completely burnt out and the strut to properly densify upon sintering.

4.2.2 Dolomite foaming

As a novel contribution to the broad field of scaffold manufacturing, here it is described an effective and easy approach to produce silicate glass-derived scaffolds

by using, for the first time in the biomedical field, dolomite powder as a foaming agent for the formation of 3D bone-like porous glass-ceramics.

The project was carried out in collaboration with the research team of Prof. Dilshat Tulyaganov, working in the Department of Natural-Mathematical Sciences of the Turin Polytechnic University in Tashkent, Uzbekistan, where foams were produced. Scaffolds characterization, instead, was entirely carried out at Politecnico di Torino.

Here, for the sake of completeness, the dolomite foaming process is briefly described.

47.5B-32, produced at Politecnico di Torino, and commercial dolomite from Dehkanabad deposit (Uzbekistan) were used as basic materials for scaffold fabrication. As bread templating, dolomite foaming, too, carries some befits from the viewpoint of sustainability, suggesting the use of waste from mining as inexpensive pore-forming additive.

Table 4.2 and **Table 4.3** summarize the compositional and physical properties of precursors, respectively.

Table 4. 2. Oxides composition of 47.5B-32 and commercial dolomite used as precursors for the production of the foams.

Composition/ wt. %	SiO_2	P_2O_5	CaO	MgO	Na_2O	K_2O	Al_2O_3	SO_3	MnO	CO_2	Others
47.5B-32	45.36	5.64	17.82	6.40	9.85	14.96	-	-	-	-	-
Dolomite	2.74	0.15	30.02	19.63	0.27	0.10	0.39	0.39	0.01	45.40	0.90

Table 4. 3. Physical properties of 47.5B-32 and dolomite powder used for the foaming process.

Precursor (powder)	Amount in the scaffold/ wt. %	Particle mean size / µm	Density ρ/ g/cm^3	Specific surface area (SSA)/ m^2/g
47.5B-32	98	16.57	2.64	0.638
Dolomite	2	12.79	2.86	0.834

The right proportion between glass and dolomite powders, reported in **Table 4.3**, was identified on the basis of a previous study, in which glass foams were obtained starting from sheet glass wastes and fly ash resulting from an extinguished thermal power plant. In that study, carbonates, specifically dolomite $CaMg(CO_3)_2$ and calcite-based material comprising about 99% $CaCO_3$ and deriving from the marble cutting process, were used as foaming agents [218].

Considering the fact that appreciable foaming efficiency might be achieved at relatively low temperatures (~800 °C) with just 2 wt.% of dolomite incorporation, the formulation of the experimental batches in the current investigation was fixed at 98 wt.% of 47.5B-32 and 2 wt.% of $CaMg(CO_3)_2$.

A schematic diagram describing the procedure followed for the production of dolomite-foamed scaffolds is schematically depicted in **Figure 4.5**.

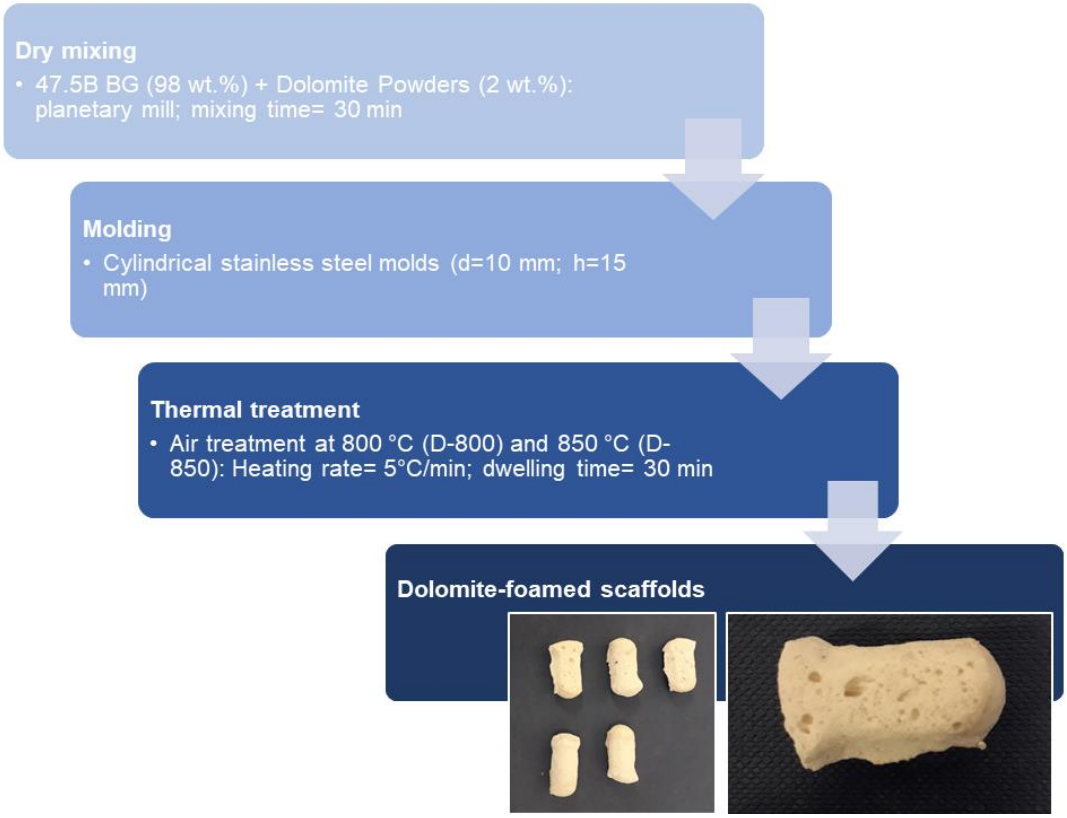

Figure 4. 5. Schematic diagram of dolomite foaming process

Glass and dolomite powders were dry-mixed for about 30 minutes in a planetary mill to obtain a homogeneous dispersion of dolomite powders within the batch. Afterwards, the mixture was transferred to cylindrical stainless-steel molds having diameter and height of 10 mm and 15 mm, respectively.

In order to allow the thermal decomposition of dolomite, which underpins the process here described, a high temperature heat treatment was performed in air at 800 °C and 850 °C for 30 min, using a heating rate of 5 °C/min (Carbolite type 3216 box furnace, Carbolite, Sheffield, UK); the obtained samples will be referred to as DFS-800 and DFS-850 scaffolds, respectively, where the acronym DFS stands for *Dolomite-Foamed Scaffolds*.

After cooling to room temperature, the scaffolds were removed from the molds for further investigations.

4.2.3 Robocasting

An adequate control on porosity, pore size and mechanical properties is fundamental to induce proper tissue ingrowth and cell migration through the whole 3D volume of the bone grafts.

Compared to the fabrication strategies described above, additive manufacturing (AM) offers the fascinating possibility to easily tailor graft properties by providing an accurate control both on the design and the processing parameters. The object, in fact, is built layer-by-layer according to a pre-determined. stl file or a text script, thus guaranteeing high reproducibility of scaffolds features even within different production batches.

In the past, 47.5B-32 glass was demonstrated to have a great potential as basic material for making printing inks with suitable features for robocasting technology. In this regard, Baino et al. [219] and Barberi et al. [190], [220], successfully described the production of bioactive grid-like scaffolds characterized by uniform and gradient porosity, with the aim of promoting fluid flow from the periphery to the core of the scaffolds while guaranteeing higher mechanical stability upon dissolution in physiological environment.

Starting from this point, the present part of the work focused on the development of a parallel easy approach to print 47.5B-based sol-gel materials avoiding intermediate calcination treatments.
In order to do this, a new printing ink, based on organic dried-gel materials, was developed readapting the protocol described in [190], [219], [220] by substituting 47.5B-32 particles with the same volumetric amount of DG-120.
In order to optimize the new ink for the extrusion process, it was necessary to modify both the ink preparation process and the printing parameters, according to the different rheological and physical behavior of the two materials.
Results were comparatively discussed using scaffolds based on the 47.5B-32 system, analogous to that described in [190], [219], [220], as reference.

The study was carried out at the Faculty of Medicine and Health Technology of the University of Tampere, in Finland**.**

Preparation of the Pluronic® F-127 solution

First, a Pluronic® F-127 binder solution (25 wt. %) was prepared by dissolving F-127 powder ($(C_3H_6O{\cdot}C_2H_4O)_x$, CAS Number 9003-11-6, Sigma Aldrich) in water. Compared to the previous studies [190], [219], [220], the concentration of the binder was decreased from 27.5 to 25 wt.% to properly adjust the physical behavior of the ink according to the different environmental conditions of temperature and humidity.

In order to prepare 50 g of binder solution (25 wt. %), 12.5 g of F-127 were added to 37.5 ml of distilled water in a plastic pot. Then, the container was put into an ice bath to favor the Pluronic dissolution in aqueous environment under the continuous action of a magnetic stirrer (100-150 rpm). The solution was mixed overnight,

replacing the ice when necessary to keep the temperature low and maintain the solution in the liquid state. When the batch appeared clear and homogeneous, without aggregates, the container was removed from the ice bath and stored in fridge at 4 °C until usage (**Figure 4.6**).

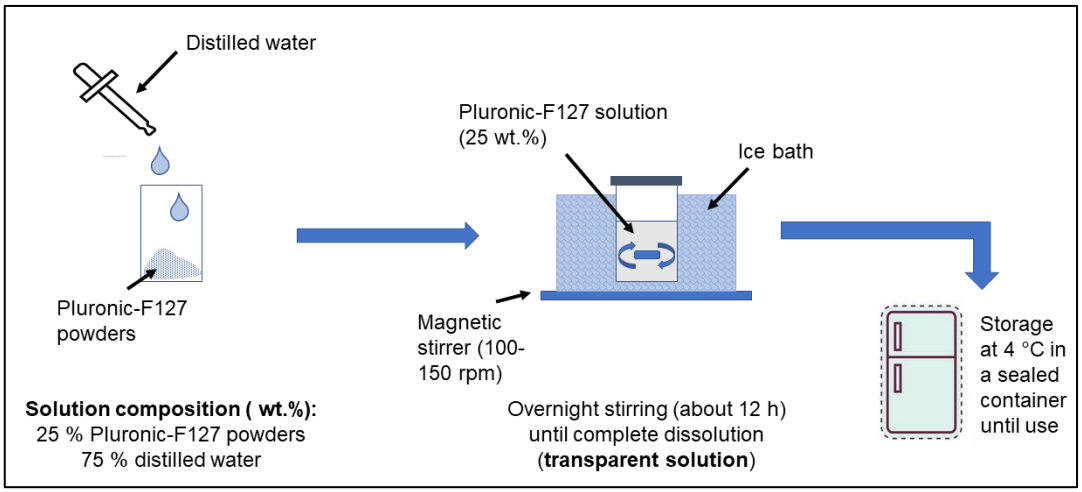

Figure 4. 6. Preparation of the F-127 binder solution.

Preparation of the printing inks

47.5B-32 and DG-120 particles were used as basic materials for the preparation of the printing inks.

DG-120 was manually grinded and sieved to get a final grain size between 38 and 150 μm. Finer particles were difficult to be obtained due to the great tendency of gel to form large aggregates.

The ink formulation, optimized by mean of some preliminary trials, included 65 vol.% of Pluronic® F-127 solution (25 wt. %) and 35 vol.% of solid particles.

The inks were prepared into small plastic pots, tuning the number of particles and binder solution to fill only 2/3 of the total volume of the printing cartridge because of the poor stability of the ink over time, rapidly changing its physical properties according to the external environmental conditions.

The amount of glass/gel and Pluronic-F127 solution was calculated in the right proportions on the basis of density values. Considering a final volume of 3 ml, the masses of each component were calculated as reported below (**Equations 4.1**, **4.2** and **4.3**):

$$m_{F127} = \frac{vol.\%_{F127} \cdot V_f}{100} \cdot \frac{1}{\rho_{F127}} \qquad 4.1$$

$$m_{47.5B-32} = \frac{vol.\%_{47.5B-32} \cdot V_f}{100} \cdot \frac{1}{\rho_{47.5B-32}} \qquad 4.2$$

$$m_{DG-120} = \frac{vol.\%_{DG-120} \cdot V_f}{100} \cdot \frac{1}{\rho_{DG-120}} \qquad 4.3$$

where ρ_{F127}, $\rho_{47.5B-32}$ and $\rho_{47.5B-32}$ are the density values of the various components, of 1.067, 2.64 and 1.39 g/cm^3, respectively and V_f is the final ink volume required to partially fill the cartridge up to 2/3 of its total volume.
The solid phase of the ink (47.5B-32 or DG-120) was directly weighed within a plastic pot and F-127 solution was added dropwise up to the required volume.

In order to improve the homogeneity of the ink, solid particles were suspended in the liquid media by vigorous mixing at 2500 rpm up to 1 min (Vibrofix VF1 electronic, Ika-Werk).
Up to this moment, the procedure followed for the preparation of the two inks was approximately the same, with minimum variations determined by the different nature of 47.5B-32 and DG-120 materials. As an example, given the higher wettability of the gel and its partial solubilization within the Pluronic solution upon mixing, it was necessary to consider a larger V_f to fill the cartridge. Thus, instead of 3 ml, **Equations 4.1**, **4.2**, **4.3** were solved considering a doubled final volume of 6 ml.

Also, the mixing procedure was subjected to little changes according to the type of solid particles used.
In the case of 47.5B-32 ink (**Figure 4.7**), it was necessary to alternate mixing with about 30s-immersion into an ice bath, in order to keep the solution liquid. The low temperature, in fact, decreased the viscosity of the solution, thus hindering the formation of air bubbles.
This mixing and cooling protocol was repeated until homogeneous and bubble-free slurries were obtained (approximately from 5 to 10 times).

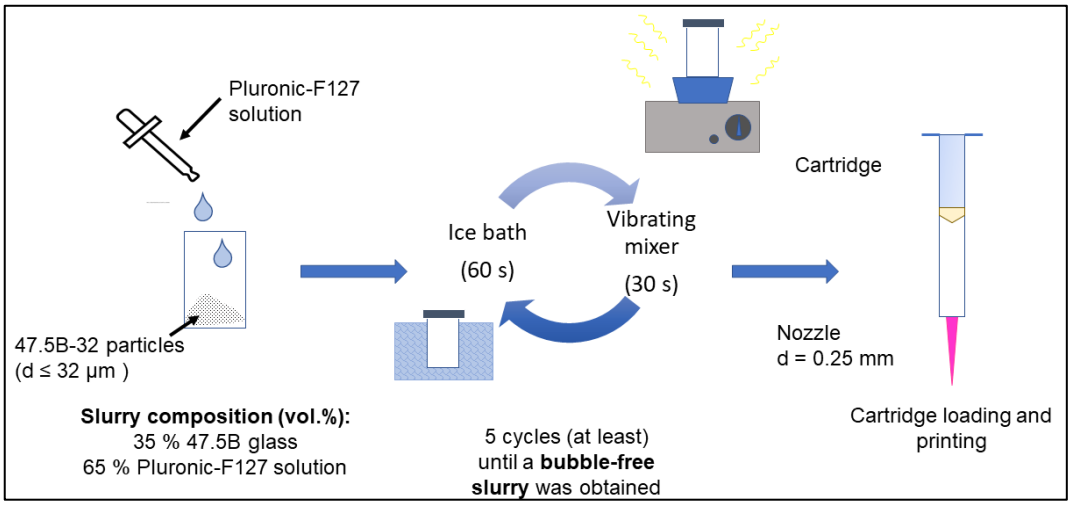

Figure 4. 7. Preparation of the 47.5B-32 ink.

In the case of DG-120 particles (**Figure 4.8**), the slurry was continuously mixed up to 5 min, until a homogeneous and milky ink, similar to liquid soap, was obtained.
As the viscosity of the material was too low for printing, an additional step was required and, as soon after mixing, the slurry was poured onto an absorbent paper sheet and hand-worked with a cold metal spatula until a moldable dough was obtained.
The procedure took from 5 to 15 min, varying according to the environmental conditions of temperature and humidity.

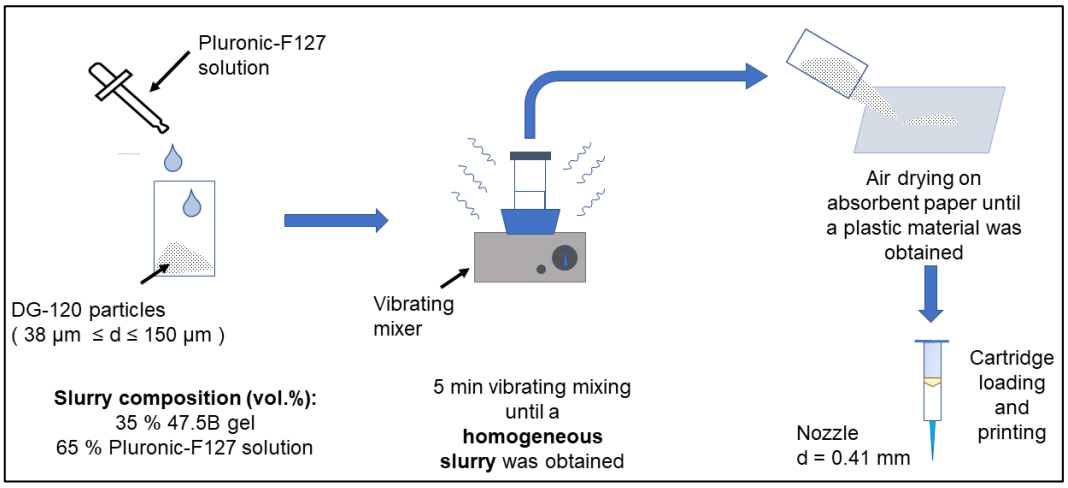

Figure 4. 8. Preparation of the DG-120 ink.

After mixing, the inks were ready to be transferred to the printing cartridge.

Typically, a printing cartridge is composed of two different parts: a plastic pipe, equipped with two terminal flaps for fixing to the airline, and a plastic plunger, acting as a valve to apply an isostatic pressure to the ink during printing.

In order not to trap too much air during the cartridge loading, first, the slurries were transferred to a common 10 ml injection syringe, removing the exceed air by simply acting on the piston until a small amount of ink came out from the tip.
Then, the syringe was connected to the cartridge by mean of an adapter and the ink was injected inside the cartridge acting on the piston by simultaneously applying a constant pressure on the plunger by mean of a rod.

Then, the cartridge was sealed with some Parafilm® and let stabilize for 15 to 30 min. to achieve the optimal viscosity for printing.
Another convenient option was to prepare the ink, fill the cartridges in advance and store them in the fridge at 4 °C until use. On the printing day, it was sufficient to let the ink rest at room temperature for about 30-60 min in order to get the proper viscosity.
In both cases (47.5B-32 and DG-120 inks) this alternative was found to have no significant effects on the printing outcome.

Robocasting and sintering

A Tabletop-3Dn (nScrypt Inc., Orlando, Florida, USA) printer with base set-up was used for robocasting (Figure 4.9 a).

The machine was composed of a printing tower, comprising two printing heads (allowing the simultaneous extrusion of different materials), and a building platform, consisting of a metal substrate.

The printing tower was allowed to move up and down along the *z* axis with an accuracy of 5 µm, while the building platform moved in the *xy* plane, with an accuracy of about 10 µm. A schematic of the operating principle of a robocasting machine is depicted in Figure 4.9 b.

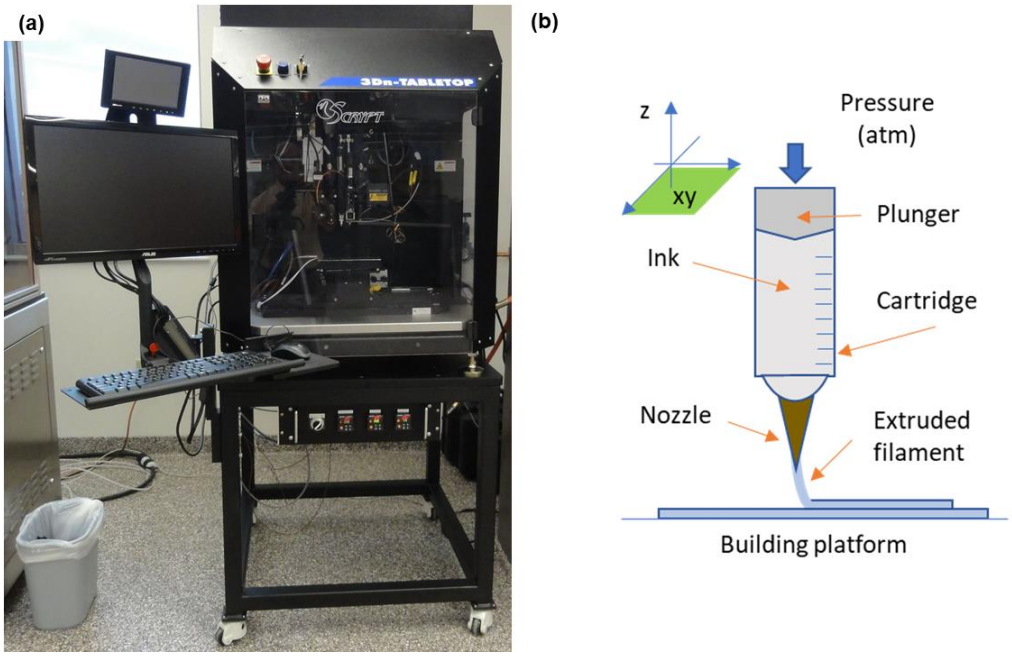

Figure 4. 9. a) Tabletop-3Dn printer; b) schematic of the operating principle of a robocasting machine.

Plastic nozzles with an inner diameter of 250 and 410 μm (Nordson EDF Optimum® SmoothFlow™) were fixed to the tip of the cartridge by a conventional screwing mechanism and used for extruding glass-based and gel-based inks, respectively.

The cartridge was fixed to one of the two printing heads perpendicularly to the printing base and coupled with the airline as shown in **Figure 4.10**.

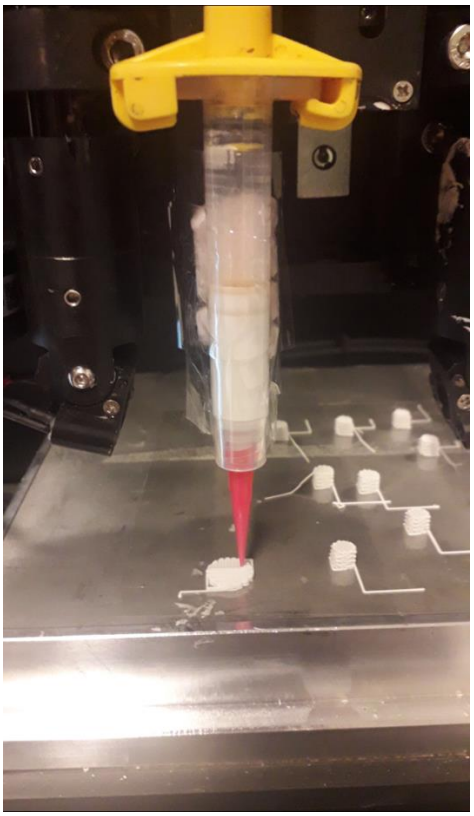

Figure 4. 10. Loaded cartridge during printing. Series production of 47.5B-32 scaffolds with different diameters.

Acetate sheets (Colour Copier and Laser Transparency OHP Film, Folex AG, Seewen, Switzerland) were placed onto the building platform and used as printing substrate. This material was able to guarantee a good adherence to the metal base, as well as a good interaction with the ink, resulting in a good adhesion of the first layer to the printing base and, at the same time, an easy detachment of the green bodies after drying.
Input parameters were inserted by mean of a dedicated software (MachineTools3.0) provided by the manufacturer *nScrypt*.

In particular, the software required:

i) The design script, i.e. a text file defining all the movements of the printing head and the building platform, according to a spatial vector.
   In the present study, cylindrical scaffolds with a grid-like porosity (about 200 μm) were obtained using a printing speed of 2 mm/s.
ii) The starting z value (zero level), manually set to ensure a slight contact between the nozzle and the acetate sheet.
iii) The feeding speed, i.e. the extrusion pressure. This parameter was optimized time by time according to the ink type and the daily environmental conditions of temperature and humidity. In general, with a printing head speed of 2 mm/min, the optimal working window identified for 47.5B-32 ink was between 1.24 and 1.45 bar, while that for DG-120 ink was between 0.83 and 1.10 bar. This difference can with certainty be attributed to the qualitatively lower viscosity of the gel-based ink.

Scaffolds with different diameters (8.5 mm, 20 layers; 4.5 mm, 20 layers) where easily obtained using the 47.5B-32 ink, while, in the case of DG-120, only scaffolds with diameter of 4.5 mm were produced due to the formation of viscosity gradients within the cartridge, attributed to the poor thermal stability of the ink over extended periods of time.

After printing, the scaffolds were left to dry in incubator at 37 °C for about 48 h in order to speed up the process and guaranteeing a more uniform drying over the whole volume, thus avoiding the formation of cracks.
After drying, the green bodies were carefully detached from the acetate sheet and moved to an alumina plate for sintering.

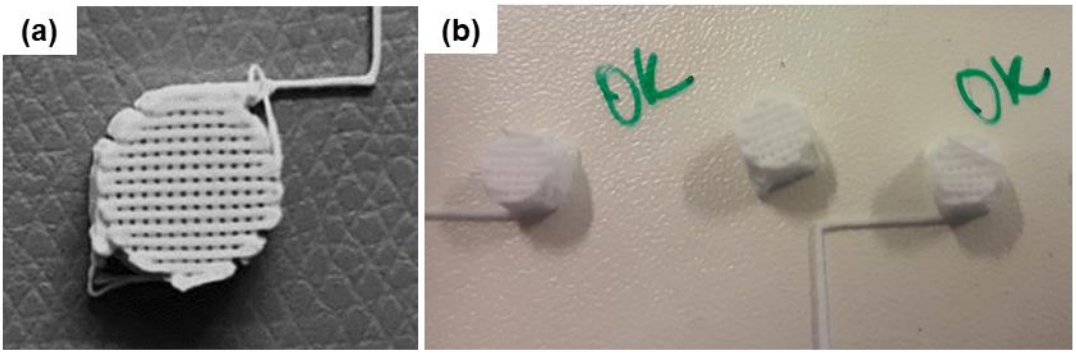

Figure 4. 11. Green bodies: a) 47.5B-32 and b) DG-120 scaffolds before sintering

The sintering treatment was performed in air, setting a multistage heating program, as represented in Figure 3.2 a, **Chapter 3**.

Sintered scaffolds obtained by robocasting will be referred to as RCS-md and RCS-sg, indicating respectively robocasted scaffolds based on melt-derived and sol-gel 47.5B multicomponent bioactive materials.

4.3 Characterization of 47.5B-based glass and glass-ceramics for scaffold manufacturing

Table 4.4 provides an overview of the analysis techniques used to characterize FRM, BDS, DFS and RCS.

If used to characterize scaffolds, the techniques already described in the section on glass/glass-ceramics are not repeated here.

Table 4.4. Characterization analyses performed on 45.5B-based scaffolds produced by different manufacturing technology.

Characterization technique	Aim of the analysis	Samples analysed
Total Porosity assessment	Preliminary evaluation of porosity features	FRS, BDS, DFS, RCS
Mechanical tests	Mechanical behaviour under compressive loading conditions	FRS, BDS, DFS
Bioactivity tests	Surface evolution upon soaking in Simulated Body Fluid (HA deposition)	BDS, DFS, RCS
X-Ray diffraction before and after bioactivity tests	Individuation of crystalline phases nucleated upon sintering, detection of the HA reaction layer upon bioactivity tests	FRS, BDS, DFS, RCS
Scanning electron microscopy/Energy dispersion spectrometry before and after bioactivity tests	Analysis of morphological and compositional features of scaffolds surface, morphological and compositional characterization of the HA layer upon soaking in Simulated body Fluid	FRS, BDS, DFS, RCS
Ion release	Quantitative analysis of the ion-exchange mechanisms occurring upon soaking in Simulated body fluid	RCS
Intrinsic permeability assessments	Preliminary evaluation of scaffolds mass transport properties as function of the sintering treatment	FRM-Tsn
Micro-CT	Analysis of changes occurring in porosity features as a result of the sintering treatment	FRM-Tsn
Complete characterization of the porous microstructure	Determination by mathematical modelling of parameters describing the microporous architecture as function of the sintering treatment	FRM-Tsn

Basic characterization analyses performed on 47.5B-based FRM, BDS, RC and DF scaffolds
Total porosity, morphological and compositional assessments

The total porosity ε_0 of the scaffolds produced was assessed by gravimetric method [221], according to Equation 4.4:

$$\varepsilon_0 = 1 - \frac{\rho_s}{\rho_m} \quad \textbf{4.4}$$

where ρ_s is the apparent density of the scaffold, calculated as mass-to-volume ratio, and ρ_m is the density of the bulk material (2.64 g/cm^3), assessed in a previous study by Archimedes Principle [219].
Total porosity results were expressed as mean value ± standard deviation. The number of samples analyzed for determining the total porosity of scaffolds produced by different manufacturing strategies is reported in **Table 4.5**.

Table 4. 5. Number of samples considered for total porosity assessment for each scaffold type analyzed.

Sample type	N° of samples analyzed
FRS	4 (per each sintering group)
BDS-a	5
DFS	5 (per each sintering group)
RCS-md	10
RCS-sg	10

Morphological features of the scaffolds were investigated by scanning electron microscopy (SEM) (field-emission SEM equipped with EDS; Supra TM 40, Zeiss, Oberkochen, Germany), using an inspection voltage of 15 kV.

Before the analysis, scaffolds were sputter-coated with a conductive 7 nm-thick layer of chromium.

Mechanical characterization

The compressive strength of scaffolds was evaluated through destructive crushing tests by using an MTS machine (QTestTM/10; cell load 2.5 kN, cross-head speed set at 0.5 mm/min). The failure stress was calculated as the ratio between the maximum load registered during the test and the resistant cross-sectional area, according to **Equation 4.5**:

$$\sigma_c = \frac{F_{Max}}{A} \quad \textbf{4.5}$$

where σ_c (MPa) is failure stress, F_{Max} (N) is the maximum load and A (mm^2) is the cross-sectional area. The results were expressed as mean ± standard deviation. The surfaces of all the samples were rectified before the test by gentle polishing, using SiC grit paper (#600, #800).

Table 4. 6. Number of samples considered for compression strength assessment for each scaffold type analyzed.

Sample type	N° of samples analyzed	Cross section
FRS	4 (per each sintering group)	Circular
BRS-a	4	Square
DFS	5 (per each sintering group)	Circular

Bioactivity tests in Simulated Body Fluid and Ion Release

Simulated Body Fluid (SBF) was prepared according to the protocol reported by Kokubo and Takadama [194] and in vitro bioactivity of the samples was investigated upon soaking at 37 °C.

A mass-to-volume ratio of 1.5 mg/ml was used, as suggested in a previous study by the Technical Committee 4 (TC04) of the International Commission on Glass (ICG) [195]. At each time point, pH value was monitored in order to qualitatively evaluate the ionic exchange between the material and the solution. At the end of the experiment, the samples were gently rinsed with distilled water, dried overnight at 37 °C in incubator and stored in a sealed plastic box for future investigations.

In **Table 4.7**, the testing conditions and the number of samples considered for each manufacturing technology are reported.

Table 4. 7. Testing conditions and number of samples subjected to bioactivity evaluation in Simulated Body Fluid.

Sample type	N° of samples analyzed	Testing conditions	Time points
BRS	2 (per each time point)	Static/refresh every 48 h	24 h, 48 h, 1 week
DFS	2 (per each time point)	Static/refresh every 48 h	48 h, 1 week. 2 weeks
RCS-md	3 (per each time point)	Orbital shaker/no refresh; 100 rpm	24 h, 48 h, 72 h, 1 week, 2 weeks
RCS-sg	3 (per each time point)	Orbital shaker/no refresh; 100 rpm	24 h, 48 h, 72 h, 1 week, 2 weeks

After bioactivity tests, SEM/EDS morphological and compositional analyses were performed to monitor surface's evolution upon soaking in simulated body fluid.

Additionally, scaffolds produced by robocasting technology were subjected to ion release assessments: at each time point indicated in **Table 4.7**, 1 ml of SBF was withdrawn and diluted with 9 ml of HNO_3 (1 M) to be analyzed by inductively coupled plasma optical emission spectroscopy (ICP-OES) (5110 ICP-OES, Agilent Technologies) in order to quantify the concentration of ions within the solution.

4.3.1 Comprehensive assessment of FRS permeability: experimental measurements by pressure wave drop, mathematical modelling and µCT-based analysis of porosity

Intrinsic permeability characterizes both scaffold architecture and mass-transport properties, quantifying the ability of a porous material to conduct fluid flow through its whole volume.

However, an accurate determination of intrinsic permeability is a little more complex compared to other morphological features, which can instead be easily determined by conventional imaging techniques.

Over time, some mathematical models have been developed, which put in relation intrinsic permeability with morphological features, such as porosity, pore size and orientation and inter-pores connectivity, thus allowing to indirectly determine this crucial parameter.

In the present part of the study, carried out in cooperation with the Italian National Institute of Metrological Research and the Iceland Innovation Center the overall changes occurring in the porous microstructure of foam replicated BG-based scaffolds upon different sintering conditions were determined by combining accurate experimental intrinsic permeability measurements and detailed μ-CT-based pores analysis in a complex mathematical model.

Theoretical background: costitutive equation and model development

The starting point for the development of the mathematical model was the Forchheimer equation [222], according to which the pressure loss of a one-directional fluid flow through a permeable material can be described as the sum of two different contributions, i.e. a viscous energy loss term, proportional to the linear flow velocity U, and an inertial loss term, proportional to the velocity squared U^2 (**Equation 4.6**):

$$-\frac{\partial P}{\partial x} = \mu a U + \rho b U^2 \qquad \textbf{4.6}$$

where x is the flow direction, ∂P is the pressure gradient, and a and b are two empirical parameters related to the fluid dynamic viscosity μ and the fluid density ρ, respectively.

According to the Ergun model [223], revised by Niven in 2002 [224], the characteristic length scale of the internal structure of a porous medium can be assumed as the average pore diameter d_p (for pores of arbitrary shape [225], [226]), as also reported by Chor et al. and Wadell et al. [227], [228], as well as in the recent Wu-Yu-Yun resistance model [229].

As a direct consequence, the two empirical constants a and b of the Forchheimer equation (**Equation 4.6**) can be expressed as function of morphological parameters (**Equation 4.7** and **Equation 4.8)**, with a well-defined physical meaning:

$$a = 72\tau \frac{(1-\varepsilon)^2}{\varepsilon^3} \cdot \frac{1}{\varphi_p^2 d_p^2} \qquad \textbf{4.7}$$

$$b = 0.75\tau \frac{(1-\varepsilon)}{\varepsilon^3} \cdot \frac{1}{\varphi_p d_p} \cdot \left(\frac{3}{2} + \frac{1}{\beta^4} - \frac{5}{2\beta^2}\right) \qquad \textbf{4.8}$$

where d_p is the average pore diameter, φ_p is the pore shape factor (sphericity), ε is the effective porosity, τ is the pore tortuosity and β is the ratio of d_p to throat diameter d_t, i.e. $\beta = d_p/d_t$, according to [229], [230].

According to the model proposed by Niven [224], the pores diameter d_p can be calculated from **Equation 4.9**:

$$d_p = \frac{6V_p}{A_p \varphi_p} \quad \textbf{4.9}$$

where V_p is the volume of a single (non-spherical) pore and A_p is its internal surface area.

Pore sphericity (φ_p) indicates how closely the shape of a pore resembles that of a perfect sphere. Accordingly, it is defined as the ratio between the maximum radius of the sphere inscribed in the pore of any arbitrary shape R_{in} and the minimum radius of the sphere circumscribed in the same pore r_{cir} [226] (**Equation 4.10**):

$$\varphi_p = \frac{R_{in}}{r_{cir}} \quad \textbf{4.10}$$

The effective porosity ε is defined as the fractional volume of the pores that actually allow fluid flow within the permeable material. It is given by the difference between the total porosity ε_0 (calculated from **Equation 4.4**) and the closed porosity ε_c, determined by the presence of voids of dead-end pores and closed pores, according to **Equation 4.11**:

$$\varepsilon = \varepsilon_0 - \varepsilon_c \quad \textbf{4.11}$$

β is a parameter related to the effects of contracting and expanding pore cross-sections, and can be expressed as function of ε, according to **Equation 4.12**:

$$\beta = \frac{1}{1 - \sqrt{1 - \varepsilon}} \quad \textbf{4.12}$$

To improve clarity the physical meaning and geometrical representation of φ_p and β is schematically depicted in **Figure 4.12**.

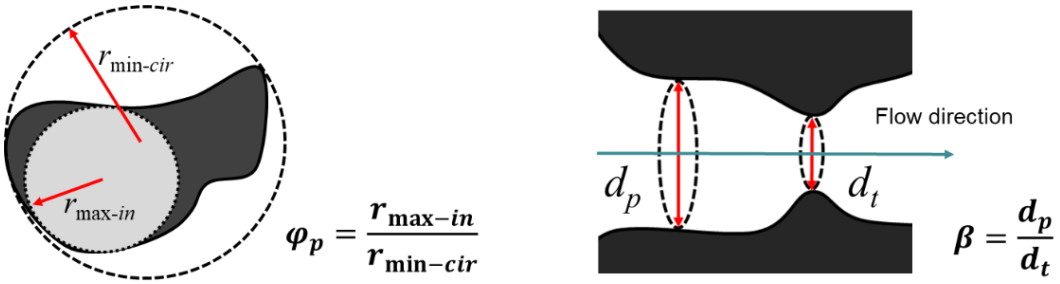

Figure 4. 12. The pore sphericity and the pore cross-section change, due to a throat, in the flow direction.

The tortuosity τ is defined as the ratio between the length L_s of the permeable medium (scaffold), along the macroscopic pressure gradient in the x-direction, and the actual length L_p of the tortuous pore, i.e. $\tau = L_p/L_s$. It can be estimated from the comprehensive Yu and Li's geometrical model [231] according to **Equation 4.13**:

$$\tau = \frac{1}{2}\left[1 + \frac{1}{2}\sqrt{1-\varepsilon} + \sqrt{1-\varepsilon}\,\frac{\sqrt{\left(\frac{1}{\sqrt{1-\varepsilon}} - 1\right)^2 + \frac{1}{4}}}{1-\sqrt{1-\varepsilon}}\right] \qquad \textbf{4.13}$$

Although **Equation 4.13** derives from a geometrical approximation, it is considered adequate enough to represent tortuosity in porous media, as demonstrated also by Koponen and coworkers in [232], [233].

By explicating the correct relationships among terms, the pressure loss is given by **Equation 4.14**:

$$-\frac{\partial P}{\partial x} = \mu\left[72\tau\frac{(1-\varepsilon)^2}{\varepsilon^3}\cdot\frac{1}{\varphi_p^2 d_p^2}\right]U + \rho\left[0.75\tau\frac{(1-\varepsilon)}{\varepsilon^3}\cdot\frac{1}{\varphi_p d_p}\cdot\left(\frac{3}{2} + \frac{1}{\beta^4} - \frac{5}{2\beta^2}\right)\right]U^2 \qquad \textbf{4.14}$$

where this constitutive equation has to be intended only for stiff, solid, permeable materials.

At the macroscale level, in laminar regime, the flow of a fluid through a permeable material can be described by the Darcy's transport model, according to which a proportional relation between the fluid velocity and the pressure drop gradient can be established (**Equation 4.15**):

$$-\frac{\partial P}{\partial x} = \frac{\mu}{k}U \qquad \textbf{4.15}$$

where *k* is the intrinsic permeability of the porous medium.

By combining **Equation 4.6** and **Equation 4.15**, it is possible to relate the intrinsic permeability *k* with the morphological parameters *a* and *b* (**Equation 4.16**):

$$\frac{\mu}{k}U = \mu a U + \rho b U^2 \qquad \textbf{4.16}$$

If *U* is low enough, the inertial losses, dependent on U^2, can be overlooked [228]. This condition occurs when the interstitial Reynolds number R_i is close to 1, where the interstitial Reynolds number R_i can be calculated from **Equation 4.17**:

$$R_i = \frac{\rho d_p U \varphi_p}{\mu(1-\varepsilon)} \qquad \textbf{4.17}$$

Under the assumption of laminar flow, i.e. R_i<1 and $\frac{\rho b U^2}{\mu a U} \leq 0.01$, the intrinsic permeability k of a permeable material (scaffold) can be determined in the linear Darcy's region as only function of pores morphological features (**Equation 4.18**):

$$k = \frac{\mu U}{\mu a U + \rho b U^2} \cong \frac{1}{a} \rightarrow k \cong \frac{\varphi_p^2 d_p^2}{72\tau} \cdot \frac{\varepsilon^3}{(1-\varepsilon)^2} \qquad \textbf{4.18}$$

Intrinsic permeability measurements: the experimental set-up

Intrinsic permeability measurements were performed in collaboration with Dr. Alessandro Schiavi, in the Applied Metrology and Engineering Division of the National Institute of Metrological Research (INRiM) (Turin, Italy).

When R_i is lower than 8.6, the fluid flow through the permeable material is assumed as laminar and non-linear effect are lower than 10% [228], [234].

According to what said above, the intrinsic permeability k can be determined in the Darcy's linear region, by measuring the volumetric flow rate and the pressure loss through a permeable sample, as described by **Equation 4.19**:

$$k = \mu \frac{Q_v}{\Delta P} \cdot \frac{L_s}{A_s} \qquad \textbf{4.19}$$

where μ is the dynamic fluid viscosity, Q_v is the volumetric flow rate ($Q_v = U \cdot A_s$), ΔP is the pressure differential upstream and downstream the permeable material along the length L_s of the sample, and A_s is the surface area of the sample perpendicular to the flow direction.

The intrinsic permeability of FRS sintered at different temperatures was determined by a novel acoustic technique.

Unlike the methods reported in literature up to now for assessing the permeability of biomedical scaffolds, this technique relies on the measurement of the sinusoidal pressure component, using air instead of water as fluid media and requiring only a single transducer (a low frequency microphone) for the measurement of the pressure drop upstream and downstream of the scaffold.

A schematic diagram of the experimental apparatus used for permeability measurements is represented in **Figure 4.13**.

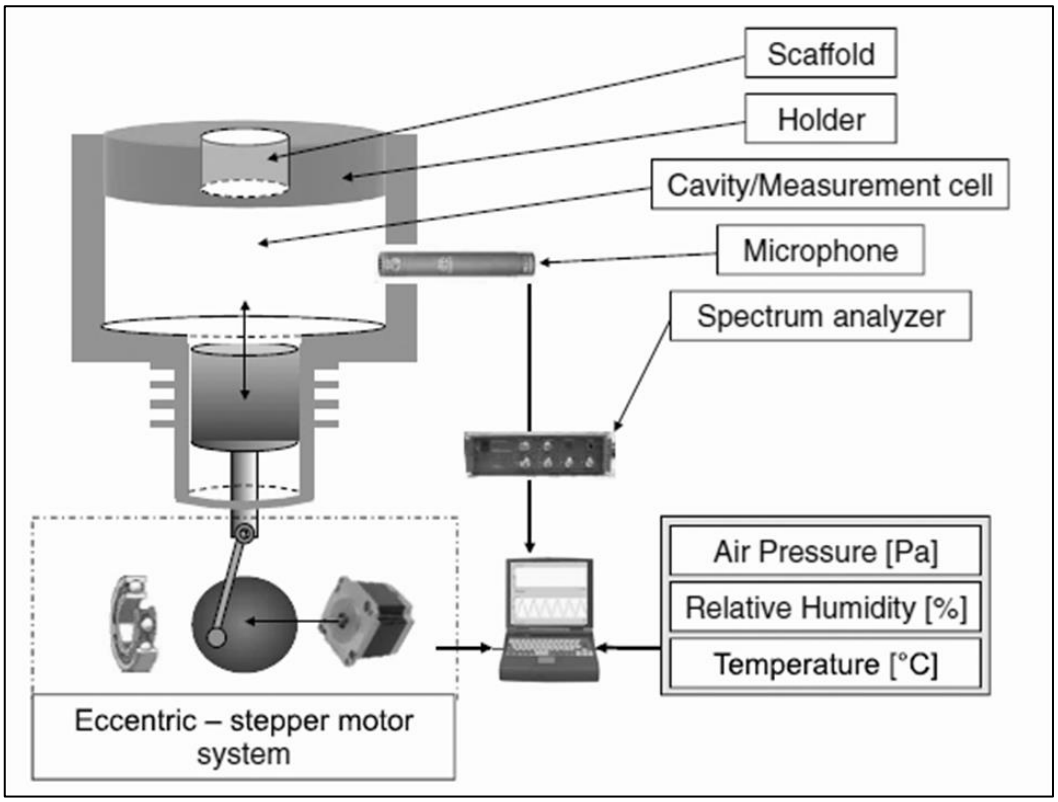

Figure 4. 13. Schematic of the experimental apparatus used for intrinsic permeability measurements. Figure reproduced with permission from Schiavi et al. [235].

The permeability k was determined on the basis of the ratio between the r.m.s. volumetric airflow rate and the r.m.s. pressure, according to Darcy's law (**Equation 4.20**):

$$k = \mu \frac{q_{v,\mathrm{rms}}}{p_{\mathrm{rms}}} \cdot \frac{L_s}{A_s} \qquad \textbf{4.20}$$

The alternating r.m.s. volumetric airflow $q_{v,\mathrm{rms}} = \pi f h A_k (\sqrt{2})^{-1}$ depends on the surface area A_k of the piston, the peak-to-peak piston stroke h and the frequency of oscillation f, while the sinusoidal r.m.s. pressure component $p_{\mathrm{rms}} = 1.4 p_0 \, \partial V (V_0 \sqrt{2})^{-1}$ depends on the atmospheric static pressure p_0 and the sinusoidal volume variation ∂V induced by the motion of the piston on the volume of air V_0 closed between the permeable sample and the piston. The dynamic viscosity μ of the air, for acoustic applications, was calculated by applying Rasmussen model [236], on the basis of environmental air temperature T_{air} and relative humidity RH conditions during the measurements.

By using f=0.15 Hz, and considering the geometry of the measurement system (A_k=1.9·10^{-3} m^2 and h=1.7·10^{-3} m), it resulted $q_{v,r.m.s}$ =1.09·10^{-6} m^3/s.

A schematic representation of the principle of measurement is depicted in **Figure 4.14**.

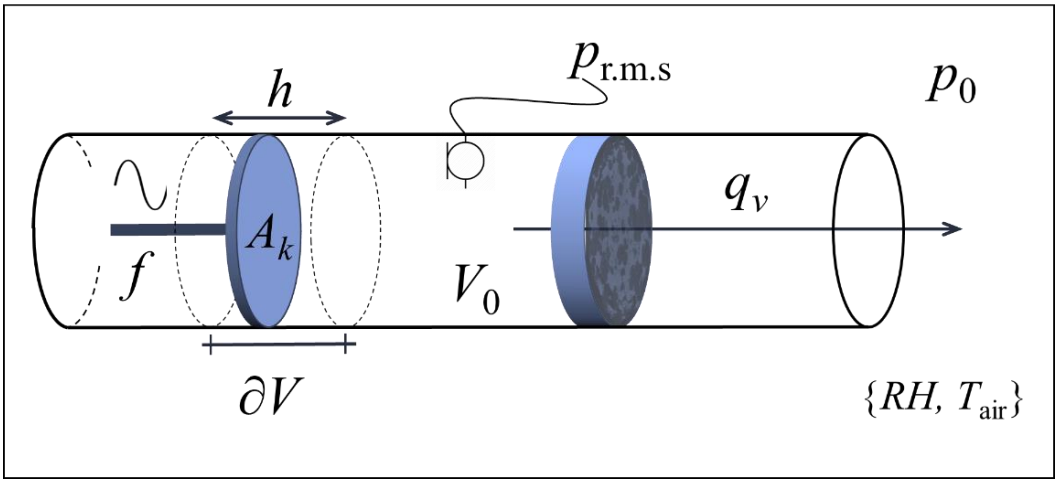

Figure 4. 14. The principle of intrinsic permeability measurement by using an alternating airflow.

μ-CT analysis: average pore diameter, sphericity assessment and pore interconnectivity

Micro-CT images were acquired at the Innovation Centre Iceland (Reykjavík), in Iceland, in collaboration with the research team of Prof. Gissur Orlygsson.

Glass and glass-ceramic scaffolds (FRS-T_{sn}) were analyzed in air by a Phoenix Nanotom S X-ray μ-CT scan (Waygate Technologies/General Electric Sensing and Inspection Technologies GmbH, Wunstorf, Germany). Projection images were collected using a source voltage of 110 kV and a source current of 110 μA, employing no X-ray filters. A translational motion compensation was used in order to avoid any mismatching between the 0° and the 360° shadow images in case of accidental movements of the sample during data acquisition.
A 10-fold magnification with a voxel size of 5.00 μm, rotation step size of 0.50 °, exposure time of 1.5 s and tube mode 0 with maximum target power 2.7 W, were used. Before image acquisition, a reference image was collected (blank), integrating three images for each rotation step.
Virtual volumes were reconstructed from the projection images using the *datos-x* reconstruction software provided by manufacturer and structural features of the scaffolds were determined by using the VGStudio Max 3.3 software (Volume Graphics, Heidelberg, Germany) based on the Cauchy-Crofton approach, through the add-on modules Coordinate Measurement and Foam/Powder Analysis.
A virtual cylinder was fitted into each reconstructed scaffold model and the cylinder size maximized without extending out of the scaffold contours. The cylinder was extracted as a separate virtual volume and a 3×3×3 median filter was applied to the data for de-noising before an isovalue-based surface determination procedure was run.
The Foam/Powder analysis module was used to extract foam structure data (merge threshold= 95%). The use of this module allowed the segmentation of data into topologically disconnected components which can be visualized and subjected to statistical analysis.

Information on number of pores, on pore shape and size (surface area A_p, volume V_p, sphericity $\varphi_p = A_{sphere}/A_p$) as well as on pore interconnectivity (open, closed, border) were collected and used for calculations and statistical analysis.

Determination of the effective porosity and tortuosity

On the basis of the accurate experimental data obtained from μ-CT analysis (pore average diameter d_p, sphericity φ_p) and from the measurement of intrinsic permeability k, it was possible to define the overall pore-related microstructural properties as a function of effective porosity ε by applying **Equation 4.18** to each scaffold.

In particular, by expressing pore tortuosity as function of the effective porosity (**Equation 4.13**) in **Equation 4.18**, it is possible to obtain **Equation 4.21**:

$$\frac{72k}{\varphi_p^2 d_p^2} = \frac{\varepsilon^3}{(1-\varepsilon)^2} \cdot \left[\frac{1}{2} \cdot \left(1 + \frac{1}{2} \cdot \sqrt{1-\varepsilon} + \sqrt{1-\varepsilon} \cdot \frac{\sqrt{\left(\frac{1}{\sqrt{1-\varepsilon}} - 1\right)^2 + \frac{1}{4}}}{1-\sqrt{1-\varepsilon}} \right) \right]^{-1} \qquad \textbf{4.21}$$

The only unknown parameter in **Equation 4.21** is the effective porosity ε, which can be graphically calculated from the zero-values of the function. In this case, the equation was solved using an online available graphic calculator (GeoGebra).

Once the effective porosity ε was determined, the full set of microstructural parameters was obtained solving the equations previously reported.

Moreover, the actual interstitial Reynolds number R_i, the viscous loss term $a\mu U$ and inertial loss term $b\rho U^2$ were definitively quantified.

Assuming laminar flow conditions, the friction factor f_c was determined by **Equation 4.22** [237]:

$$f_c = \frac{72\tau}{R_i} + 0.75\tau \qquad \textbf{4.22}$$

Finally, an estimation of the permeability k as a function of both viscous and inertial effects was achieved and compared to experimental values.

Statistical methods

Scaffold diameter D_s, length L_s, surface area A_s and volume V_s, were expressed as mean value ± standard deviation, obtained from 12 independent measurements for each sintering group.

The intrinsic permeability k was determined in quadruplicate for each sintering group. Results of permeability were expressed in the range between the 1st and the 3rd quartile.

Analogously, average pore diameter and related data dispersion were expressed in the range defined by the 1st and the 3rd quartile. Besides, a careful selection of outliers was carried out by using the Chauvenet's criterion: any values that fall

outside the probability band P=1-(1/2n) centered on the mean value of the n-size sample, was excluded.
Two reasons for data exclusion were supposed: i) unexpected damages or breakage of the pore walls due to the inherent brittleness of the glassy material and ii) possible misinterpretations of the μ-CT image processing.

Chapter 5

Analysis and discussion of results- Part 1

5.1 An introduction to 47.5 B bioactive system

One of the most interesting aspects related to the use of bioactive glasses in clinical practice certainly derives from the possibility to impart a specific therapeutic action upon dissolution by the sustained release in the physiological environment of active elements involved in osteogenetic and angiogenetic processes. Hence, the addition of specific elements within the glass composition, such as magnesium, copper, iron, silver, fluorine, boron and strontium could be a valuable strategy to modulate the chemical, biological and structural performances of bioactive glasses in contact with body fluids [238].

Magnesium (Mg^{2+}) is the fourth most abundant cation in the body: it takes part in a number of important metabolic reactions within cells, including the maintenance of cytoskeletal integrity, proteins and nucleic acids synthesis, as well as the cell cycle itself [239].

The involvement of Mg in bone tissue development was demonstrated by several authors in the field. Among the main functions, regulation of active calcium transport, bone remodeling and skeletal development deserve special attention [240]. In addition, Mg^{2+} is one of the most important divalent ions associated to biological apatite, the main component of the inorganic mineral phase of bone tissue [241].

Some studies reported the direct influence of Mg ions on bone calcification level, determining the mineral density and thus, the fragility of bones [242].

As a direct consequence, insufficient Mg levels have been often associated to hindered bone growth, poor osteoblastic-osteoclastic activity and osteoporotic disease [243].

Over time, all these findings led to an increasing scientific interest in Mg-based medical products (biomaterials) for clinical applications in contact with calcified tissues [244]. This is mainly due to the Mg capability of promoting the adhesion and proliferation of osteoblastic cells, whose interactions with a given substrate are primarily mediated by membrane-associated adhesion receptors belonging to the integrins superfamily [245].

The importance of Mg in the human body, as well as the capability of MgO to modify the chemical, physical and structural properties of BGs led several research groups to deepen the influence of Mg introduction within the silica-based network, paying particular attention to thermal properties, crystallization behavior, *in vitro* bioactivity and biological response in contact with bone cells both in vitro and in vivo [245].

The role of MgO within the glassy network is, most of the times, compared to that of CaO, which acts as a network modifier. However, considering some characteristic elemental parameters, as charge-to-size ratio and Pauling electronegativity, Mg^{2+} is at the borderline between modifiers and intermediates. For example, in highly disrupted silica networks, MgO may also act as an intermediate oxide within a specific area of the ternary diagrams, identified between the extension of the glass forming region and lower SiO_2 mole fractions, as described by McMillan in [246].

On this matter, one of the most relevant studies was carried out by Watts and coworkers [247], who investigated the effect of magnesia on the structural and thermal behavior of bioactive glasses belonging to the system $49.5SiO_2–1.1P_2O_5–(23.0(1-x))CaO–xMgO–26.4Na_2O$ mol.%, where CaO was progressively replaced by MgO.
Results revealed that just a portion of MgO (up to 14%) acted as an intermediate oxide, forming MgO_4 tetrahedral structures within the silica network. This led to a decrease both in the glass transition temperature and the dilatometric softening point value, while the thermal expansion coefficient was found to increase together with the MgO content. All these aspects can be likely attributed to the strength of Mg-O bonds, remarkably lower compared to Si-O bonds and responsible for an overall weakening of the glass network.

Magnesium oxide has been incorporated in BGs by numerous research groups all over the world. **Figure 5.1** shows the increase in literature publications regarding the synthesis and characterization of Mg-containing bioactive glasses from the early 90's to the present day.

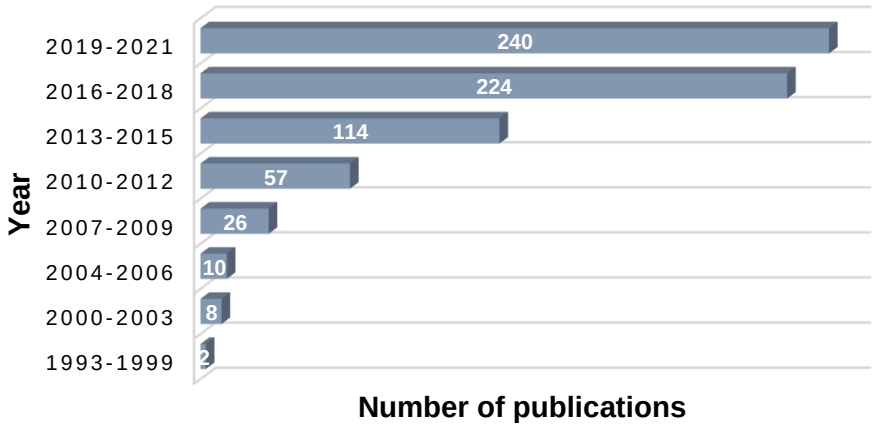

Figure 5. 1. Number of publications regarding the synthesis and characterization of Mg-containing bioactive glasses from 1993 to the present day. Data collected on Scopus® database inserting *"bioactive glasses" + "magnesium" + "magnesium release"* within article title, abstract and keywords.

This is the scientific background which has given rise to the experimental study carried out by Verné and coworkers [191] at Politecnico di Torino in 2009, leading to the design, production and preliminary characterization of 47.5B bioactive glass, selected as basic material for all the manufacturing processes here described.

The original aim of the study was to investigate the surface reactivity of six different bioactive glasses belonging to the compositional system SiO_2-P_2O_5-CaO-MgO-Na_2O-K_2O, paying particular attention to the role of CaO for MgO substitution in defining the physical, chemical and biological properties of the material.
The study demonstrated the effective capability of MgO to deeply influence glass properties in terms of both chemical stability in aqueous environment and characteristic temperatures upon heating, thus allowing to tune the behavior of the system by simply adjusting the composition [191].

The starting point for materials design was the original 45S5 Bioglass® composition, properly adjusted in order to introduce MgO and K_2O at the expense of CaO and Na_2O, respectively.

Among the various compositions analyzed, 47.5B stands out due to its exceptional behavior when subjected to high temperatures thermal treatments, as well as enhanced bioactive potential even upon partial crystallization, which makes it a promising candidate as basic material for scaffolds manufacturing intended for clinical use in BTE applications.
Most of manufacturing strategies currently available for the production of glass and glass ceramic porous struts are indeed based on high-temperature sintering processes, which allow to achieve the thermal consolidation of adjacent glass particles by viscous flow thanks to the progressive formation of sintering necks [121], [122].

Introducing MgO within a silica network could be highly beneficial to favorably tune the thermal behavior of glasses upon heating, thus optimizing all the sintering-related parameters to obtain mechanically performant 3D foams.

From a thermo-chemical point of view, the most relevant effects resulting from the addition of increasing MgO content are the decrease in the glass transition and the increase in the crystallization temperature, respectively T_g and T_x, resulting in a final broadening of the glass sintering window, i.e. the temperature range defined between the T_g and the T_x [245].
On the decrease of the T_g, sufficient explanations have been already provided above. Concerning the increase observed in the T_x, instead, this has to be attributed to a sort of crystallization inhibitory effect of MgO [245].

Other compositional peculiarities playing a pivotal role in affecting crystallization tendency of bioactive glasses are the high CaO-to-Na_2O (which, however, is not the case of 47.5B composition), as well as the addition of specific oxides. In this regard, Sola et al. [248] demonstrated that replacing sodium oxide with specific amounts of potassium oxide is an effective strategy to improve the sinterability of glasses while preserving their amorphous nature.

Part of the experimental results reported in the present chapter have been already published in:

- *Baino, F.; Fiume, E. Materials Letters 2018, 224, 54-58.*
- *Fiume, E.; Verné, E.; Baino, F. Biomedical Glasses 2019, 5, 46-52.*
- *Fiume, E.; Migneco, C.; Verné, E.; Baino, F. Materials 2020, 13, 540.*
- *Fiume, E.; Serino, G.; Bignardi, C.; Verné, E.; Baino, F. Applied Sciences 2020, 10, 8279.*

5.2 Early results on melt-derived 47.5B

The DTA curve and the XRD pattern related to the as-quenched 47.5B bioactive glass ($d_g \leq 32$ μm) are depicted in Figure 5.2 a and Figure 5.2 b, respectively.

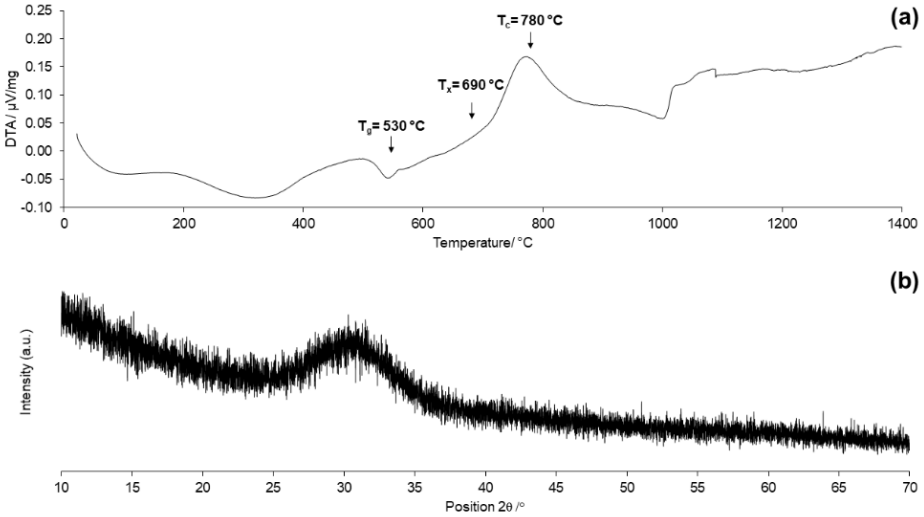

Figure 5. 2. DTA termograph (a) and XRD pattern related to as-quenched 47.5B-32 glass powder.

As can be seen from the DTA thermograph, 47.5B compositional system is characterized by a wide workability window of about 200 °C, showing an enormous potential for future use in the production of highly densified structures maintaining the amorphous nature of the original material. The XRD pattern, indeed, does not reveal the presence of diffraction peaks associated to the presence of crystalline phases, showing the typical appearance of a glassy silicate system, with an amorphous halo between 25° and 35°.

SEM analysis performed on 47.5B-32 particles revealed a quite uniform distribution of particles' size, morphologically characterized by the presence of sharp edges, (Figure 5.3 a-b) resulting from the mechanical grinding. The size distribution, assessed by granulometric measure, was between ~ 0.2 and ~30 μm, consistently with the mesh used for material sieving (Figure 5.3 c).

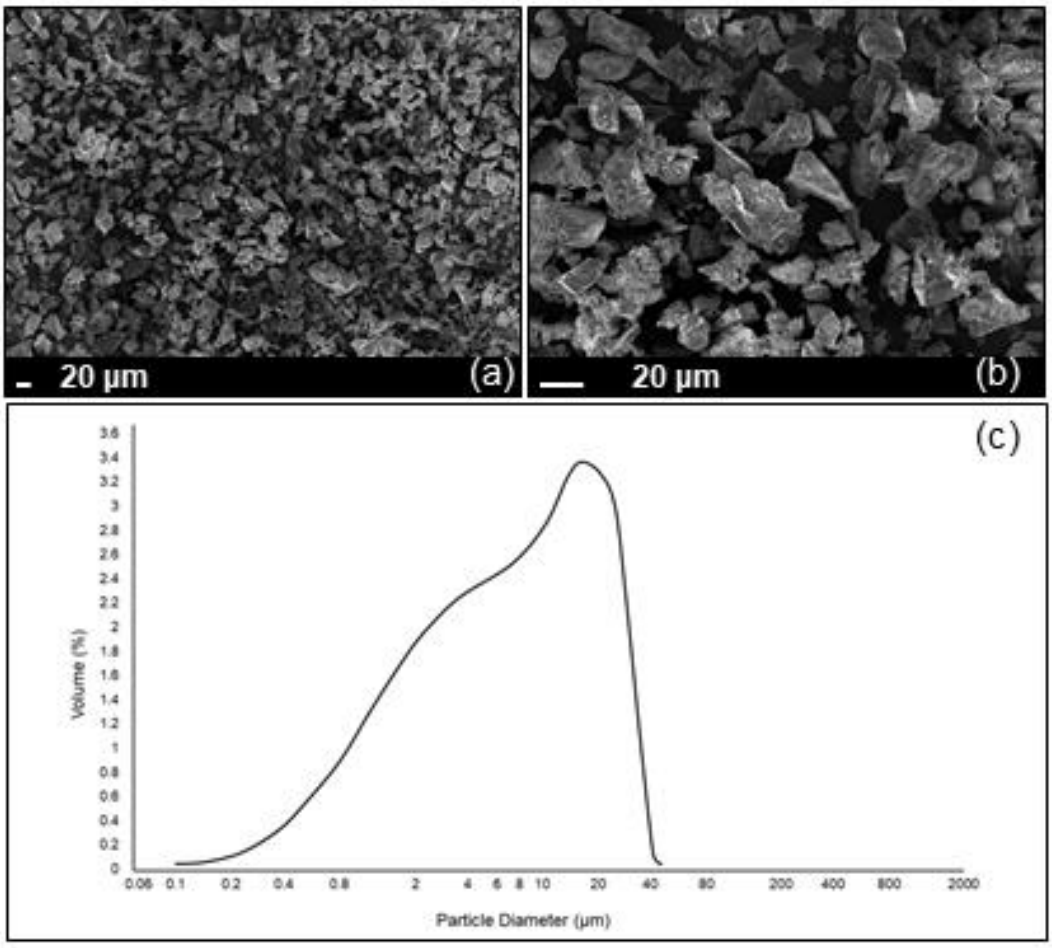

Figure 5. 3. Morphological SEM images and particles size distribution of 47.5B-32 glass powder used for scaffold manufacturing.

Starting from the bioactive glass originally designed by Verné et al in 2009 [191], the present research work focused on the development and characterization of new biomaterials based on the original 47.5B compositional system, as well as the optimization of 47.5B-based scaffolds to be used as bone substitutes in tissue engineering.

5.3 47.5B melt-derived glass: a promising material for scaffold manufacturing

Sintering of bioactive glass particles is maybe the most crucial step required for the fabrication of complex 3D porous structures to be used in load-bearing bone tissue engineering applications.
However, glass densification upon sintering has a number of secondary effects on the final product, not always desirable, which can potentially jeopardize the good performances of the scaffold both *in vitro* and *in vivo*. Among these, the nucleation and growth of crystalline phase deserve special attention.
Over the years, several bioactive glasses have been designed to exhibit proper sinterability levels as well as fast apatite deposition kinetics also in in the form of glass-ceramics.

47.5B melt derived glass, designed at Politecnico di Torino in 2009, is definitely a good representative of both categories and thus, its potential as basic material for the production of sintered products has been already recognized to be enormous.

Here, the mechanisms of densification and crystallization of 47.5B bioactive glass upon heating treatment will be analyzed in detail, with an emphasis on devitrification process, analyzed by mean of proper physical models. The results will be critically discussed referring to the golden standard of bioactive systems, the original 45S5 Hench's composition (Bioglass®).

5.3.1 Sintering behavior and crystallization mechanism of 47.5B bioactive glass

Among the reasons which still limit the widespread use of 3D porous BG-based bone grafts in clinical practice, the intrinsic brittleness of glass materials has to be mentioned.
Dealing with 3D porous scaffolds, this peculiar aspect can be directly related to the unexpected failure of the device after implantation and thus, it has to be carefully considered and hopefully predicted to guarantee a successful and safe treatment.
Over time, several strategies have been proposed and optimized in order to improve the mechanical response of BG-based scaffolds.
Drawing inspiration from the natural toughening mechanism of bone, the creation of composite substitutes obtained by coating or infiltrating the scaffold with a degradable polymer is one of the most implemented strategies. However, mismatching in mechanical properties as well as different dissolution rates and thermal behavior of the polymeric organic part compared to the inorganic glass represent very critical aspects potentially able to dramatically affect interfacial bone/scaffold interaction [182], [249].
Another very common strategy relies on material's densification phenomena upon sintering processes. This approach, based on a basic physical process, is relatively easy to be implemented, but could led to undesired and poorly predictable secondary effects, including decrease in porosity, poor mass transport properties, as well as the occurrence of devitrification phenomena affecting the chemical reactivity of the material in contact with body fluids [144], [250].

Most BGs, indeed, exhibit the tendency to partially crystallize during sintering, thus transforming into glass-ceramic materials exhibiting lower reaction kinetics and HA deposition rates [251].
Anyway, the nucleation of crystalline phases could be sometimes a favorable event. As a representative example, in the treatment of dentinal hypersensitivity (DH) disorder, the use of glass-ceramic particles is advisable as the presence of crystalline phases results in the absence of sharp cutting surfaces typical of mechanically grinded glassy materials, which can lead to gum irritation, bleeding and enamel damage during the daily brushing routine [252].

When a glass devitrifies, the formation of crystalline phases within the amorphous matrix plays a dual role: on one side it remarkably improves the mechanical strength of the material, and, on the other, the crystallization of the system increases the chemical stability [129], [142]. Most of the ion release phenomena involved in the deposition process of HA, in fact, are mainly related to the residual amorphous phase and thus, the higher the content of the crystalline phase, the lower the interaction of the material with the body.
Hence, improving the chemical stability of bioactive materials could be intrinsically conflictual: most of them, in fact, are properly designed to rapidly react in contact with the biological environment to boost the osteintegrative process of the material, thus guaranteeing what is commonly called primary stability.

All these aspects automatically help in identifying what is known as *sintering window*, previously mentioned, i.e. a temperature range defined between the temperature of glass transition T_g and the temperature of crystallization onset T_x of the material in which it is possible to sinter the material while avoiding the nucleation of crystals.
Within this range, in fact, the thermal energy provided to the system is not high enough to trigger atoms reorganization into crystalline structures, but sufficient to allow the formation of sintering necks between adjacent glass particles through viscous flow and diffusive mechanisms, thus ideally preserving the maximum bioactive potential of the material.

Apart from the sintering temperature, identified on the basis of the characteristic temperatures of the system, the nucleation and growth of crystalline phases within the amorphous matrix is notoriously a time-dependent process. Thus, at the same sintering temperature, the relative proportion between crystalline and amorphous phase can sensitively vary according to the duration of the treatment.

45S5 Bioglass® is the most striking example of bioactive glass which cannot be sintered without undergoing crystallization [253]. The Q^n (Si) distribution (n= number of bridging oxygens) of the original Hench's composition results in a structure dominated by chains of Q^2 metasilicates, occasionally cross-linked through Q^3 units, whereas the Q^1 species terminate the chains distribution.
The final outcome is a highly disrupted silicate network, highly reactive in physiological environment, as well as low glass transition temperature and

enhanced devitrification tendency upon heating (i.e. the material evolve toward a more stable system) [254].
It has been demonstrated that the onset time of HA formation on the surface the 45S5 material increases from 8 to 25 h when the crystalline fraction increases from 0 to 60% [129]; despite that, devitrification phenomena in Bioglass® do not completely suppress the bioactive potential of the material in physiological environment [142], [255], [256].

However, Bioglass® does not represent an isolated case and similar results have been also reported for other silicate and phosphate bioactive compositions (e.g. S53P4, $53SiO_2$-$20CaO$-$23Na_2O$-$4P_2O_5$ wt.% [257] and $50P_2O_5$-(40 – x) CaO_xSrO-$10Na_2O$ with x = 0, 20, and 40 mol.%) [258], respectively).

In order to overcome this issue, several bioactive glasses have been designed to exhibit a wide workability window (e.g. 13-93, $53SiO_2$-$6Na_2O$-$12K_2O$-$5MgO$-$20CaO$-$4P_2O_5$ wt.%) [179] and/or fast reaction kinetics, also in the form of glass-ceramics (e.g. CEL2, $43.8SiO_2$-$15.0Na_2O$- $6.1K_2O$-$4.6MgO$-$23.6CaO$-$6.9P_2O_5$ wt.%) [163], exhibiting suitable features for the production of mechanically resistant 3D scaffolds.

In this regard, 13-93-based amorphous scaffolds with increased mechanical properties have been successfully obtained by Fu and coworkers, but their apatite foaming ability was remarkably lower compared to glass-ceramic 45S5 structures [259].
Another study comparing CEL2 and 45S5 glass-ceramic foams, instead, revealed faster reaction kinetics in the former system, supported by the thicker reaction layer formed on the surface of the samples, compared to the control [260].

Thus, it can be stated that the nucleation of crystalline phases is not the only factor affecting the reactivity of BGs and an optimal design of glass composition could be effective in conferring high bioactive potential to the material despite devitrification phenomena.

This aspect will be later discussed in the dissertation, with a focus on the 47.5B composition, here analyzed.

Analysis of the sintering behaviour

The sinter-crystallization of 47.5B-32 glass was critically analyzed referring to its suitability for the fabrication of mechanically competent bone like foams for tissue repair.
In order to do this, combined Differential Thermal Analysis (DTA) and Hot Stage Microscopy (HSM) measurements were carried out under isothermal condition to simulate the dwelling stage of a plausible sintering thermal treatment for scaffold manufacturing. Six different programs have been implemented, corresponding respectively to six different sintering treatments defined in the range 600-850 °C, were the boundaries were selected so as to coincide approximately to the beginning

of viscous phenomena and the end of the crystallization process (referring to DTA thermogram reported in Figure 5.2 a).
Then, XRD measurements were performed to identify the crystalline phases nucleated upon heating.

These measurements, preparatory to scaffold manufacturing (see results reported in **Chapter 6**), aimed at assessing a consistent relationship between sintering/thermal behavior of the glass and mechanical/mass-transport properties, e.g. between processing parameters and scaffold performances.

This actually represents a key step towards the rationale design of optimized scaffolds for tissue repair, in order to achieve the right balance between all the aspect mentioned above.

The characteristic temperatures identified for each sintering group are summarized in **Table 5.1**.

Table 5. 1. Characteristic temperatures of 47.5B bioactive glass sintered at different temperatures assessed by DTA measurements under isothermal conditions.

Sintering temperature T/ *°C*	*Glass transition* T_g/ *°C*	*Crystallization onset* T_x/ *°C*	*Crystallization* T_p/ *°C*
600	527	-	-
650	528	-	-
700	528	-	-
750	527	690	750
800	530	707	750, 783
850	531	697	772

For each isothermal DTA curve reported in **Figure 5.4**, the T_g was identified in correspondence of the inflection point and varied in the range 527-531°C, while the T_x was identified at the onset point of the exothermic peak (Figure 5.4 d-e-f), between 690 and 707 °C.
These results are in good agreement with the temperature ranges previously identified under non-isothermal testing conditions.

Figure 5.4 a-b show the DTA isothermal curves related to 47.5B-32 glass powder sintered below the crystallization onset, respectively at T_{s1}= 600 °C and T_{s2}= 650 °C. As expected, both the curves are characterized by no exothermic peaks.
The only signal observed was a step-like increase corresponding to the beginning of the dwell stage, most likely attributed to the shift to isothermal conditions in the program settings.
A similar signal, although very weak, can be observed up to a sintering temperature of 750 °C (Figure 5.4 c-d), but is completely hidden for the glasses heated at higher temperatures (Figure 5.4 e-f), due to the overlap of the exothermic crystallization peaks, producing more pronounced signals.

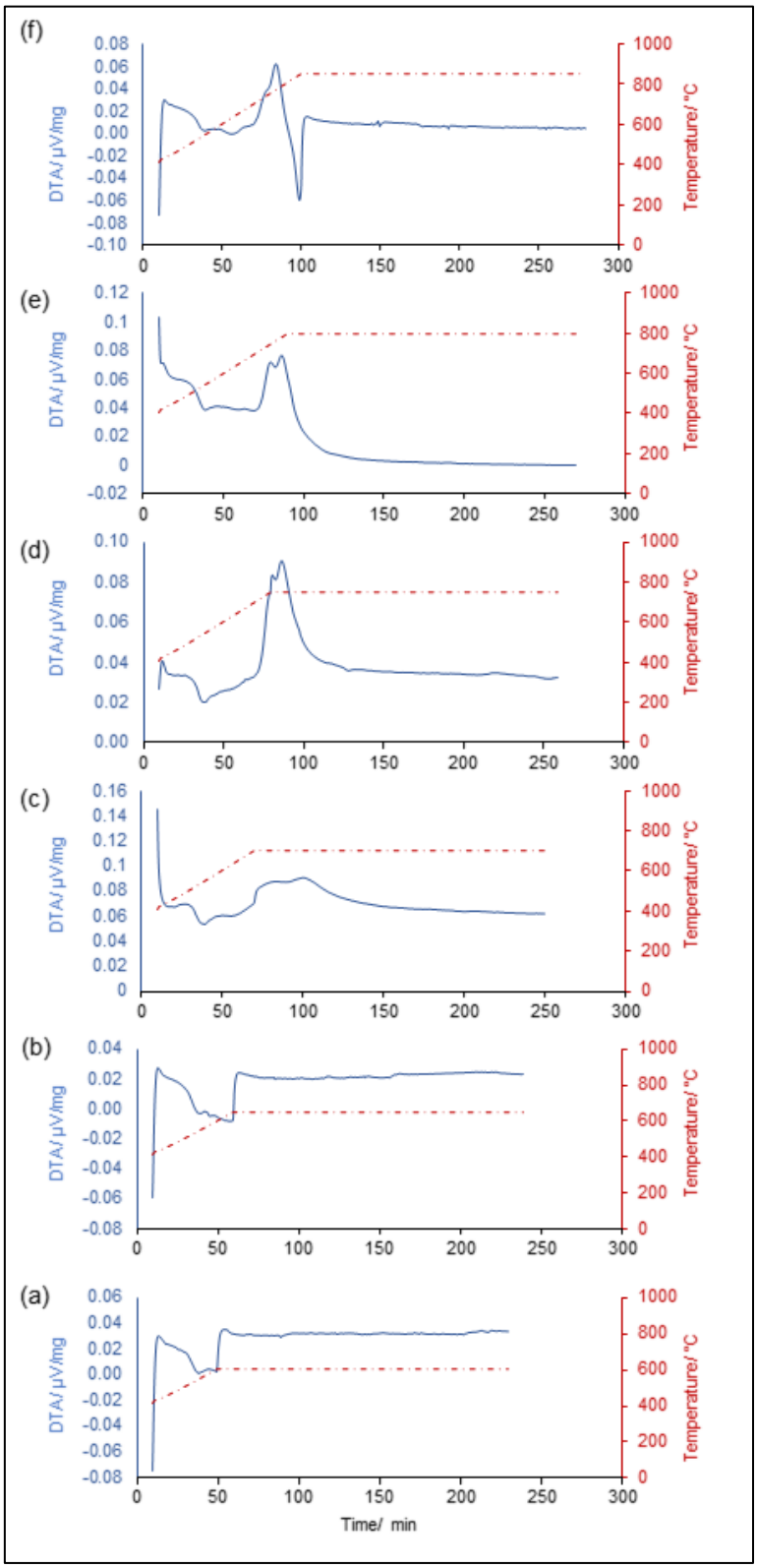

Figure 5. 4. Isothermal DTA thermographs acquired at different temperatures: a) 600 °C, b) 650 °C, c) 700 °C, d) 750 °C, e) 800 °, f) 850 °C.

A mild crystallization was observed for a sintering temperature of 700 °C, after about 30 minutes from the beginning of the dwelling stage, as depicted in Figure 5.4 c; differently from the DTA thermographs acquired at 600 °C and 650 °C,

presenting a flat trend in stasis, this curve evolved in a broad hump, indicating the beginning of devitrification phenomena, consistently with the range of crystallization onset previously identified.

Approaching higher sintering temperatures, the "hump" observed for T_{s3}= 700°C evolved into sharp exothermic peaks, corresponding to the maximum rate of crystallization of the system (Figure 5.4 d-e-f).

On first approximation it would seem that the exothermic signals observed at 750 and 800 °C present analogous features.
Both of them, in fact, consist of two different peaks, closely located. Nevertheless, some additional considerations could be made considering the position of these signals with respect to the temperature-time dashed curve.

In the system treated at T_{s4}= 750 °C, the two exothermic peaks were both registered at a constant temperature of about 750°C, immediately after the beginning of the stasis (Figure 5.4 d).
On the contrary, the peaks observed in Figure 5.4 e were registered upon heating and overlap the ramp at 750 and 783 °C, respectively, spaced of about 6 minutes.

The curve related to the glass sintered at 850°C, instead, exhibited a single exothermic peak at 772 °C, ending in correspondence of the beginning of the dwell at 850 °C, thus indicating that glass devitrification phenomena are already completed before the beginning of the stasis (Figure 5.4 f).

In order to explain this, two different hypotheses have been proposed:

i) the nucleation of a metastable crystalline phase at 750 °C, gradually evolving to a second more stable crystalline system, resulting in a second exothermic signal at temperatures T ≥ 800 °C;
ii) the nucleation of two different metastable phases at 750 °C and 780 °C, which evolve to a third crystalline system stable at temperatures ≥ 850 °C.

XRD analyses performed on 47.5B tablets sintered at different temperatures confirmed the nucleation and progressive growth of crystalline species with the temperature increase.

XRD patterns related to the samples sintered at different temperature are depicted in **Figure 5.5**.

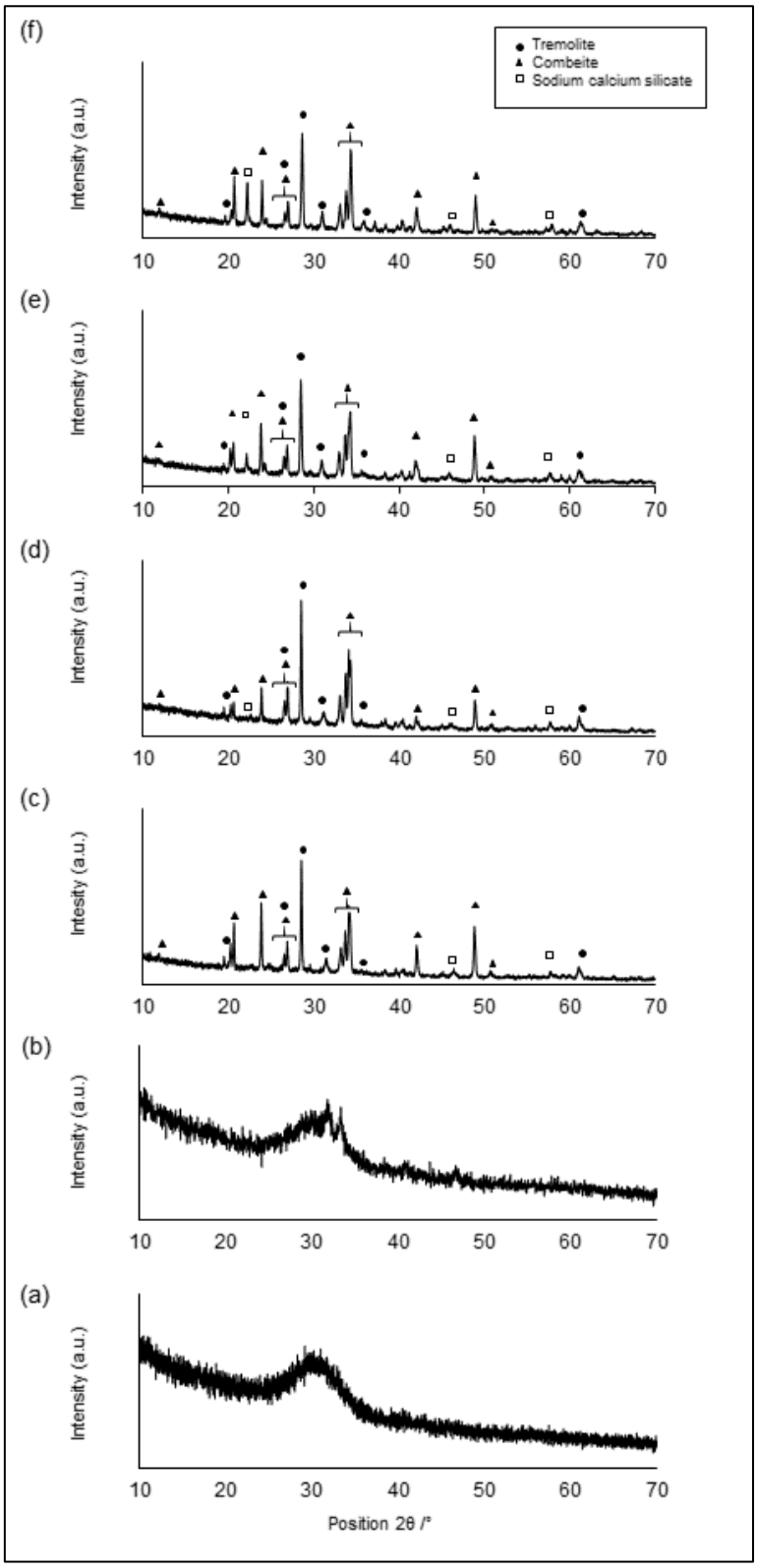

Figure 5. 5. XRD patterns of 47.5B tablets sintered at different temperatures: 600 °C (a), 650 °C (b), 700 °C (c), 750 °C (d), 800 °C (e) and 850 °C (f)

As expected, specimens sintered below the crystallization onset, at 600 and 650 °C (Figure 5.5 a-b), revealed no diffraction peaks and were predominantly amorphous. An amorphous halo for 2θ values ranging between 25° and 35° was observed, thus

indicating that almost no microstructural changes occurred within the material as a result of these sintering treatments.

On the contrary, the patterns of samples treated at 700, 750, 800 and 850 °C were characterized by the presence of multiple diffraction peaks, typical of glass-ceramic materials, as might be predicted from DTA thermograms.

All the crystalline phases detected above the crystallization onset are collected in **Table 5.2**.

Table 5. 2. Crystalline phases detected in 47.5B samples sintered at 700, 750, 800 and 850 °C.

Ref. code	Compound name	Chemical formula	Crystal system
01-075-1686	Combeite	$Na_2Ca_2(Si_3O_9)$	Rombohedral
00-002-0455	Tremolite	$CaMg_3(SiO_4)_3$	Monoclinic
01-075-1332	Sodium-calcium silicate	$Na_{15.6}Ca_{3.84}(Si_{12}O_{36})$	Cubic

The analysis carried out on all the samples sintered at temperatures ≥ 700 °C revealed the presence of two main crystalline species, i.e. combeite ($Na_2Ca_2(Si_3O_9)$) and tremolite ($CaMg_3(SiO_4)_3$), together with other sodium-calcium silicates with different stoichiometry, to a lesser extent.

The formation of combeite ($Na_4Ca_4(Si_6O_{18})$) and akemanite ($Ca_2Mg(Si_2O_7)$), a calcium-magnesium silicate similar to tremolite, was already observed upon sintering treatment at high temperature (≥ 950 °C) in a silica-based experimental composition above, named CEL2, exhibiting the same oxides system of 47.5B [261].
Moreover, sodium-calcium silicate (combeite-type) phases were also reported to be the main crystalline species nucleating above 550 °C in 45S5 Bioglass®, commonly adopted as the positive control material among BGs in terms of bioactivity and cytocompatibility standards [129], [262].

DTA results were integrated with hot-stage microscopy (HSM) analysis (**Figure 5.6**) to quantify the volumetric shrinkage of glass samples upon sintering.
The sample shrinkage was quantified in terms of height percentage (h%), in relation to the original height of the sample (3 mm), as a function of both time and temperature; the shrinkage values related to each sintering group are summarized in **Table 5.3**.

Table 5. 3. Maximum 47.5B-32 samples shrinkage upon 3h-sintering at different temperatures

T_s/ °C	h%
600	0.24
650	0.28
700	0.27
750	0.18
800	0.21
850	0.29

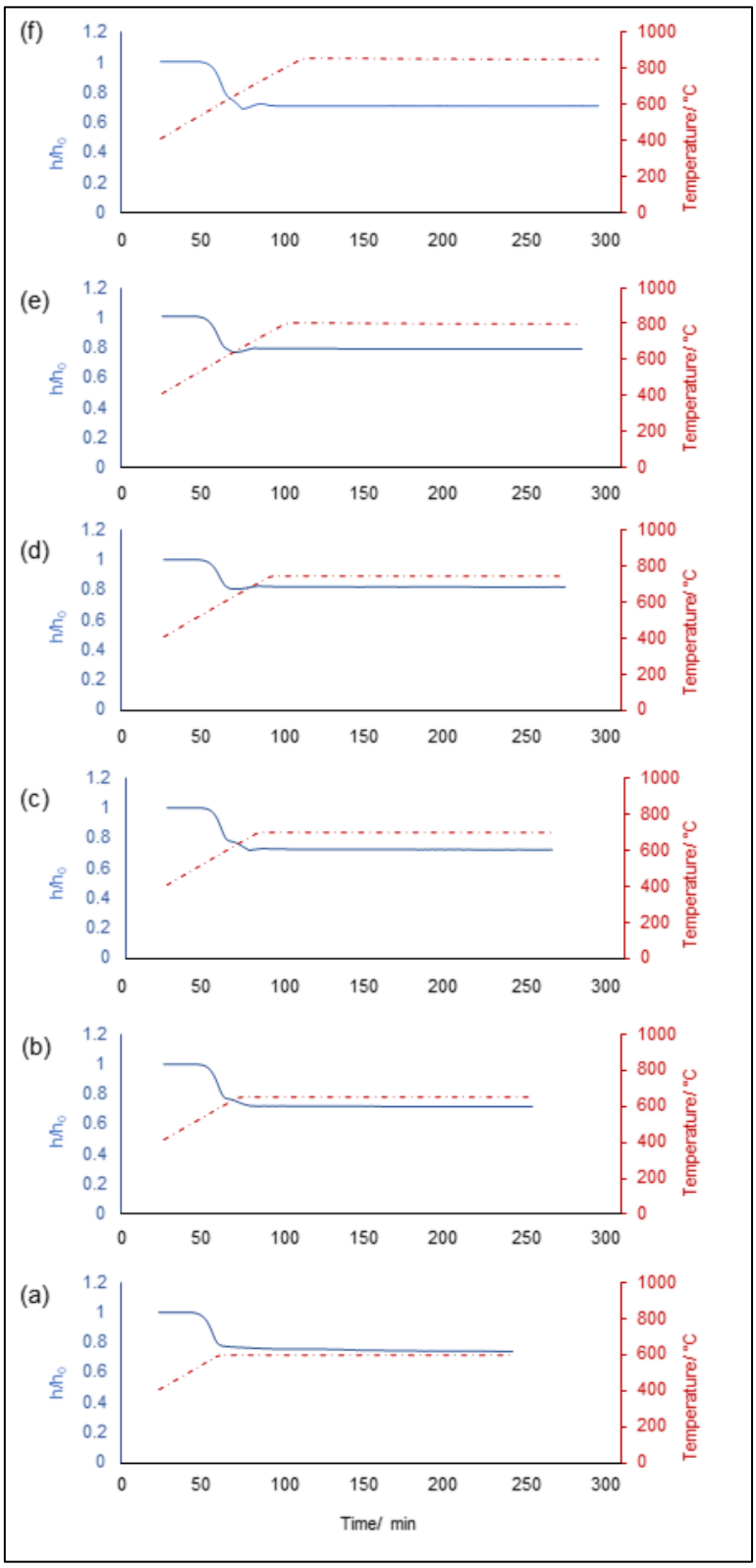

Figure 5. 6. HSM analyses simulating the sintering treatment at different temperatures: 600 °C (a), 650 °C (b), 700 °C (c), 750 °C (d), 800 °C (e) and 850 °C (f)

Regardless of the sintering conditions, comparable values were registered for all the samples and no clear trends were identified as function of the sintering temperature. Interestingly, the specimens sintered at 750 and 800 °C seemed to

densify less than all the others, with a height reduction of 0.18% and 0.21%, respectively. This could be likely attributed to microstructural adjustments resulting from the progressive devitrification of the amorphous matrix, which becomes progressively stiffer due to the development of crystalline species, which might inhibit densification phenomena. This is consistent with previous results reported by Huang et al. about the sinter-crystallization of 45S5-derived glass-ceramic scaffolds [263].

A similar trend was also observed by Erasmus and coworkers [264] in borosilicate, boro-phosphate and phosphate glasses for bone regeneration. The study, indeed, reported that the density of the samples decreased as the sintering temperature increased due to the inhibition of viscous flow between adjacent particles caused by crystallization phenomena at the material surface, thus reducing the densification ability of the material.

This was thought to have a clear effect on the mechanical performance of foam-replicated 47.5B-based scaffolds sintered at the same temperatures, as will be discussed in **Chapter 6**.

Analysis of the crystallization process

Over time, different models based on mathematical equations have been proposed to investigate the crystallization mechanism of glass materials. However, in biomedical field, most of these studies were addressed to the 45S5 Hench's composition, with a paucity of interest for other bioactive systems [265]–[267].

In the present section, the activation energy for crystallization and viscous flow for 47.5B-32 glass powder have been assessed.

DTA analyses were performed under non-isothermal conditions at different heating rates (β_1= 10; β_2=20; β_3=30; β_4=40 °C/min).
All the DTA plots depicted in **Figure 5.7** revealed the presence of a single crystallization peak, consistently with previous investigations.
A shift toward higher temperatures of both glass transition and crystallization exothermic peak was observed with increasing heating rate. Specifically, glass transition temperature T_g and crystallization temperature T_p varied within 527-567 °C and 765-848 °C, respectively.

Characteristic temperatures registered at each heating rate are summarized in **Table 5.4.**

Table 5. 4. Characteristic temperatures of 47.5B glass at different heating rates.

β/ °C/min	**T_g/ °C**	**T_x/ °C**	**T_p/ °C**
10	527.3	727.8	765.4
20	541.8	760.0	808.9
30	550.7	786.5	841.7
40	567.4	794.7	848.8

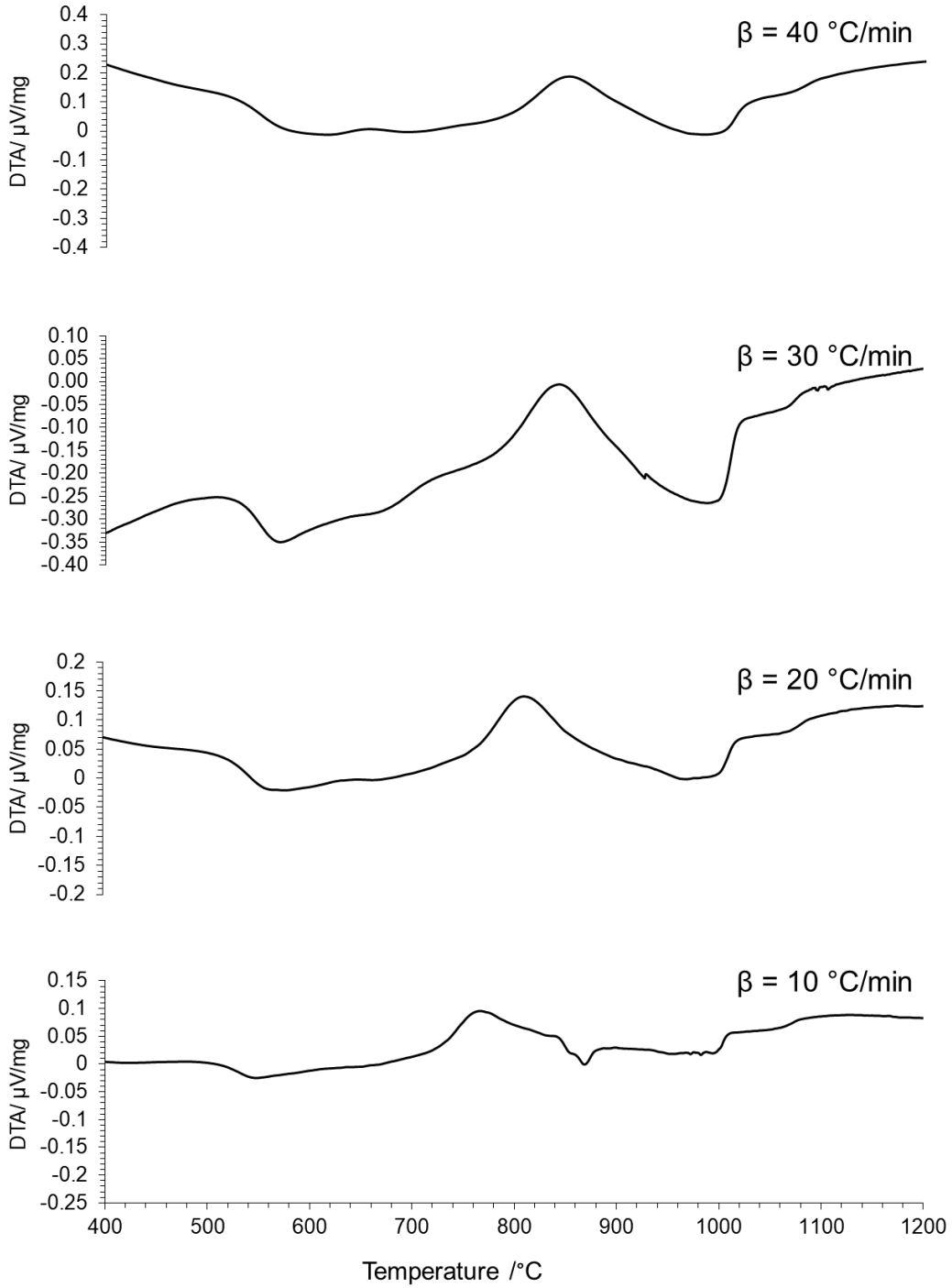

Figure 5. 7. DTA curves of 47.5B-32 glass acquired at different heating rates.

First, the JMA coefficient n was estimated from the Ozawa plots considering five different temperatures within the range 770-810 °C, 10 °C-spaced, selected on the basis of DTA thermograms by considering the overlapping area of the crystallization peaks.

The value assessed for the n coefficient was 1.4 ± 0.03, comparable to that obtained by implementing the Augis-Bennet method, equal to 1.8 ± 0.2.

The Ozawa plots for the determination of the JMA coefficient, as well as the fitting equations used, with the relevant R^2 goodness of fit coefficients are depicted in **Figure 5.8**.

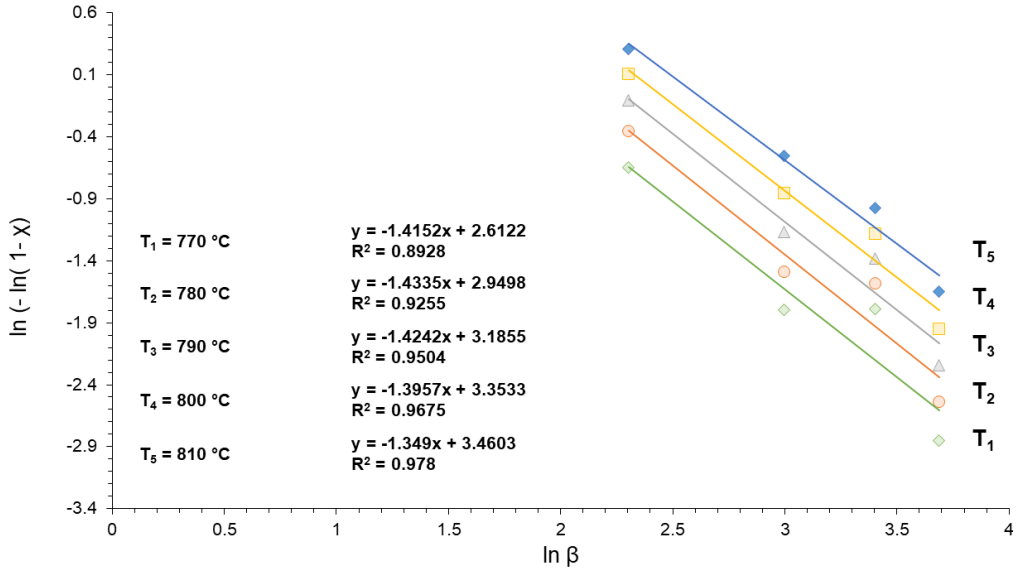

Figure 5. 8. Ozawa plots for the determination of the JMA parameter (n).

The Kissinger plot for determining the activation energy for crystallization $E_{c,K}$ is depicted in **Figure 5.9**.

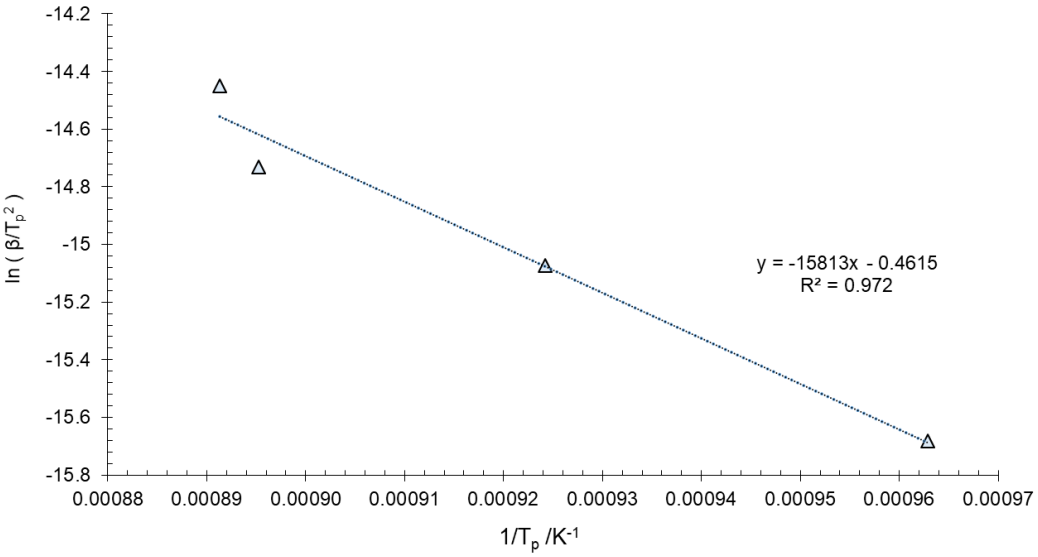

Figure 5. 9. Kissinger plot to determine the apparent activation energy for crystallization E_{ck}.

The $E_{c,K}$ value, assessed by least squares fitting, was equal to 131 kJ/mol.

However, according to what previously said in **Chapter 3**, as the JMA coefficient assessed both by the Ozawa model and the Augis-Bennet method was greater than 1, the use of the Kissinger model could lead to an underestimation of the activation energy for crystallization of the analyzed system.

For this reason, the Matusita and Sakka model [203] was implemented, in order to obtain a more realistic estimate of this value.
In order to do this, first of all it was necessary to calculate the crystal growth dimensionality m. Considering the nucleation of a non-constant number of nuclei, as it occurs during a DTA measurement, m was calculated as n-1 and it was assumed to be approximately equal to 1 [268], [269].
If m=1, it is possible to state that surface crystallization phenomena are preponderant in 47.5B glass particles, assuming a one-dimensional rod-like crystallization.

The plot used for the calculation of the correct activation energy for crystallization E_C, according to the mathematical model proposed by Matusita and Sakka is represented in **Figure 5.10**.

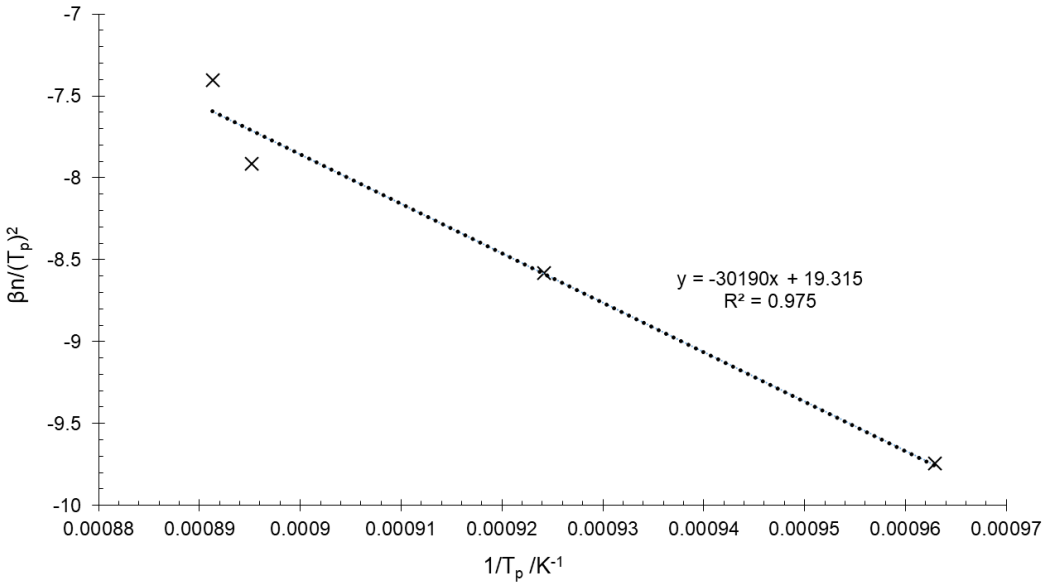

Figure 5. 10. Plot in accordance with the Matusita and Sakka equation to determine the correct activation energy for crystallization (Ec).

By implementing the model proposed by Matusita and Sakka, E_C value was found to 251 kJ/mol, almost twice greater than that obtained by solving the Kissinger's equation.

According to Erol and coworkers [270], it is possible to calculate the real activation energy for crystallization E_C starting from the $E_{c,K}$ assessed by the Kissinger's model. In particular, if m≠n≠1, such as in the case of 47.5B-32 glass, **Equations 3.4** and **3.5**, reported in **Chapter 3**, can be combined to obtain **Equation 5.1**:

$$E_C = \frac{n}{m} E_{c,K} - 2\frac{n-1}{m} RT_p \qquad \textbf{5.1}$$

In most oxide glass system, it is verified that Ec >> 20RTp [36], thus the term $2\frac{n-1}{m}RT_p$ can be considered negligible, introducing a small error (e< 10%) in the *Ec* value estimation.

Hence, E_c can be simply obtained using **Equation 5.2**:

$$E_C \approx \frac{n}{m} E_{c,K} \qquad \textbf{5.2}$$

where all the parameters are defined as reported above in the dissertation.

In this way, the activation energy for crystallization E_C is equal to 236 kJ/mol, differing by only 6.4% from the value assessed by Matusita-Sakka interpolation (251 kJ/mol).

For comparison, let consider 45S5 glass powder having same grain size. Non-isothermal DTA thermographs acquired at different temperatures are reported in **Figure 5.11**.

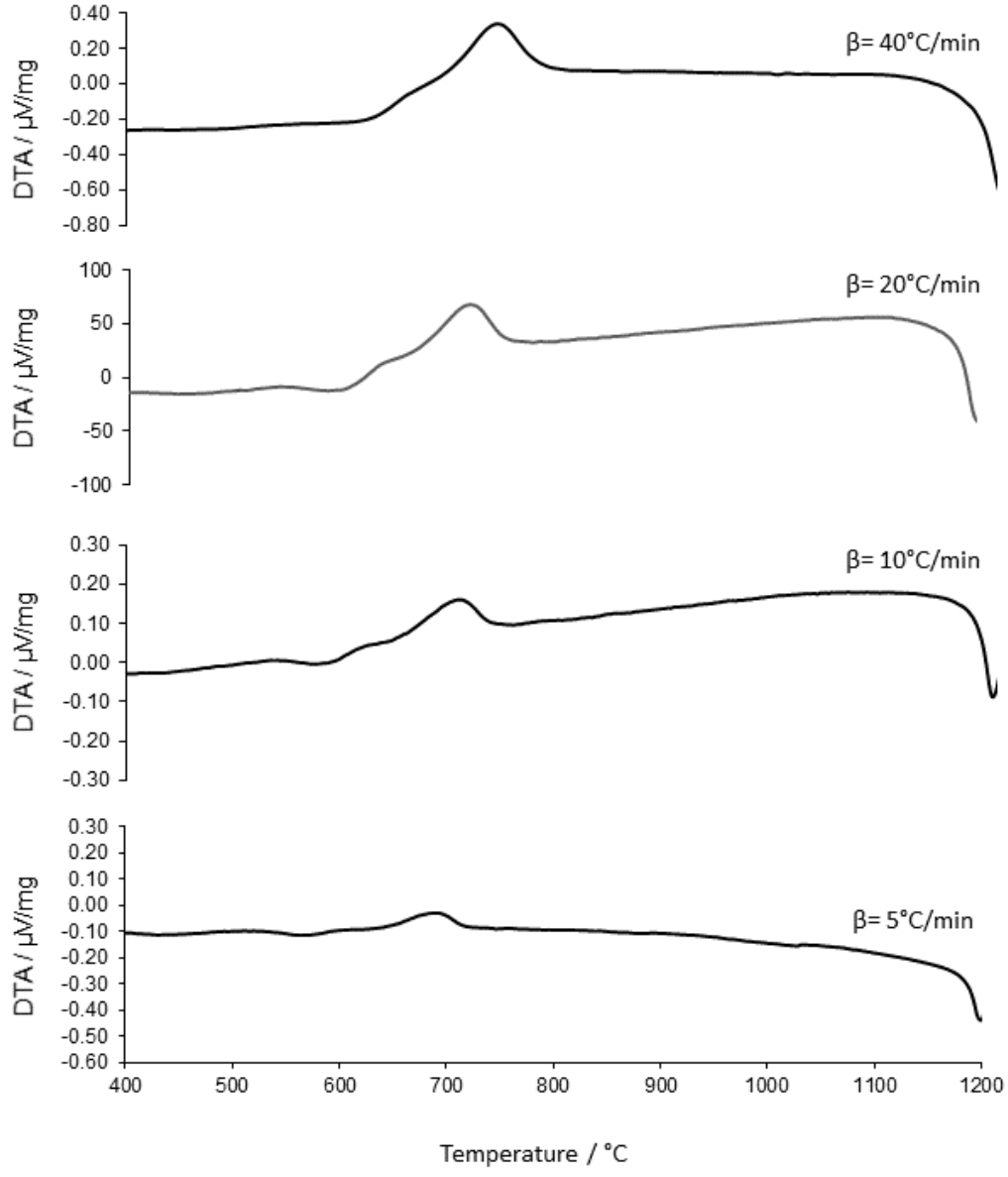

Figure 5. 11. DTA thermographs of 45S5 powder collected at different heating rates under non-isothermal conditions.

T_g and T_p were defined within 542–574 °C and 690–742 °C, respectively, and increased with increasing heating rate, analogously to what previously observed for 47.5B composition.

The JMA coefficient was calculated from the Ozawa plots (**Figure 5.12**) at different temperatures (660, 670, 680, 690 °C), identified from DTA data analysis, as specified above.

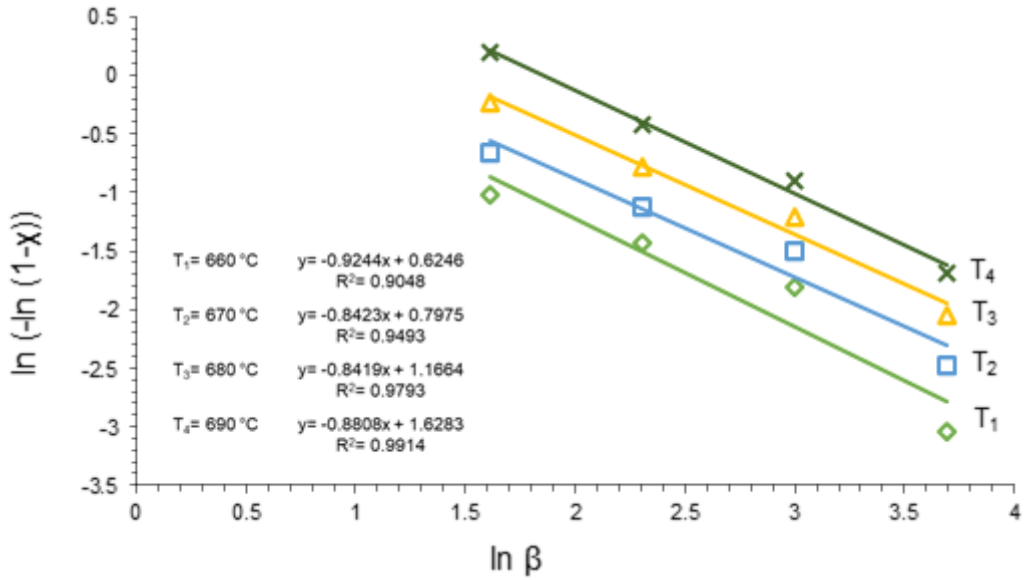

Figure 5. 12. Ozawa plots for the determination of JMA coefficient n related to 45S5 glass powder below 32 µm.

Differently from 47.5B composition, in this case the Kissinger model was found to be suitable for determining the apparent activation energy for crystallization (**Figure 5.13**), assuming both JMA value and m coefficient equal to 1.

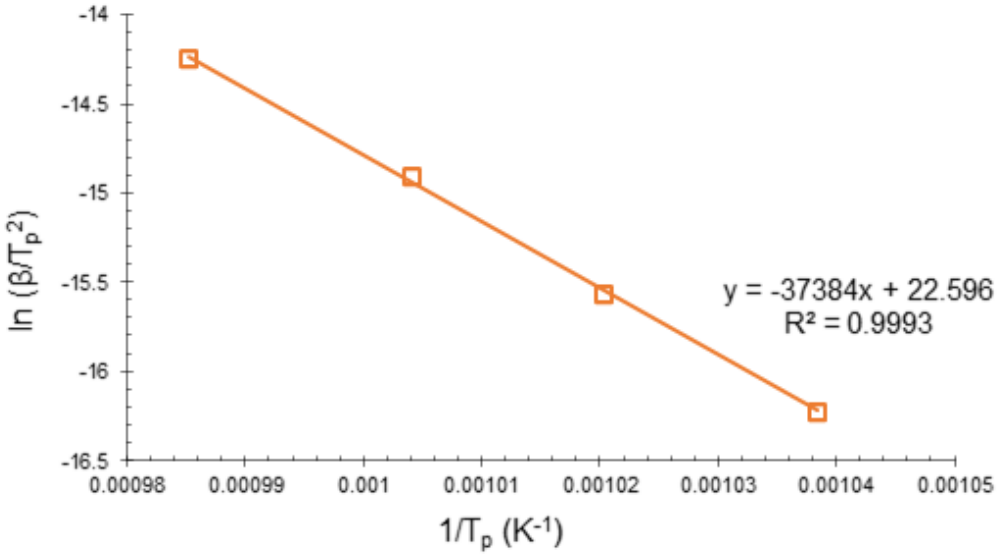

Figure 5. 13. Kissinger plot for the determination of the activation energy for crystallization of 45S5 glass powder below 32 µm.

The E_c for 45S5 glass powder below 32 μm (311 kJ/mol) was comparable to that reported by Massera et al. [271] for 45S5 glass powder below 45 mm (338 kJ/mol); Moreover, a similar result was also achieved by Xu and coworkers [272], who studied the devitrification of a ternary silicate glass in the system SiO2-Na2O-CaO having particle size below 50 μm, associated to the nucleation and growth of $Na_2Ca_2Si_3O_9$, the same crystalline phase developing upon thermal treatment of 45S5 Bioglass between 550-600 °C [262], [273].

A comparison between the most relevant crystallization parameters related to 45S5 and 47.5B systems is provided in **Table 5.5**.

Table 5. 5. Thermal and kinetic parameters of 47.5B glass compared to commercial 45S5 Bioglass®.

Glass	n	m	E_c / kJ/mol	E_{vf} / kJ/mol	K_H [a]
47.5B-32	1.4-1.8	1	251	181	0.40
45S5 Bioglass®	1	1	311	338	0.0 [163]

[a] *The Hruby parameter for 47.5B glass was determined using β= 20 °C/min in the DTA experiment, with T_g = 542 °C, T_x = 670 °C and T_m = 990 °C.*

Interestingly, the value of *Ec* calculated for 47.5B glass powder was lower than that observed for 45S5 Bioglass® with the same particle size range below 32 μm.

This can be explained by considering compositional differences existing between the two systems, i.e. the bonding energies involved.

As suggested by Clupper and Hench [267], crystallization process is expected to likely involve the breakage of modifier-O bonds, for which the bonding energies are lower than Ec, rather than Si-O and P-O.
In particular, K–O bonds having a significantly low bonding energy [274] are present in 47.5B glass and absent in 45S5 Bioglass®, which suggests that the former may require a comparatively lower activation energy for crystallization.
Furthermore, it is worth observing that the crystalline phases formed during devitrification of the two materials are different, and this could also justify the different values of E*c*.
In fact, 47.5B tends to crystallize to $Na_2CaSi_3O_8$, whereas other phases were reported to develop in 45S5 Bioglass®.
In this regard, phase assignment of crystallized 45S5 Bioglass is not unanimous. Over the years, different research groups suggested different possible scenarios, *i.e.* crystallization of $Na_2Ca_2Si_3O_9$ [129], [267] or $Na_2CaSi_2O_6$ [179], [253] as the main phase, with the optional presence of $Na_2Ca_4(PO_4)_2SiO_4$ (silicorhenanite) as a secondary phase [262].

In the attempt to solve this controversy Bellucci *et al.* [275] hypothesized the coexistence of $Na_2Ca_2Si_3O_9$ and $Na_2CaSi_2O_6$, but this topic is still under debate.

It is also interesting to highlight that previous SEM observations on partially-devitrified 47.5B glass revealed the needle-like morphology of $Na_2CaSi_3O_8$ crystals [191], which is in agreement with the dimensionality of crystal growth (m = 1, one-dimensional rod-like) assessed in this work.

The Kissinger-type plots used for estimating the viscous flow activation energy of 45S5 and 47.5b bioactive glasses are shown in **Figure 5.14** and **5.15**, respectively.

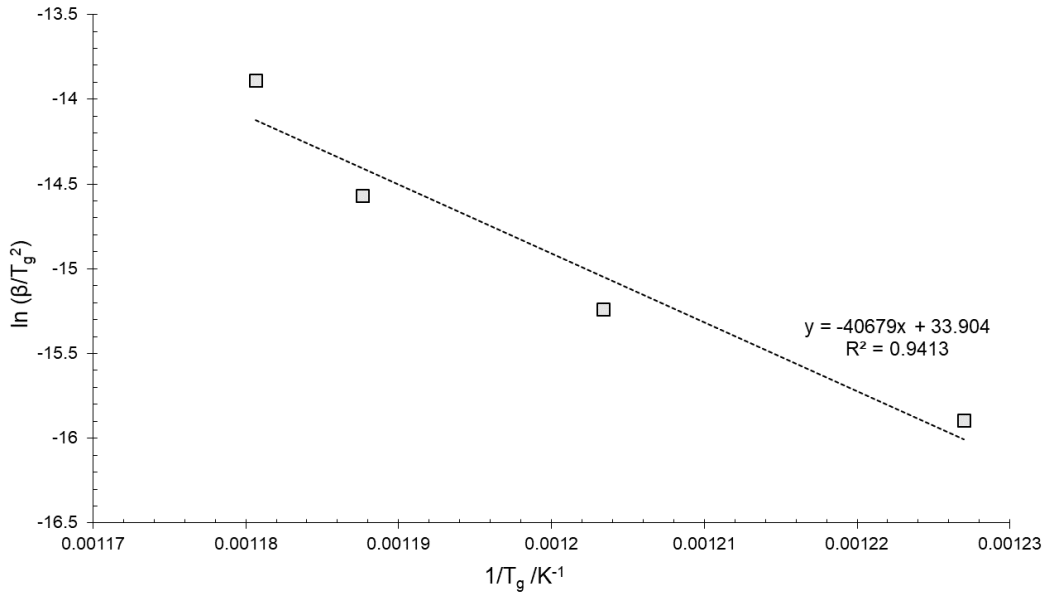

Figure 5. 14. Kissinger-type plot for the determination of the activation energy for the viscous flow (E_{vf}) related to 45S5 bioactive glass particles (≤ 32 µm).

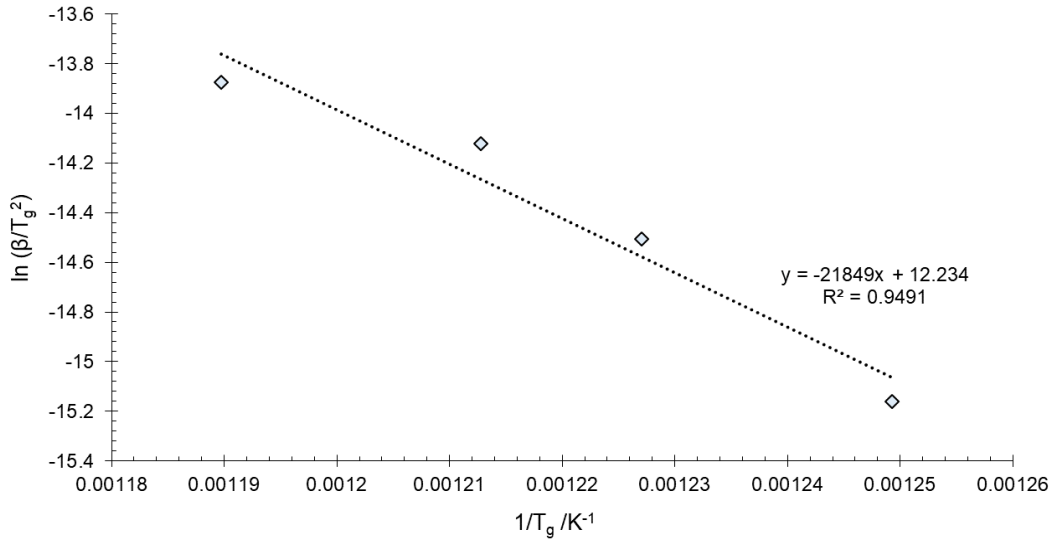

Figure 5. 15. Kissinger-type plot for the determination of the activation energy for the viscous flow (E_{vf}) related to 47.5B bioactive glass particles (≤ 32 µm).

The least squares interpolation yields E_{vf} values of 338 and 181 kJ/mol for 45S5 and 47.5B.

For 45S5 Bioglass, E_{vf} was found to be greater than Ec, thus indicating that the energy required for diffusive mechanisms to progress the crystallization is lower

than that required for viscous flow to occur. This value quantitatively confirms the rapid tendency of 45S5 glass to crystallize during high-temperature thermal treatment, prior to achieve significant sintering.

In the case of 47.5B bioactive glass, instead, *Evf* was lower than *Ec*, showing that the energy needed for viscous flow to occur is lower than that required for diffusion to progress the crystallization.

This confirmed that 47.5B glass is characterized by high stability against crystallization as compared to 45S5 Bioglass®, which exhibits a rapid tendency to crystallize just above the glass transition temperature.

This behavior was further confirmed by calculating the Hruby parameter K_H, which provides a measure of the glass stability against crystallization: the larger K_H of a certain glass, the greater its stability against crystallization upon heating [276]. K_H can be easily determined from the characteristic temperature of the system, according to **Equation 5.3** [277]:

$$K_H = \frac{T_x - T_g}{T_m - T_x} \qquad \textbf{5.3}$$

where T_x is the temperature of crystallization onset and T_m is the melting temperature determined from DTA plot in correspondence of the insertion point of the exothermic peak and the endothermic peak, respectively.

As shown in **Table 5.5**, the K_H parameter of 47.5B glass (0.40) was six times higher than that reported by Baino et al. for 45S5 Bioglass® powder (0.066) [16] under the same experimental conditions.

The JMA model validity was assessed by applying the method proposed by Malek both to 45S5 and 47.5B bioactive glasses [198]. This test is based on the analysis of a probe function z(χ) dependent on the heat flow and the temperature

It was found that both the crystallization kinetics and crystal structure of 45S5 Bioglass and 47.5B experimental composition cannot be properly described by the Johnson-Mehl- Avrami (JMA) model. Referring to the probe function, in fact, the JMA model can be considered valid only if the maximum of the function located at $\chi = 0.63 \pm 0.02$ [206].

Figures 5.16 and **5.17** show the z(χ) function obtained for the 45S5 and 47.5B, respectively. As can be seen, both functions were characterized by the typical bell-like shape. However, the maxima of z(χ) functions, mediated on different heating rates, were respectively located at 0.55 and 0.44.

As a result, it was concluded that the JMA model is not applicable to describe the crystallization process of both the glasses here analyzed. Concerning 45S5 glass, this finding was in good agreement with previous studies [271], in fact, 45S5 glass

is actually characterized by a more complex crystallization behavior than a simple nucleation-growth process, as liquid-liquid phase separation takes place upon crystallization [266].

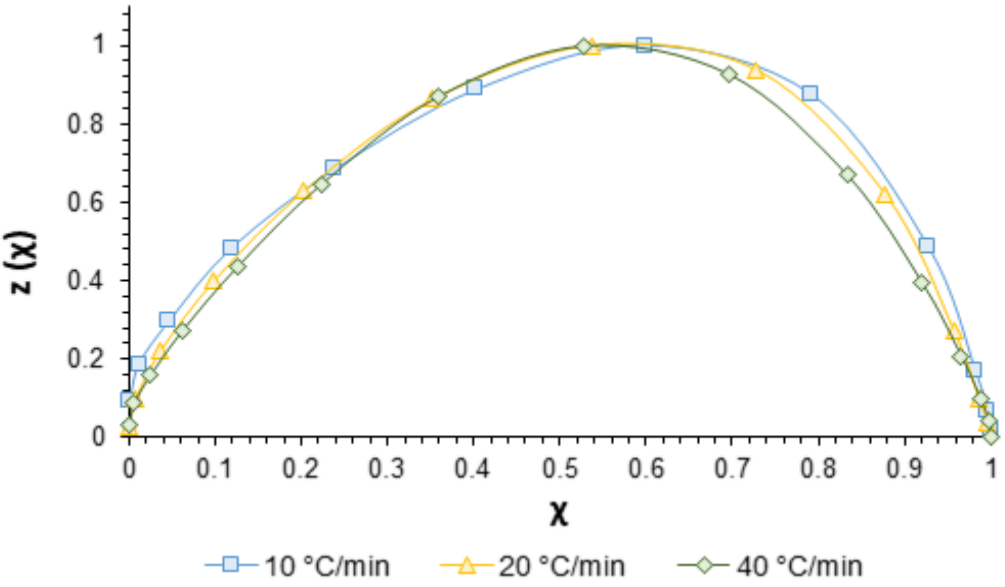

Figure 5. 16. z(χ) probe function related to 45S5 composition.

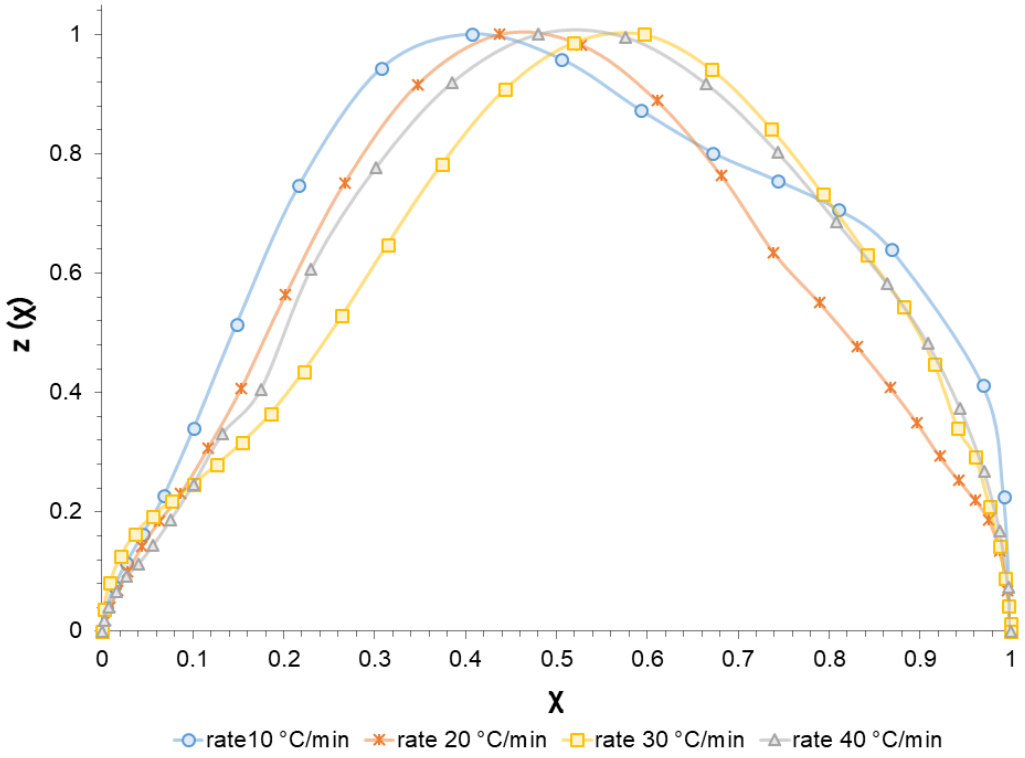

Figure 5. 17. z(χ) probe function related to 47.5B composition.

Concerning 47.5B system, future investigations could be addressed to elucidate whether, for example, glass-in-glass phase separation takes place during the crystallization of 47.5B, as observed, as an example, in the control system [253], [266], [271].

5.3.2 Biological response of 47.5B glass products

In vitro and *in vivo* biological tests represent a fundamental step towards the validation of a given biomaterial intended as substitute for a biological tissue in order to exclude any risks to the patient arising from its use.

In the study of Vernè et al. [191], carried out in 2009, in vitro cellular tests were performed on the 47.5A composition (with 0 mol.% of MgO). No toxic effects on the cellular line tested (fibroblasts belonging to the 3T3 cell lineage) were found, observing a good adhesion and proliferation of cells on the glass substrate both before and after immersion in SBF. However, no biocompatibility tests were performed on the 47.5B composition.

In the frame of this Ph.D research work, both *in vitro* and *in vivo* experiments were carried out in order to assess the biocompatibility of 47.5B-32 glass.

In vitro studies

In particular, in vitro cytocompatibility assessments were performed on 47.5B-bulk slices 10 mm-diameter ceramized at 650 °C for 3 h, a sintering temperature representing a good compromise between structural and chemical properties in physiological environment. At this temperature, in fact, the amorphous nature of the material is almost preserved, but, at the same time, sintering by viscous flow is favored, thus allowing to eventually obtain properly densified struts.

Bone marrow stromal cells (BMSCs), human bone osteosarcoma epithelial cells (U2OS) and human endothelial somatic cells (EA. hy962) cells were used as representative for self-healing recruitment, bone and blood vessels, respectively.

Main results related to cell viability onto the analysed substrate are summarized in **Figure 5.18**.

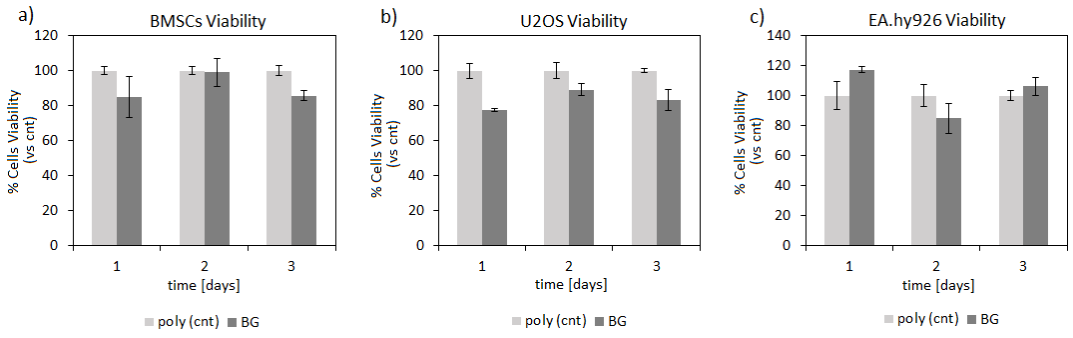

Figure 5. 18. Specimens' cytocompatibility. Results were comparable (>80%) between test BG and polystyrene control (poly cnt) at each tested time-points for all the cells lines.

The specimens analysed resulted as cytocompatibility towards all the tested cell lines and significant differences were observed by comparing the viability of cells directly cultivated onto specimens' surface and the ones cultivated onto polystyrene gold-standard. Therefore, test specimens can be considered as safe towards the assayed cell lines.

The cell morphology of BMSCs, U2OS and EA. hy926 cells was visualized by using digital light microscopy.

Representative images are collected in **Figure 5.19**.

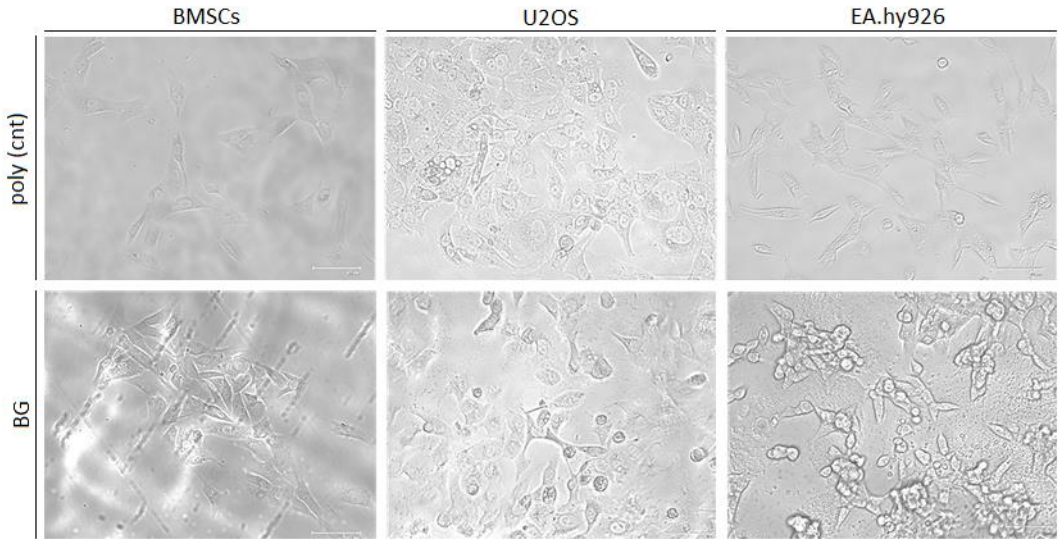

Figure 5. 19. Digital light microscopy images showing cells' adhesion spread and morphology.

The analysis revealed that all the cells were as correctly adhered and spread onto BG's surface; moreover, the cell morphology was comparable to that of cells cultivated onto polystyrene positive control.

In vivo studies

Despite preliminary cytocompatibility results were highly promising, testing cytocompatibility *in vitro* cannot be sufficient to ensure the safety of biomedical implants.

In this regard, animal models still represent a mandatory path toward the validation of both clinical devices and drugs.

Concerning the *in vivo* use of bioactive glasses, the crucial point is the possible toxicity related to degradation products, which can provoke secondary side effects to vital high-metabolic-rate organs participating in the excretion of waste substances.

While low-dose intraperitoneal administration did not produce any effect, higher doses led to impairment of motor skills and reduction of hunger and thirst, without provoking death.

Apart from the symptoms observed at intraperitoneal toxicity, intragastric administration route led to lethargy, shaking, convulsions, salivation and mortality was registered after 8 days. According to mortality data provided in **Table 5.6**, the average lethal dose LD_{50} was 4522.92±248 mg/kg.

Table 5. 6. Mortality data resulting from intragastric toxicity assay.

Intragastric administration

Dose, mg/kg	Mortality rate/%
4000	0
4100	16.7
4250	33.3
4500	66.7
4750	66.7
5000	100

Thus, according to the classification of substances by toxicity after intragastric administration, 47.5B glass was classified as slightly-toxic substance [278], [279].

The osteointegration level of 47.5B glass particles, as well as the interaction of the material with the host tissue was evaluated according to the following criteria:

i) the presence of an inflammatory response;
ii) the formation of new woven bone at the periphery of the wound;
iii) the formation of new woven bone at the centre of the wound;
iv) the conversion of woven bone into mature lamellar one.

No adverse immunologic reactions occurred after implantation over the whole observation period.

In particular, after 1-month post-surgery, no inflammatory infiltrate (usually appearing within 2-3 weeks) was observed neither in the C nor in the T group, confirming the good biocompatibility of 47.5B glass as bone graft material.

Material resorption proceeded gradually over time, in parallel with the osteointegration of the implant.

After 1-moth from the surgery, non-resorbed glass particulates were clearly visible, while, after 3 months, just few residues of glass embedded into bone trabeculae were observed, thus indicating the full resorption of the graft, in good agreement with previous *in vivo* studies [212], [280].
The upper area of **Figure 5.20** shows the presence of compact laminar tissue developed at the expense of glass particles, gradually degraded over time according to the physiological healing time of bone. The boundaries of bone tissue and biomaterial merge suggesting high level of osteointegration of 47.5B bioactive glass.

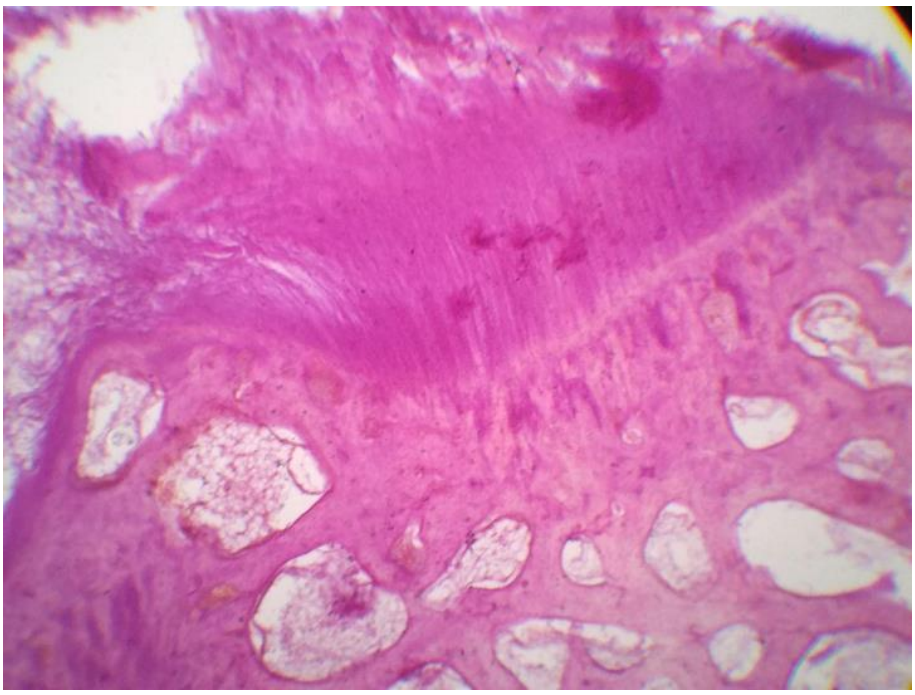

Figure 5. 20. Experimental group: bone and tissue healing after 3 months. In the upper section, a homogeneous dense tissue similar to calcified bone, in the lower fragment of the osteoid bone plate around the blood vessels. Haematoxylin and eosin stain x 10.0.

Figure 5.21 shows the histological image related to the control group, in which the defect remained unfilled and left to heal spontaneously.
Differently from the experimental group, immature connective tissue can be observed in the central region of the defect area, which is indicative for a delay in the regeneration of the tissue.

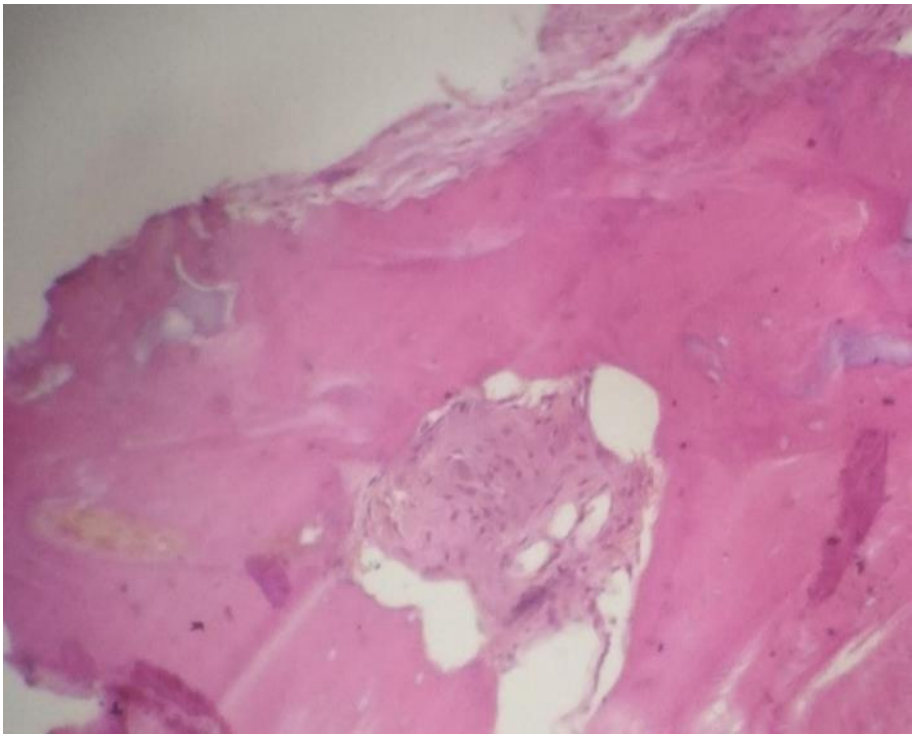

Figure 5. 21. Control group: bone and tissue healing after 3 months. Immature connective tissue in the defect area (central region, index of delayed regeneration. Haematoxylin and eosin stain x 10.0

Wilcoxon-Mann-Whitney test used to perform statistical analysis revealed a meaningful difference in bone formation score comparing the C and the T groups at all the tested periods of implantation, as reported in **Table 5.7**.

Table 5. 7. Bone formation score for T and C groups according to the histological scoring scale.

Testing sample		**1**			**2**				**3**			
T	Group	1	2	3	7	8	9	10	15	16	17	18
	Score	3	3	4	4	4	5	5	5	5	6	7
C	Group	4	5	6	11	12	13	14	19	20	21	22
	Score	1	2	2	2	3	3	3	3	4	4	3

These studies demonstrated the true osteogenic effect of 47.5B bioactive glass, definitely supporting its enormous potential as bone grafting material.

Considering the possibility to use 47.5B glass as basic material for sintering-based scaffold manufacturing, additional studies shall be carried out in order to determine the effect of crystallization on the osteogenic effect of the material.

5.4 Why realizing multicomponent sol-gel bioactive materials based on the 47.5B composition?

Silica-based bioactive glasses exhibit very unique properties which still make them materials of choice in TE applications.

However, most of melt-derived bioactive glasses, included the original Hench's 45S5 composition, are affected by important limits, including [114]:

i) High processing temperatures required for obtaining glass products;
ii) The necessity to include high sodium contents within the composition to facilitate glass processing, which is associated to the formation of high pH environment upon dissolution, potentially cytotoxic for osteoblasts;
iii) Bioactivity limited to restrained compositional ranges, i.e. $SiO_2 \leq 60$ mol.%;
iv) Low sinterability, which makes it difficult to obtain mechanically performant 3D scaffolds.

In this regard, sol-gel process offers the possibility to obtain, at lower processing temperatures, highly reactive materials with simpler oxide systems compared to those produced by conventional melt-quenching.

The most evident effect of this aspect is the preponderant presence in literature of studies describing the sol-gel synthesis of glasses and glass-ceramics based on relatively simple binary (SiO_2-CaO) or ternary (SiO_2-CaO-P_2O_5) compositions, eventually modified with therapeutically active dopants aimed at conferring multifunctional properties to the system, such as silver and copper for antibacterial effect and iron to induce a magnetic response for applications in tumor treatment.

Sol-gel 45S5 glass actually represents one of the few "quaternary" exceptions. Such a targeted interest has to be certainly attributed to the undisputable innovation represented by its parent melt-derived system, despite of all the issues mentioned above.

The sol-gel synthesis of 45S5 bioactive glass was first described in 2011 by Chen and Thouas [281], who were the first to succeed in introducing Na_2O in in the chemical process, using sodium nitrate ($NaNO_3$) as oxide precursor.

A later study by Cacciotti and coworkers [282] successfully demonstrated the possibility to tune the crystallinity, the bioactive kinetics and the reaction mechanism of sol gel 45S5 biomaterials by performing proper post/synthesis thermal treatments.
In particular, the study focused on the effect of the calcination temperature and the dwelling time on the porosity features, in terms of pore dimension and interconnectivity of the fired materials.

The effect of the aging time and temperature was also investigated in relation with structural properties and in vitro bioactivity of sol-gel 45S5 glass-ceramics.
In particular, an increase in both aging time and temperature was found to improve crystallization tendency, whereas bioactivity decreased with increasing aging time without being significantly influenced by the aging temperature [283].

In a more recent study, Faure et al. [284] innovatively introduced the use of an organic acid, i.e. citric acid, instead of nitric acid as catalyst for the sol-gel process, thus considerably reducing the concentration of the acid solution required to catalyze the hydrolysis of silicon and phosphorus alkoxides. A slight increase of the SSA was observed in the sol-gel material with respect to the melt-derived counterpart (from 0.4 m^2/g to 0.9 m^2/g), as well as a moderate improvement of the apatite forming ability in contact with SBF.

Despite enthusiastic and interesting results have been already achieved by several research groups, sol-gel strategy for the production of 45S5 glass-ceramics is still seldom applied and most of commercially available BG-based products are obtained by traditional melting rather than chemical synthesis.

The synthesis of glasses via sol-gel, in fact, can be still considered in some respects a real chemical challenge, requiring an accurate control on environmental conditions and multiple synthesis parameters.

This is particularly true for sol-gel materials based on complex multicomponent oxides systems, where some of the most recurrent issues regard solubility limits of precursors within the solvent, ions recombination in the liquid medium and/or formation of precipitates, which could determine a consistent deviation from the theoretical composition.

Although the addition of multiple modifier/intermediate oxides is not strictly required in sol-gel synthesis to facilitate material's processing and/or improve the reactivity of the silica network in contact with body fluids, there are specific oxides whose action is not only related to the structure of the silica network, but produces

highly beneficial cellular response, stimulating osteoblastic metabolic activity and enhancing the physiological healing process of the tissue.
Among these, CaO and MgO were reported to play a key role in determine new bone formation, bone cell adhesion and stability [238], [285], [286].
Thus, including these oxides within the synthesis of bioactive and multifunctional sol-gel systems may be of considerable clinical interest.

Given the promising physical and chemical properties assessed for 47.5B melt-derived glass, multicomponent sol-gel materials based on the same nominal compositional system were produced by sol-gel route and characterized in terms of morphological/compositional properties, microstructural/textural features and bioactive behavior in Simulated Body Fluid (SBF).

The main aim of the study was to impart to the 47.5B compositional system superior textural properties for future use in scaffold manufacturing by robocasting technology, as described later in **Chapter 6**.

Apart from reporting for the first time the synthesis of this multicomponent glass by sol-gel process, the added value of the present work lies in the lack of similar literature studies aimed at directly compare melt-derived and sol-gel glass and glass-ceramic materials having same oxide composition.
To date, in fact, most of these studies are almost limited to the original 45S5 Hench's composition, as previously mentioned.

47.5B-32 glass powder, produced by traditional melt-quenching, was used as reference system, paying particular attention relevant variations in microstructural/textural properties, as well as HA deposition rates resulting from the synthesis route used.

First of all, basic characterization analyses were carried out on DG-120 dried-gel in order to follow the evolution of the material upon subsequent thermal treatments.

In particular:

i) DTA/TGA measurements allowed assessing the thermal behavior/mass loss of the gel upon heating, thus qualitatively identifying the most relevant thermal events.
   More precisely, the measurement was carried out to define the most suitable calcination temperature to obtain a sol-gel glassy material;
ii) XRD analysis allowed detecting the crystalline phases within the material after the drying treatment at 120°C;
iii) SEM/EDS allowed qualitatively and semi-quantitatively characterizing material's morphological and compositional features, respectively.

Figure 5.22 shows the output of DTA-TGA measurements related to DG-120.

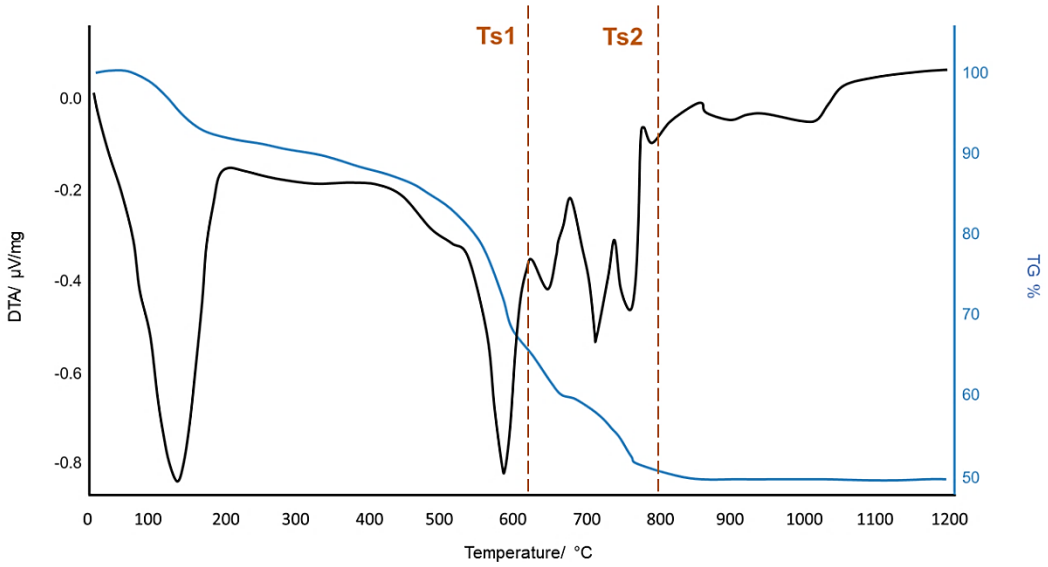

Figure 5. 22. DTA/TGA thermographs related to DG-120 material.

The total mass loss of upon heating assessed by TGA measure (blue curve, **Figure 5.2**) was about 50 wt. %, reaching a plateau above 800 °C.

Such an important mass reduction can be likely attributed to two different events:

i) the elimination of residual water within the gel, approximately at T~110 °C. Despite the material was treated at 120°C and it was supposed to be fully dried, the presence of some moisture was justified by the high wettability of the material in contact with air;
ii) the thermal decomposition of residual organic compounds and nitrates used as oxide precursors in the sol-gel process (400 °C ≤T≤ 780 °C).

Originally, two criteria were considered to determine the final calcination temperature:

i) The final material should have been preferably amorphous;
ii) The final material should have not contained organic residuals deriving from synthesis precursors.

However, as evident from the DTA/TGA curves, it was not possible to properly define a suitable workability window able to certainly satisfy both the requirements listed above.

Thus, it was decided to use two different calcination temperatures, T_{s1}= 625 °C and T_{s2}= 800 °C, identified as follows:

i) According to previous literature, T_{s1} was selected as the lowest calcination temperature able to ensure the thermal decomposition of most nitrates and organic compounds within the batch; moreover, according to DTA curve depicted in **Figure 5.22**, this temperature was below the first crystallization peak registered during the measure (exothermic peak centered at about 680 °C) and was very close to that used to sinter 47.5B robocasted scaffold

produced in previous studies (600 °C) [190], [219]. This aspect will be further clarified in **Chapter 6**;

ii) According to TGA measurement, T_{s2} corresponded to the maximum mass loss and thus, to the complete thermal stabilization of the material before reaching the melting temperature.

Consistently with DTA output, the XRD pattern of DG-120, depicted in **Figure 5.23**, revealed the presence of diffraction peaks associated to $NaNO_3$, as well as traces of other N-containing organic compounds deriving from the oxide precursors introduced in the sol-gel process.

The drying stage, indeed, was performed below the minimum temperature required for the beginning of thermal decomposition processes of nitrates, which was reported to be approximately between 500 and 800 °C, depending on the specific metal element and on the heating rate, as will be discussed more in detail later in the dissertation.

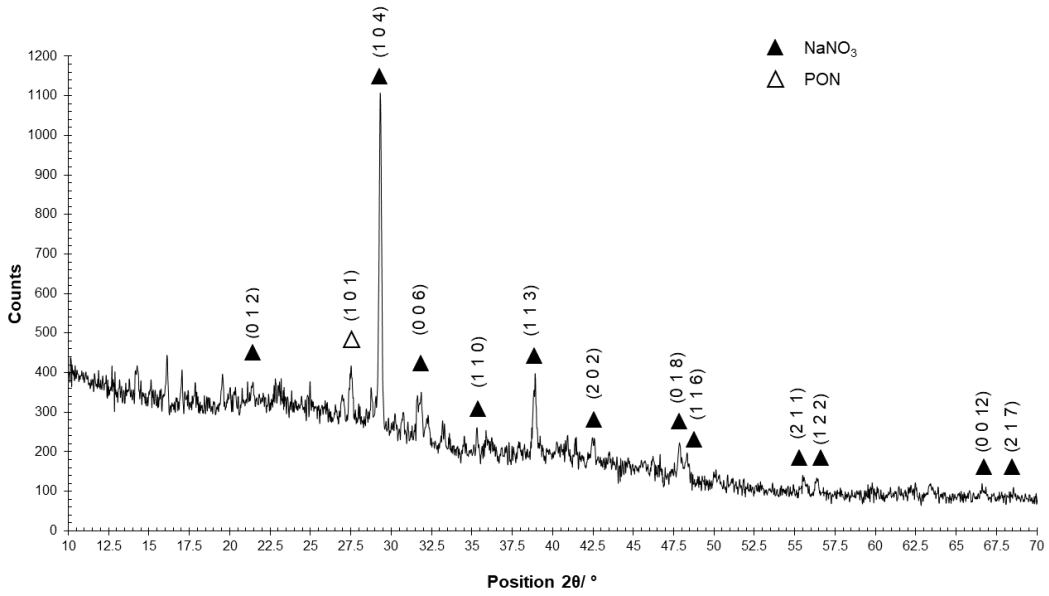

Figure 5. 23. XRD pattern related to DG-120 material.

As soon after drying, DG-120 was characterized by a whitish color, with a similar consistency to the touch to that of solid soap or wax candles.

From a morphological view point, DG-120 material was composed of coarse granules above 100 μm, poorly homogeneous both in shape and size due to the impossibility of effectively sieving the material because of its high hygroscopic behavior and tendency to form larger aggregates (Figure 5.24 a-b)

At higher magnification (Figure 5.24 c), an ordered tile-like structure was observed.

Consistently both with DTA/TGA and XRD measurements, EDS analysis confirmed the presence of nitrogen within the material in (Figure 5.24 d).

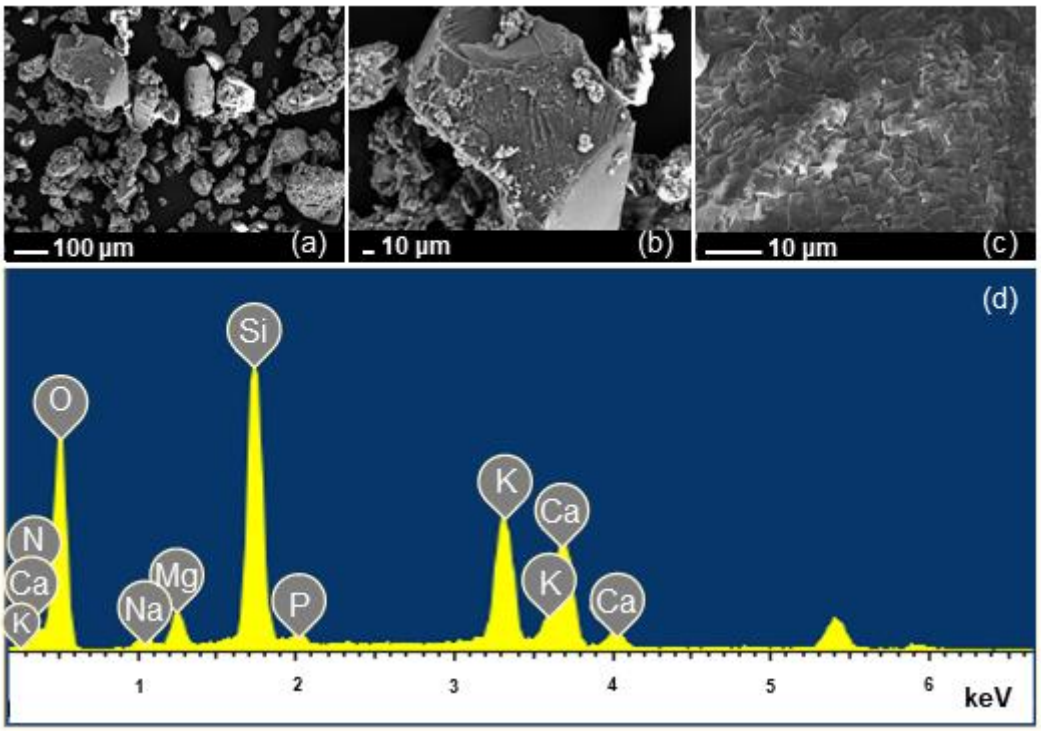

Figure 5. 24. SEM images at different magnification (a, b and c) and EDS spectra (d) of DG-120 gel.

Elemental compositional features of DG-120 material (mean value ± standard deviation) mediated on three different areas of the sample are summarized in **Table 5.8**.

Table 5. 8. Elemental composition of DG-120 sol-gel material.

Element	Average Weight %	Average Atomic %
N	4.1±1.3	5.6±1.5
O	60.5±2.8	72.7±1.1
Na	2.7±1.0	2.3±0.8
Mg	2.3±0.0	1.8±0.1
Si	13.2±1.6	9.1±1.4
P	0.6±0.1	0.4±0.0
K	8.5±1.7	4.2±1.0
Ca	8.1±1.7	3.9±0.9

The XRD pattern of SG-625 and SG-800 multicomponent sol-gel materials are depicted in Figure 5.25 a and 5.25 b, respectively.

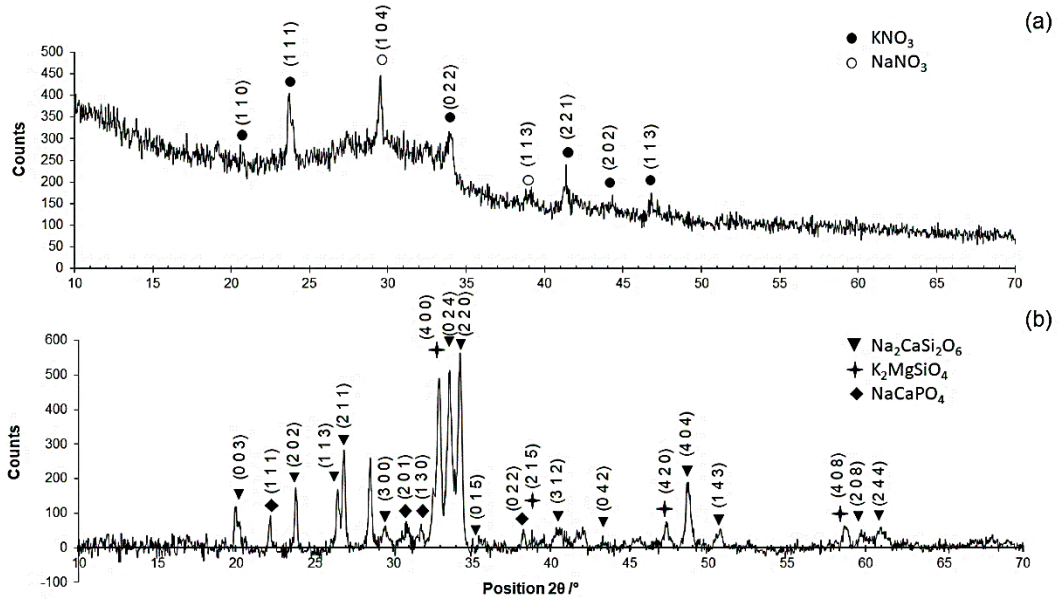

Figure 5. 25. XRD pattern related to SG-625 and SG-800 sol-gel materials.

As can be seen, differently from 47.5B-32 powder, that was completely amorphous (Figure 5.2 b), both XRD patterns related to the analyzed sol-gel materials were characterized by multiple diffraction peaks, indicating the presence of crystalline phases within the specimens.
The XRD pattern of SG-625 (Figure 5.25 a) had the typical appearance of a glass-ceramic material, characterized by the presence of an amorphous halo within the 2θ range 25-35°, along with some diffraction peaks attributable to potassium and sodium nitrates.
On the other hand, SG-800 exhibited sharp diffraction peaks (Figure 5.25 b) indicating the clear development of multiple crystalline phases upon calcination.

A combined analysis of XRD patterns (**Figure 5.25**) and DTA curve (**Figure 5.22**) allowed to associate the sharp exothermic peak observed at about 680 °C to the crystallization of a combeite-type crystalline phase (not detected in the material calcined at lower temperature), interestingly the same detected in melt-derived 45S5 Bioglass® after sinter-crystallization above 600 °C [163], [287].

A similar calcium-silicate phase ($Na_2CaSi_3O_8$) was also detected by Verné et al. in 47.5B melt-derived glass, nucleated upon thermal treatment performed above the glass crystallization onset.

The list of all the crystalline phases detected in SG-625 and SG-800, along with reference codes, formulas and crystal systems, are provided in **Table 5.9**.

Table 5. 9. Crystalline phases detected in SG-625 and SG-800 sol-gel materials.

Sample	Phase name	Reference code	Formula	Crystal system
SG-625	Niter	01-071-1558	KNO_3	Orthorhombic
	Nitratine	00-036-1474	$NaNO_3$	Rhombohedral
SG-800	Sodium calcium silicate (combeite-type)	01-077-2189	$Na_2CaSi_2O_6$	Rhombohedral
	Potassium magnesium silicate	00-048-0900	K_2MgSiO_4	Orthorhombic
	Rhenanite	00-029-1193	$NaCaPO_4$	Orthorhombic

The significant persistence of nitrates, observed in SG-625, despite a partial thermal decomposition at about 580 °C, is actually consistent both with the remaining sections of the DTA/TGA curves ($T \geq 580$ °C) and literature results reported by other authors.

As an example, Zheng et al. [288], observed the presence of $NaNO_3$ in sol-gel 45S5 glass-ceramic even after thermal stabilization (calcination) at 700 °C. In fact, 450-800 °C is the extended range reported for the thermal decomposition of sodium nitrate in three subsequent/concurrent reactions, using an heating rate of 5 °C/min [289].

Differently from what reported by Cacciotti et al. [282] for the synthesis of sol-gel 45S5 glass, who identified the thermal decomposition of nitrates at 529 °C, here a shift of the endothermic peak towards higher temperatures (from 529 to 580 °C) was observed.

This can be likely attributed to higher chemical complexity of the 47.5B system compared to the 45S5, as well as to the differences in processes parameters used to carry out the thermal analyses.
First of all, different heating rates were used to acquire the thermographs. It is known in fact that increasing heating rates could lead to a shift of the characteristic temperatures toward higher values.
The other important difference concerns compositional variations.
In particular, 47.5B system contains a considerable amount of MgO, which is absent in the 45S5 composition.
In this regard, Hoshino and coworkers [289] investigated the effect of several oxides on the thermal decomposition of sodium nitrate, finding an interesting relation between the temperature of decomposition of the compound and the acidity of each specific oxide.
In particular, the higher the acidity of the influencing oxide, the lower the temperature required for decomposing the nitrate.
Strong acid oxides, such as silica and titania, remarkably accelerate the decomposition of sodium nitrate. On the other hand, the reaction between sodium nitrate and magnesia, considered a basic oxide, led to the formation of O_2 within

the temperature range 500-600°C, responsible for the delay in the decomposition reaction [289].
This hypothesis actually represents a realistic possibility, as $Mg(NO_3)_2 \cdot 6H_2O$ starts to decompose before sodium nitrate at 350 °C and, at 600 °C, it has already mostly converted to MgO [290].

Endothermic peaks at about 712 and 755 °C were finally attributed to further stages of the thermal decomposition of nitrates, specifically sodium and potassium nitrate, for which the decomposition ranges are reported to be respectively 450-900 °C [289] 650-790 °C [291].

SEM morphological analyses of SG-625 and SG-800 acquired at different magnifications are collected in **Figure 5.26**.

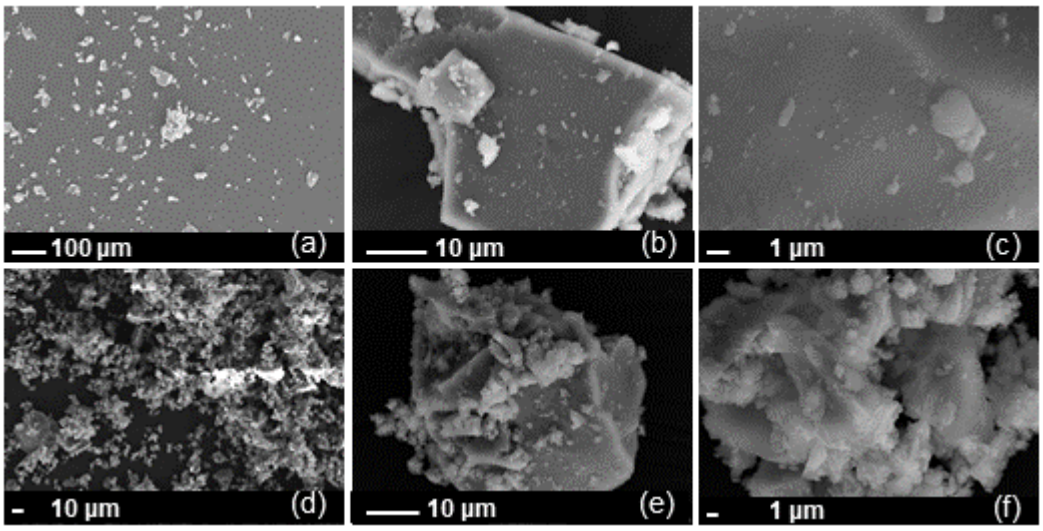

Figure 5. 26. SEM morphological analysis of SG-625 (a-b-c) and SG-800 (d-e-f) multicomponent sol-gel materials acquired at different magnifications.

Finer particles with qualitatively more uniform size were observed for SG-625 and SG-800 as a direct result of the sieving process. In both cases, smaller particles tended to form aggregates on the surface of bigger ones.

Traces of N were detected in SG-625, consistently both with DTA and XRD results, as a direct result of the low temperature used for the calcination process. On the other hand, no nitrogen was detected in the glass-ceramic calcined at 800 °C.
Results of EDS semi-quantitative analysis performed on SG-800 glass-ceramics, mediated on three different areas, are collected in **Table 5.10**.

Table 5. 10. Theoretical vs experimental oxide composition of SG-800 glass-ceramics (mol.%).

Oxide	Theoretical composition	Experimental composition
SiO_2	47.5	45.6±2.4
P_2O_5	2.5	1.5±0.2
CaO	20	21.0± 2.5
MgO	10	12.2±3.3
Na_2O	10	11.5±0.0
K_2O	10	8.1±3.6

Globally, the experimental composition of 47.5B sol-gel glass ceramics calcined at 800 °C was found to be in good agreement with the theoretical one.

BET results related to 47.5B-32, SG-625 and SG-800 materials are summarized in **Table 5.11**.

Table 5. 11. Brunauer-Emmett-Teller (BET) analysis results.

Material	Thermal treatment	SSA /m^2/g	Pore volume/ cm^3/g
47.5B-32	As-quenched	0.64	0.001
SG-625	625 °C/3h	2.23	0.017
SG-800	800 °C/3h	1.23	0.003

SG-625 and SG-800 exhibited higher SSA compared to MD-47.5B, thus confirming the role played by the synthesis process (sol-gel vs. melt-quenching) in determining the final textural properties of the material.
Moreover, a strict correlation between the calcination temperature and the textural properties was observed. In particular, as the calcination temperature was increased from 625 to 800 °C, the SSA decreased by a factor 2. A similar trend was observed for the pore volume, too.
In general, the values of surface area exposed to the external environment by the sol-gel materials here described were remarkably lower (from one to two orders of magnitude) than those observed in other sol-gel silicate biomaterials [192], [292]: this might be attributed to the complex composition of the six-oxide system produced as well as to the presence/development of crystalline phases causing the closure of the nanoporous texture, but further studies are required to better investigate this peculiar aspect in the future.

The formation of a hydroxyapatite layer in SBF is commonly recognized to be a valuable criterion to predict the bioactive potential of (bio)materials. However, the relationship between *in vitro* results and *in vivo* behavior is not always verified.

In this regards, Kokubo and Takadama [194] reported convincing evidence that hydroxyapatite formation on the surface of a given material in SBF can actually be predictive of its bioactivity *in vivo* (i.e., bone-bonding ability). On the other hand, Bohner and Lemaitre [293] recognized important limitations of the approach, claiming the need for significant improvements,

To date, the importance of preliminary *in vitro* tests in SBF is univocally recognized by the scientific community, although being aware that *in vitro* conditions can only roughly match those in the human body.

Figure 5.27 shows the pH increase observed upon powders immersion in SBF up to 336 h (2 weeks) as a result of ion exchange between the materials and the solution.

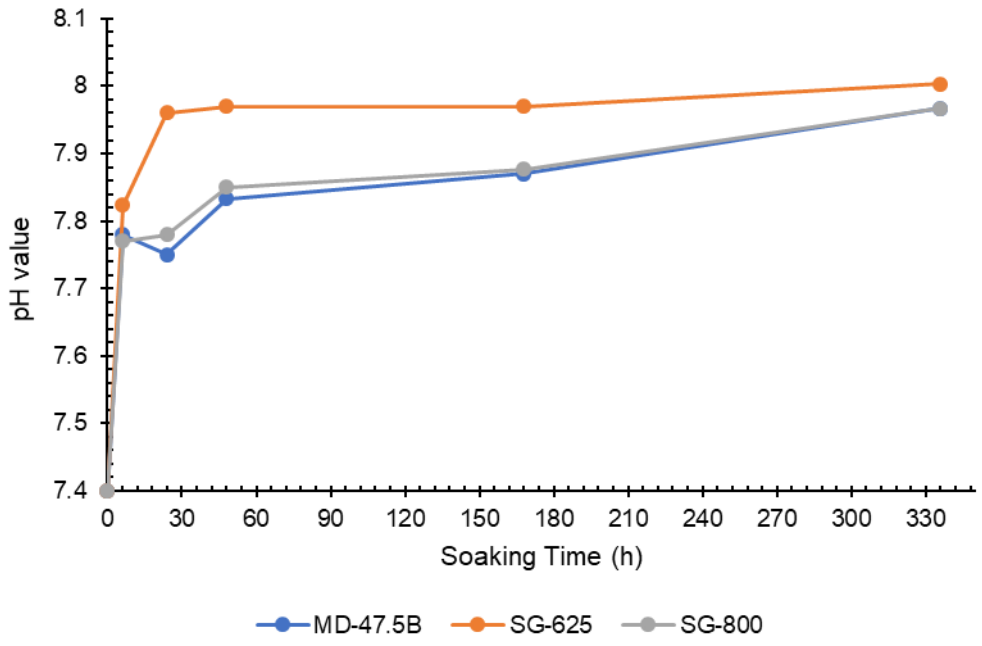

Figure 5. 27. pH variation upon soaking in SBF up to two weeks.

Although no statistically significant differences were observed for the three systems, some observations could be made:

The system showing the highest value of SSA was the one for which the highest pH increase was registered (i.e., SG-625), thereby suggesting a direct correlation between SSA and reactivity of the material in aqueous solution in other words, the higher the SSA, higher the reactivity.

For SG-625 glass-ceramic, the pH value stabilized after 48 h immersion with the achievement of a plateau at around 7.95, while a continuous increase up to two weeks was observed in the case of MD-47.5B and SG-800. This may suggest that most of the in vitro bioactivity reactions of SG-625 took place within two days from the beginning of the test; afterward, a chemical equilibrium was reached.

The curves related to SG-800 and 47.5B-32 materials were instead characterized by both comparable trends and pH values, suggesting comparable reaction rates of the two materials in SBF.

In all the systems analyzed the pH was below 8. It has been demonstrated that a moderate increase of pH toward alkalinity, like in the present case, is beneficial to promote osteoblastic activity [294].

Dealing with sol-gel bioactive glasses, this aspect is quite uncommon. Most of sol-gel bioactive materials proposed in literature reveal, in fact, a tendency to markedly increase the pH of surrounding fluids due to high reactivity in SBF.
In this regard, thermal treatment and, hence, crystallinity can play a role: for example, gel-derived 45S5 glass thermally treated at 700 °C led to a pH above 9.5 after seven days in SBF, while the same material calcined at 1100 °C (glass-ceramic) exhibited a lower reactivity (pH around 8.5 at one week) [282].

SEM morphological analyses after bioactivity tests in SBF (**Figure 5.28**) revealed an excellent apatite-forming ability of both melt-derived and sol-gel 47.5B-based materials, regardless of the production route used and calcination temperature.

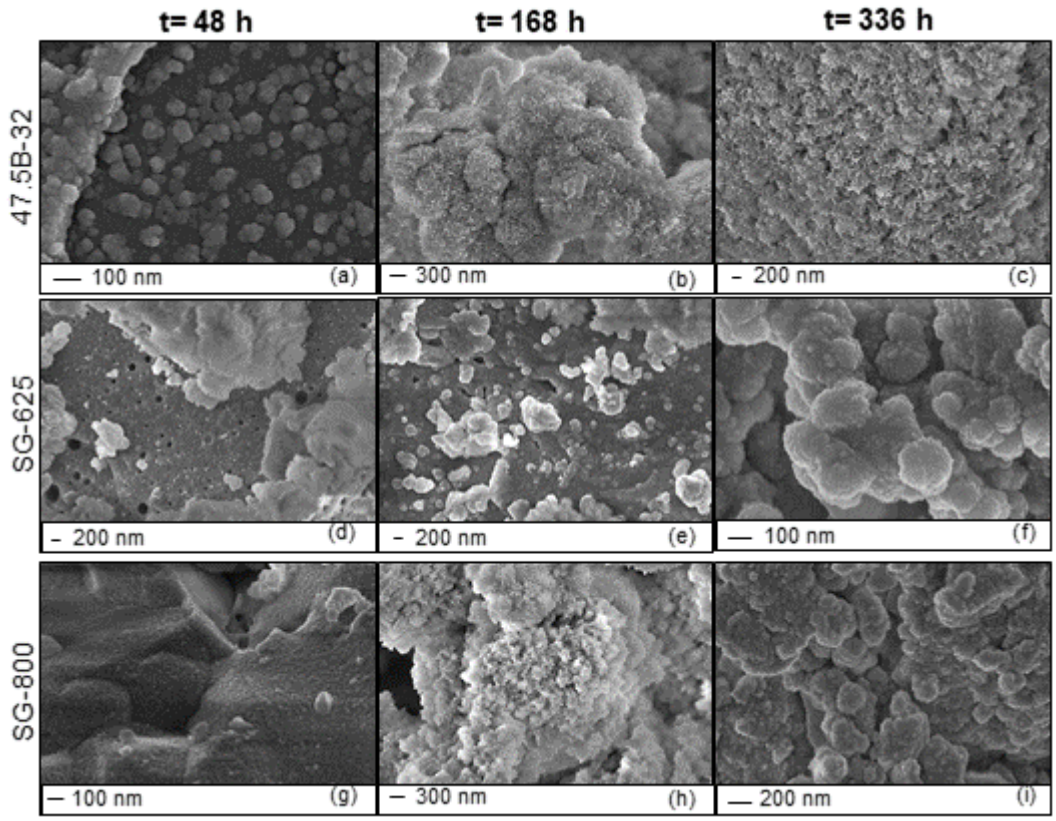

Figure 5. 28. Bioactivity tests in SBF: SEM morphological images showing the surface modification at different time points.

Calcium phosphate agglomerates were detected on the surface of all the samples after just 48 h immersion in SBF. However, some differences can be observed:

i) HA nucleated on the surface of 47.5B-32 sample constituted a uniform layer, characterized by the typical cauliflower morphology;

ii) HA observed on the surface of the sol-gel materials showed different features according to the calcination temperature. While larger calcium phosphate agglomerates patchy formed on SG-625, a quite uniform, thin layer was observed on the surface of SG-800 powders.

iii) Unlike 47.5B-32 and SG-800, nanopores in the range of 50–100 nm were observed on the surface of SG-625, suggesting a probable correlation between SSA values and the observed nanostructures.

iv) Despite the presence of crystalline phases in both sol-gel materials, the bioactivity mechanism was not inhibited and, after a two-week immersion in SBF, calcium phosphate coatings formed by nanostructured globular agglomerates, the morphology of which closely resembles that of hydroxyapatite, were observed on the surface of all the samples.

EDS measurements proved that a progressive deposition of calcium and phosphorus took place at the interface with the simulated physiological environment in all the materials analyzed.
At the end of the test, atomic Ca/P ratios for 47.5B-32, SG-625 and SG-800 were 1.65, 1.63 and 1.48, respectively (average calculated on five sites per sample). The Ca/P ratios of MD-47.5B and SG-625 were quite close to that of stoichiometric hydroxyapatite (Ca/P = 1.67).
Interestingly, no nitrogen was detected in the composition of the reaction layer formed on the surface of SG-625, probably remained entrapped within the silica network.

The formation of a hydroxyapatite layer on the surface of partially crystalline materials derived from a parent bioactive glass is not so obvious as devitrification can decrease bioactivity, as clearly demonstrated for melt-derived glass-ceramics in the SiO_2–Na_2O–CaO–P_2O_5 system [129]. Nevertheless, it was shown that sol-gel glass-ceramics based on the 45S5 or 70S30C (70SiO_2–30CaO mol %) systems retain a good apatite-forming ability, regardless of the formation of crystalline phases [295]. Thus, results achieved in the present work are consistent with these previous ones.

When necessary, the apatite-forming ability of sol-gel materials can be considerably improved combining sol-gel process with supramolecular chemistry, as comprehensively described in the next paragraph.

5.5 Considerations on 47.5B sol-gel materials: criticisms and possible strategies to improve textural properties

The presence of mesopores in sol-gel glasses led to improved ion release and faster HA deposition kinetics.
However, in traditional sol-gel synthesis, mesopores are randomly organized and their size distribution can largely vary between 2 and 50 nm, dramatically affecting the final mechanical properties of the material and making it really difficult to control and predict the reaction mechanism and the dissolution behavior.

Among BG-based materials for BTE applications, much attention has been recently addressed to MBGs because of their enhanced bioactivity and their intrinsic attitude to act as carriers for drugs and biologically active molecules able to perform a specific therapeutic action [137], [138].
This is due to the presence of a well-organized mesoporous texture, which confers interesting properties to the material in physiological environment [137].

In drug delivery systems, for example, mesostructured texture allows a better control on release kinetics, thus making the treatment more effective and confined to the target area [118].

The production of MBGs is based on sol-gel synthesis combined with supramolecular chemistry. Differently from traditional sol-gel materials, in MBGs

the formation of mesopores is driven by a structure-directing agent included in the synthesis, acting as templating agent for the ordered mesoporous texture. This important aspect makes it possible to exactly tailor and design material's nanostructural features according to each specific application [136].

Under specific and controlled pH and temperature conditions, the surfactant molecules self-organize and create the meso-texture following an evaporation-induced self-assembly (EISA) process [153]: briefly, the molecules of the surfactant self-organize into micelles by exposing hydrophilic heads to the synthesis solution that contains glass precursors. The obtained mixture is then subjected to a thermal treatment (drying) for the complete removal of solvent; high-temperature treatments (calcination) are eventually necessary to remove the template and consolidate the material.

The final part of this PhD research activity was dedicated to the design of MBGs based on the multicomponent 47.5B system, to study physical and chemical changes determined by the addition of a mesostructure directing agent (P123).

An early stage investigation was addressed to the determination of the role played by each precursor in the liquid environment synthesis in relation with the meso-template.
Particular attention was payed to solubility limits of each reagent in relation to the ternary state diagram H_2O-C_2H_5OH-P123.

Different synthesis protocols have been designed, aimed at optimizing the synthesis by studying the effect of the variation of different parameters:

i) The amount of templating agent
ii) The solvent type (H_2O, C_2H_5OH, H_2O+C_2H_5OH)
iii) The oxides' precursors

The so-obtained materials were preliminarily characterised in terms of textural properties, assessed by BET analysis, for determining the Specific Surface Area (SSA), pore volume and pore width. Sol-gel 47.5B system was used as control system for the present study.

Unfortunately, due to the global COVID-19 pandemic emergency, the activity related to the development of 47.5B-based MBGs was interrupted in an embryonic state, thus making it impossible to optimize material synthesis and finalize a complete dissertation.

Chapter 6

Analysis and discussion of results – Part 2

6.1 Bioactive glasses and porous scaffolds guiding bone regeneration in critically sized bone defects

The high versatility characterizing glass processing is certainly the primary strength which makes these unique materials so appreciated in a wide range of technological applications.

At the very beginning of their history, the clinical use of BGs was mainly limited to powders and particulates acting as fillers for the regeneration of restrained bone defects, or to bulk products for the complete substitution of small bones, such as those composing the ossicular chain of middle hear and finger phalanges [134]. Nowadays, BGs are affirmed biomaterials especially in dentistry and orthopedics due to their high bone remineralization potential [114], [296] and their suitability to be used as bioactive coatings for metal implants (i.e. dental screws and femoral prosthesis), mostly characterized by inert surfaces in contact with the physiological environment [297]–[300].

However, as deeply discussed in **Chapter 1**, biological bone is characterized by a very peculiar architecture which develops in the three-dimensional (3D) space, determining both its structural and, indirectly, biological properties, as a consequence of its influence on cell metabolic activity.

In recent years, driven by the desire to improve 3D bone tissue engineering (BTE) strategies for the regeneration of critically-sized bone defects, researchers focused on the optimization of glass and glass-ceramic porous scaffolds exhibiting proper mechanical, biological and mass-transport properties to support tissue ingrowth and regeneration until complete bone healing [145].

In the present chapter, results obtained by the processing of 47.5B bioactive glass by mean of both traditional and additive manufacturing technologies will be critically discussed.

In the frame of this Ph.D activity, innovation elements were introduced within each one of the manufacturing technologies described in **Chapter 4**, thus producing a direct effect on the features of the final products.

In the first part, the dissertation will be focused on the relation existing between thermal/crystallization properties and effects on the porous microstructure/mass transport properties and mechanical performances of the device. In order to do this, traditional foam replica method, a simple and affordable technology affirmed since 15 years, was used, modifying the conventional protocol to improve the reproducibility of the overall process.

Afterwards, the discussion will move towards the description of two novel manufacturing strategies, i.e. bread replica method and dolomite foaming, both derived from a creative reinterpretation of conventional techniques. A consistent part of this specific research, indeed, was addressed to the development and characterization of more sustainable and eco-friendlier BTE scaffolds obtained from waste materials, through a transversal approach combining different industrial/technological fields.

Finally, in the attempt to overcome current limitations existing in the 3D printing of sol-gel materials, grid-like scaffolds were produced using dried-gels as basic materials for ink formulations, thus avoiding intermediate calcination processes responsible for undesired devitrification phenomena, as well as decrease in textural properties of sol-gel materials.

Part of the results discussed in the present section have been published in:

- *Fiume, E.; Schiavi, A.; Orlygsson, G.; Bignardi, C.; Verné, E.; Baino, F. Acta Biomaterialia 2021, 119, 405-418.*
- *Fiume, E.; Tulyaganov, D.; Ubertalli, G.; Verné, E.; Baino, F. Materials 2020, 13, 628.*
- *Fiume, E.; Serino, G.; Bignardi, C.; Verné, E.; Baino, F. Applied Sciences 2020, 10, 8279.*
- *Fiume, E.; Serino, G.; Bignardi, C.; Verné, E.; Baino, F. Molecules 24, 2954.*

6.2 Investigating porous-microstructure changes occurring in glass and glass-ceramic foam-replicated scaffolds *u*pon different sintering conditions: mathematical modeling and advances micro-CT pores analysis

The production of scaffolds for BTE cannot prescind from an accurate design of porous microstructure and mass transport properties. Both of them, in fact, actively

contribute to define the biological performance of the scaffold, influencing cell attachment, penetration depth (cell migration) and the formation of a well-organized vascular network responsible for proper tissue oxygenation, from the periphery to the inner core.
Among the most important basic requirements that a scaffold should exhibit, comprehensively reviewed in **Chapter 1**, total porosity ($\varepsilon_0 \geq 50$ vol.%), pore size (d_p = 100-500 μm), high interconnectivity of the porous network (i.e. presence of adequate interpore window) [121], as well as sufficient compressive strength (2 MPa) [251] are usually considered as representatives for the final biological response, obviously according to the reference values characterizing trabecular bone.
However, the present list is not exhaustive and the reference ranges for the above-mentioned parameters are in principle quite broad.

The relative ease in assessing both total porosity ε_0 and mean pore size d_p usually makes them the characteristic parameters most often used to evaluate the potential suitability of new scaffolds for BTE applications and/or compare different scaffold types.

Nevertheless, there is convincing evidence that porosity and pore size distribution alone can just provide a very preliminary (and sometimes too approximate) assessment of the scaffold biological suitability.

As an example, in contrast with the general idea of higher porosity values promoting a more efficient tissue ingrowth [221], Hollister et al. [301], [302] reported no statistically significant difference in regenerated bone volume within poly (propylene fumarate)/tricalcium phosphate (TCP) composite scaffolds with different porosity levels (30, 50, 70 vol.%). Moreover, the same research group reported that differences in pore size in polycaprolactone (PCL) scaffolds (d_p= 350-800 μm) had an almost negligible influence on bone regeneration rates [303].

At a first glance, these results may appear conflicting if the interdependency of scaffold porous microstructural features and their mutual effect on the bone regeneration process [304] are not considered; moreover, the inherent differences existing between different scaffold materials (e.g. inert polymer vs. osteoinductive TCP) should not to be neglected due to their capability of variously influencing cell response, as well as their ability to determine the compliance of the final struts and, thus, fluid flowing inside the pores.

In order to achieve a more reliable comparison between ceramic scaffolds and trabecular bone, Falvo D'Urso Labate et al. [305] proposed the use of a multiparametric score based on the combined evaluation of six microstructural parameters (total porosity, pore interconnectivity, pore size distribution, specific surface area, connectivity density and degree of anisotropy), thus partially overcoming the limitations mentioned above.

As briefly introduced in **Chapter 4**, intrinsic permeability *k* is a key property characterizing all porous materials. In BTE applications it is strictly related to the biological performances of the scaffold, both *in vitro* (i.e. in dynamic cultures inside bioreactors) and *in vivo*, favoring scaffold colonization by osteoprogenitor cells and the synthesis of new bone matrix directly inside the synthetic graft: therefore, adequate permeability values would promote both the material (osteo)integration and the healing process, ensuring a proper mass transport, which is usually one of the most critical aspects dealing with 3D tissue engineering (TE) approaches.

As can be easily deduced, the ability of a porous material to conduct fluid flow relies on a combination of porosity, pore size, pore orientation, pore tortuosity and interconnectivity among adjacent pores.

Compared to the other morphological features mentioned above, i.e. porosity and pore size distribution, easier to quantify by mass-to-volume measures and various imaging techniques, an accurate measure of *k* is a challenging issue.
The available methods used for assessing the intrinsic permeability of TE scaffolds, essentially based on the implementation of the Darcy's Law, have been comprehensively reviewed by Pennella et al. [234] in 2013.
An ASTM standard, published in 2014, describes the procedures to follow in order to obtain a mean value of Darcy's coefficient for TE porous scaffolds, where the value of *k* is derived by measuring the pressure gradient generated by fluid flowing across the scaffold by using three transducers, two for measuring the upstream and downstream pressures and one for the flow rate [306].
However, this approach may be inadequate for highly brittle and/or resorbable scaffolds, which could be damaged by the fluid flow during the measurement execution, as usually a liquid medium is used.

In this work, intrinsic permeability assessment of 47.5B *FRS* was carried out by mean of an highly accurate acoustic method based on the use of a single transducer for the measure of the low-frequency sinusoidal pressure component of air flow, applied for the first time to commercial calcium carbonate porous scaffolds in 2012 [235]. Results, combined with non-destructive tomographic analysis, were used as input data for a theoretical mathematical model based on the Forchheimer's Theory, aimed at achieving a detailed characterization of scaffold microstructural features changes with sintering temperature within a given range (approximately between the beginning of viscous flow phenomena and the end of crystallization processes).

The major strength of the constitutive equation here proposed lies in the absence of empirical relations among terms. This allowed to properly derive scaffold's physical/microstructural properties by using as input parameters accurate experimental data supported by a robust statistical analysis.

For the correct implementation of the model, proper assumptions and boundary conditions were required, in order to identify its validity limits.

Many different formulations for "pore size", indeed, are available and discussed in literature, according to the various features and morphologies of permeable media [307]–[310]. As a result, depending on the considered model, slightly different results can be achieved.

Here, it was assumed that the average pore diameter d_p was the characteristic length scale of the internal structure of the porous medium, i.e. the effective scale of the microstructure [228].

Moreover, given that glass and glass-ceramic materials can be considered highly stiff solid materials, pore morphology was assumed not to vary as a function of the dynamic stresses induced by alternating fluid flow [311].

In the end, no-slip condition at airflow/pore walls interface was placed. Differently from liquid fluid flows, obeying no-slip boundary conditions at the solid walls, gases may actually slip along the solid walls (in this case, the internal surface of the pores) because of the small scale of the pore cross-section [312]. However, when the mean free path λ of gas is considerably smaller compared to the pore diameter, a no-slip condition can be assumed: namely, the mean free path of air, at the atmospheric pressure, is λ~0.07 μm, which is greatly smaller than scaffold pore diameters required for a successful TE treatment [313], thus making this assumption relevant to the context analyzed.

The general macro-scale features of *FRSs* sintered at different temperatures are summarized in **Table 6.1**.

Table 6. 1. Primary and derived geometrical dimensions (diameter D_s, length L_s, volume V_s, cross-sectional area A_s), apparent density ρ_s and total porosity ε_0 of 47.5B-*FRS*, expressed as mean value ± standard deviation, calculated on 6 specimens.

	Sintering Temperature /°C					
	600	**650**	**700**	**750**	**800**	**850**
D_s / mm	8.3±0.3	8.2±0.6	10.3±0.5	10.7±1.0	10.7±0.6	11.0±0.6
L_s / mm	7.1±0.7	6.7±0.6	8.1±0.5	6.7±0.3	6.9±0.1	6.1±0.4
A_s / mm^2	54.6±4.5	53.3±7.5	82.8±8.2	90.4±17.0	90.6±11.0	94.5±11.0
V_s / mm^3	389.0±66.0	355.2±77.0	670.0±100.0	607.9±140.0	624.3±84.0	577.2±100.0
ρ_s /g/cm^3	0.68±0.10	0.78±0.04	0.42±0.01	0.69±0.04	0.66±0.05	1.18±0.05
ε_0	0.79±0.03	0.71±0.01	0.84±0.01	0.74±0.02	0.75±0.02	0.55±0.02

The total porosity ε_0 of all the scaffolds produced was within the typical range of human trabecular bone, thus satisfying the minimum BTE requirements for allowing proper cell infiltration, attachment and new tissue ingrowth ($\varepsilon_0 \geq 50$ vol.%) [50], [314]–[316].
More specifically, depending on the sintering conditions, ε_0 values varied between 55 and 84 vol.%, where the upper and the lower limit of the interval were respectively registered at T_{s3}= 700 °C and T_{s6}= 850 °C.

However, as can be seen in **Figure 6.1**, no clear trend was observed as a function of the sintering temperature over the considered thermal range and the low value of R^2 coefficient indicated that no linear relation can be established between the

decrease in porosity values and the increase in sintering temperature. This is probably due to the concurrence of crystallization and sintering, as also explained below. Perhaps, a more definite relation could be determined in a wider thermal range.

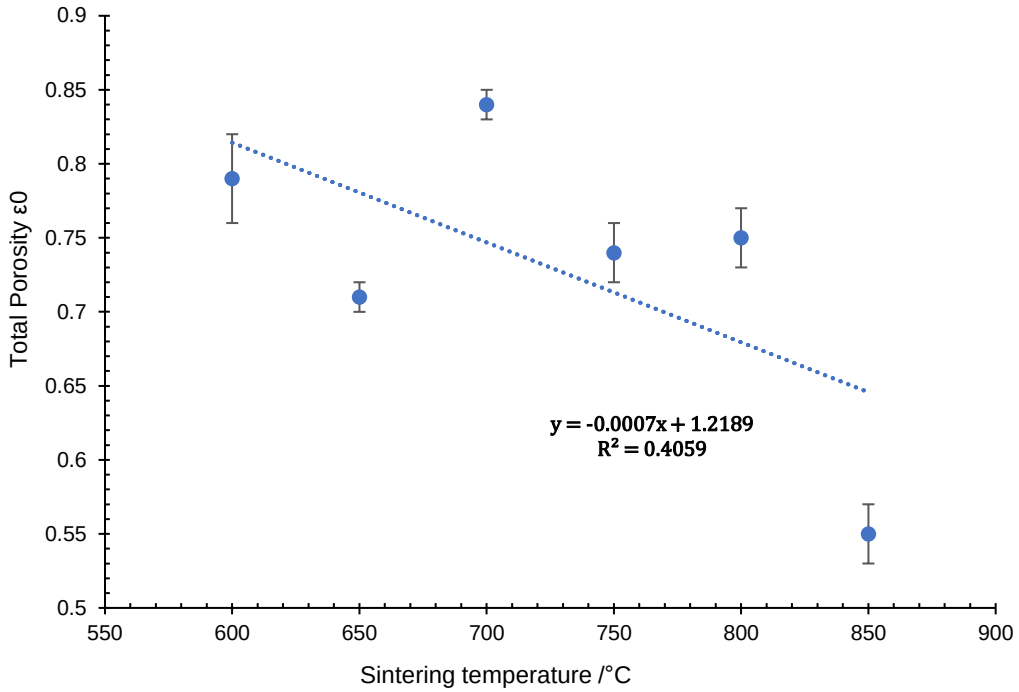

Figure 6. 1. Total porosity of 47.5B-*FRS* as function of the sintering temperature.

Among all the available techniques used for bone scaffold manufacturing, maybe the replication of proper polymeric templates, like PU foams, is the one that allows obtaining the best "bone-like" trabecular morphology through a conceptually easy and affordable procedure.

In the present study, although all the trabecular architectures observed somehow reminded the spongy one typical of PU foams used as macroporous template, they were not a perfect "carbon-copy" replica of the original template, as the sintering treatment and the concomitant nucleation of crystalline phases upon heating led to important changes in morphological characteristic of the porous structures.

Above the crystallization onset (T_x ~ 690 °C), in fact, significant modifications occurred compared to the PU sponge, with a reduction of the pore diameter from 410-920 μm for scaffolds sintered at 600°C to 170-280 μm for scaffolds sintered at 850 °C (**Figure 6.2)**.

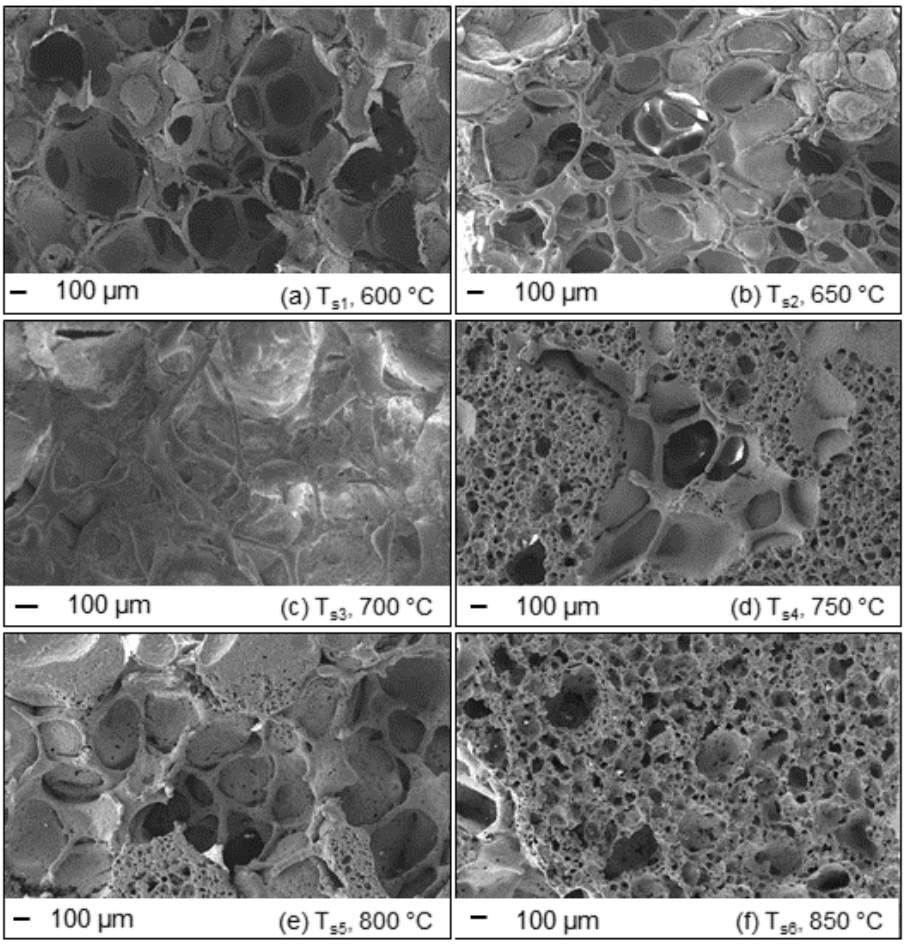

Figure 6. 2. SEM micrographs of 47.5B-*FRS* derived from commercial PU sponges.

Specifically, *FRSs* sintered at lower temperatures (Figure 6.2 a-b-c) exhibited the typical open-cell trabecular morphology of glass-based scaffolds produced by foam replica method [150], [156], [259], analogous to that of human cancellous bone [317].

Pore size and trabecular thickness estimated by a dedicated analysis software tool were between 200-500 µm and 70-100 µm, respectively.

However, such a typical morphology was observed only up to 700 °C, approximately corresponding to the temperature of crystallization onset (T_x ~ 690 °C) of 47.5B glass, as identified in **Chapter 5**.

Just after crystallization (Figure 6.2 d-e), indeed, pore size followed a double distribution, with larger pores between 200 µm and 500 µm, defined by trabeculae, and smaller ones, having no specific shape, even below 50 µm.

At the end of the crystallization (T_{s6}= 850°C), a consistent drop in ε_0 was observed (**Table 6.1**), along with more homogeneous porous structure: Figure 6.2 f shows that pores with size of about 100-150 µm were preponderant, while the number of bigger pores, reaching 300-400 µm, was remarkably lower.

Cross- sectional images acquired by µ-CT scanning of FRS sintered at different temperature are collected in **Figure 6.3**.

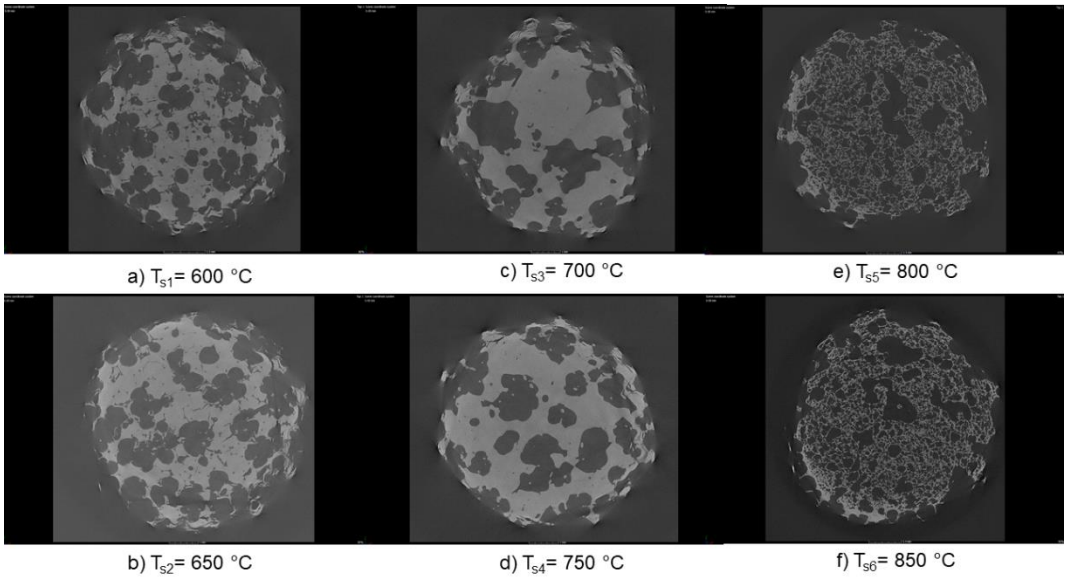

Figure 6. 3. Micro-CT images showing the cross section of FRS sintered at different temperature. Relevant changes in porous microstructure can be clearly appreciated.

The presence of larger macropores in mild sintering conditions could be likely attributed to the lower shrinkage of the material upon heating. According to the HSM thermographs reported in **Figure 5.6**, **Chapter 5**, indeed, the volumetric shrinkage of the sample at the end of the thermal treatment (T_{s1}= 600 °C) was about 24%, while, upon thermal treatment in correspondence of the crystallization onset, the sample underwent a 27% volumetric shrinkage (**Table 5.3**, **Chapter 5**). As a result, the final pore dimension in FRM-T_{s1} (410-920 μm) was definitely comparable to that of the original PU template, ranging between 350 and 900 μm.
On the other hand, at higher sintering temperatures, morphological changes and reduced pore diameter likely derived from a microstructural reorganization determined by devitrification processes. The hypothesis of a higher densification upon heating, in fact, was not supported by experimental data, which revealed a lower volumetric shrinkage, due to the inhibition of densification phenomena by viscous given by the progressive nucleation of crystalline phases and material's stiffening (**Table 5.3**, **Chapter 5**).
Despite this, the macropore dimension of scaffolds sintered at 800 and 850 °C could still be included within the minimal range recommended for allowing cell migration and nutrients supply within the graft [50].

Figure 6.4 shows the SEM surface analysis carried out at higher magnifications in correspondence of three different significant temperatures, defined according to DTA results previously discussed in **Chapter 5**, specifically **a)** before crystallization (T_{s1}=600 °C), **b)** at the crystallization onset (T_{s3}~T_x=700°C) and **c)** at the end of the crystallization process (T_{s6}=T_f=850°C).

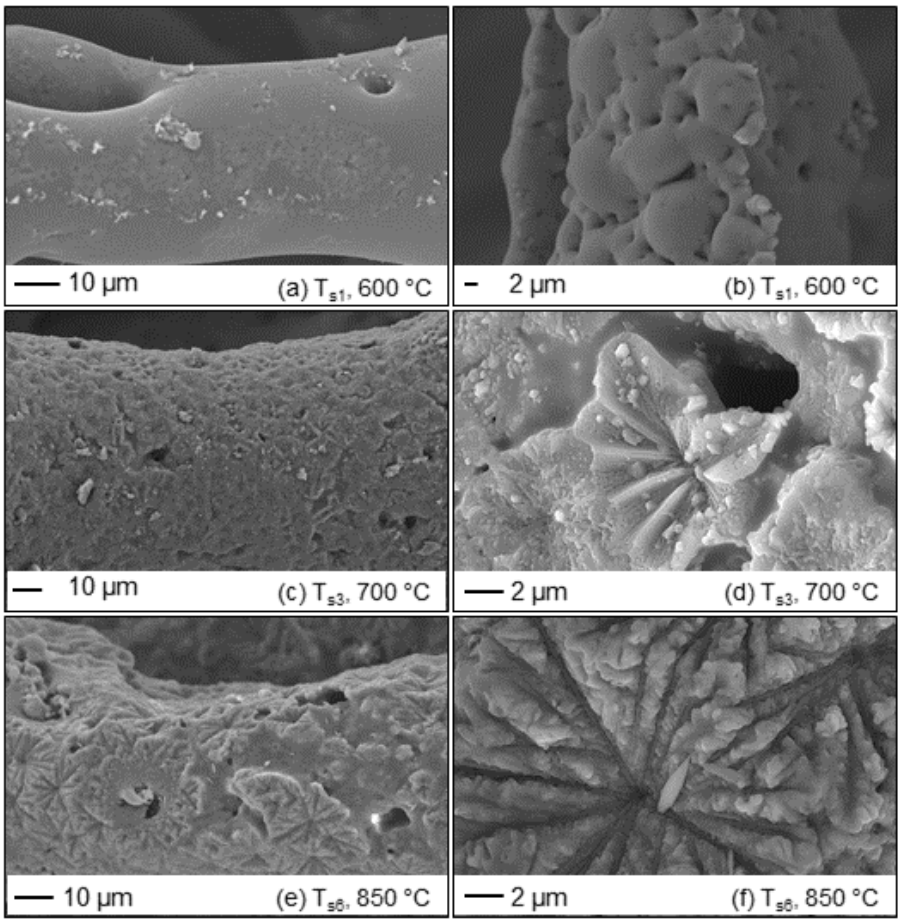

Figure 6. 4. SEM images of 47.5B scaffold surfaces at different magnification sintered at 600°C (a-b), 700°C (c-d) and 850°C (e-f). Material devitrification resulted in the formation of flower-like crystals associated to the nucleation of combeite.

The surface of scaffolds sintered at lower temperature (Figure 6.4 a) appeared smooth and topographically homogeneous, exhibiting the typical features of an amorphous material. Consistently with XRD results (*Paragraph 5.3.1*, **Figure 5.5**), no crystalline phases were observed.

At higher magnifications (Figure 6.4 b), sintering necks between adjacent glass particles and interstitial pores resulting from viscous flow phenomena upon heating were clearly visible, together with the presence of micrometric and submicrometric interstitial pores.

Approaching the crystallization temperature, evidences of the system devitrification appeared on the scaffold surface. At 700 °C, indeed, flower-like crystals in the range of 10-12 µm were observed, surrounded by the glassy amorphous matrix (Figure 6.4 c-d).

In scaffolds sintered at 850 °C, the trabecular surface appeared completely covered by these crystalline structures (Figure 6.4 e), bigger and more defined in shape (Figure 6.4 f) compared to that observed at 700 °C, as a result of the growth process of crystalline phases upon high temperature treatments.

In **Chapter 5**, two main different crystalline phases where detected in samples sintered above the crystallization onset, i.e. combeite ($Na_2Ca_2(Si_3O_9)$) and tremolite ($CaMg_3(SiO_4)_3$).

In this regard, local EDS analyses performed in correspondence of these structures was not resolutive in achieving a univocal identification of the crystals, as all the elements composing 47.5B glass were detected, accordingly to the proportions of the theoretical composition. Despite this, in the light of the above considerations (see **Chapter 5**), no adverse biological effects on bone cellular species are expected.

A detail of trabecular morphology in correspondence of each sintering temperature is provided in **Figure 6.5**.

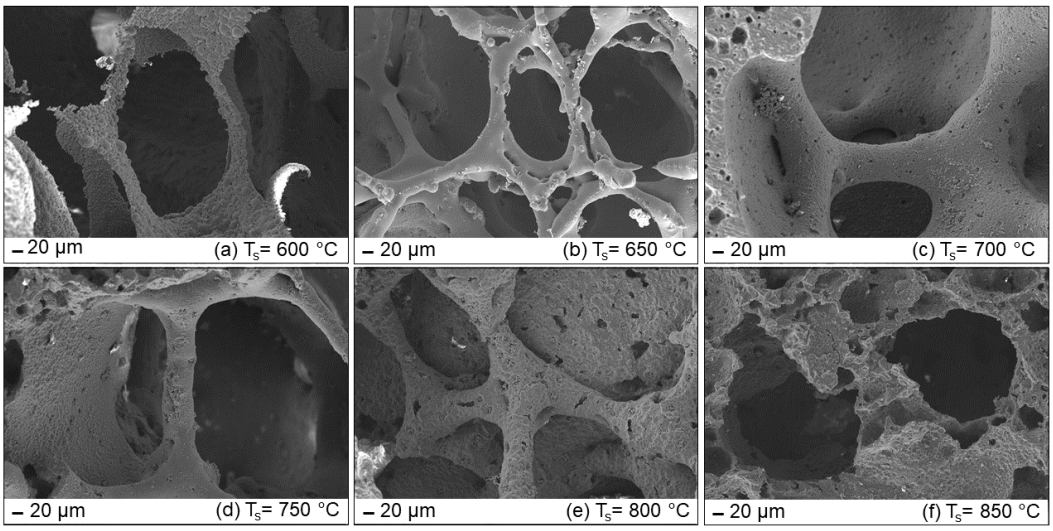

Figure 6. 5. SEM images of 47.5B glass and glass-ceramic scaffolds sintered at different temperatures: 600 °C (a), 650 °C (b), 700 °C (c), 750 °C (d), 800 °C (e) and 850 °C (f).

Improved densification of the 3D struts was observed as the sintering temperature increased. In fact, from 600 to 700 °C, contact points between adjacent particles progressively increased in number and sintering necks became gradually thicker, resulting in reduced interstitial voids (Figure 6.5 b-d).
As a consequence, for Ts ≥ 650°C, continuous trabecular surfaces were obtained. However, approaching the crystallization onset, surface smoothness progressively decreased (Figure 6.5 d-e-f), in good agreement with a surface crystallization mechanism.

The post processing of accurate µ-CT data allowed to calculate the pore diameter d_p of each single arbitrarily-shaped pore using **Equation 4.9**, **Chapter 4**, putting in relation the pore diameter d_p with the non-spherical volume V_p, the internal surface area A_p and the shape factor φ_p, provided as output by the software together with the pore type, indicating the existence of connections between a pore and the adjacent ones.
The software used for µ-CT data analysis (VGStudioMax) operated a distinction between connected, border and isolated pores in relation to the position of pores within the scaffold volume and their relative level of interconnection, basing the overall analysis on the Cauchy-Crofton approach.

Considering the final purpose of the present study, from this point forward, exclusively connected and border pores will be considered, i.e. all those pores communicating each other by the presence of interpore windows. However, the issue of closed pores will be resumed later in the dissertation.

Representative μ-CT projections supporting advanced pore analysis are collected in **Figure 6.6**, where different colors are used to distinguish adjacent pores on the basis of dimensional and geometrical parameters defined by internal algorithms.

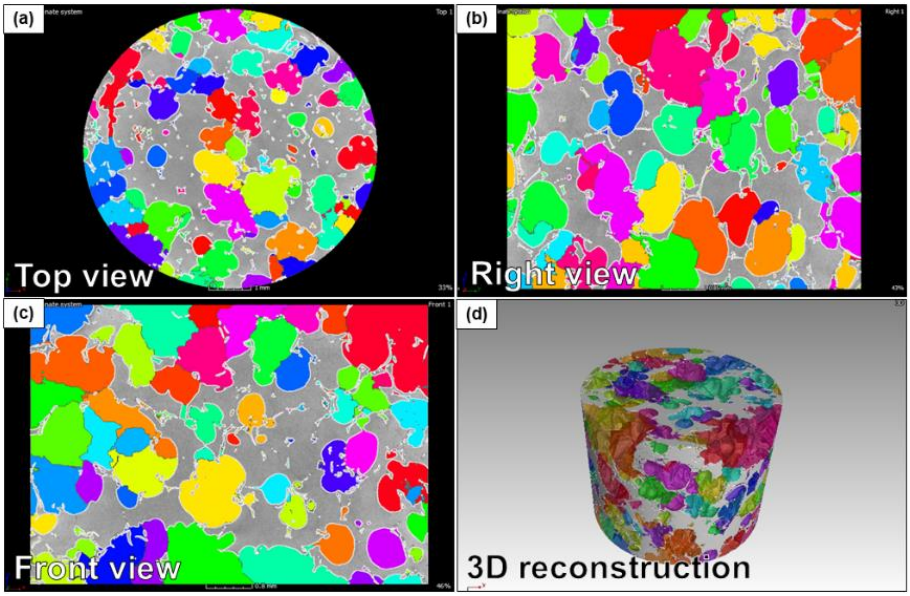

Figure 6. 6. Example of μ-CT images of foam-replicated cylindrical scaffolds: Top, right, front views and 3D reconstruction of a 47.5B-glass scaffold sintered at T_{s1}= 600°C; merge threshold 95%.

Statistical results related to d_p analysis are summarized in **Table 6.2**, while the distribution of the overall pore diameter at each sintering temperature is graphically represented in **Figure 6.7**

Table 6. 2. Pore diameter: experimental data and statistical results.

	Sintering Temperature /°C					
	600	**650**	**700**	**750**	**800**	**850**
N. Pores	730	199	1793	6601	9345	2434
N. Outliers	0	2	20	85	133	21
Mean $\overline{d_p}$ */mm*	0.67	0.78	0.33	0.30	0.26	0.22
σ_d */ mm*	0.34	0.43	0.16	0.12	0.11	0.22
Median (d_p) */mm*	0.68	0.78	0.33	0.30	0.26	0.22
1^{st} *quartile /mm*	0.41	0.48	0.26	0.25	0.22	0.17
3^{rd} *quartile /mm*	0.92	1.05	0.43	0.37	0.32	0.28
Max d_p */mm*	1.68	1.94	1.03	0.92	0.82	0.91
Min d_p */mm*	0.02	0.01	0.14	0.14	0.12	0.01
$\overline{\varphi_p}$	0.286	0.345	0.268	0.260	0.247	0.185
σ_φ	0.064	0.081	0.091	0.084	0.088	0.071

By increasing the sintering temperature, pore size shifted towards lower values and the number of pores per unit of volume increased, consistently with preliminary

SEM morphological investigations. Moreover, a decrease in d_p data dispersion was observed with increasing temperature.

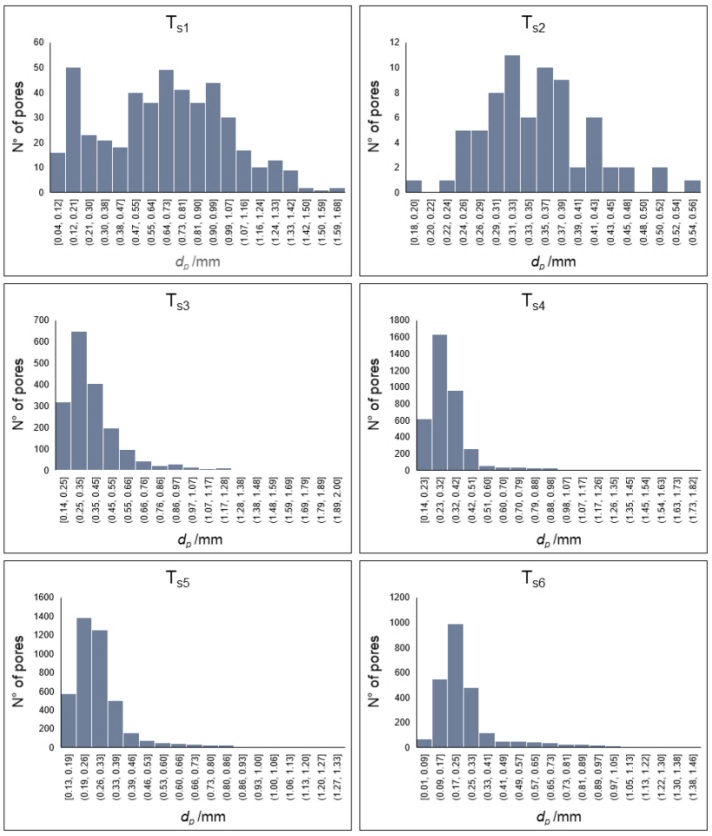

Figure 6. 7. Actual distribution of pore diameters d_p within 47.5B scaffolds sintered at different temperatures. Each histogram represents the pore size distribution within a representative sample for each sintering group.

For T_s=T_{s1}, T_{s2}, in fact sub-optimal sintering had probably determined the accidental breakage of trabecular network in specific points, thus determining the union between two or more pores, detected as a larger one by the analysis software, and yielding an overall higher dispersion of pore sizes.

Also pore sphericity φ_p decreased with increasing temperatures as densification/ devitrification phenomena led to important deviation from the morphology of the original template characterized by tetrakaidekahedral pores.

Under the assumption listed above, the intrinsic permeability k of each sample was determined in the linear Darcy's region making a negligible error related to inertial effects (~1%). The linear flow velocity U through a cylindrical sample with a 9-10 mm diameter, indeed, was ~ $1.2 \cdot 10^{-2}$ m/s, low enough to maintain a laminar flow through the volume of the sample, with an interstitial Reynolds number R_i close to unity, as will be seen later.

In a preliminary phase of the analysis, permeability data were analyzed and related to d_p values, separately considering the mean value of *connected*, *border*, *border+connected* pores. The six sintering groups were further distributed in two

macro-groups identified according to the characteristic temperatures of the 47.5B system and delimited by the temperature of crystallization onset (T_x~700°C), i.e. the first group identified all the scaffolds sintered below T_x and the second one all the scaffolds sintered above T_x.

Specifically, graphical data in Figure 6.8 a refer to scaffolds sintered at 600, 650 and 700 °C, while data represented in Figure 6.8 b refer to scaffolds sintered at 750, 800 and 850 °C.

Regardless of the sintering temperature, the mean diameter of connected pores was significantly lower than that of border ones in all the samples analyzed. Considering the position in relation to scaffold geometry, border pores, exposed to the external environment, are delimited by discontinued trabeculae, more susceptible to accidental breakage. Moreover, in relation to the manufacturing protocol, a lower deposition of glass slurry at the periphery of the scaffold is highly probable and likely related to the difference in diameter observed between border (external) and connected (internal) pores.

Interestingly, before crystallization onset, border and connected pores equally contributed to the determination of the mean pore diameter (connected+border), while after crystallization, the mean value *border+connected* shifted towards the mean pore value related to *connected* pores.

Moreover, by analyzing separately the two temperature ranges considered, it could be observed that intrinsic permeability decreased with temperature increase following approximately a linear trend.

The complete plot resulting from the union of Figure 6.8 a and b is provided in Figure 6.8 c.

Decreasing permeability values were observed with the increase of the T_s, following approximately a linear trend, discontinued by samples sintered at 700 °C, at which a pronounced permeability drop was observed. This aspect will be deepened later in the dissertation.

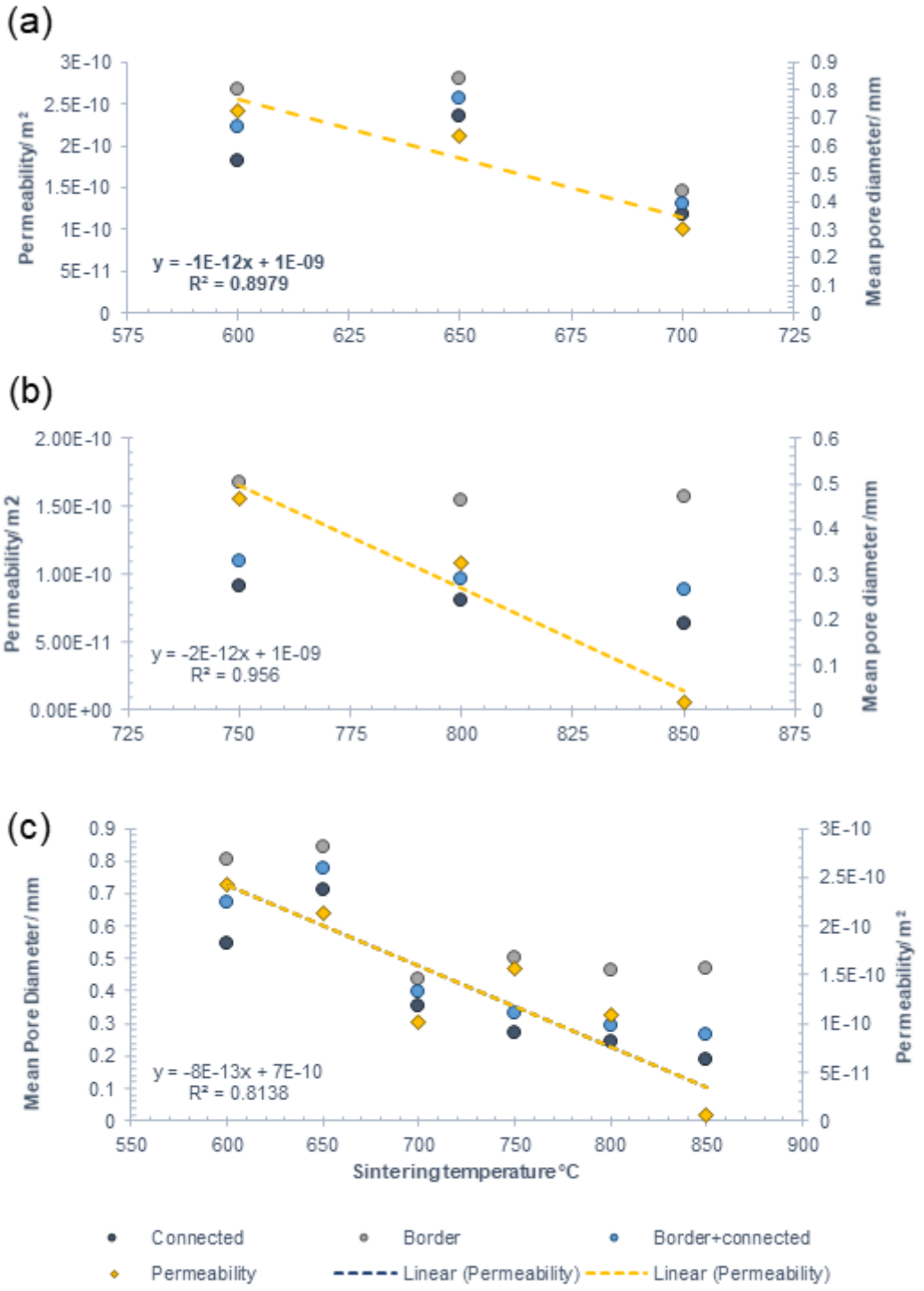

Figure 6. 8. Mean pore diameter and permeability as function of the sintering temperature before (a), after the crystallization onset (b) and over the complete sintering range (c).

Interestingly, k variation as a function of the sintering temperature followed approximately the same trend of d_p, thus suggesting a preponderant role of pore size in determining fluid flow through the porous media.

Experimental data obtained for each sintering group are shown in **Table 6.3**.

Table 6. 3. Intrinsic permeability experimental results and statistical analysis.

	Sintering temperature /°C					
	600	**650**	**700**	**750**	**800**	**850**
$k/\cdot 10^{-10}\ m^2$	2.49-2.81	2.59-2.85	1.10-1.29	1.42-1.70	1.03-1.16	0.04-0.06
$Max\ k/\cdot 10^{-10}\ m^2$	3.04	2.95	1.35	1.72	1.30	0.08
$Min\ k/\cdot 10^{-10}\ m^2$	2.08	2.54	0.96	1.39	0.81	0.02

Comparable results were obtained by Ochoa et al. [318] and Li et al. [319] for Bioglass®-based scaffolds with 90-95 vol.% porosity produced by the same manufacturing process ($1.96\cdot 10^{-9}$ m^2) and 70 vol.% porous calcium phosphates ($2.13\cdot 10^{-10}$ m^2), respectively. Moreover, the values obtained were comparable to the reference ranges reported by several authors for human trabecular bone belonging to different anatomical sites, thus confirming the potential suitability of 47.5B-derived foam-like scaffolds for BTE applications.
Specifically, the reference ranges related to human trabecular bone considered for comparison are collected in **Table 6.4**.

Table 6. 4. Intrinsic permeability values of human trabecular bone.

Material	**Origin/anatomical site**	**Permeability (m^2)**	**Ref**
Human trabecular bone	Fresh frozen calcanei of cadavers	$0.4\text{-}11.0\cdot 10^{-9}$	[320]
Human trabecular bone	Vertebral body	$1.5\text{-}12.1\ 10^{-9}$	[321]
Human trabecular bone	Proximal femur	$0.01\text{-}4.7\cdot 10^{-9}$	[321]

The only scaffolds which did not fulfill the minimum permeability requirements were those sintered at 850 °C, for which the permeability was 2 to 3 orders of magnitude lower.

Interestingly, both total porosity and mean pore size of the scaffolds belonging to this sintering group were still in the typical ranges reported for trabecular bone [50], [322]; however, as discussed above, these two parameters alone are not enough to reliably estimate whether a scaffold would be architecturally suitable or not for TE applications and a reliable assessment of effective porosity and related parameters are fundamental to achieve a clearer picture.

Graphical solution of **Equation 4.21** for the calculation of the effective porosity at each sintering temperature in the physically-meaningful range (0-1) is depicted in **Figure 6.9**.

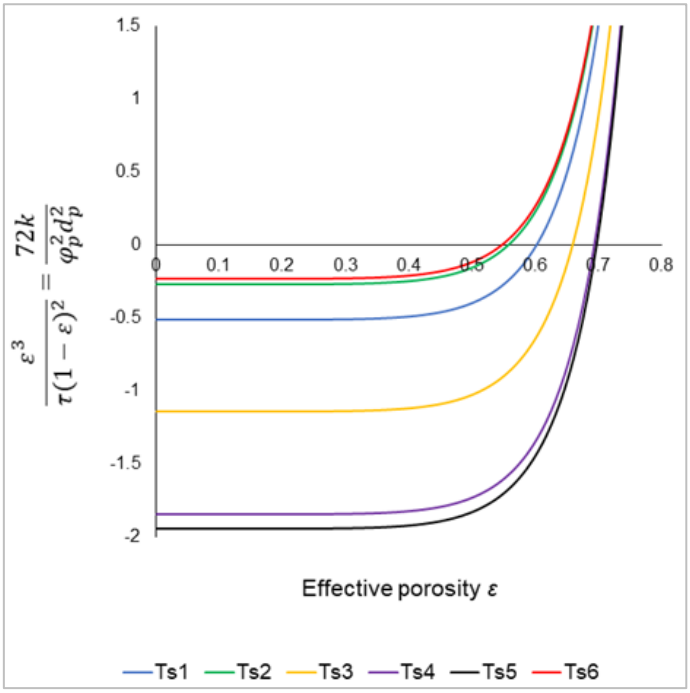

Figure 6. 9. Graphical solutions of Equation 17, assessed by using experimental data of permeability k and average pore diameter d_p.

Finally, the assessment of the effective porosity allowed achieving a comprehensive characterization of scaffold porous microstructure and mass transport properties, as summarized in **Table 6.5**.

Table 6. 5. Microstructural and transport properties of scaffolds produced at different sintering temperatures.

	Sintering temperature /°C					
	600	**650**	**700**	**750**	**800**	**850**
Effective porosity ε	0.54	0.48	0.61	0.66	0.66	0.46
Total porosity ε_0	0.75	0.71	0.84	0.74	0.75	0.55
Closed porosity ε_c	0.21	0.23	0.23	0.08	0.09	0.09
Open-to-close ratio r	2.57	2.09	2.65	8.25	7.33	5.11
Pore diameter/throat β	1.30	1.35	1.24	1.21	1.20	1.37
Tortuosity τ	1.40	1.50	1.30	1.26	1.25	1.53
Sample length L_s/ m	0.007	0.007	0.008	0.007	0.007	0.006
Pore length L_p/ m	0.010	0.010	0.011	0.008	0.009	0.009
Reynolds num. R_i	0.56	0.71	0.20	0.18	0.15	0.06
Friction factor f_c	179.78	153.44	466.01	492.11	587.53	1882.28
aμu /pa·m^{-1}	1334.0	1379.3	1879.6	1348.6	1878.4	40846.8
bρu^2/pa·m^{-1}	2.9	4.4	1.2	0.7	0.8	11.8
Linearity deviation (%)	0.22	0.32	0.06	0.05	0.04	0.03
k/·10^{-10} m^2	2.679-2.802	2.633-2.811	1.277-1.291	1.636-1.650	0.245-1.166	0.051-0.052

Referring to **Table 6.5**, for scaffolds sintered at 850 °C, the combination of several factors, including insufficient effective porosity (40 vol.%), high pore tortuosity (1.53) and pore size close to the lower recommended limits (~100-150 μm), as well

as the significant reduction in permeability values could likely determine a negative picture of the scaffold performances both in vitro and in vivo.

In keeping with previous comments, the values of interstitial Reynolds number R_i, calculated for the proper flow linear velocity U in each scaffold, were always <1; at very low Reynolds number $R_i < 1$, the roughness and irregular shape of pore walls have a negligible influence on the flow resistance and, under laminar conditions, the friction factor f_c is independent of the surface roughness, varying linearly with the inverse of Reynolds number.

The pore morphology-dependent parameter β relates the pressure drop to the effects of pore cross-sectional area variation on the fluid flow [229], [230]; specifically, according to previous experimental findings, the pressure gradient decreases with increasing β [323].

The open-to-close pore ratio *r* was found to remain roughly constant (below 2.7) up to T_{s3} = 700 °C and increased for scaffolds sintered at higher temperature. This reveals that, above the crystallization onset, open porosity - derived from the macropores of the original template - became strongly predominant over the closed one as the latter tended to significantly decrease.

In these regards, **Figure 6.10** compares the trends of effective porosity and intrinsic permeability as function of the sintering temperature.

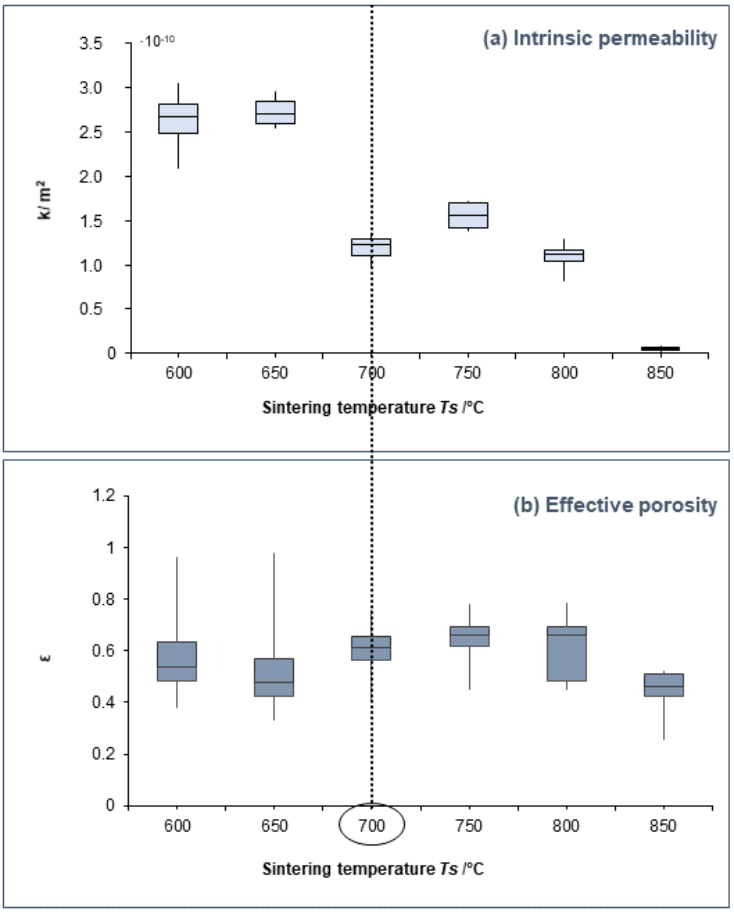

Figure 6. 10. Analysis of intrinsic permeability related to effective porosity.

As previously mentioned, an important drop of permeability values was observed in the scaffolds treated at 700°C (i.e., the onset of crystallization), where the early-stage nucleation of crystalline phases led to a reorganization of the scaffold structure at the micro-scale, which was likely related to the higher percentage of closed porosity compared to that observed for Ts ≥ 750 °C.

However, despite samples sintered between 600 and 700°C exhibited comparable values of closed porosity and scaffolds sintered at 700 °C were characterized by higher effective porosity, it seemed that mass transport properties remarkably decreased.

In this regard, some consideration on the origin of closed pores could be crucial to clarify these apparently conflicting results.

The formation of closed pores within open-cell structures produced by powder sintering is, most of the times, determined by technological issues either related to inefficient sintering conditions or over-densification and microstructural reorganization upon heating.

Considering the scaffolds treated at 600 and 650 °C, it was reasonable to relate the presence of closed pores to interstitial spaces between particles, as clearly shown in Figure 6.3 b.

On the other hand, topographical analysis performed on the scaffolds sintered at 700 °C, did not reveal the presence of residual interstitial porosity (Figure 6.3 d) and, in this case, closed pores likely formed from the closure of interpore windows during the sintering process, which undoubtedly have a major role in determining scaffold mass transport properties compared to interstitial micropores, thus justifying the observed permeability drop.

Mechanical properties of FRS were evaluated on a different sample set, characterized in **Table 6.6**.

Table 6. 6. Geometrical characterization of FRS used for mechanical testing. Values are expressed as mean value ± standard deviation, calculated on 3 samples for each sintering group.

	Sintering Temperature /°C					
	600	**650**	**700**	**750**	**800**	**850**
Mean Diameter D_s /mm	8.6 ± 0.3	8.0 ± 0.6	10.6 ± 0.4	8.9 ± 0.1	9.7 ± 0.1	8.7 ± 0.5
Mean Length L_s /mm	7.0 ± 0.1	6.1 ± 0.1	6.2±0.4	6.0 ± 0.6	7.5± 0.4	6.7 ± 0.3
Cross sectional area A_s /mm^2	58.3±3.7	51.1±7.7	88.8±6.9	61.8±2.0	73.8±1.8	59.7±6.3
Mean scaffold mass m_s m/g	0.25±0.02	0.24±0.01	0.29±0.02	0.33±0.03	0.25±0.03	0.26±0.02

Numerical values resulting from the physical and structural characterization of FRS sintered at different temperatures are collected in **Table 6.7**.

Table 6. 7. Physical and structural parameters of 47.5B-based bioactive glass and glass-ceramic scaffolds sintered at different temperatures within the range of 600-850 °C.

Sintering temperature T/ °C	Apparent density ρ_s /g/cm^3	Total porosity ε_0	Maximum shrinkage ΔL_s/ %	Compressive strength σ_{max}/ MPa
600	0.62 ± 0.06	0.76 ± 0.2	24	0.49 ± 0.08
650	0.72 ± 0.07	0.72 ± 0.03	28	1.02 ± 0.44
700	0.41 ± 0.02	0.85 ± 0.01	27	1.47 ± 0.09
750	0.87 ± 0.03	0.67 ± 0.01	18	1.93 ± 0.06
800	0.47 ± 0.01	0.82 ± 0.01	21	1.61 ± 0.29
850	0.71± 0.03	0.73 ± 0.01	29	2.09 ± 1.02

As expected, higher sintering temperatures led to an overall improvement in compressive strength, attributable either to viscous flow sintering or the concomitant development of crystalline species within the amorphous matrix, according to the specific sintering group considered.

Interestingly, fully amorphous 3D structures treated at 600 °C revealed a compressive strength value comparable to that of 45S5 glass-ceramic scaffolds sintered at higher temperatures produced by the same technique (σ_{max} = 0.3-0.4 MPa) [214]. This important achievement is directly related to the high sinterability of the glass selected in the present study for the realization of 3D struts, as a further proof of its suitability as basic material for the production of highly densified amorphous struts for bone substitution.

The increase in compressive strength observed in the temperature range of 600-750 °C followed a highly linear trend with R^2 coefficient equal to 0.9986. However, a drop in mechanical properties was observed at 800 °C, probably related to the decrease in structure density. However, even including the samples treated at 800 and 850 °C, the overall strength-T_s relationship still remains linear with R^2 = 0.8393 (**Figure 6.11**).

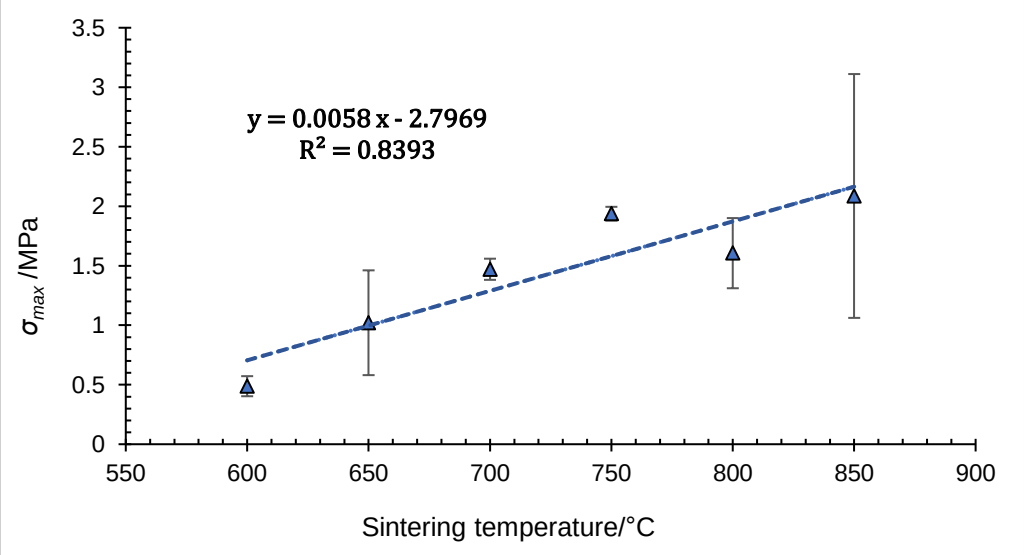

Figure 6. 11. Compressive strength of 47.5B glass and glass-ceramic scaffolds as a function of the sintering treatment.

Despite the higher sintering temperature, it should be noticed that the total porosity of scaffolds sintered at 800 °C was remarkably higher with respect to the sample treated at 750 °C, but comparable to that treated at 700 °C, for which a similar compressive resistance was observed. This suggests that both porosity features and scaffolds architecture play a predominant role in defining the mechanical behavior of the scaffolds under compressive loads, as compared to the development of crystalline phases.

This latter aspect will provide food for thought in the comparison between 47.5B-based 3D porous scaffolds produced by different manufacturing technologies, as gradually discussed in the chapter.

6.3 From stale bread to dolomite quarry debris: a contribution to the development of highly-sustainable scaffold manufacturing strategies minimizing industrial waste

In the frame of this Ph.D research work, two novel strategies for the development of highly-sustainable BG-based scaffold have been developed using 47.5B glass as basic material. In particular, stale bread coming from industrial wastes was used as a novel sacrificial template to produce bioactive glass scaffolds by replication method, while dolomite quarry debris were used as foaming agent to produce BG porous and interconnected foams upon thermal decomposition of carbonates.

In both cases, well established technologies, abundantly described in literature (i.e. foam replica methods, glass foaming) have been combined with easily accessible waste materials at the end of their commercial life cycle, resulting in an interesting and useful contribution to alimentary waste disposal and development of transversal, highly-sustainable and cost-effective approaches for the manufacturing of artificial bone substitutes.

6.3.1 Bread-templated scaffolds

The starting point for this activity was the strong conviction that, despite progress in biomedical and engineering field is often associated to high cost and advanced technologies, sometimes, as already happened in the past, it is possible to make a difference by simply reinventing something “old” into something completely different from its original intended use.

The suitability of a scaffold for BTE applications greatly relies upon its structural and microstructural parameters, as widely discussed in Paragraph 6.2. Moreover, when the production of the scaffold is based on the reproduction of a certain sacrificial template, of course the characteristic of the selected porous material will dictate the morphological features of the final structure.

Almost everybody is familiar with a common slice of bread, but how many can say they know its porous architecture at the micro-scale?

In a very preliminary phase of the study, SEM morphological analyses were carried out on different bread samples in order to select the best one showing greater potential for BTE applications, according to the minimum requirements listed and discussed in Chapter 1.

In general, an open-cell porous architecture, with pore size and distribution potentially suitable for BTE scaffold production was observed. However, the most relevant issue concerning the selected template was directly related to the origin of porosity within a given volume. It is known indeed that bread crumb porosity is the result of a natural process, known as leavening, and thus, hardly controllable, especially in home-made processes.

Hence, it was decided to compare the morphology of both homemade and industrial bread, in order to select the template with the most regular and reproducible 3D architecture (Figure 6.12).

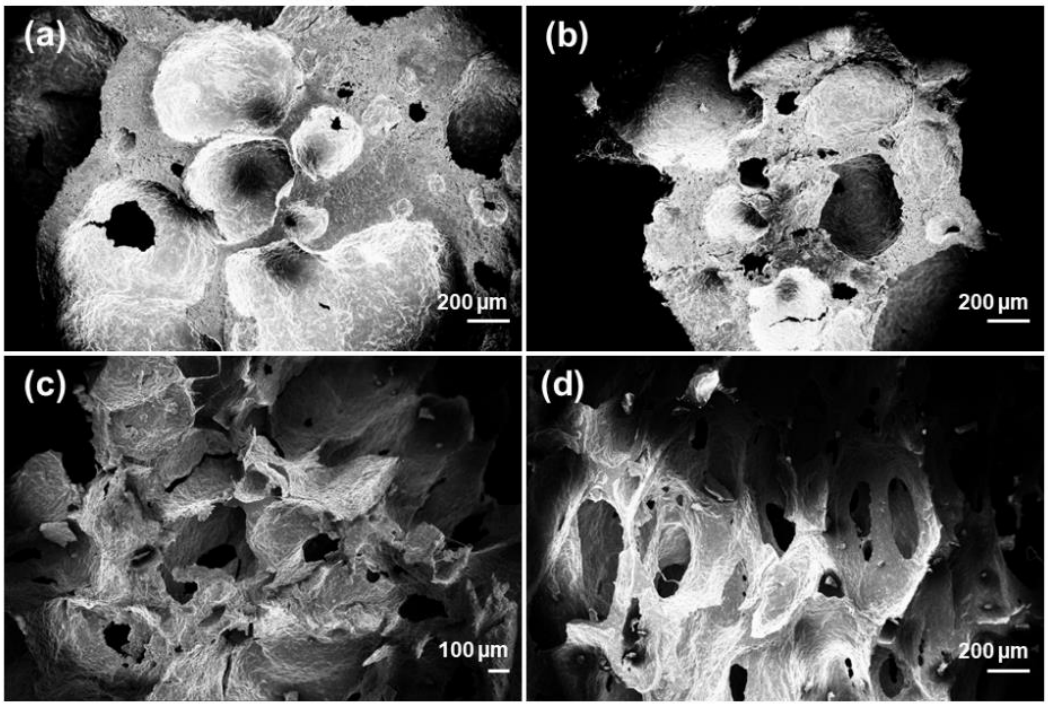

Figure 6. 12. SEM micrographs of home-made bread (a-b) and industrial bread (c-d).

As can be seen, home-made bread was characterized by a sort of bubble-like morphology (Figure 6.12 a-b), similar to that typical of scaffolds produced by foaming methods [324]; however, low inter-pore connectivity and irregular pore size (lack of reproducibility), led to role out this option. On the other hand, industrial bread slices (those commercialized in packaged formats) revealed a trabecular morphology almost resembling that of trabecular bone, with a more regular pore size and shape, and pores homogeneously distributed and interconnected (Figure 6.12 c-d). Large macropores within 100-300 µm and smaller ones between 10-20 µm can be seen, which are definitely within the reference ranges for trabecular bone [50]. Therefore, expired commercial bread, not suitable for sale, was selected as a sacrificial template for this study.

Sponge replica method was properly revised to adapt the process to the new organic template. Particular efforts were dedicated to the design of a suitable strategy to preserve the template integrity upon soaking, avoiding the collapse of the structure and the closure of porosity caused by the excessive weight of the liquid on the crumb struts.

This issue was addressed by acting on two different fronts:

A preliminary drying process was performed in order to confer higher stiffness to the template;

The composition of the slurry was optimized in order to reduce the viscosity of the slurry and facilitate its permeation within the pores in the shortest possible time.

Considering the compositions reported in Table 4.1, the winning strategy was definitely represented by the decrease of PVA from 6 wt.% to 1 wt.%. Green bodies indeed revealed a homogeneous distribution of the glass slurry in the whole volume of the bread cuboid, without obstructing peripheral pores.

XRD patterns of the as-quenched glass and powdered scaffolds after sintering (Ts= 750 °C, 3h) are compared in Figure 6.12.

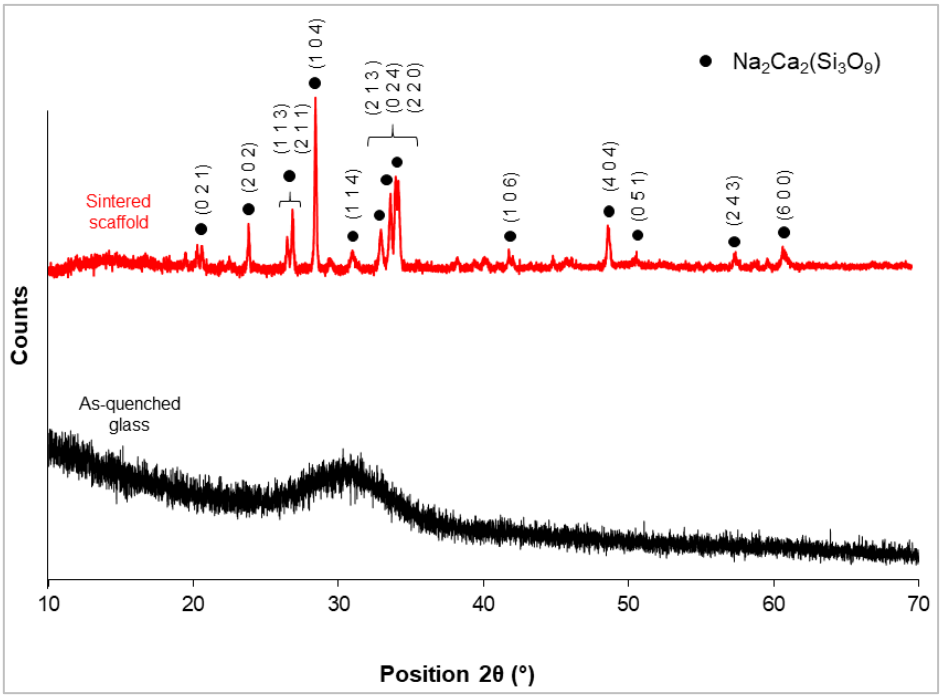

Figure 6. 13. XRD patterns of as-quenched 47.5B bioactive glass (black) and sintered powdered scaffold (red).

As expected, the XRD pattern of the sintered scaffolds exhibited sharp diffraction peaks associated to the devitrification of the system upon sintering, consistently with what previously reported.

The sintering temperature in fact, was deliberately chosen above the crystallization onset to achieve adequate mechanical properties for BTE applications by inducing the nucleation of crystalline phases (combeite, $Na_2Ca_2Si_3O_9$, PDF code: 01-078-1648) within the amorphous matrix.

In **Figure 6.14**, the SEM micrographs related to BDS obtained by varying the slurry composition are collected.

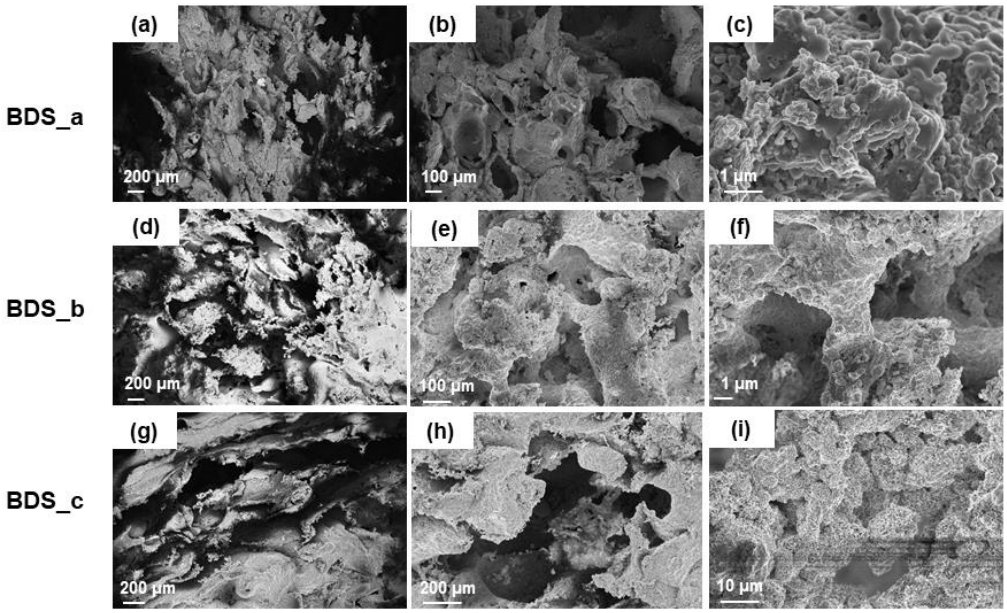

Figure 6. 14. SEM morphological analyses performed on BDS-a (a-b-c), BDS-b (d-e-f) and BDS-c (g-h-i) scaffolds at different magnifications.

The total porosity assessed by gravimetric value was between 70-85 vol.%, with no significant differences observed among the three groups (*BDS-a*, *BDS-b* and *BDS-c*). These values definitely lie in the upper range of those of human trabecular bone. However, upon sintering, all the scaffolds underwent important morphological modifications with respect to the original organic template, especially in terms of pore size distribution and interpore connectivity. In addition, significant morphological differences can be observed among the three systems analysed.

Scaffolds belonging to the system b and c, indeed, were characterized by a highly irregular surface and disorganized porous structure. By analysing the 2D cross-section, important voids within the structure were observed, potentially able to negatively affect the mechanical performance of the scaffold upon implantation. Despite this, it was difficult to define the degree of interconnectivity between adjacent pores. It is possible that such voids resulted from a poor/suboptimal impregnation of the template, responsible for the absence of material in the core of the structure.

On the contrary, BDS-a samples, successfully preserved the morphology of the original template, despite a reduction in pore size was observed as a result of both the densification of the strut upon sintering and the volume reduction upon drying, previously discussed in **Chapter 4**. Despite this, pore size assessed by SEM analysis was found to be still within the minimum range required for BTE applications, with inter pores windows defined between 20 and 100µm, potentially suitable for allowing cell migration and neovascularization within the graft [221].

At higher magnifications (Figure 6.14 c-f-i), all the scaffolds exhibited the same wrinkled surface of the original template, regardless of the slurry composition. Such a micro-texture could even be beneficial to cell-device interactions. In fact, it is

known that micrometric roughness on the implant surface can promote protein-mediated cell adhesion [325], thus leading to a faster osteointegration.

In the light of these preliminary findings, samples belonging to the BDS-a system were selected to be further investigated in terms of *in vitro* bioactivity and mechanical properties as the most promising among the three systems.

Mechanical characterization of the scaffolds obtained from BDS-a slurry, with total porosity of 72±1.47 vol.%, mediated on 4 samples, revealed a compressive strength of 0.62 ± 0.2 MPa, which fells within the lower range reported for human trabecular bone (0.1-16 MPa [50]).

The compressive strength of bread templating scaffolds was interestingly found to be twice that of PU-derived glass-ceramic 45S5 Bioglass® foams proposed by Chen et al. in 2006 [150]. However, compared to *FRS* sintered at the same temperature, characterized by analogous total porosity values (72 vol.% and 67 vol.%, respectively), the use of stale bread as sacrificial template led to a significant deterioration of the mechanical performances of the final structure.

The stress strain curve depicted in **Figure 6.15** revealed the typical behaviour of a cellular ceramic, characterized by a multi-peak trend related to multiple fractures events occurring during the compression test [326].

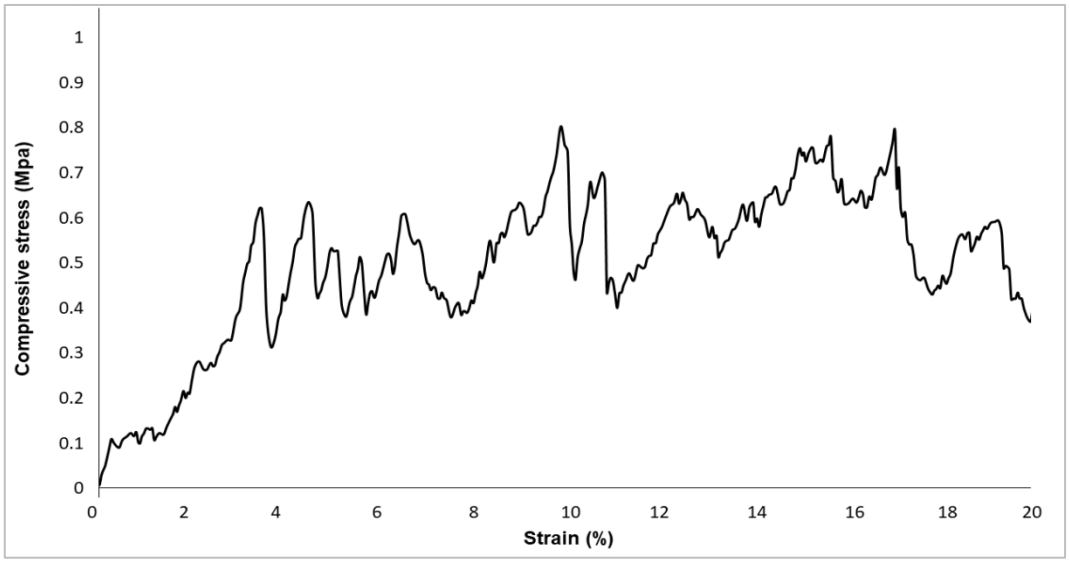

Figure 6. 15. Typical stress-strain curve related to BDS_a scaffold.

The hydroxyapatite (HA) forming ability of BDS-a samples was assessed by static soaking tests in Simulated Body Fluid (SBF) up to 7 days.

The pH variation observed over time is graphically presented in **Figure 6. 16**.

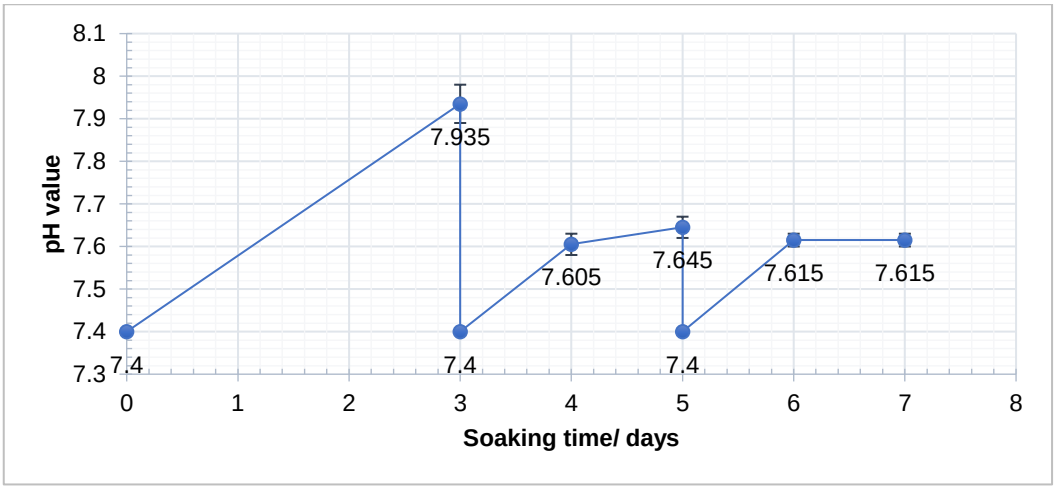

Figure 6. 16. Bioactivity assessment of BDS-a samples in SBF: pH values at different time points.

The ramps between each time point indicate the increase of pH associated to the release of ions from the surface of the scaffold to the solution, consistently with the *in vitro* bioactivity mechanism typical of silica-based bioactive glasses [107]. The drop of pH observed every 48 h-72 h, instead, was due to the complete replacement of the solution, performed to simulate fluid recirculation in physiological conditions.

A sustained increase of pH up to 7.935 ± 0.045 was observed within the first 3 days-soaking as a result of the rapid ion exchange between the glass-ceramic surface and the external environment.

In these regards, it was demonstrated that the viability of osteoblastic cell line is deeply influenced by the acidity of the culture media in which they are grown; thus, several research groups investigated the effect of alkaline pH environments on osteoblast activity. Among these, Galow and coworkers characterized cell differentiation and osteoblastic cell function both at pH 7.4 (physiological conditions) and under alkaline conditions (pH= 7.8 and pH= 8.4) up to 2 weeks. In particular, it was found that under alkaline conditions, the expression of ATF4 and DMP1 were significantly upregulated. In particular, DMP1 is an important marker indicating the transition from osteoblasts to osteocytes and thus, indicate a faster differentiation and maturation process [294].

Thus, while in the presence of acidic environments autophagy and apoptosis increased significantly [327], elevated pH could be beneficial for the cultivation of bone cells and may also provide therapeutic value in bone regeneration therapies.

Up to day 5, pH continued to increase with a lower slope up to 6.645±0.025. After the last refresh, pH continued to slowly increase, reaching a plateau after about 24 h. The average value at the end of the test was 7.615 ± 0.015.

Compared to 47.5B-32 (**Figure 5.27**, **Chapter 5**), the pH value measured after 1 week-immersion was markedly lower, due both to the greater surface exposed by free powders, which increases the number of reaction sites available for ion exchange, and the presence, in sintered scaffolds, of crystalline phases improving the chemical stability of the material in physiological environment.

Despite the partial devitrification of the system upon heating, scaffolds obtained by the replica of stale bread preserved the exceptional apatite-forming ability of the original glass, as can be seen in **Figure 6.17**.

After just 48 h (Figure 6.17 a-b-c), the scaffold surface appeared to be covered by a thick silica gel layer (with its typical cracks), on which calcium phosphate globular aggregates were already visible; after 1 week (Figure 6.17 c-d-e), HA aggregates with the characteristic cauliflower morphology completely covered the scaffold surface, thus indicating the continuous evolution of the reaction layer resulting from ion exchange between the scaffold and the SBF. At the nanometric scale, globular aggregates were characterized by typical acicular crystals (Figure 6.17 f)

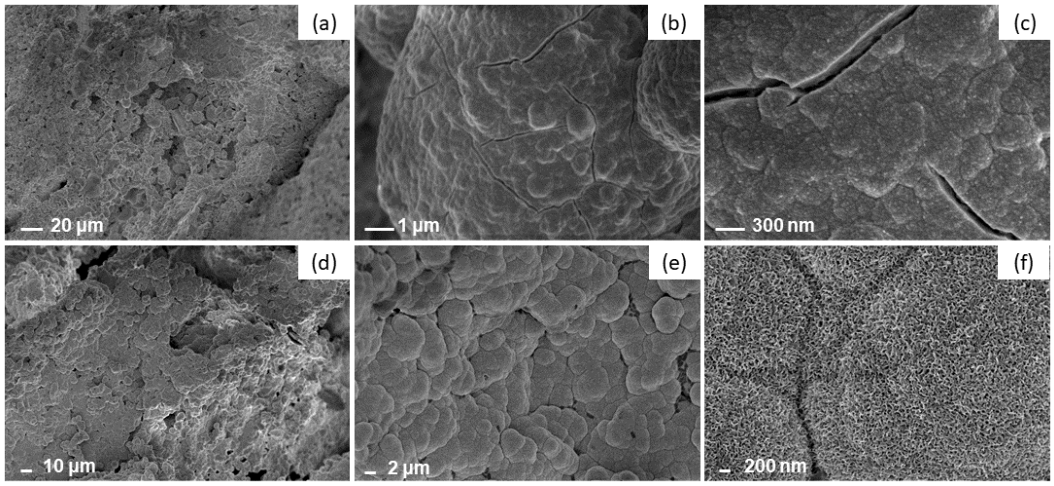

Figure 6. 17. Surface evolution at different magnifications after 48h (a,b,c) and 1 week (d,e,f) in SBF.

EDS surface analysis confirmed the progressive deposition of Ca and P on the scaffold surface, compared to the sample analyzed at the beginning of the test, confirming the progressive growth of an HA layer at the interface with the simulated biological environment. After 7 days soaking, the Si peak completely disappeared from the EDS spectrum indicating that the scaffold surface had been completely covered by a thick layer of globular HA (**Figure 6.18**) and, as a result, it was possible to quantify the Ca/P molar ratio without signal interferences coming from the surface of the underlying silica glass-ceramic material.

At the end of the test, the Ca/P molar ratio mediated on 5 different areas of the sample surface was 1.14 ± 0.13, still far from the stoichiometric one of 1.67.

Calcium-deficient HA is actually quite common on the surface of bioactive glasses and analogous results have been already reported in previous literature [138]. It is strongly believed that a further increase of the Ca/P ratio is likely to be observed by extending the duration of the test up to 14–21 days, as already done in a previous work on 3D-printed glass scaffolds based on the same compositional system [190], [219].

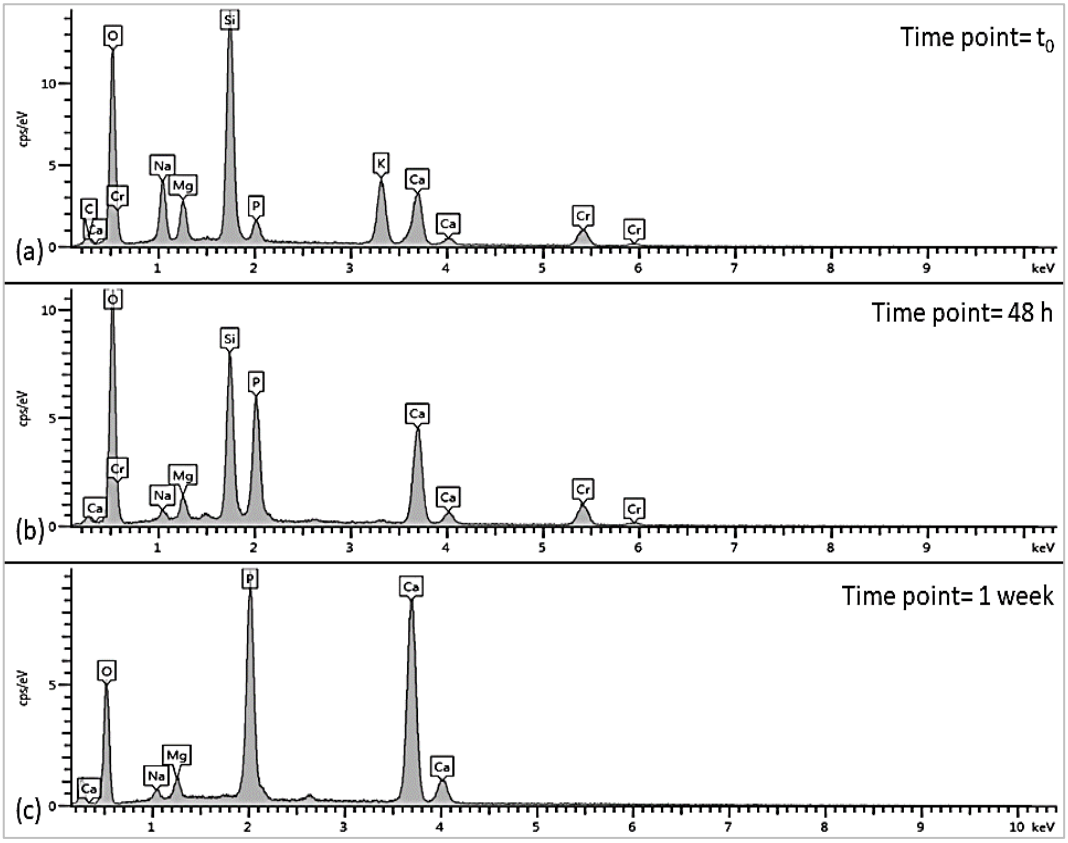

Figure 6. 18. EDS spectra of the scaffold's surface before in vitro bioactivity tests (a), after 48 h- (b) and after 1 week-immersion in SBF(c).

6.3.2 Dolomite-foamed scaffolds

As a further contribution to the wide world of scaffolds manufacturing, here glass-based foams for TE applications were produced using dolomite quarry debris (Ca Mg $(CO_3)_2$) as a foaming agent to obtain a porous and interconnected 3D structure for potential bone replacement in small-to-mid size bone defects.

Although the suitability of dolomite as foaming agent has been already demonstrated in a previous study, in which glass foams were successfully obtained from waste materials [218], in biomedical field the technique has never been used before.

The generation of macropores within the structure basically relies on the process of thermal decomposition of dolomite powders at high temperatures. Upon heating, the thermal reaction produces gaseous CO_2, as main product, as well as additional small amounts of calcium and magnesium, according to **Equation 6.1**, **6.2**:

$$CaMg(CO_3)_2 \leftrightarrow CaCO_3 + MgO + CO_2 \qquad \textbf{6.1}$$

$$CaCO_3 \leftrightarrow CaO + CO_2 \qquad \textbf{6.2}$$

The choice of the thermal treatment selected for inducing the thermal decomposition of carbonates was based on previous DTA measures performed on Ca Mg $(CO_3)_2$ powder. The thermographs revealed the presence of two different endothermic peaks, located at 800 °C and 890 °C, associated to **Equation 6.1** and

6.2, and corresponding respectively to the thermal decomposition of magnesium carbonate and calcium carbonate [218], [328].

According to the reactions reported above, the choice of dolomite as foaming agent for the production of scaffolds intended for bone regenerative applications is potentially intriguing on multiple fronts. In fact, on one side, the production of gaseous CO_2 is involved in the formation of the interconnected porous architecture of the scaffold, thus determining its mechanical behavior and mass transport properties. The second relevant aspect concerns the release of additional amounts of CaO and MgO, which could enter the glass network, modifying its chemical stability and improving its dissolution behavior in the physiological environment. Moreover, as comprehensively reviewed in **Chapter 5**, both Mg^{2+} and Ca^{2+} are bivalent cations actively involved in the metabolic activity of bone tissue and, when released from the surface of bioactive glasses, beneficially interact with osteoblastic cells, stimulating regenerative pathways and bone self-repair [238].

More specifically, Ca is known to increase osteoblast proliferation, differentiation and ECM mineralization, while triggering the secretion of growth factors, i.e. IGF-I and IGF-II, which are fundamental for bone metabolism [238]. Moreover, additional amounts of Ca could determine an increase in the Ca/P ratio within the glass composition, thus positively affecting the HA forming ability of the material in physiological environment, analogously to what observed in the first bioactive composition 45S5, characterized by a high Ca/P ratio and exceptional bioactive potential [109]. On the other hand, magnesium has a positive effect on cell adhesion because of the beneficial interaction between integrins and magnesium ions [238].

SEM images of the cross section of dolomite-foamed scaffold (*DFS)-800* and *DFS-850* at different magnifications are collected in **Figure 6.19**.

From a morphological point of view, the porous architecture observed by SEM investigation resembled the typical bubble-like structure of sol-gel foams, obtained introducing proper surfactants (i.e. Teepol) to the sol-batch in order to stabilize bubbles obtained upon vigorous agitation [166], [324]. Pore were approximately spherical, with a diameter ranging from 100 µm to 250 µm and inter-pore windows up to 50 µm. Predictably, at higher magnifications (Figure 6.19 c-f), crystalline structures, analogous to that depicted in **Figure 6.3**, were observed.

Within the volume analyzed, a quite homogeneous distribution of pores was observed in both the samples. However, upon higher sintering temperature, smaller inter-pore channels were observed. This result perfectly matched with total porosity assessment, which revealed a higher pore content in *DFS-800* compared to DF-850, of respectively 83.1 ± 2.2 vol.% and 65.5 ± 7.1 vol.%. Despite this, both the calculated values still fell within the typical ranges of trabecular bone (50-90 vol.%) [50], thus preserving their potential to be used in BTE applications.

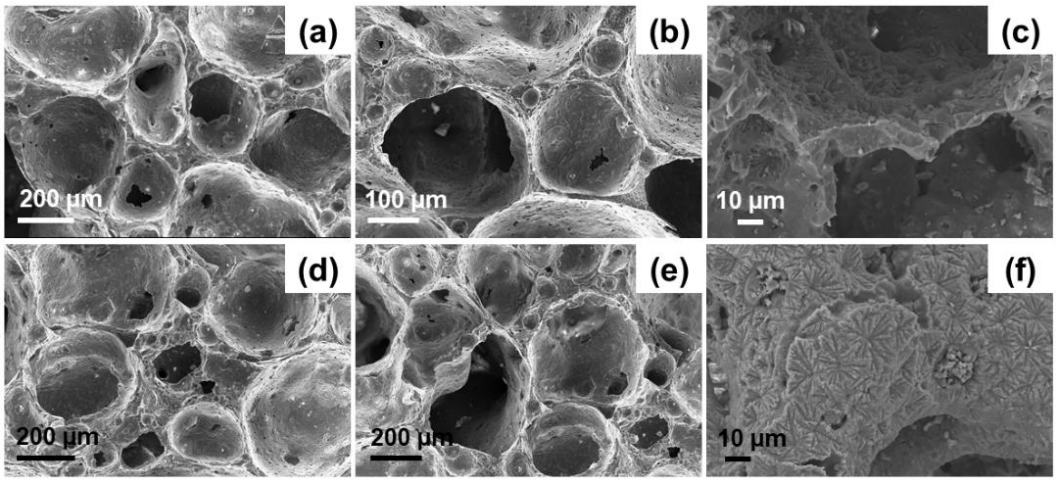

Figure 6. 19. SEM images of dolomite-foamed scaffolds D-800 (a-b-c) and D-850 (d-e-f) at different magnifications.

Apart from the characteristic elements of the base glass composition (Mg, Ca, Si, Na, P, K and O), carbon was detected in both the scaffolds analyzed, likely indicating the uncomplete conversion of dolomite upon thermal treatment. Despite this, no traces of further impurities related to the presence of dolomite residuals (sulfur (S), manganese (Mn), aluminum (Al) or others) were found. In part, this could be attributed to the EDS detection threshold, as in the case of Mn and Al. However, even if present in small quantities, no adverse effects on BG-properties and bone regenerative potential are expected.

In fact, Al_2O_3 is commonly added to BG-based products to improve their mechanical resistance under compressive loads and elastic modulus, with no relevant adverse cytotoxic effects on cells [329]–[331].

In addition, several studies demonstrated that the addition of divalent cations such as manganese (Mn^{2+}) has a concentration-dependent influence on the integrin affinity to ligands, cell adhesion to extracellular matrix proteins, tissue ingrowth inside the graft and its osteointegration [332].

Interestingly, in 2014, Miola and coworkers [333] modified a bioactive glass belonging to the same system of 47.5B introducing different amounts of MnO. Compared to the undoped systems, MnO-containing glasses led to enhanced expression of alkaline phosphatase (ALP) and bone morphogenetic proteins (BMPs), revealing a great promise in bone regenerative applications.

Regarding S, the thermal decomposition of sulfur (VI) oxide SO_3, originally present in dolomite powders, is an oxygen-generating decomposition reaction that proceeds above 227 °C, reaching higher conversion kinetics above 727 °C, preferably in the presence of a proper catalyst (usually noble metals and some transition metal oxides) [334]. Thus, the temperature used for scaffolds sintering were sufficiently high to justify the absence of S within the material.

The residual amount of C was lower in the *DFS-850* (6.8 wt .%), due to the more advanced stage of reaction compared to *DFS-800* (8.8 wt .%).

This result definitely matched with XRD analysis.

In **Figure 6.20**, the XRD patterns of dolomite, 47.5B glass and powdered scaffolds sintered at different temperatures are collected.

A direct comparison between the XRD pattern of pure dolomite with those of *DFS-800* and *DFS-850* allowed to detect the presence of the main peak of CaMg $(CO_3)_2$ in the diffraction patterns of the sintered scaffolds in correspondence of a 2θ value of 31.2°, thus explaining the presence of carbon in the EDS elemental analysis.

Consistently with SEM observations, XRD patterns referred to *DFS-800* and *DFS-850* showed the presence of diffraction peaks associated to the crystalline phase $Na_4Ca_4(Si_6O_{18})$ (ref. code: 01-079-1089), in perfect agreement with what reported in our study about bread-derived glass-ceramic scaffolds sintered at 750 °C.

In theory, it would be possible to achieve the full decomposition of dolomite by increasing the sintering temperature above 850 °C; however, it is strongly believed that sintering at higher temperatures might be an inconvenient strategy for the intended purpose as the progress of the crystallization process may led to a dramatic suppression of the bioactivity of the glass and the porosity of the overall structure (as demonstrated for *FRS* sintered at 850 °C). In addition, higher sintering temperatures might cause an increase in the stiffness of the structure as consequence of crystals growth, thus creating an excessive mismatch between scaffold and bone properties.

Thus, in order to achieve a proper balance between morphological/structural properties, sintering /crystallization behavior and apatite forming ability, T = 850 °C was deliberately selected as maximum sintering temperature for the present study; however further studies deserve to be performed in order to evaluate the cytocompatibility of our devices [129], [262].

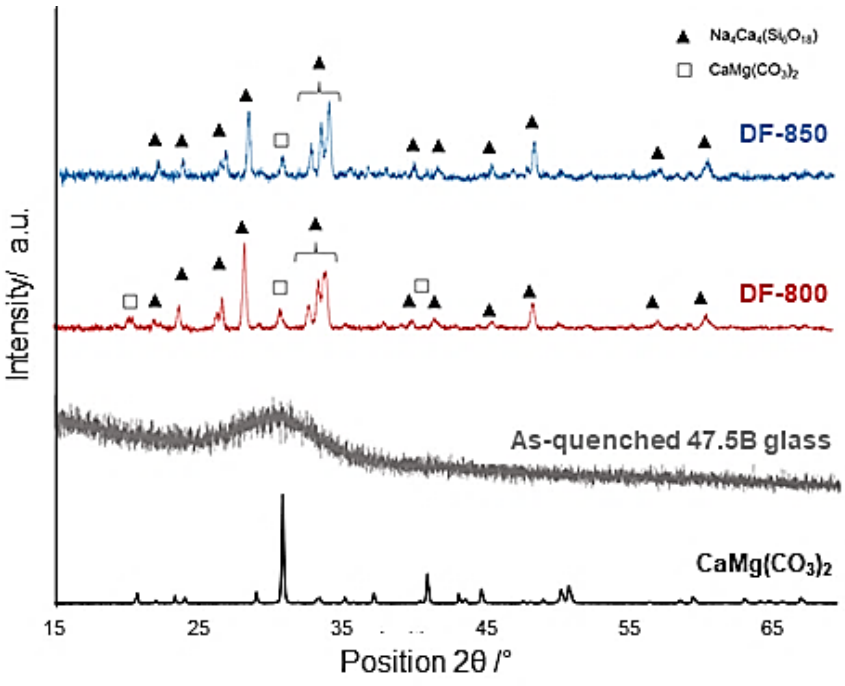

Figure 6. 20. XRD patterns of pure dolomite (black), 47.5B glass (grey), D-800 (red) and D-850 (blue) powdered scaffolds.

More specifically, further studies should be addressed to the determination of dolomite effect on bone cells. In this regard, it is worth mentioning that bone response to dolomite and its osteogenic potential were previously studied in a rat calvarial model by Moreschi et al. [335], who observed a moderate inflammatory response with no osteoconductive activity. Despite this apparently negative results, the bone repair process appeared to be favored in the presence of dolomite compared to the negative dolomite-free control [335].

Figure 6.21 shows a couple of examples of stress-strain curves related to *DFS-800* (Figure 6.21 a) and *DFS-850* (Figure 6.21 b) scaffolds.

Both the curves are characterized by the typical trend of a cellular ceramic material, with several peaks associated to multiple fractures that occurred upon compression until collapse was achieved by brittle crushing, according to the Ashby's model [336]. Furthermore, these curves were definitely comparable to the stress-strain curve obtained for *BRS-a* samples, depicted in **Figure 6.15**.

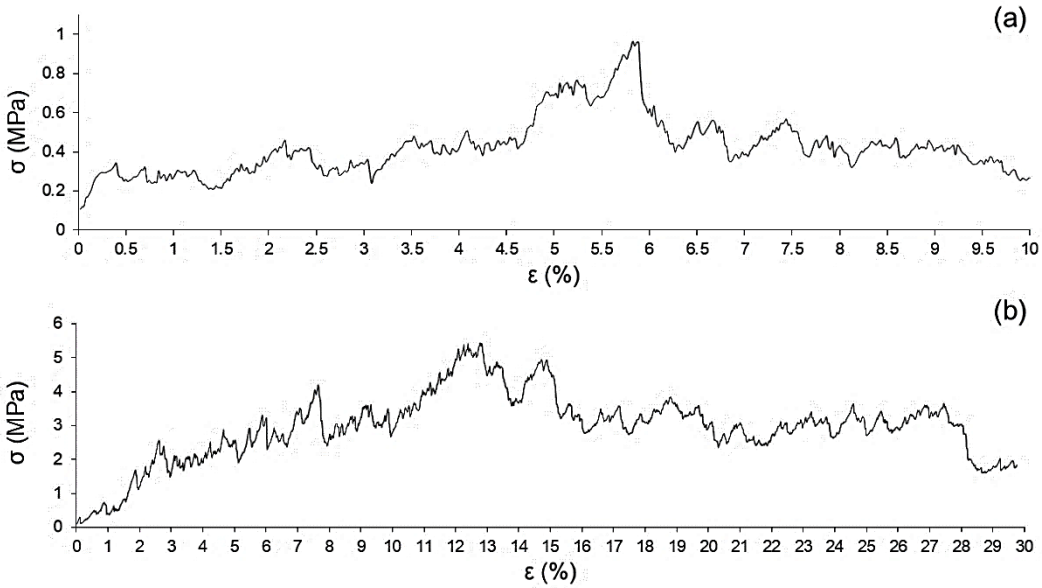

Figure 6. 21. Stress-strain (σ-ε) curve of dolomite-foamed scaffolds sintered at 800 °C (a) and 850 °C (b).

A summary of the structural features of dolomite-foamed scaffolds produced in this study compared to the reference ranges of human trabecular bone (each range was defined by considering different anatomical sites) is provided in **Table 6.8**.

Table 6. 8. Structural parameters of *DFS* compared to human trabecular bone.

Sample	**Apparent Density ρ_s/ g/cm^3**	**Porosity ε_0/ vol.%**	**Compressive strength σ_c/ MPa**
Trabecular bone	0.18 – 0.56 [337]	50 – 90 [50]	0.1 – 16.0 [50]
DFS-800	0.45 ± 0.050	83.1 ± 2.2	1.3 ± 0.4
DFS-850	0.91 ± 0.17	65.5 ± 7.1	3.9 ± 0.9

All the parameters reported showed compatible values to that of human trabecular bone, thus further confirming the potential suitability of glass-ceramic scaffolds obtained by dolomite foaming for TE applications.

It is reasonable to attribute the better σ_c of *DFS-850* scaffolds (3.9 ± 0.9 MPa) both to the higher crystalline content and the improved densification achieved upon heating. Despite the compressive tests performed on *DFS-800* yielded σ_c = 1.3 ± 0.4 MPa, which is one third than that of *DFS-850*, this value is still above the lower limit of human trabecular bone (0.1-16 MPa [50]) and remarkably higher than the results reported for foam-replicated 45S5 Bioglass® scaffolds (0.2-0.4 MPa) [150].

It is interesting to notice that, both the dolomite-foamed and the PU-replicated scaffolds treated at 800 °C, exhibited a total porosity around 80.0 vol.% and a comparable compressive strength of 1.3 ± 0.4 MPa and 1.6 ± 0.3 MPa, respectively. On the other hand, considering a sintering temperature of 850 °C, the foaming process yielded a lower total porosity of the final struts (65.5 ± 7.1 vol. %) compared to that exhibited by *FRS*, resulting in a higher compressive strength (3.9 ± 0.9 MPa).

The variation of pH as a function of the soaking time in SBF is plotted in **Figure 6.22**.

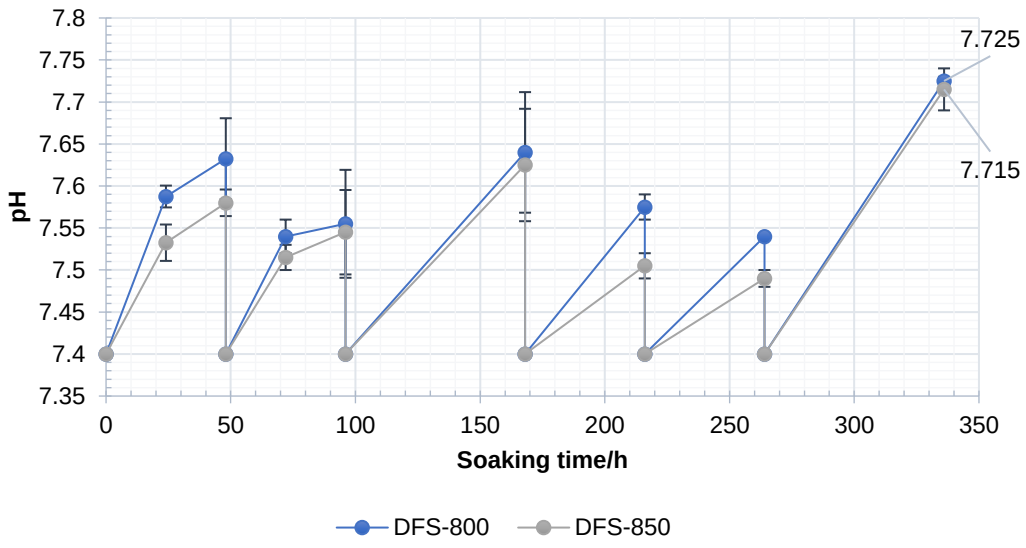

Figure 6. 22. Bioactivity tests in SBF: pH variation as a function of the immersion time (a); SEM surface evaluation of D-800 (b-c-d) and D-850 (e-f-g) scaffolds after immersion in SBF at different time points.

The curves obtained for *DFS-800* and *DFS-850* scaffolds showed comparable trends upon soaking.

No problems of pH-related toxicity induced by the materials are forecast, as the maximum value of pH reached upon soaking was around 7.7 for both scaffolds, which could be even beneficial to the synthesis of new bone matrix by osteoclastic cells [338].

The apatite-forming ability of *DFS* was good, without being affected by the high sintering temperatures and the devitrification of the system at all (**Figure 6.23**). In these regards, despite the crystalline content was supposed to be higher in scaffolds sintered at 800 and 850 °C, the pH value at 1 week registered for DFS was slightly higher compared to that observed for *BRS* sintered at 750 °C. Although this difference can be almost neglected, a probable cause could be the presence of a large number of smaller pores in *DFS* resulting from foaming and likely determining a larger exposed surface of the scaffold. Moreover, as concerns SBF refresh, it was carried out with some differences between the two sample sets due to laboratory organizational needs and it is not possible to exclude *a priori* an effect of such a change on the observed final result.

After just 48 h-immersion, the surface appeared to be covered by a thin carpet of HA, below which a cracked reaction layer of silica gel was clearly visible (Figure 6.23 a-d). Small globular aggregates were observed also onto the inner surface of the pores, suggesting a good permeation of the fluid within the whole volume of the scaffold and, thus, a good interpore connectivity degree.

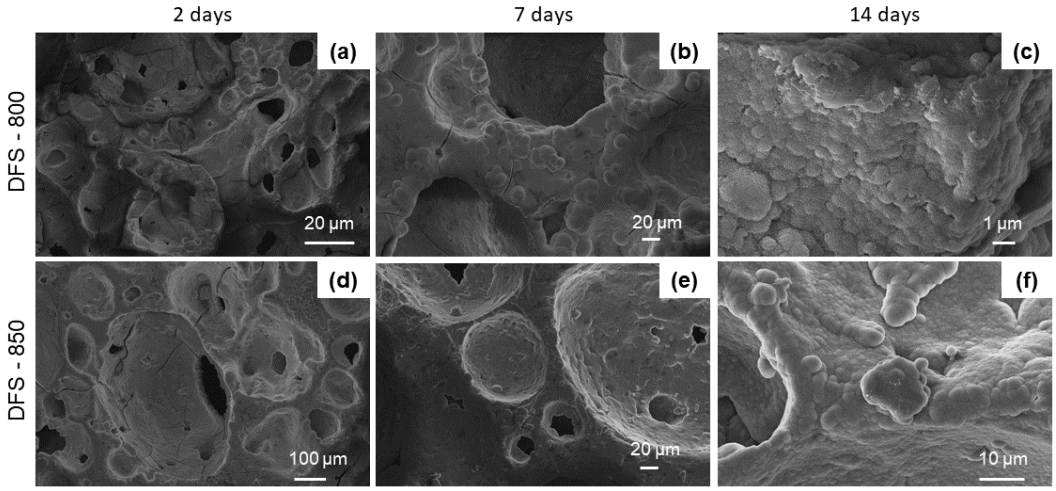

Figure 6. 23. Bioactivity tests in SBF: evolution of the scaffold surface upon soaking at different time points.

An increasing number of globular agglomerates could be observed after 7 days (Figure 6.23 b-e) as a proof of the continuous ion exchange between the glass and the solution and the progress of the bioactivity mechanism over time.

After 2 weeks, the surface of the scaffolds appeared to be completely covered by a homogeneous layer of globular HA characterized by its typical cauliflower morphology (Figure 6.23 c-f).

For direct comparison, **Figure 6.24** shows a detail of the HA nanostructure grown on the surface of both *DFSs*, totally comparable, both in morphology and dimension of the globular aggregates, to that observed after 1 week on the surface of *BRS*.

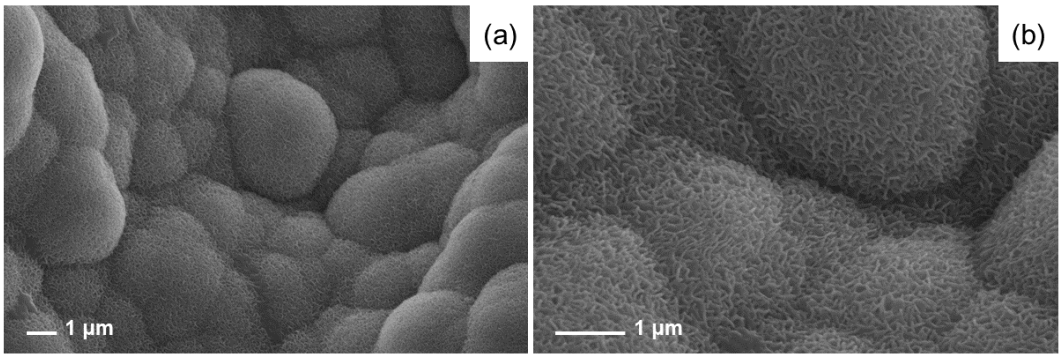

Figure 6. 24. Acicular nanostructure (b) of globular HA (a) observed on the surface of DFSs after 1-week immersion in SBF.

At the nanoscale level, HA globular aggregates presented the same acicular morphology observed after 1 week

Semi-quantitative EDS analyses of the scaffold surface revealed an increase of the Ca/P molar ratio over time up to 1.60 and 1.56 for *DFS-800* and *DFS-850* samples, respectively, definitely close to the stoichiometric one of biological HA (1.67). This indicates an advanced stage of the conversion reaction of the glass surface to HA, which might result in a better interaction between the scaffold and the host tissue due to the higher similarity to the calcium-phosphate mineral phase of bone.
Analogously to what observed for bread-templating scaffold, the Si peak completely disappeared after 1-week immersion in SBF, thus indicating that the surface of the scaffolds was completely covered by a thick layer of HA.

These results were finally confirmed by XRD analyses.
As a further proof of the good apatite-forming ability of the scaffolds, diffraction patterns of *DFS-800* (**Figure 6.25**) and *DFS-850* (**Figure 6.26**) samples immersed up to 7 and 14 days in SBF were compared to that of the starting material, indicated by t_0.

The XRD patterns related to the two systems analyzed evolved following a comparable trend, consistently to what previously observed by SEM analysis. Diffraction peaks identifying crystalline phases within the scaffold were nearly no longer visible after 1-week immersion in SBF, while a broad peak can be detected at around 32° ((211) major reflection of HA), as well as the presence of a halo between 20-30° associated to the formation of the reaction layer of silica gel.
After 2-week immersion in SBF, the major peak of HA becomes a bit shaper and a secondary peak appears at 26.2°, corresponding to the (002) reflection of HA [339].

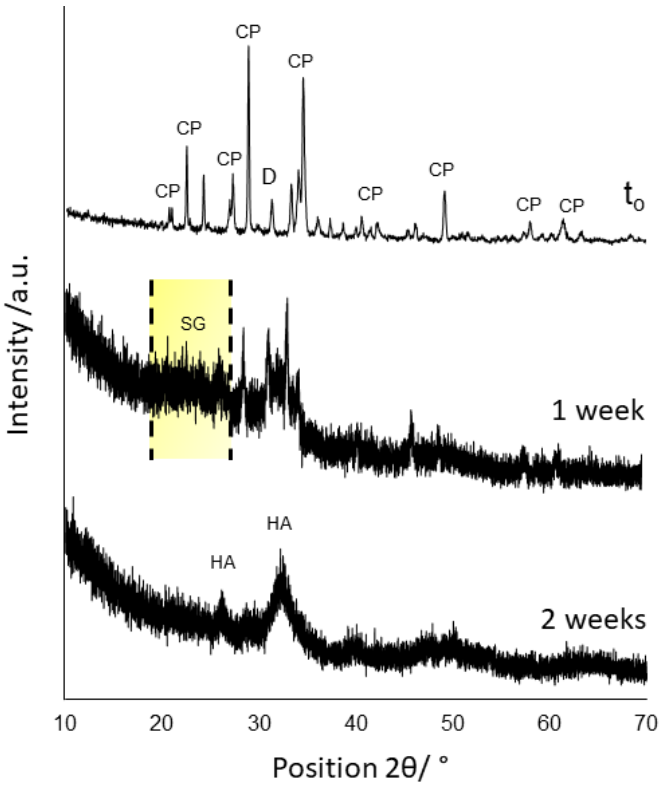

Figure 6. 25. XRD patterns of *DFS-800* soaked in SFB at different time points. CP = crystalline phase ($Na_4Ca_4(Si_6O_{18})$) of sintered glass-ceramic scaffold; D = residual dolomite; SG = halo associated to the silica gel layer; HA = hydroxyapatite.

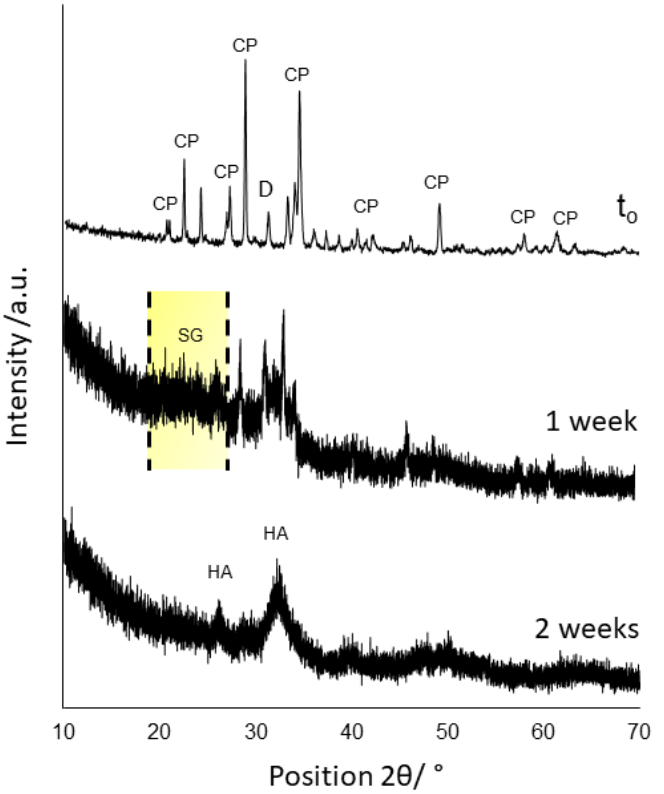

Figure 6. 26. XRD patterns of *DFS-850* soaked in SBF at different time points. CP = crystalline phase ($Na_4Ca_4(Si_6O_{18})$) of sintered glass-ceramic scaffold; D = residual dolomite; SG = halo associated to the silica gel layer; HA = hydroxyapatite.

Taken together, EDS, SEM and XRD data of *DFS-800* and *DFS-850* performed after *in vitro* bioactivity tests suggest no significant influence of the sintering treatment on the HA-forming ability of samples, as HA deposition kinetics and morphological features were comparable in both the systems analyzed.

6.4 Melt-derived vs sol-gel grid-like scaffolds produced by robocasting technology

Dealing with health sciences, the reliability and reproducibility of manufacturing processes, as well as the necessity to achieve an accurate control on the characteristic of the final device, are considered moral imperatives to guarantee a safe and effective medical treatment to the patient. However, traditional scaffolds manufacturing processes are not always able to fully satisfy these important requirements, thus leading to a growing gap between experimental and clinical practice.

Of course, the introduction of solid freeform fabrication technologies (SFF) in the early 80's constituted an important turning point in TE field, allowing an easy tailoring of scaffold's properties by acting on process parameters [81].

In particular, the high control on porosity, pore size and interpore connectivity achievable by additive manufacturing, allows, *inter alia*, to tune the mechanical properties of the device according to the final destination site, minimizing operator-dependent tasks, which are efficiently replaced by dedicated instruction scrips and properly design execution software.

This certainly shows a great promise for large-scale production at industrial level, where high reproducibility and automation of processes are strictly required.

Among all the available SFF techniques, robocasting (see **Chapter 2**) is probably the most common and powerful direct ink-writing technique for the processing of glass and glass-ceramic materials and their composites.

However, compared to biocompatible calcium phosphates, derivatives and composites, the fabrication of scaffolds by robocasting becomes a bit more complex when bioactive glasses are used, due to their extreme reactivity in aqueous environment. For example, the use of 45S5 Bioglass® for ink production turned out to be quite challenging due to the excessive leaching of Na^+ and the consequent increase in pH, which remarkably hinder an efficient dispersion of solid particles within the binder solution [340].

This is even more evident when glasses are obtained by sol-gel chemical synthesis. In fact, the intrinsic porosity typical of sol-gel glasses, so beneficial to the bioactivity process, introduces further difficulties in the ink preparation process as most of the dispersing liquid portion is absorbed by the porous structure of the material, thus becoming not available for flowing.

Ben-Arfa et al. [341], [342] recently managed this issue by optimizing simultaneously the heat treatment temperature (HTT), particle size (PS), particle size distribution (PSD) and porous fraction of the powder. These features, in fact, were found to be responsible of the packing ability and the flow behavior of the ink.

In this way, scaffolds with different macro-pore sizes (300–500 μm) with solid loadings up to 40 vol.% were successfully obtained by robocasting technology starting from porous sol-gel glasses [341].

Another very common issue related to the processing of glass materials by robocasting deals with the poor stability of the amorphous network upon heating, which induces devitrification phenomena, as previously discussed in **Chapter 5**. When sol-gel glasses are used as basic materials within the ink composition, it may result in additional issues related to the effect of the high temperature treatment on the mesoporosity, which could potentially determine a dramatical decrease in the bioactivity of the system. Furthermore, considering MBGs, whose synthesis is purposely designed to produce a highly ordered mesoporous texture for drugs and biomolecules loading, this inconvenient could likely compromise the functionality of the entire system.

Within the present research work, a new and facile approach for the robocasting of sol-gel materials has been developed, basically aimed at by-passing some of the most recurrent issues related to the design of ink formulations suitable for extrusion.

In a preliminary phase, it was intended to optimize a robocasting ink using calcined sol-gel materials, specifically SG-625, SG-800 (synthetized in **Chapter 3** and characterized in **Chapter 5**), to be compared to 47.5B-32 inks, optimized in the frame of a previous research work concerning the production, by robocasting, of grid-like monoporous and graded silica-based scaffolds for BTE applications in load-bearing sites.

However, this approach would have been unsatisfactory to our original purpose, as it would have been necessary to perform an additional treatment for the thermal degradation of the binder, with the possibility to further decrease the textural properties of the starting materials, already low compared to the standards reported in literature.

Thus, it was decided to develop a new ink composition based on the use of dried gels as solid load. Although the optimization of the preparation process was initially challenging due to the very high wettability of the gel compared to the melt-derived glass used as control system, in the end it was possible to achieve suitable characteristics for extrusion through a thin nozzle.

In these regards, specific variations with respect to the original one [190], [219], were crucial to obtain a good printing outcome. In particular, mixing phase, cartridge loading and printing nozzle where opportunely changed in order to adapt the process to the different physical behavior of the gel-based ink.

Figure 6.27 shows the optical micrographs of melt-derived and sol-gel green bodies before sintering.

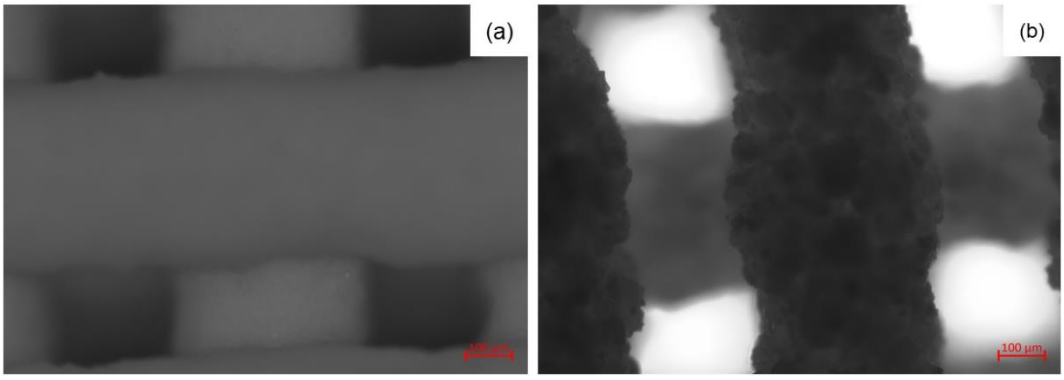

Figure 6. 27. Robocasting of melt-derived and sol-gel materials based on the 47.5B composition: a) green bodies obtained using 47.5B-32 ink and b) green bodies obtained by using DG-120 ink.

Scaffolds porosity was built by a grid-like architecture made of parallel channels with rectangular section. In this regard, no relevant differences related to the use of different printing inks were observed. Both the images, indeed, revealed high regularity. Nevertheless, it was possible to observe some bending in proximity of the contact points between overlapped layers, determining some variations in the rod cross-sectional area.

The most striking distinction between the control and the experimental ink, was in the surface appearance, definitely smoother and more homogeneous in the first case (Figure 6.27 a). The use of DG-120 based inks, on the other hand, produced a sort of grainy surface (Figure 6.27 b).

Geometrical/physical characteristic and derived parameters related to sintered robocast scaffold (*RCS)-md* and *RCS-sg* specimens are collected in **Table 6.9**.

Table 6. 9. Geometrical and physical characterization of *RCS-md* and *RCS-sg* specimens produced by robotic deposition.

Scaffold type	D_s/mm	L_s/mm	A_s/mm^2	V_s/mm^3	m_s/g	ε_0
RCS-md	4.31±0.12	4.25±0.18	14.58±0.82	61.89±2.51	0.029±0.004	0.46±0.03
RCS-sg	4.24±0.15	4.17±0.11	14.14±1.01	58.98±4.84	0.089±0.004	0.81±0.03

The starting printing code was the same for both the scaffold types and primary geometrical features, i.e. scaffold height L_s and diameter D_s were definitely comparable, with a minimum standard deviation calculated on 10 samples per each group. This actually was a further proof for the high reproducibility and reliability of the manufacturing process.

Total porosity values, instead, differ appreciably, with ε_0= 0.46±0.03 and ε_0= 0.81±0.03 in *RCS-md* and RCS-sg, respectively.
In the first case, the value obtained was in good agreement with our previous study [219] on monoporous scaffolds produced by robotic deposition, for which a porosity value of 42.5 ± 4.5 vol.% was obtained. Interestingly, compared to the previous work, some measures adopted during ink production and printing allowed to significantly lower the standard deviation, showing an improvement of the overall manufacturing process.

Despite this porosity value was very close to the minimum threshold of acceptability recommended in BTE strategies, pore size (120-130 μm) was suitable for allowing proper cell migration and vascularization of the graft. Moreover, the 3D architecture of the scaffolds, characterized by the presence of highly regular, straight channels, would be potentially able to determine a positive performance in terms of mass transport properties, as all the macropores within the structure cross the volume from side to side, constituting a linear path for fluid flow.

As discussed in the previous section, total porosity accounts both for open pores, i.e. interconnected macroscale pores, and for closed ones, typically associated to technological issues either related to the accidental closure of macropores or to suboptimal sintering conditions determining the formation of interstitial porosity.

In this case, macroporosity was constituted by parallel channels resulting from overlapped perpendicular rods. Referring to **Figure 6.28**, it was possible to notice some differences concerning the dimension of both rectangular pores and rods. In particular, the average thickness of the rods was considerably higher in *RCS-md* compared to *RCS-sg*, of 340 μm and 260 μm, respectively. The passing section of the pores was consequently, although not significantly, slightly larger in *RCS-sg*.

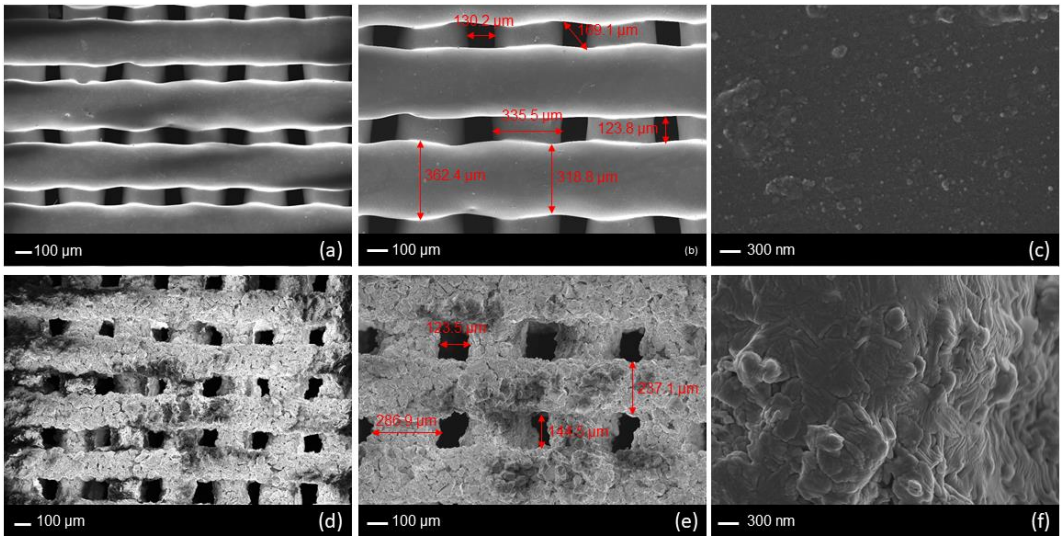

Figure 6. 28. SEM images showing the morphology of grid-like sintered scaffolds obtained by robocasting technology: a), b), c) *RCS-md* and d), e), f) *RCS-sg* at different magnifications.

This was due to the very high wettability of the DG-120 material, determining a higher shrinkage of gel-based ink upon drying and thus, thinner rods. In the case of *RCS-md*, indeed it would seem that the rods underwent a sort of expansion upon thermal treatment, passing from an initial rod dimension of 250 micron (which was the nozzle diameter) to a final one of approximately 330 μm.

Of course, no expansion occurred. The extrusion behavior of printing inks and, more specifically inks based on F127 binding solutions, like in this case, is strongly dependent on the environmental conditions (temperature and humidity), able to dramatically affect the viscosity and the strength of the ink, i.e. its capability to retain the original shape after extrusion. In the present study, a previously optimized ink formulation was used. However, the two activities were carried out in different

periods, and thus, some changes in environmental variables were highly probable. This likely determined a partial flattening of the rods upon contact with the underlaying layers, resulting in the bending effect observed in Figure 6.28 b. Interestingly, this bending effect in gel-derived scaffolds was hardly appreciable after sintering and the diameter of each single rod appeared almost constant.

However, the halving of total porosity cannot be attributed exclusively to differences in macroporosity and inter-particles voids, clearly visible in Figure 6.28 e should be considered. Even upon thermal treatment, in fact, the surface of gel-derived scaffolds retained the grainy appearance of green bodies (Figure 6.27 b).

On the other hand, optimal sintering levels were observed in *RCS-md* sintered at 625 °C, remarkably improved compared to *FRS* sintered at 600 and 650 °C. In fact, neither sintering necks nor interstitial pores were visible after sintering and the surface appeared continuous (Figure 6.28 c). In these regards, it should be pointed out that, although the sintering temperature was the same, the overall thermal treatment of *RCS-md* was much longer.

Here, the choice of the thermal treatment was dictated by the need to ensure the slow and complete degradation of the binder upon heating. It was reported, indeed that the thermal decomposition of Pluronic F127 occurs between 200 and 400 °C [343]. At the beginning it was thought that such a slow and prolonged calcination treatment would had been beneficial also to the degradation of residual organics within the gel; however, as reported in **Chapter 5**, both potassium and sodium nitrates were detected also after the high temperature treatment. Nevertheless, 625 °C was selected in both cases, for direct comparison between the two systems analyzed.

Another important point positively affecting the sintering level of *RCS-md* was certainly the optimal particles dispersion achieved during ink preparation (which was one of the optimized steps), undoubtedly better compared to the mild mixing conditions used for the preparation of the glass slurry in foam replica method. This allowed to limit the formation of concentration gradients within the printing paste, thus improving the homogeneity of the ink.

Scaffold bioactivity was investigated by mean of soaking tests in SBF up to 14 days, in mild-shaking conditions (100 rpm), to favor fluid recirculation. Differently from bioactivity tests performed on other scaffold types, described in the previous sections, no refresh was needed.

The pH increases within the solution, as a result of the ion exchange mechanism between the surface of the scaffold and the fluid was monitored at established time points, i.e. 6 h, 24 h, 48 h, 72 h, 168 h and 336 h.

The pH-time curve showing pH variation upon soaking at different time point is shown in **Figure 6.29**.

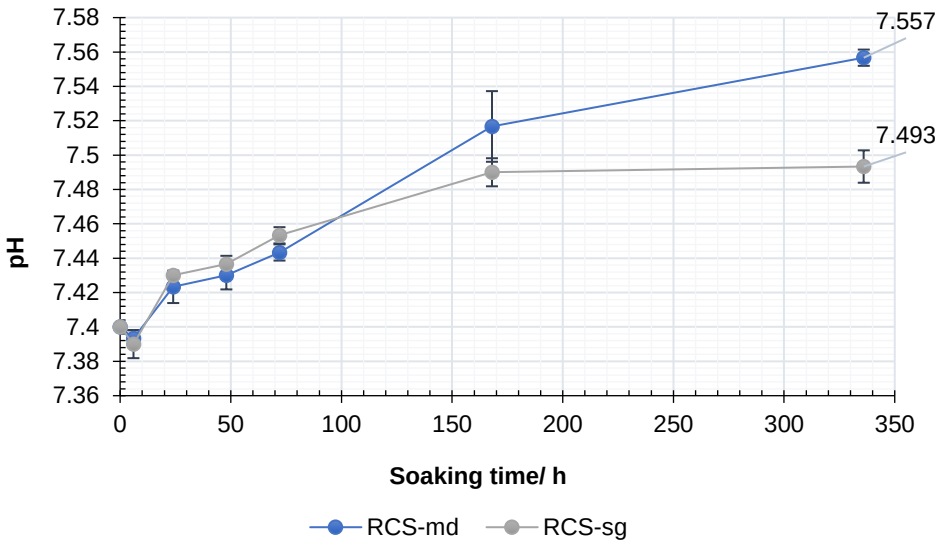

Figure 6. 29. pH increase upon soaking in SBF.

Within the first 24 h-soaking, the pH rapidly increased, as indicated by the high slope of the curve. Then, up to 72 h, the increase in pH slowed down. As can be seen, within the first 3 days of the test, the pH increase was slightly higher in *RCS-sg* (indicated by the grey curve), maintaining comparable increasing rates. After the third day, up to 1 week, this trend reversed, leading to higher pH value in *RCS-md* samples, with a higher slope. Moreover, while the pH stabilized after 1 week-immersion for sol-gel derived scaffolds, a sustained increase up to 7.6 was observed for melt-derived ones. This value was lower compared to that obtained in our previous study (~7.8) [219]. Such a difference can be likely related to the surface roughness and the different sintering quality achieved.

Differently from *RCS-md*, pH curve related to *RCS-sg* stabilized at pH~7.5 after just 1-week immersion. This result differs considerably from what previously seen for powdered samples. In **Chapter 5**, indeed, the pH increase related to SG-625 powder was the highest one among the three systems analyzed, consistently with the SSA values obtained by BET analysis. In this regard, it is possible that gel interaction with F127 binder solution led to some relevant modifications at molecular level, leading to a decrease in the bioactivity of the system compared to the melt-derived ones.

The stepwise evolution of *RCS-md* and *RCS-sg* surface upon soaking in SBF was characterized by mean of XRD and SEM/EDS analyses, performed at different time points.

XRD patterns acquired on *RCS-md* and *RCS-sg* samples for different time frames revealed the formation of HA on the surface of both sample types (**Figure 6.30**).

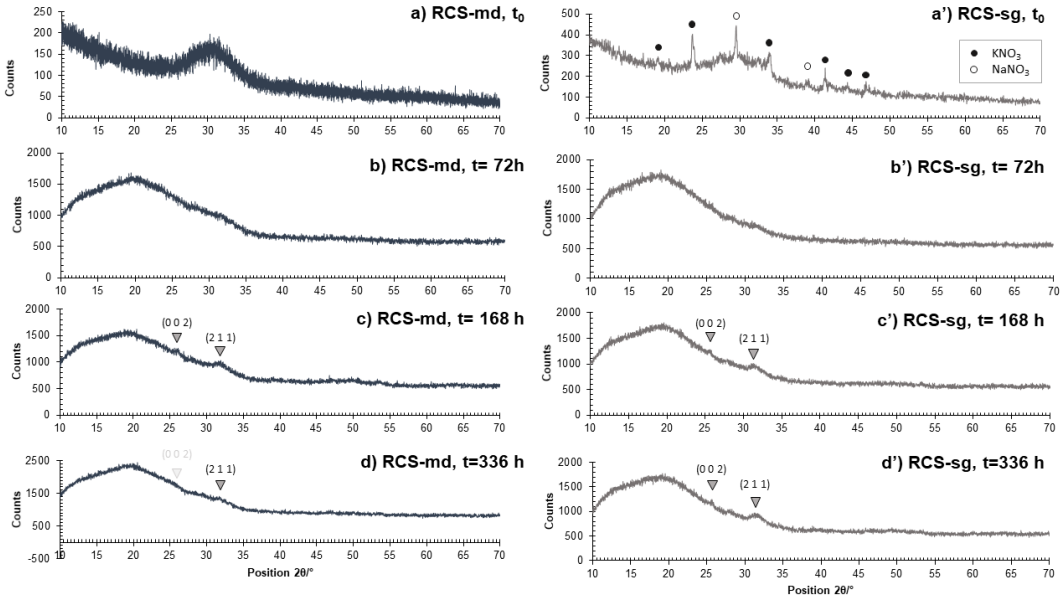

Figure 6. 30. XRD analyses of *RCS-md* and *RCS-sg* scaffolds at different soaking times in SBF compared to un-soaked scaffolds (t_0). Characteristic peaks of HA, are clearly visible after 1-week immersion in both sample sets, even if a very weak signal can be observed after just 72-h from the beginning of the test. HA peaks, identified by the corresponding Miller indices *(h k l)* are indicated by inverted triangles.

At $t=t_0$, the XRD pattern of *RCS-md* and *RCS-sg* scaffolds were characterized, respectively, by the typical amorphous halo of silica-based glassy materials and a basic amorphous halo along with multiple diffraction peaks related to the presence of residual nitrates within the sol-gel system, as previously discussed in **Chapter 5**. After 3-day soaking, it was possible to observe the progressive appearance of an amorphous halo at lower 2θ-values, corresponding to the formation of a thick layer of silica gel, in good agreement with the bioactivity mechanism described in **Chapter 2**.

Although very weak signals were already visible after 72 h, after 1 week-immersion, the two characteristic peaks of HA were clearly appreciable, respectively at 25.68° (0 0 2) and 31.79° (2 1 1), indicating the presence of a well-defined crystalline structure at the nanoscale [339].

SEM results were definitely in good agreement with XRD findings.

In order to avoid reporting redundant results, SEM morphological images related to *RCS-md* surface modification upon soaking in SBF will be shown in **Chapter 7**, where a comparison between different bioactivity testing conditions will be performed.

Figure 6.30, related to *RCS-sg*, clearly shows an exceptional apatite forming ability of the material: after just 72 h-immersion, a homogeneous layer of globular nanostructured HA was observed on the surface of *RCS-sg*.

Images acquired at higher magnification after 2 weeks-immersion Figure 6.30 f clearly shows the cracked silica gel layer below HA aggregates exhibiting the typical cauliflower morphology.

At the end of the test, the Ca/P ratio calculated by semi-quantitative EDS area analysis was 1.55 and 1.10 in *RCS-md* and *RCS-sg*, respectively, indicating the progressive deposition of both Ca and P on the surface of the scaffold.

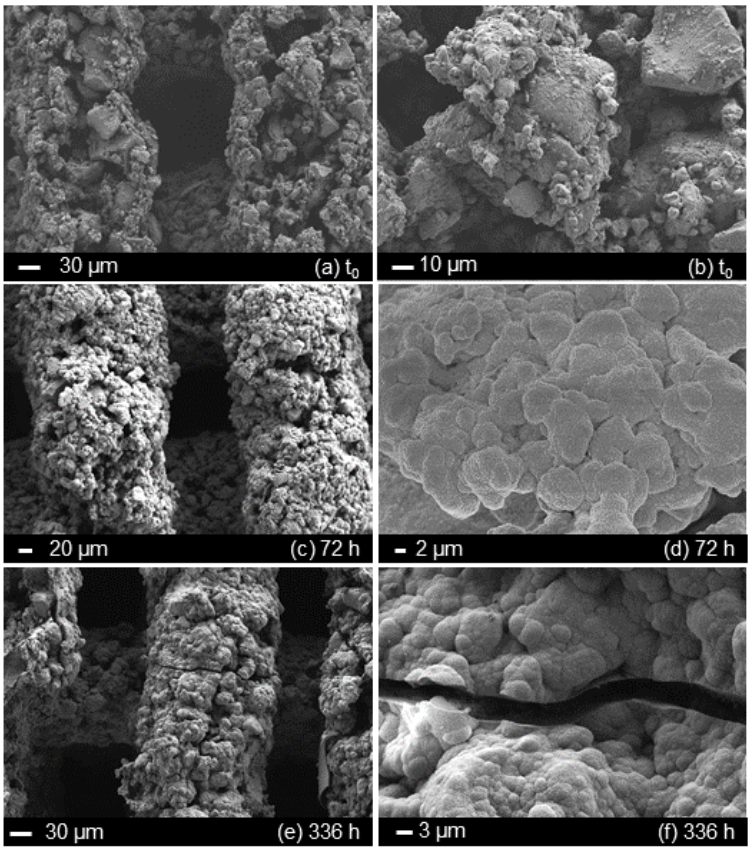

Figure 6. 31. SEM micrograph showing the surface evolution upon soaking in SBF of *RCS-sg* at different time points.

The release kinetics of Ca, P, Mg, Si and K were evaluated by ICP analysis, quantifying the concentration of these ions within the solution at different time points (**Figure 6.32**, **6.33**, **6.34**, **6.35** and **6.36**). The release of sodium was not investigated: the high concentration of Na within the SBF composition, in fact, would result in the oversaturation of the detector used for the analysis, thus leading to unreliable results.

Even if comparable trends were observed for all the ionic species considered, regardless of the scaffold type considered, higher concentration of ions within the solution were detected for the traditional melt-derived glass, in agreement with pH measurements reported in **Figure 6.29**. In fact, according to the bioactivity mechanism commonly accepted for silica-based bioactive glasses [107], the pH of the physiologic solution is modified according to the extent of the ion exchange between the material and the fluid, gradually becoming less intense as the thickness of the HA surface layer increases upon soaking.

Calcium was rapidly released from the surfaces of both scaffold types within the first 24 h. Then, the concentration remained almost constant up to 72 h. On the other hand, the trend related to P release was characterized by a negative slope from the beginning until the end of the test, indicating the continuous sequestration of this

ion from the solution, resulting in a sustained precipitation of calcium phosphate over the whole duration of the test.

As can be seen, after 72h-immersion a relevant decrease of both Ca and P was registered, corresponding to the formation of HA on the samples surface. This was in good agreement both with SEM and XRD results previously discussed.

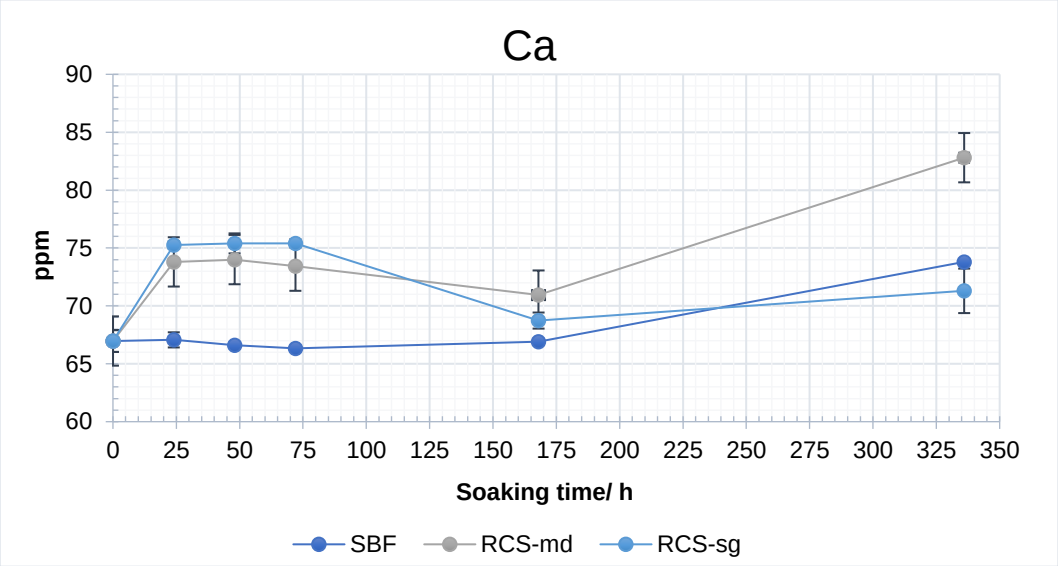

Figure 6. 32. ICP analysis: Calcium release

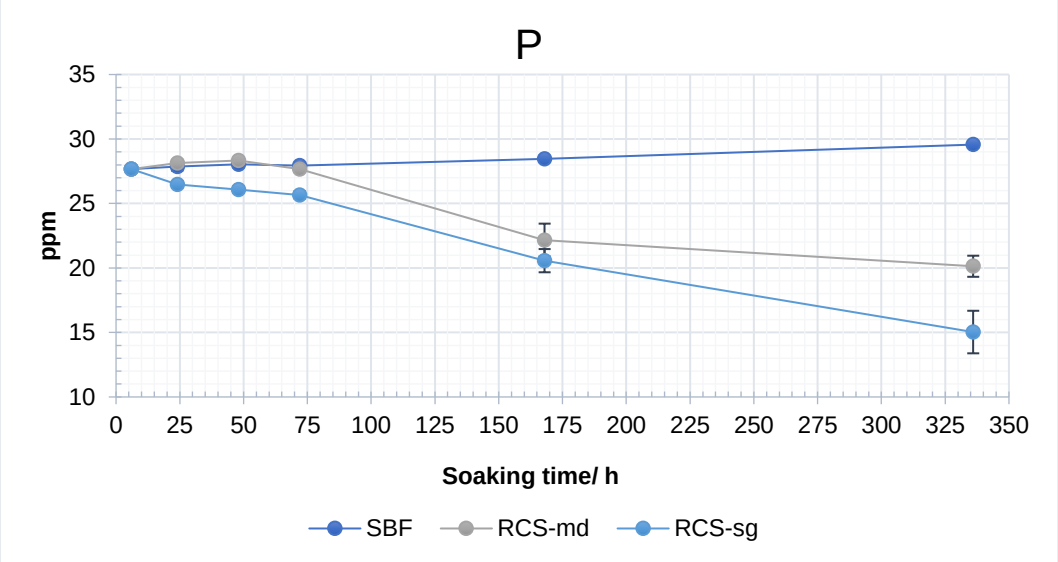

Figure 6. 33. ICP analysis: Phosphorus release.

Mg, Si, and K trends were definitely consistent with the dissolution mechanism of silica-based bioactive glasses and glass-ceramics, exhibiting comparable trends characterized by a rapid increase within the first 24 h and an approximately constant part between 24 h- and 72 h-soaking.

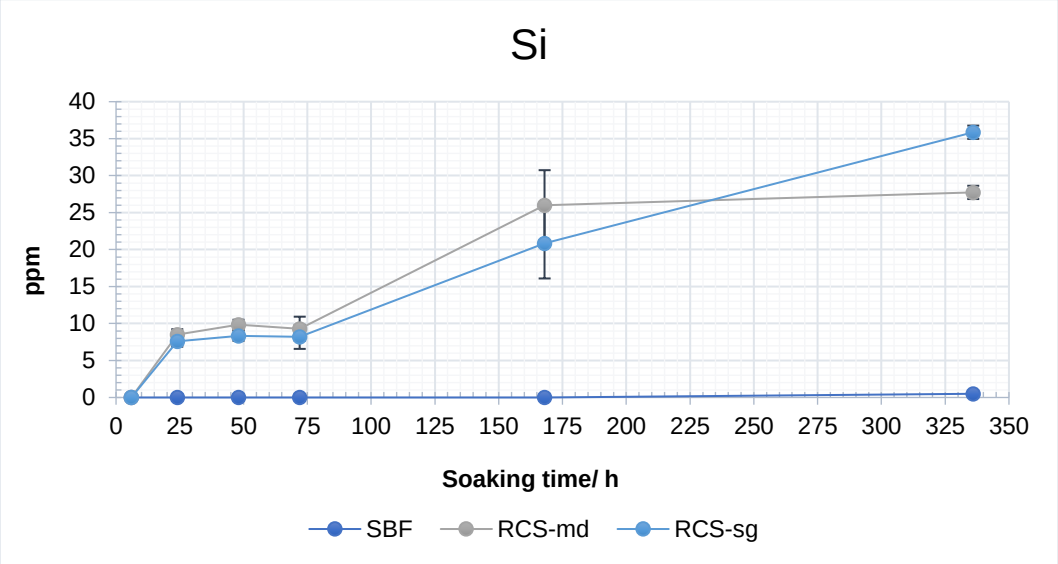

Figure 6. 34. ICP analysis: Silicon release

Concerning Si concentration, analogous trends were observed in the two systems up to 1 week, characterized by a sustained increase corresponding to the release of soluble Si $(OH)_4$ from the silica gel layer.

However, while the curve related to melt-derived scaffolds (*RCS-md*) reached a plateau after 1 week, in *RCS-sg*, Si concentration continued to increase at the same rate until the end of the test.

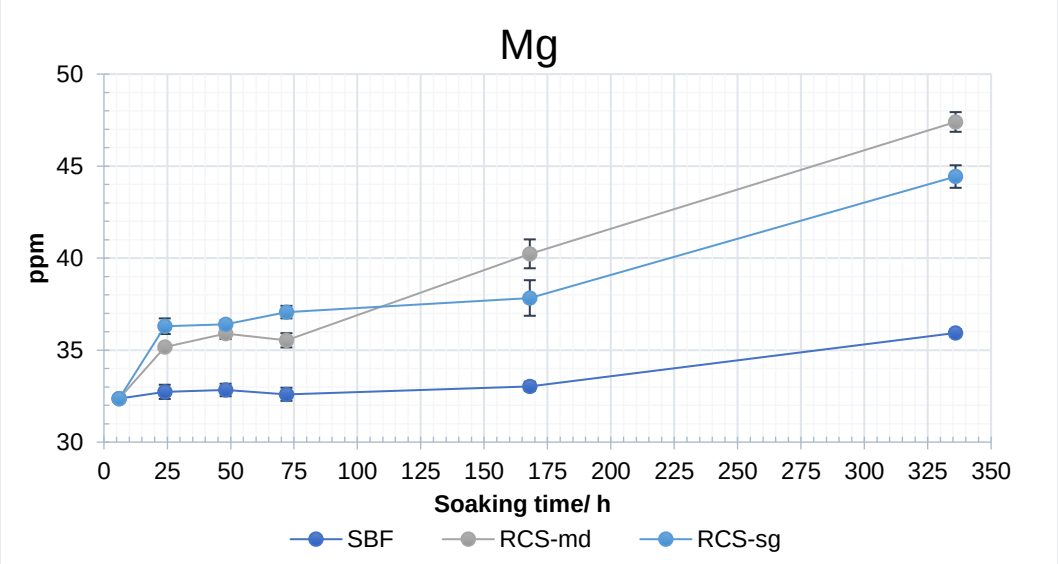

Figure 6. 35. ICP analysis: Magnesium release.

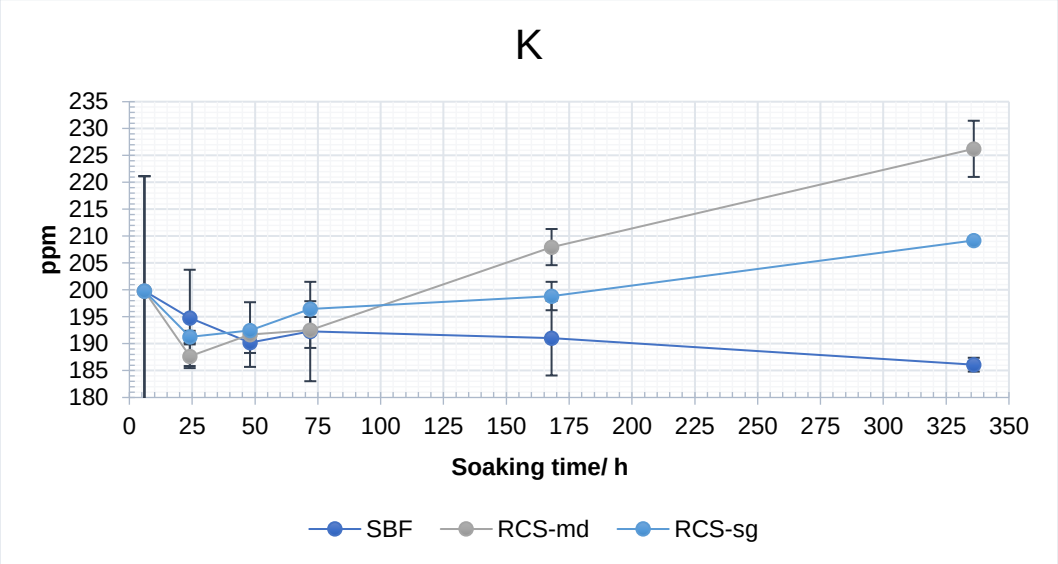

Figure 6. 36. ICP analysis: Potassium release.

In general, concerning *RCS-md* samples, the final concentration of ions at the end of the test was found to be definitely comparable to those reported in a previous study [219], as a further proof of the robustness of the overall manufacturing process, including glass production and processing, ink preparation, robocasting and sintering thermal treatments.

Moreover, although the concentration of most of the species analyzed did not stabilized, both *in vivo* and *in vitro* preliminary tests performed on 47.5B-32 glass, presented in **Chapter 5**, did not reveal any cytotoxic effect related to the exposure of the material to cellular species, thus supporting a potential use of *RCS-md* scaffolds in TE applications.

For this reason, among all the scaffolds optimized within the present Ph.D research activity, it was decided to select this scaffold type for further investigations concerning the optimization of a multifunctional perfusion bioreactor for dynamic bioactivity tests, cell seeding and culture. This activity was carried out in parallel with the research group of Dr. Diana Massai, working in the Department of Mechanical and Aerospace Engineering of Politecnico di Torino and will be object of discussion in the last Chapter of this thesis (**Chapter 7**).

Chapter 7

Design and optimization of a multifunctional perfusion bioreactor for bone tissue engineering

7.1 Introduction

Over the last years, the growing demand in synthetic bone substitutes has placed Bone Tissue Engineering as one of the most influencing emerging fields of our century.

Compared to traditional approaches, in which the synthetic bone graft is implanted as- produced and its colonization by osteoprogenitor stem cells occurs only after implantation, modern BTE strategies, aim at the production of functional implantable biomaterials previously cellularized *in vitro*, thus achieving extended colonization of the 3D graft before implantation which leads to an improved implant-bond fixation strength. In this way, it is possible to significantly reduce the overall healing time, with a major benefit to the patient and the overall sanitary costs [344], [345]. Moreover, the possibility to use cells directly harvested from the patient sensibly reduces the risk of rejection, which is the greatest issue related to allo-transplants and xeno-transplants [32].
This inevitably leads to the compelling need to optimize culture conditions, shifting from traditional 2D static cultures – efficient only for bidimensional, layer-like constructs - to 3D dynamic ones, able to ensure, under specific, *in vivo*-like conditions, adequate nutrient/oxygen supply and catabolites elimination, as well as a more faithful reproduction of the dynamic biological environment.

In this framework, bioreactors have gradually become the main actors in the development of functional substitutes, optimizing mass transport and providing adequate physical/chemical cues under strictly-controlled and highly-reproducible operating conditions [30], [92].

In particular, dealing with bone tissue, considerable efforts have been addressed to the development of multifunctional devices able to support bone tissue regeneration by:

i) Providing adequate shear stress, able to mechanically stimulate the proliferation and differentiation of human osteoblasts, improving bone formation and leading to an overall increase in bone mass [94], [102];
ii) Providing suitable electric and magnetic fields, to actively stimulate 3D muscle maturation and osteogenesis by promoting differentiation to an osteoblastic phenotype [346]–[348].

The present part of the research activity described in this doctoral dissertation was aimed at the development of a multifunctional perfusion bioreactor system able to support both cells seeding and tissue maturation in BTE strategies.

The activity, started in July 2018, was carried out thanks to the valuable contribution of the research group of Dr. Diana Massai, working in the Department of Mechanical and Aerospace Engineering, Politecnico di Torino. The project required a highly-interdisciplinary approach, characterized by the synergistic combination of skills in different engineering fields, including 3D Computer Aided Design (CAD) modelling, computational analysis and simulations, materials science and biology, resulting in the fruitful cooperation of four different departments:

- Department of Mechanical and Aerospace Engineering - Politecnico di Torino, coordinating the activity and involved in the conceptualization, design and optimization of the bioreactor system and physical simulations by computational analysis;
- Department of Applied Science and Technology - Politecnico di Torino, involved in the design of the bioreactor and the perfusion system, scaffolds manufacturing and optimization of dynamic bioactivity tests;
- Department of Electronics and Telecommunications - Politecnico di Torino, involved in the fabrication of the bioreactor by Additive Manufacturing Technologies and optimization of the electrical stimulation system;
- Department of Health Sciences - Università degli Studi del Piemonte Orientale, in charge of carrying out biological tests on bone cells to investigate the seeding efficiency of the system and its capability to support bone tissue maturation by combining different physical stimuli.

The overall activity was organized identifying five main tasks, separately developed over time by the four different parties listed above:

i) Design and development of the culture chamber and realization of prototypes for preliminary function tests;
ii) Design and development of a perfusion system adaptable both for seeding and culture conditions;
iii) Design of bioactivity testing protocols to investigate the effect of dynamic flowing on the characteristic of the hydroxyapatite reaction layer at the interface with a simulated body fluid solution (SBF);
iv) Development of a stimulation system based on the combination of mechanical and electrical stimulation, including preliminary computational simulation, realization of the electrodes and coupling with the culture chamber, as well as optimization of fluid flowing conditions to generate adequate shear stress on cell constructs. This specific point was addressed in the context of another doctoral thesis and therefore will not be covered by this dissertation;
v) Biological *in vitro* tests (ongoing).

7.2 10 steps to a new multifunctional culture system: project requirements and operative strategy

If opportunely designed, bioreactors can serve multiple purposes. In this case, bioreactor design was optimized to facilitate seeding procedures, guaranteeing a uniform cell distribution over the whole volume of the scaffold, and to support tissue maturation by providing, together with optimal mass transport and waste removal, combined physical stimulation, specifically electromagnetic fields and physiological shear stress provided by hydrostatic forces inside the perfusion circuit.

The specific requirements addressed within the present project are summarized in **Table 7.1** (on the next page).

For these purposes, the bioreactor system was equipped with:

a) A culture chamber, of which several prototypes were fabricated using different materials depending on the progress of the device;
b) Different silicone sample holders, adaptable to scaffolds with different diameters;
c) A peristaltic pump (*Masterflex® L/S® Peristaltic Pump, Cole-Parmer* for dynamic bioactivity tests and *REGLO Analog MS-4/6, Ismatec*, in the optimized system for cell seeding and perfusion);
d) *Puri-Flex®-Pump Tubing* (based on *silicone - Masterflex®-6419*);
e) A medium reservoir;
f) Stainless steel circular planar electrodes externally connected to a stimulator to deliver for delivering electrical stimuli.

Table 7. 1. Design and development of a BTE bioreactor: project requirements and strategies to address each specific need.

N°	Requirements	Operative strategy
1 *2*	**Cytocompatibility** **Sterilizability**	Use of non-toxic, autoclavable materials in contact with culture medium, cells and scaffolds
3	**Water tightness**	Development of a smart closing mechanism avoiding coupling of different materials and minimizing material wear
4	**Ease of use**	Optimization of a compact and handy design, suitable for use in confined environments (i.e. hood, incubator) and conform to Good Laboratory Practice (GLP). User-friendly and intuitive interface, minimizing human error.
5	**Versatility and adaptability to different culture conditions**	Use of a reverse flow peristaltic pump to easily shift from seeding to culture condition
6	**Ease of cleaning**	Development of a simple design avoiding sharp edges and stagnation areas to facilitate cleaning procedure by tools and techniques easily available in biological laboratories
7	**Direct perfusion**	Development of soft, deformable holders able to easily adapt to the scaffold profile in order to seal the side surface and make it unavailable for fluid flowing.
8 *9*	**Electrical stimulation** **Mechanical stimulation**	Controlled delivery of tunable and combinable physical stimuli, i.e., flow-induced shear stress and electrical stimulation suitable for promoting tissue maturation.
10	**Modularity/scalability**	Development of a system composed of different elements separated or separable from each other. Possibility to perform simultaneously two or more cultures by coupling in parallel different culture chambers based on the same design.

7.3 The culture chamber: Minimal design, a statement of precise choice

The culture chamber, both prototypes and optimized last version, was fabricated by different Additive Manufacturing Technologies (AMTs) starting from a customized model realized in Solidworks 2017 (Dassault Systemes), a commercial computer aided design (CAD) software.

In the first prototype, the culture chamber was externally characterized by a cylindrical geometry resulting from the coupling of two different parts, a top and a bottom, modelled as hollow cylinders.

The total height of the coupled system was 59 mm and the external diameter was 40 mm, matching approximately the average size of a common chicken egg. The dimensions of the chamber have been deliberately kept small to minimize the quantity of culture medium required to fill the perfusion system (priming volume) and to facilitate the usage of the bioreactor system under hood, as well as its placement inside laboratory incubators for the maintainance of the correct temperature and humidity conditions.

Two extruded parts were added at the top and the bottom, to facilitate opening and closure of the chamber, as well as the coupling with the tubing system by mean of dedicated connectors.

The three-dimensional view and the cross-section in the frontal plane of the coupled system are shown in Figure 7.1 a-b, respectively.

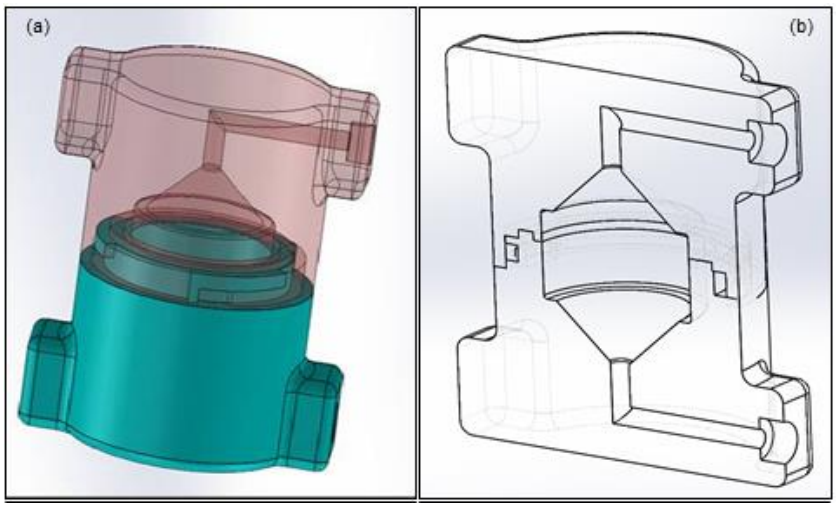

Figure 7. 1. Design of the culture chamber: 3D (a) and cross-sectional (b) views of the coupled system.

The two components, shaped like two hollow cylinders equipped with a medium inlet and a medium outlet placed on the same side (Figure 7.1 b), were coupled by a rapid bayonet coupling system, similar to the famous Fulg-o-tooth™ mechanism, consisting in *a toothed door that rotates to fit in the appropriate hub so as to transmit the load evenly on the parts of the neck that are in contact with the "teeth"* [349].

The chamber was thought to be entirely realized with the same material and this dictated the choice of the coupling system, according to three different needs:

i) speed up and simplify the opening mechanism of the chamber to facilitate operators at the most in loading/unloading scaffolds operations under hood;
ii) minimize the wear of materials due to the relative sliding between the components
iii) avoid the coupling of different materials characterized by different expansion coefficient upon heating, as well as different hardness (i.e. metal/polymers)

Internally, the chamber was designed to be symmetrical with respect to the frontal and transversal planes, to optimize bilateral seeding conditions, avoiding gradient formation and favoring homogeneous cell distribution over the whole volume of the scaffold. In this way, it was ideally possible to reproduce the same conditions upstream and downstream the scaffold after cell inoculation within the circuit.

Geometrical details related to the design of the top and bottom components of the bioreactor are provided in **Figure 7.2**.

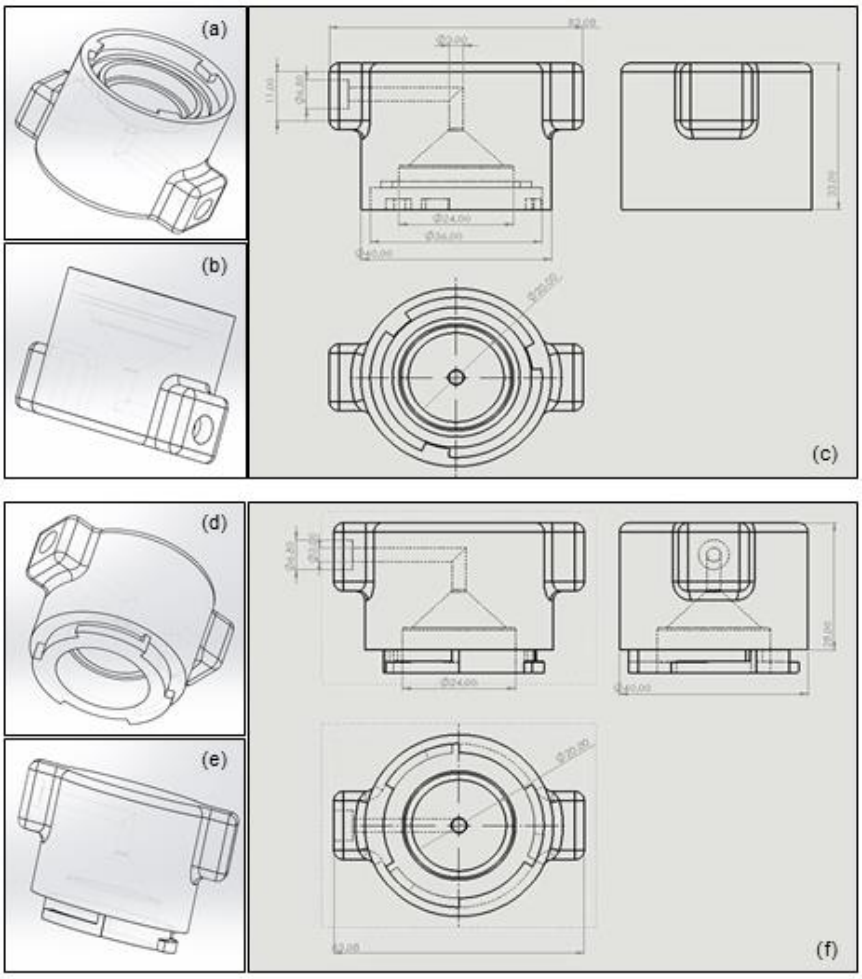

Figure 7. 2. Design of the culture chamber, prototype 1: CAD models of the upper (a,b) and lower (d,e) parts and relative orthogonal projections (c, f).

The housing for the sample holder was obtained half inside the top and half inside the bottom of the culture chamber, to facilitate the extraction of the holder by tweezers. A circular ring groove was modelled in the top as housing for the O ring, aimed at guaranteeing the weathertightness of the chamber.

In order to reduce the priming volume, the cavities above and below the sample holder were initially modelled as cones. However, preliminary computational analysis of fluid flow inside the chamber revealed the formation of backwater areas and vortexes (flow rate Q_v = 5 ml/min), making it necessary to introduce a variation of internal geometry in subsequent prototypes.

The first prototype was 3D-printed by Fused Deposition Modeling (FDM, uPrint SE Plus, Stratasys), using acrylonitrile butadiene styrene (ABS) as basic material (**Figure 7.3**). ABS is a common thermoplastic polymer, with operating temperature between -40 °C and 80 °C, not intended for cellular use but widely appreciated for the realization of small, light and stiff prototypes.

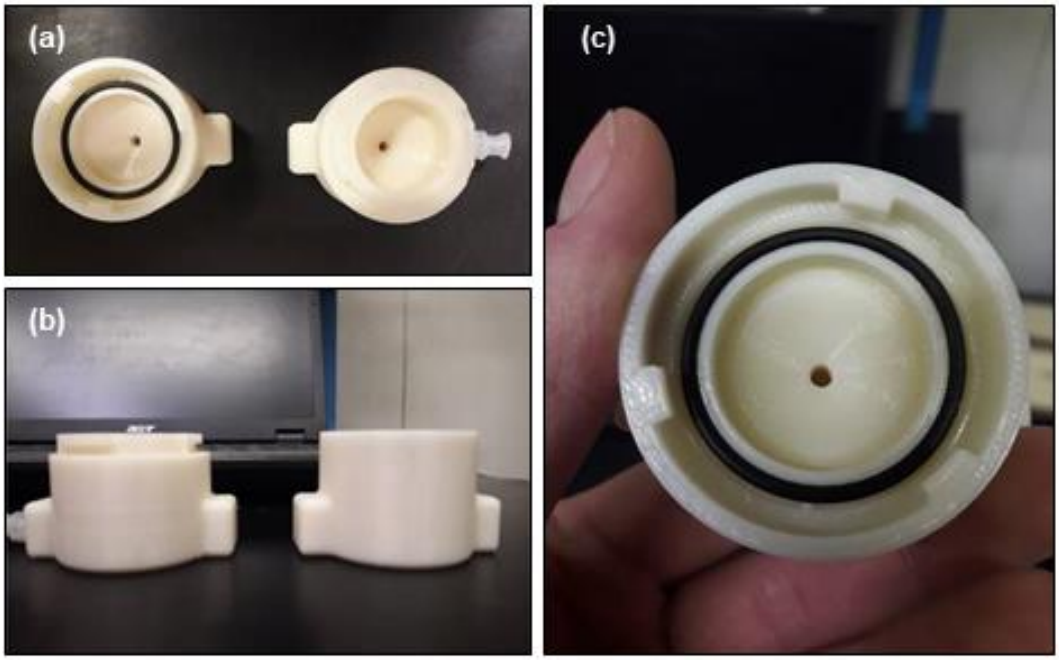

Figure 7. 3. First prototype of the culture chamber realized in Acrylonitrile butadiene styrene (ABS) by Fused Deposition Modelling.

Rapid prototyping is a powerful tool to identify the most critical issues related to the design of an experimental device.

As an example, in this case, it was possible to observe that the "teeth" for mechanical anchoring were too thin and fragile to guarantee a prolonged use of the device overtime.

For this reason, it was decided to modify their shape by tapering the ends and expanding the base, thus providing a certain inclination which made the coupling more efficient and robust.

To avoid formation of backwater areas, the internal geometry of the chamber was optimized turning conical voids upstream and downstream the scaffold holder into cylindrical ones and the relative positions of medium inlet and outlet were modified creating an S-shaped path of the fluid inside the chamber.

Moreover, in order to improve grip and avoid slippage upon use, it was decided to add a ring to the bottom of the chamber, to be knurled in subsequent upgraded version of the device.

In the final version, the culture chamber presented a total height of 57 mm, an outer diameter of 54 mm and a priming volume of about 10 ml.

CAD models of the upgraded culture chamber are collected in **Figure 7.4**.

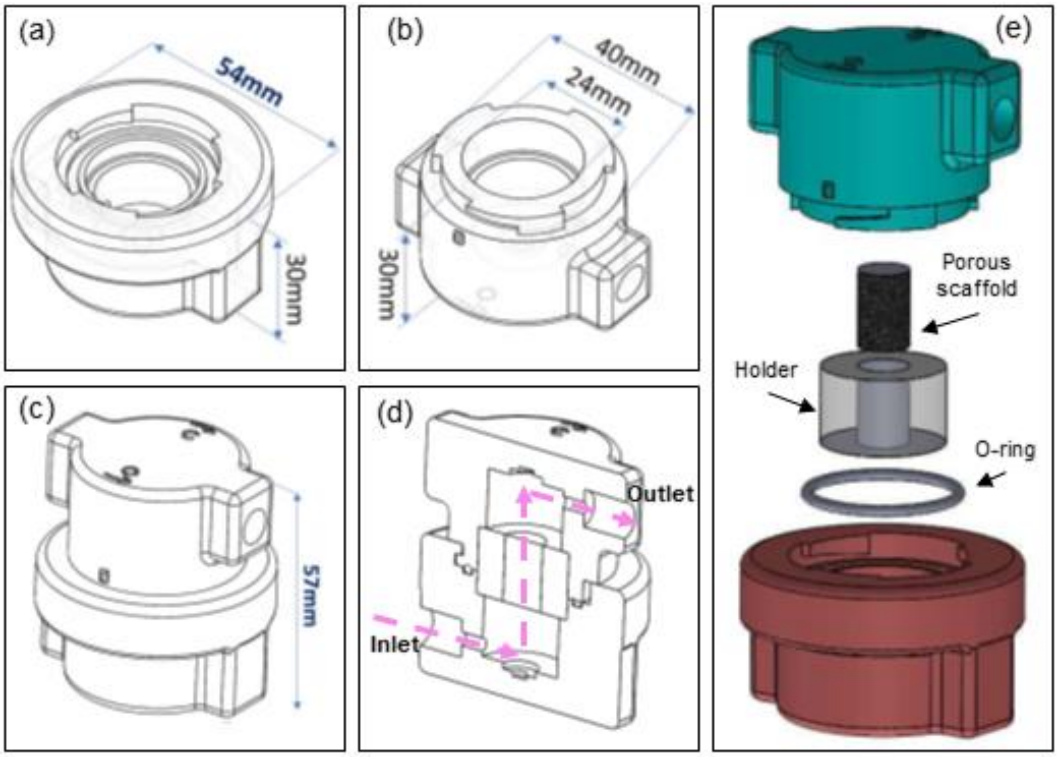

Figure 7. 4. Design of the culture chamber, last version: CAD models of the upper (a) and lower (b) parts, 3D and exploded view of the coupled system (c and d, respectively) and cross-sectional view showing the internal geometry of the chamber. Images courtesy of the Solid and Fluid Biomechanics Group – Department of Mechanical and Aerospace Engineering.

FDM technology used for the realization of the first prototype allowed to identify inaccuracies and critical issues related to the geometrical design of the chamber but provided no information on the performances of the device concerning water tightness, due to the suboptimal adhesion of overlapped layers constituting the part, causing the water leakage observed at the bioreactor walls.

For all the reasons mentioned above, the upgraded version of the culture chamber was realized by stereolithography technology (Form 3, FormLabs [350]) using (DentalSG resin, FormLabs), a biocompatible Class 1 photocurable resin (EN-ISO 10993-1:2009/AC:2010, USP Class VI), conventionally used to realize temporary surgical implants [351].

7.4 The sample holder

Four silicon holders of a hollow cylindrical shape were realized by casting Polydimethylsiloxane (PDMS) (Sylgard 184, Dow Corning) into customized molds with different diameters, in order to be adaptable to the greatest possible number of stiff porous struts (i.e. ceramic scaffolds). The molds, designed in Solidworks 2017 (Dassault Systemes), were realized in ABS by FDM printing (uPrint SE Plus, Stratasys).

In particular, holders were designed to perform a double function: (i) guarantee direct perfusion through the volume of the scaffold and (ii) make the chamber adaptable to different kind of scaffolds.

The geometrical characteristic of the holders produces are provided in **Table 7.2**.

Table 7. 2. Geometrical characteristics of scaffold holders.

Holder	Outer diameter /mm	Inner diameter /mm	Height /mm
a	24	7	15
b	24	8	15
c	24	9	15
d	24	10	15

7.5 The perfusion system

The perfusion system was optimized to be used both for cell seeding and dynamic perfusion thanks to the presence of a reversible flow peristaltic pump.

In detail, the circuit was composed of (Figure 7.5 a):

1. A reservoir for the culture medium (0-500 ml);
2. A peristaltic pump, allowing reverse flow;
3. Oxygen-permeable tubing system (~2 m);
4. 3-way stopcocks, to allow changing the configuration of the system from perfusion (blue arrows) to seeding (red arrows) and *vice versa;*
5. Filters, to avoid cell dispersion;
6. Injection sites (cell inlets), placed upstream and downstream the culture chamber.

In this configuration, the designed perfusion system is potentially able to support both dynamic cells seeding, imposing a bidirectional flow (0.1-1 ml/min), and dynamic perfusion, imposing a unidirectional flow (0.5-3 ml/min) for the mechanical stimulation of cell constructs, where the ranges indicated were identified by an accurate analysis of the available literature studies.

As can be seen from **Figure 7.5**, the perfusion system was actually composed of a main loop (perfusion loop), connecting the reservoir, the chamber and the peristaltic pump, and two smaller loops connected in parallel, placed upstream and downstream the culture chamber. These additional loops, containing filters for

confining cells within a closed volume in the vicinity of the culture chamber, were thought to be isolated from the main loop during simple perfusion and connected only during seeding procedures.

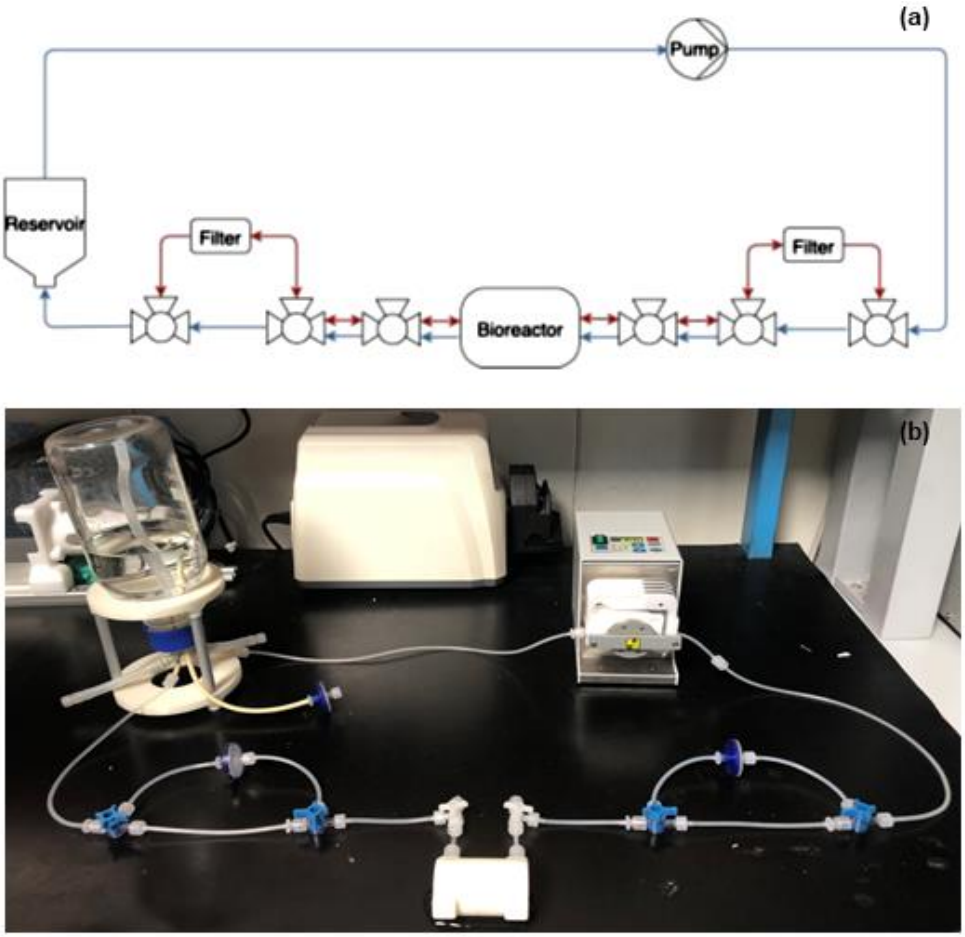

Figure 7. 5. The perfusion system: a) schematic diagram, courtesy of the Solid and Fluid Biomechanics Group – Department of Mechanical and Aerospace Engineering and b) experimental set-up.

7.6 Dynamic bioactivity tests: preliminary results future developments

Preliminary bioactivity tests have been performed under continuous SBF flowing conditions in order to evaluate the influence of fluid flow on the formation of the HA reaction layer. Static and semi-dynamic bioactivity tests were performed for comparison.

Indeed, previous studies demonstrated that the mechanism and rate of apatite deposition on the surface of bioactive glasses differ according to the test regime [352]. In particular, dynamic bioactivity tests have been recognized to be a better and more realistic approach to study the bioactivity of glass-based products *in vivo* via the *in vitro* assays [353]. Moreover, when 3D-porous scaffolds are used, forcing SBF flowing inside the pores by the action of a pumping system could help in achieving material's conversion even in the core of the graft, thus favoring a more complete osteointegration of the implant.

7.6.1 Materials and Methods

The experimental set up for dynamic tests (Figure 7.6 a) was composed of:

a) Simplified ABS culture chamber, machined for milling with a CNC milling machine, housing holder and scaffold (Figure 7.6 b-c-d)
b) Non-permeable Puri-Flex®-Pump Tubing (based on silicone - Masterflex®-6419).
c) Peristaltic pump (Masterflex® L/S® Peristaltic Pump, Cole-Parmer).
d) Reservoir filled with SBF, kept between 36.5 and 37.5 °C, and equipped with a port for pH sampling
e) Hot plate equipped with a temperature controller

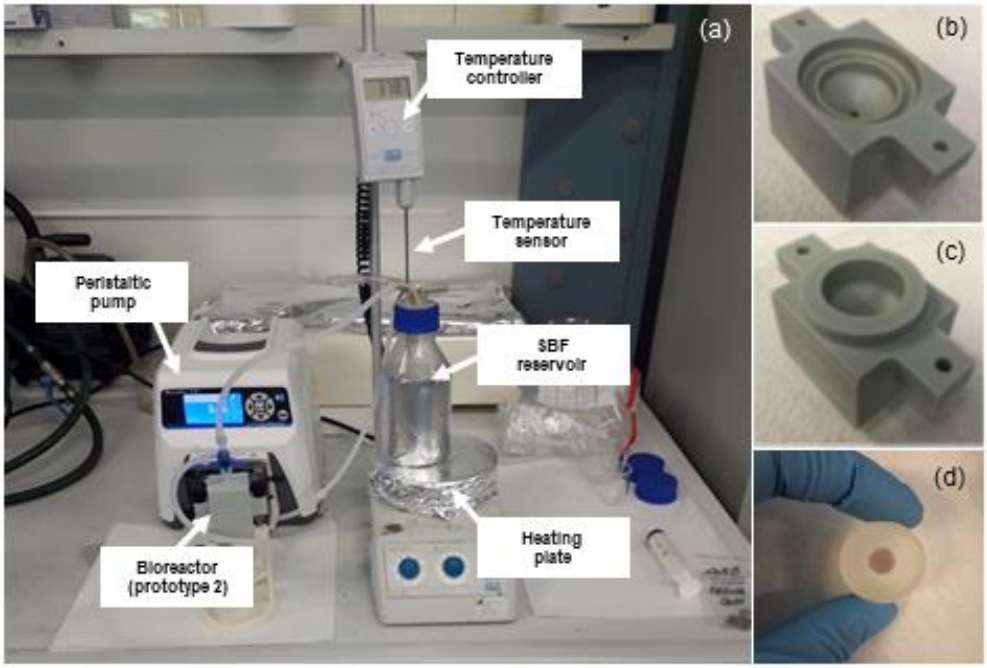

Figure 7. 6. Dynamic bioactivity tests: a) experimental set up, b) top and c) bottom of the bioreactor culture chamber (simplified version), d) glass-scaffold produced by robocasting technology inserted inside the sample holder.

The simplified culture chamber used for bioactivity tests presented the same internal geometry described for the first prototype and, analogously, it was characterized by two different components (Figure 7.6 b-c). However, in this case, the top and the bottom of the chamber were cube-shaped and coupled by mean of two metallic screws. This solution, this solution, although not optimal for prolonged use over time, was enough performing for the intended purpose, allowing us to go ahead with the tests while waiting for the realization of the optimized prototypes.

Robocast scaffold based on the melt-derived 47.5B bioactive glass (*RCS-md*), characterized in **Chapter 6**, were selected for the present study due to their high geometrical regularity and superior mechanical integrity [220] compared to foam replicated and dolomite-foamed scaffolds.

Preliminary tests were performed to become familiar with the device and identify possible critical issues related to the assembly of the system, temperature control and pH sampling procedures.

The geometrical characteristics (scaffold mass m_s, scaffold diameter D_s, scaffold length L_s, cross-sectional area A_s, total porosity ε_0, as well as the volume of SBF used in the test) are collected in **Table 7.3**.

Table 7. 3. Primary and derived geometrical features of RCS samples and SBF volume calculated according to the sample mass considering a mass-to volume ration of 1.5 mg/ml

	m_s /g	D_s/ mm	L_s/ mm	A_s/mm^2	ε_0	SBF/ ml
Bioreactor	0.259	8.65	4.37	58.77	0.62	173
Orbital	0.286	8.52	4.36	57.01	0.56	191
Static	0.321	8.41	4.37	55.55	0.50	214

The optimal flow rate was calculated basing on data reported in **Table 1.6**, according to which, the optimal fluid velocity within a perfusion system can be determined on the basis of scaffold's geometrical features, pore shape and total porosity ε_0 [97].

Thus, the flow rate Q_v was calculated by **Equation 7.1**

$$Q_v = v_f \cdot A_s \qquad \textbf{7.1}$$

Where v_f is the fluid velocity and A_s is the cross-sectional area of the scaffold, calculated according to **Equation 7.2**:

$$A_s = \pi \left(\frac{D_s}{2}\right)^2 \qquad \textbf{7.2}$$

RCS scaffolds were characterized by rectangular pores ranging between 100 and 200 µm, as assessed by SEM morphological analyses.
Considering a total porosity of about 60 vol.%, a flow rate of 1 ml/min was imposed, corresponding to an average fluid velocity applied to *A* of about 0.3 mm/s.

This flow rate was also used by Rámila et al. [353] and Izquierdo-Barba et al. [354], who demonstrated that SBF exchange with 1 ml/min flow allowed to maintain ionic concentration and pH almost constant and close to human plasma.

In order to allow the complete development of fluid flow before reaching the scaffold surface, the sample holder (c, **Table 7.2**) was inserted in the bottom of the culture chamber, placing the scaffold in the highest part.

pH was monitored at specific time points, i.e. 24 h, 48 h, 120 h, 168 h, 192 h, 216 h and 336 h, taking 5 ml from the dedicated port connected to the reservoir, to avoid introducing contaminants within the circuit. The pH value was measured at a temperature of 37.0 ± 0.5 °C. Afterwards, the SBF sample was reintroduced in the reservoir, to keep the volume constant until the end of the test.

Static and semi-dynamic bioactivity tests, carried out in static and orbital-shaker incubator (100 rpm) at 37°C, respectively, were performed following the same procedures described in **Chapter 4**.
In static bioactivity tests, the volume of SBF was completely substituted with fresh solution at 48 h, 120 h, 168 h and 216 h to simulate physiological recirculation of body fluids, while no refresh was planned for tests performed under mild-shaking conditions.
Finally, morphological and compositional features of the HA layer were assessed by Scanning Electron Microscopy (SEM) and Energy Dispersive Spectroscopy (EDS) analysis, respectively.

7.6.2 Results and discussion

pH variation upon exposure to SBF under dynamic, semi-dynamic and static condition is shown in **Figure 7.7**.

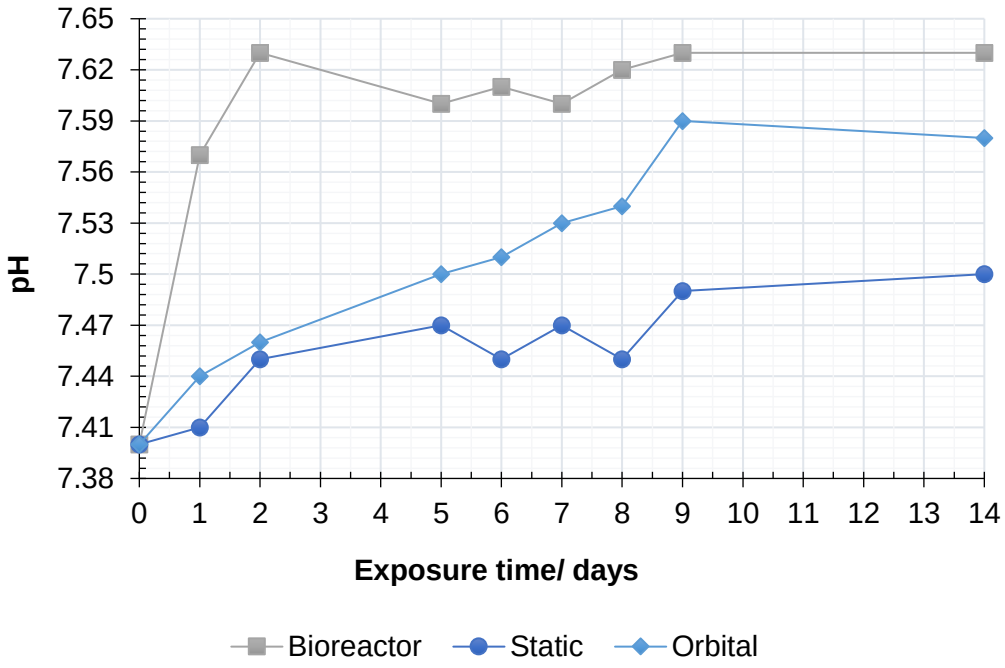

Figure 7. 7. pH variation upon exposure to SBF under dynamic, semi-dynamic and static conditions.

All the curves revealed an increasing trend with exposure time, consistently with the bioactivity mechanism accepted for bioactive silicate glasses immersed in a simulated physiological environment [107].

Direct perfusion seems to remarkably improve ion exchange mechanisms, leading to highest pH values compared to mild-shaking and static conditions. It is known, indeed, that pH changes within the solution are directly related to the dissolution rate of the material [355]. This result is in good agreement with previous studies, reporting a faster bioactivity mechanism under dynamic dissolution configurations compared to static conditions [356].

This is an encouraging evidence, proving a more efficient interaction between the scaffold surface and the solution given by the action of the peristaltic pump, which forces the liquid to enter the scaffold pores, thus involving the whole exposed surface in ion exchange mechanism.

All the curves reached a plateau after 9 days, indicating an early stabilization of the systems upon exposure to SBF even under different testing conditions.

Although the test was completed up to day 14, at the beginning of the second week, a white deposit was observed at the bottom of the reservoir, as well as in the tubing system.

The behavior of SBF within the circuit had been preliminary investigated in the absence of the scaffold, without observing relevant issues. This allowed excluding a relation between the particulate observed and a poor stability of SBF within the perfusion system.

SEM morphological analyses, showing scaffolds cross-section after 2-week exposure to simulated physiological fluids, were useful in clarifying this aspect (**Figure 7.8**). In fact, differently from what observed for static and semi-dynamic tests, no HA deposited layer was detected onto the inner pore surface of scaffolds subjected to dynamic flowing conditions. Nevertheless, a silica-gel layer, typical of the first reaction stages of the bioactivity mechanisms of silica-based bioactive glasses was clearly visible, as indicated by the white arrow in Figure 7.8 b, and its thickness was definitely comparable to that observed for the other two systems analyzed.

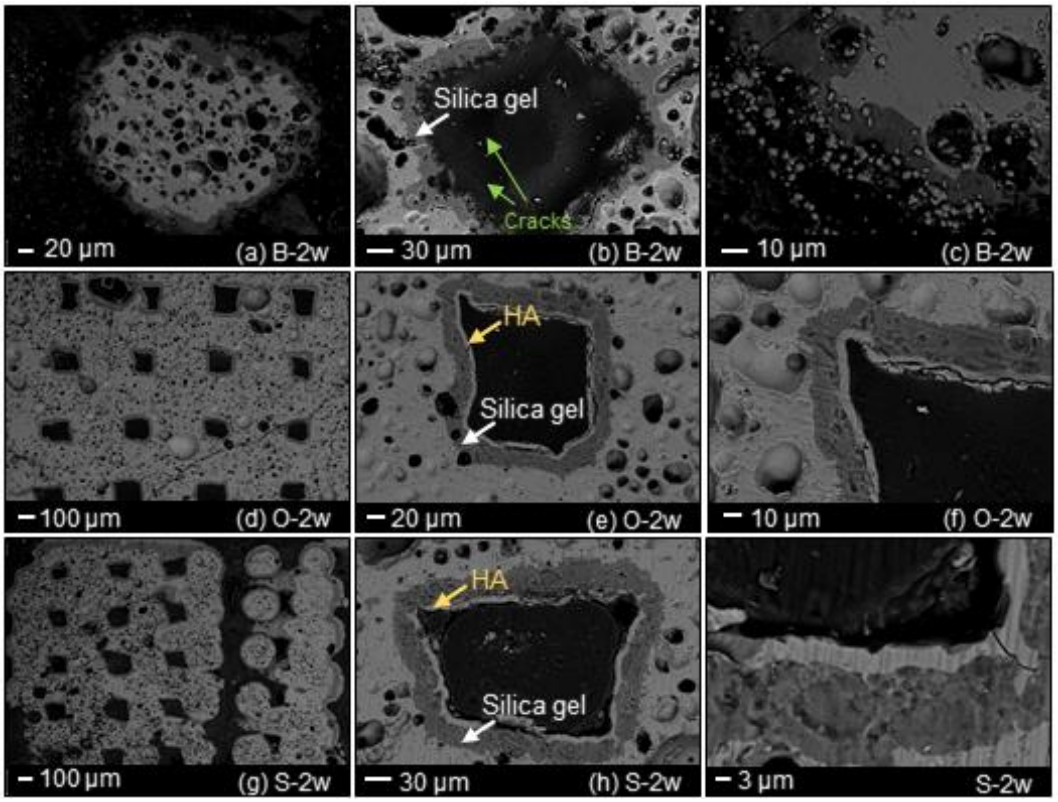

Figure 7. 8. SEM morphological analysis showing the reaction layer formed upon exposure to SBF in perfusion bioreactor (B-a,b,c), orbital shaker (O-d, e, f) and static incubator (S-g, h, i) after 2 weeks.

On the other hand, scaffolds soaked in SBF under mild-shaking and static conditions (Figure 7.8 d-e-f and Figure 7.8 g-h-i, respectively) where covered by an HA reaction layer, approximately 4-5 µm-thick, indicated by the yellow arrows in Figure 7.8 e-h.

EDS analyses performed on the reaction layers upon 14-day exposure to SBF in dynamic, semi-dynamic and static condition (**Figure 7.9**, **7.10**, **7.11**, respectively), confirmed that a bi-layered reaction layer formed both in static incubator and orbital shaker, while a single Si-rich layer was detected for the bioreactor system.

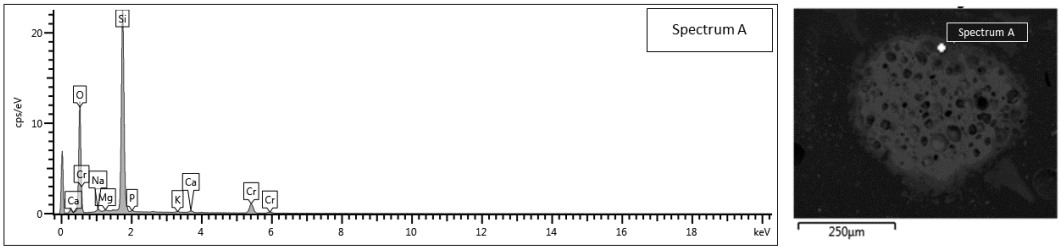

Figure 7. 9. EDS compositional analysis: reaction layer formed on the surface of RCS sample subjected to continuous SBF flowing conditions.

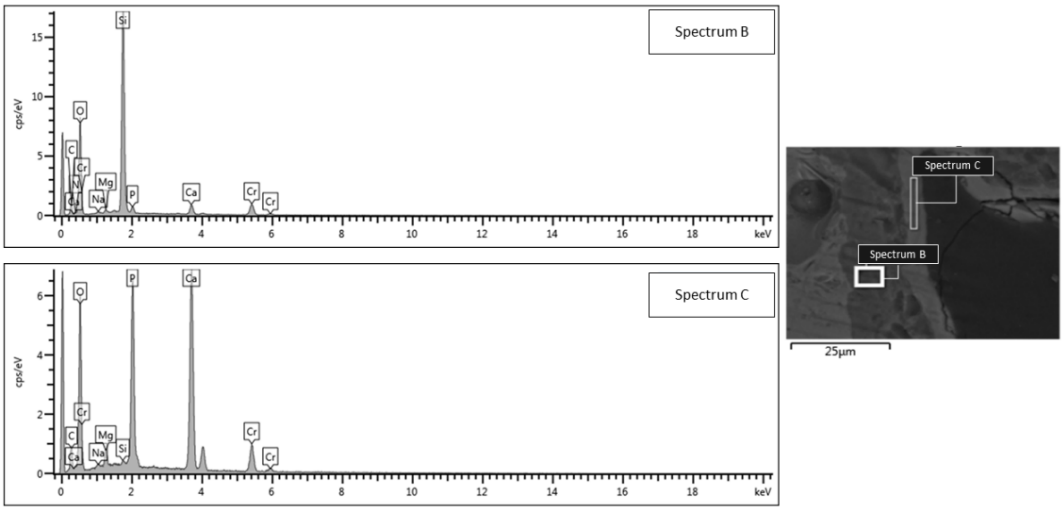

Figure 7. 10. EDS compositional analysis: bi-layered reaction layer formed on the surface of RCS sample subjected to SBF mild-shaking conditions in orbital shaker incubator.

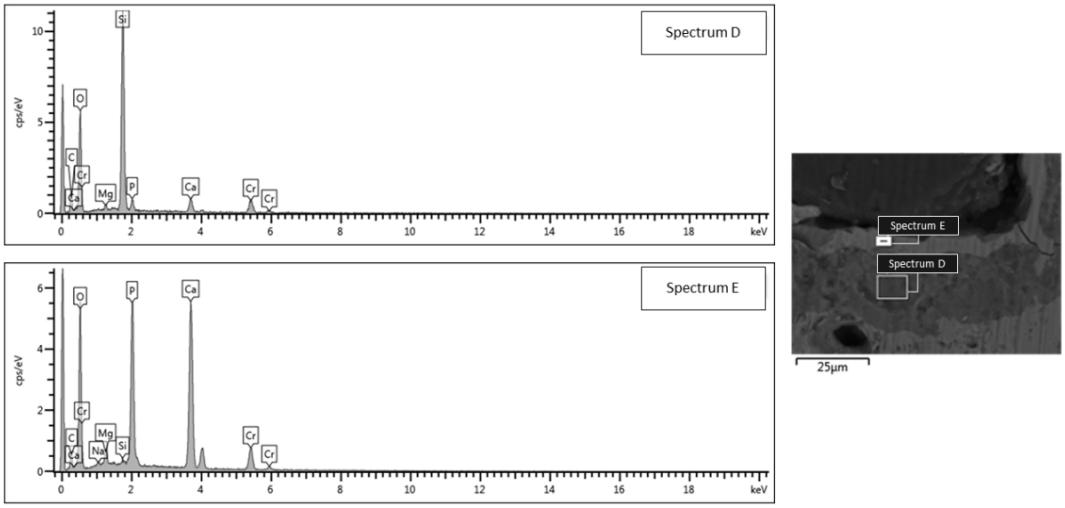

Figure 7. 11. EDS compositional analysis: bi-layered reaction layer formed on the surface of RCS sample subjected to static soaking in traditional incubator.

The Ca/P ratio at in static and mild shaking condition was respectively 1.48 and 1.55, quite close to the stoichiometric one of 1.67.

Local dynamics had a significant impact on the outcome of the test. Although the same flow rate had been already used for performing dynamic bioactivity tests, with promising result, in the present study a detachment of the reaction layer was observed.

In these regards, the shape of the sample (porous scaffolds instead of sintered tablets [353]), as well as the direct perfusion regime imposed through the porous volume, likely played a crucial role. In fact, it is highly probable that, considering the intrinsic flow resistance provided by a porous media, the flow rate imposed within the perfusion system was actually too high to preserve the integrity of the deposited layer, dispersing it inside the circuit.

This hypothesis is supported by a recent study by Höner and coworkers [357], investigating the alterations of a bioactive glass surface (13-93) in a SBF reactor,

optimizing flowing conditions on the basis of Computational Fluid Dynamic simulations in order to mimic the physiological environment. In the study, although a flow rate of 10 ml/min was imposed at the inlet and the outlet of the bioreactor chamber, the flow rate at the surface of the scaffold was much lower and equal to 3 μl/s, corresponding to 0.18 ml/min, about 1/5 of the value imposed in this study.

These results clearly suggest the need for further experiments aimed at optimizing the perfusion conditions of BG-based porous scaffolds in order to preserve the integrity of the HA deposition layer, thus allowing a more accurate characterization in terms of compositional and morphological features.

Chapter 8

Conclusions and future developments

Main results

This Ph.D thesis deals with manufacturing processes and characterization techniques related to three-dimensional (3D) porous bioactive glass (BG) and glass-ceramic scaffolds for bone tissue engineering (BTE) applications.

The experimental activity was carried out on two strands:

1. the development and optimization of new tools and devices to facilitate the advanced characterization of BG-based grafts at different stages of the production/validation process;
2. The introduction of novel BG synthesis and manufacturing processes for their production and subsequent processing as porous bone substitutes.

47.5B bioactive glass (47.5SiO_2-2.5P_2O_5-20CaO-10MgO-10Na_2O-10K_2O, mol.%) was the common thread through all the activities described within the present work. This glass, developed in 2009 by E. Verné and co-workers, was particularly appreciated in the past due to its advantageous thermal behaviour, directly resulting from an accurate compositional design. In addition, preliminary *in vitro* and *in vivo* tests performed in the frame of this research work revealed a great potential as osteo-stimulatory graft, associated to good cytocompatibility level and exceptional osteointegrative and osteogenetic properties, without leading to a severe inflammatory response in animal *in vivo* models.

However, 50 years of research in the field of BGs have shown how their efficacy as basic material for three-dimensional porous bone grafts relies on the complex combination of multiple factors, including BG properties, determined by the

compositional features and the synthesis method, and the implemented processing strategies for obtaining porous architectures.
As a result, a fine balance between biological performances and structural requirements should be achieved, while guaranteeing high reliability and accuracy levels.

The first part of the dissertation focused on materials properties (i.e. bioactivity, crystalline microstructure and texture) and their variation as function of the synthesis route and thermal processing.

For the first time, silicate materials with complex compositions based on a six-oxide system (47.5B) were synthesized by sol-gel chemical route, representing one of the few available studies reporting the direct comparison between melt-derived and sol-gel materials having same nominal composition.
Differently from the melt-derived counterpart, characterized by a silica amorphous network, typical of glass materials, the calcination process in sol-gel products led to the nucleation of multiple crystalline phases, in part attributed to the chemical complexity of synthesis batch. As expected, sol-gel route had a clear effect on the textural properties of the final products, depending on the calcination temperature. The specific surface area (SSA) of sol-gel 47.5B-based materials, indeed, was from two to four times higher than that of melt-derived glass, but still not comparable to the values reported for sol-gel glasses with simpler formulation (few m^2/g vs. tens/hundreds of m^2/g). Nevertheless, the bioactivity of the sol-gel materials analysed was comparable to that observed in melt-derived positive control, but future cellular tests deserve to be done to assess the cytocompatibility of the materials here investigated.

Concerning the parent melt-derived glass, characterized by high bioactivity levels and exceptional biocompatibility, its effective suitability as basic material for scaffold manufacturing was further assessed by analysing microstructural modifications and devitrification phenomena occurring within the material upon sintering, as well as their effect on material densification.

First, the crystallization process of the glass was investigated under non-isothermal conditions, by the synergistic combination of different complementary methods, i.e. the Ozawa and Augis-Bennet methods for determining the JMA exponent *n*, as well as the Kissinger and Matusita-Sakka equations for assessing the crystallization activation energy. Compared to the famous 45S5 Bioglass®, still considered the golden standard among bioactive materials, the 47.5B glass exhibited lower activation energy for viscous flow (176 kJ/mol) and higher activation energy for crystallization (271 kJ/mol), indicating the possibility to achieve significant densification before the beginning of devitrification.
This peculiar aspect, combined with the high Ca/P ratio, makes it ideally possible to obtain highly densified structures in a wide sintering range, without hindering the bioactivity mechanism in contact with body fluids even upon glass devitrification.

Preparatory studies to scaffold manufacturing were carried out to investigate the sintering behaviour of the glass upon heating by isothermal DTA analyses. Within the considered observation window, powder densification was comparable in all the samples, regardless of the sintering temperature, as a result of the inhibition in viscous flow caused by the progressive crystallization of the glassy matrix at higher temperatures, leading to the nucleation of combeite and tremolite crystals above 700 °C.

In the second part of the dissertation, the focus was on scaffold manufacturing.

In particular, a comparative study on different BG-based scaffold manufacturing processes constituted the backbone of the work. Both traditional methods and additive manufacturing technologies, in combination both with sol-gel and melt-derived materials were implemented, basing on different purposes.

One of the most critical issues concerning the application of 3D porous scaffolds in the clinical management of bone defects is directly related to the need of achieving an accurate characterization of the porous microstructure able to provide a reliable forecast of scaffold behaviour after implantation.
In these regards, the present research provides a valuable contribution, addressing the issue of microstructural modifications induced by thermal processing of glass at high temperature (sintering), fundamental to achieve adequate mechanical performance in sintered products. This was possible due to a synergistic combination of accurate experimental analyses and mathematical modelling, based on well-defined physical variables.
Specifically, intrinsic permeability assessment of trabecular-like scaffolds produced by traditional foam replication was carried out by mean of a highly accurate acoustic method based on the use of a single transducer for the measure of the low-frequency sinusoidal pressure component of air flow. Results, combined with non-destructive tomographic analysis, were used as input data for a theoretical mathematical model based on the Forchheimer's theory, aimed at achieving a detailed characterization of scaffold microstructural porous features changes with sintering temperature in a range of technological interest, defined between the temperature of glass transition T_g and the end of crystallization phenomena.
The major strength of the constitutive equation proposed lies in the absence of empirical relations among terms, thus allowing to properly derive scaffold physical/microstructural properties by using as input parameters accurate experimental data supported by a robust statistical analysis.

Compared to traditional scaffold manufacturing approaches (i.e. foam replica method), additive manufacturing and, in particular, robocasting technology confirmed its higher potential in terms of repeatability and reliability of the overall procedure, with very narrow porosity ranges observed on a larger sample population and a higher regularity of the porous architecture, although profoundly different from that of natural bone.
The process was successfully implemented both with melt-derived glasses and sol-gel materials. In particular, gel-based inks showed suitable extrusion behaviour for

robocasting processing, thus allowing the deposition of straight, parallel rods constituting the 3D architecture of the scaffold by overlapped layers.
Differently from other protocols reported in literature for the robocasting of sol-gel glasses and glass-ceramic, the ink formulation developed within the present research does not require the use of additional thermal treatments, usually associated to a detrimental effect on the superior textural properties of sol-gel materials.
However, the bioactive behaviour of sol-gel derived robocast scaffolds revealed some differences with respect to the original material, suggesting the introduction of some alterations upon processing.
In these regards, given the chemical complexity of the system analysed, it is believed that the development of robocasting inks based on gels with simpler composition could be helpful in assessing the robustness of the overall procedure, thus attributing a superior scientific relevance to the manufacturing protocol here described.

In a no waste approach, two new manufacturing processes were introduced for the first time in bone scaffolds manufacturing, both based on the use of waste materials coming from other industrial fields.

First, dolomite was used to obtain 3D porous bioactive glass-based scaffolds exploiting the gas production upon thermal decomposition of calcium carbonates compounds. This strategy represents an interesting and novel example of how waste material (e.g., dolomite powder from stone processing) could be used to fabricate high-added-value products for advanced applications, in fact, morphological, structural, and bioactive properties of the obtained glass–ceramic scaffolds were found to be potentially suitable for the intended purpose.
The increase of the sintering temperature from 800 °C to 850 °C led to a favourable improved the mechanical properties of the structures under compressive loads and did not affect bioactivity in SBF. However, the approach offered poor possibilities in operating a strict control on pores generation, resulting in a low control on mechanical properties, pores size and distribution.
Further studied with suitable cell lines deserve to be performed in order to evaluate the influence of residual dolomite on cellular viability and metabolism, as well as the capability of the porous scaffold to efficiently support fluid flow and cell migration.

The second approach proposed draws inspiration from everyday life, undisputed source of inspiration in various engineering fields.
Stale bread derived from industrial wastes was used for the first time as a macroporous template for the production of BTE bioactive glass-derived scaffolds by a revised foam replication technique, properly adapted to the new organic template.
As in the previous case, the sintering temperature selected allowed us to obtain suitable mechanical properties for trabecular bone applications while preserving the

exceptional bioactivity. Globular HA was observed on the surface of the scaffold after just 48 h immersion.
Despite the speculative nature of this very preliminary study, mainly focused on demonstrating the feasibility of the approach, it was source of inspiration for an interesting Canadian study born at the University of Ottawa during the 2020 SARS-CoV-2 pandemic. In particular, Holmes and co-workers developed and validated a yeast-free "soda bread" retaining its mechanical stability over two weeks in culture conditions. The thus obtained scaffolds where characterized by a high porous architecture supporting 3D cell proliferation belonging to different lineages, showing an enormous potential not only in TE field, but also in the development of novel future food.

The development of a custom-made perfusion bioreactor for bone tissue engineering (BTE) applications represented the culmination of this research work. Considering the state of the art, bioreactor systems are the most advanced characterization tool able to provide concrete information about the biological response of BTE scaffold exposed to an *in vivo* like environment.
The developed bioreactor presented high versatility levels, given by the possibility to be used in combination with different scaffolds, both under dynamic perfusion and cell seeding conditions, thanks to an optimized perfusion circuit.
Realization costs have been contained by using fast 3D printing technologies for the production of prototypes and additional bioreactor components.
Preliminary tests aimed at validating the device in terms of ease of use, versatility, and functionality confirmed its proper functioning, with no leakage, correct fluid advance inside the circuit, according to the configuration mode, as well as absence of stagnation areas and/or air bubbles within the chamber and the tubing system.
Bioactivity tests performed under continuous SBF flowing conditions suggested the necessity to optimize flow rate in order to correctly preserve the integrity of the HA reaction layer formed upon exposure to the simulated biological fluid.
Currently, biological tests under perfusion are ongoing in order to investigate the effect of shear stress induced by fluid flow on cell metabolic pathways. In the future, mechanical stimulation given by hydrostatic pressure will be coupled with electrical stimulation to investigate the effect of multiple stimulatory on the biological outcome.

Concluding remarks

All the studies carried out in the frame of the present activity revealed the extreme adaptability of the compositional system analysed. This made it possible to explore different solutions, spacing from more traditional manufacturing approaches to innovative processing strategies, with considerable potential in all the explored fields.
In part, this could be attributed to the characteristic versatility of BGs in terms of manufacturing and processing technologies providing, still today, a continuous input to break down limitations to new solutions.

Concerning materials characterization, the combined use of different complementary methods, allowed to achieve a detailed description of the most

relevant crystallization parameters, while the simulation of the sintering process on a smaller scale allowed to qualitatively forecast the densification behaviour of BG-porous glass foams, with significant savings in time and resources.

The modelling approach undertaken in the characterization of mass transport properties of the porous foams, as well as the use of bioreactor systems to simulate the physiological environment, definitely belong to the same operating line, offering the possibility to predict the performance of the scaffold putting in place simple and cost-effective, but very accurate and reliable, technologies.

As representative example, it was possible to identify a clear dependence between glass characteristic temperatures and permeability variation, motivating future studies on other compositions aimed at assessing if the achievements reported in this thesis can have a general validity. In that case, the developed model could potentially represent a valuable tool for the characterization of glass and glass-ceramic porous materials, even beyond the biomedical field.

Finally, zero-wastes approaches described open up new scenarios in the field of scaffold manufacturing for bone tissue applications, suggesting the possibility to join the necessity to manage industrial wastes with innovative and highly sustainable tissue engineering manufacturing processes.

Thus, the backbone idea behind these, in part provocative, approaches is finally revealed: *if the ideal bone scaffold does not exist yet, what prevent us from exploring new possibilities?*

References

[1] J. D. Black and B. J. Tadros, “Bone structure: from cortical to calcium,” Orthop. Trauma, vol. 34, no. 3, pp. 113–119, 2020, doi: 10.1016/j.mporth.2020.03.002.

[2] Q. Wu et al., “Impact response and energy absorption of human skull cellular bones,” J. Mech. Behav. Biomed. Mater., vol. 81, no. October 2017, pp. 106–119, 2018, doi: 10.1016/j.jmbbm.2018.02.018.

[3] T. Hayami, M. Oka, K. Ikeuch, T. Nakamura, H. Hiroyuki, and K. Sakaguci, “The energy-absorbing function of cancellous bone and its influence on the loosening of artificial joints,” in Clinical Biomechanics and Related Research, H. Y, S. C.B., and W. S.LY., Eds. Tokyo: Springer, 1994, pp. 138–152.

[4] F. Johannesdottir and M. L. Bouxsein, “Bone structure and biomechanics,” Encycl. Endocr. Dis., vol. 4, pp. 19–30, 2018, doi: 10.1016/B978-0-12-801238-3.03760-0.

[5] C. H. Turner, “Three rules for bone adaptation to mechanical stimuli,” Bone, vol. 23, no. 5, pp. 399–407, 1998, doi: 10.1016/S8756-3282(98)00118-5.

[6] A. G. Robling, A. B. Castillo, and C. H. Turner, “Biomechanical and molecular regulation of bone remodeling,” Annu. Rev. Biomed. Eng., vol. 8, pp. 455–498, 2006, doi: 10.1146/annurev.bioeng.8.061505.095721.

[7] C. T. Rubin and L. E. Lanyon, “Osteoregulatory nature of mechanical stimuly: Function as a determinant for adaptive remodeling in bone,” J. Orthop. Res., vol. 5, no. 2, pp. 300–310, 1987.

[8] C. Ribeiro et al., “In vivo demonstration of the suitability of piezoelectric stimuli for bone reparation,” Mater. Lett., vol. 209, pp. 118–121, 2017, doi: 10.1016/j.matlet.2017.07.099.

[9] M. Gujjalapudi, C. Anam, P. Mamidi, R. Chiluka, A. Gautamkumar, and R. Bibinagar, “Effect of magnetic field on bone healing around endosseous implants – An in-vivo study,” J. Clin. Diagnostic Res., vol. 10, no. 10, pp. ZF01–ZF04, 2016, doi: 10.7860/JCDR/2016/21509.8666.

[10] T. Calcagnotto, M. M. B. Schwengber, C. C. De Antoni, D. L. De Oliveira, T. M. Vago, and J. Guilinelli, “Magnetic Field Effects on Bone Repair after Calcium Phosphate Cement Implants: Histometric and Biochemistry Evaluation,” Ann. Maxillofac. Surg., vol. 7, no. 1, pp. 18–24, 2017.

[11] E. F. Eriksen, “Cellular mechanisms of bone remodeling,” Rev. Endocr. Metab. Disord., vol. 11, no. 4, pp. 219–227, 2010, doi: 10.1007/s11154-010-9153-1.

[12] A. C. Ahn and A. J. Grodzinsky, “Relevance of collagen piezoelectricity to ‘Wolff’s Law’: A critical review,” Med. Eng. Phys., vol. 31, no. 7, pp. 733–741, 2009, doi: 10.1016/j.medengphy.2009.02.006.

[13] Julius Wolff, Das Gesetz der Transformation der Knochen. Hirschwald, Berlin, 1982.

[14] K. I. Nakahama, “Cellular communications in bone homeostasis and repair,” Cell. Mol. Life Sci., vol. 67, no. 23, pp. 4001–4009, 2010, doi: 10.1007/s00018-010-0479-3.

[15] A. M. F. S. Mohamed, “An overview of bone cells and their regulating factors of differentiation,” Malaysian J. Med. Sci., vol. 15, no. 1, pp. 4–12, 2008.

[16] R. F. Silva, G. R. da S. Sasso, E. Sasso-Cerri, M. J. Simões, and P. S. Cerri, “Biology of bone tissue: structure, function and factors that influence bone cells,” Immuno-analyse Biol. Spec., vol. 7, no. 6, pp. 17–24, 1992, doi: 10.1016/S0923-2532(05)80182-6.

[17] U. Heider, L. C. Hofbauer, I. Zavrski, M. Kaiser, C. Jakob, and O. Sezer, “Novel aspects of osteoclast activation and osteoblast inhibition in myeloma bone disease,” Biochem. Biophys. Res. Commun., vol. 338, no. 2, pp. 687–693, 2005, doi: 10.1016/j.bbrc.2005.09.146.

[18] P. Garnero, “New developments in biological markers of bone metabolism in osteoporosis,” Bone, vol. 66, pp. 46–55, 2014, doi: 10.1016/j.bone.2014.05.016.

[19] “Bone Fractures,” Available Online: https://my.clevelandclinic.org/health/diseases/15241-bone-fractures/outlook--prognosis (Last accessed: 13th June 2021).

[20] W. Wang and K. W. K. Yeung, “Bone grafts and biomaterials substitutes for bone defect repair: A review,” Bioact. Mater., vol. 2, no. 4, pp. 224–247, 2017, doi: 10.1016/j.bioactmat.2017.05.007.

[21] A. Nauth, E. Schemitsch, B. Norris, Z. Nollin, and J. T. Watson, “Critical-Size Bone Defects: Is There a Consensus for Diagnosis and Treatment ?,” vol. 32, no. 3, pp. 7–11, 2018, doi: 10.1097/BOT.0000000000001115.

[22] G. F. De Grado et al., “Bone substitutes: a review of their characteristics , clinical use , and perspectives for large bone defects management,” 2018, doi: 10.1177/2041731418776819.

[23] V. Campana et al., “Bone substitutes in orthopaedic surgery: from basic science to clinical practice,” J. Mater. Sci. Mater. Med., vol. 25, no. 10, pp. 2445–2461, 2014, doi: 10.1007/s10856-014-5240-2.

[24] P. V. Giannoudis, H. Dinopoulos, and E. Tsiridis, “Bone substitutes: An update,” Injury, vol. 36, no. 3, pp. S20–S27, 2005, doi: 10.1016/j.injury.2005.07.029.

[25] W. R. Moore, S. E. Graves, and G. I. Bain, “Synthetic bone graft substitutes,” ANZ J. Surg., vol. 71, no. 6, pp. 354–361, 2001, doi: 10.1046/j.1440-1622.2001.2128. x.

[26] J. Henkel et al., “Bone Regeneration Based on Tissue Engineering Conceptions-A 21st Century Perspective,” Bone Res., vol. 1, no. 3, pp. 216–248, 2013, doi: 10.4248/BR201303002.

[27] M. A. Fernandez-Yague, S. A. Abbah, L. McNamara, D. I. Zeugolis, A. Pandit, and M. J. Biggs, “Biomimetic approaches in bone tissue engineering: Integrating biological and physicomechanical strategies,” Adv. Drug Deliv. Rev., vol. 84, pp. 1–29, 2015, doi: 10.1016/j.addr.2014.09.005.

[28] S. K. Sarkar and B. T. Lee, “Hard tissue regeneration using bone substitutes: an update on innovations in materials.,” Korean J. Intern. Med., vol. 30, no. 3, pp. 279–293, 2015, doi: 10.3904/kjim.2015.30.3.279.

[29] L. Roseti et al., “Scaffolds for Bone Tissue Engineering: State of the art and new perspectives,” Mater. Sci. Eng. C, vol. 78, pp. 1246–1262, 2017, doi: 10.1016/j.msec.2017.05.017.

[30] A. J. El Haj and S. H. Cartmell, “Bioreactors for bone tissue engineering,” vol. 224, no. May, pp. 1523–1532, 2010, doi: 10.1243/09544119JEIM802.

[31] V. Paramesh, S. R. Kaviya, E. Anuradha, and F. D. P. Solomon, “3D Cell Culture Systems: Advantages and Applications,” J. Cell. Physiol., vol. 230, no. 1, pp. 16–26, 2015, doi: 10.1002/jcp.24683.

[32] R. Quarto and P. Giannoni, “Bone tissue Engineering: Past-Present-Future,” in Mesenchymal Stem Cells. Methods in Molecular Biology, G. M., Ed. New York: Humana Press, 2016, pp. 21–33.

[33] A. L. Boskey, “Bone composition: relationship to bone fragility and antiosteoporotic drug effects,” Bonekey Rep., vol. 2, no. DECEMBER, pp. 1–11, 2013, doi: 10.1038/bonekey.2013.181.

[34] N. Eliaz and N. Metoki, “Calcium Phosphate Bioceramics : A Review of Their History, Structure, Properties, coating Technologies and Biomedical Applications,” Materials (Basel)., vol. 10, p. 334, 2017, doi: 10.3390/ma10040334.

[35] N. Reznikov, R. Shahar, and S. Weiner, “Bone hierarchical structure in three dimensions,” Acta Biomater., vol. 10, no. 9, pp. 3815–3826, 2014, doi: 10.1016/j.actbio.2014.05.024.

[36] J. Y. Rho, L. Kuhn-Spearing, and P. Zioupos, “Mechanical properties and the hierarchical structure of bone,” Med. Eng. Phys., vol. 20, no. 2, pp. 92–102, 1998, doi: 10.1016/S1350-4533(98)00007-1.

[37] X. Wang et al., “Topological design and additive manufacturing of porous metals for bone scaffolds and orthopaedic implants: A review,” Biomaterials, vol. 83, pp. 127–141, 2016, doi: 10.1016/j.biomaterials.2016.01.012.

[38] D. J. Hadjidakis and I. I. Androulakis, “Bone remodeling,” Ann. N. Y. Acad. Sci., vol. 1092, no. October 2018, pp. 385–396, 2006, doi: 10.1196/annals.1365.035.

[39] X. Feng and J. M. McDonald, “Disorders of Bone Remodeling,” Annu. Rev. Pathol. Mech. Dis., vol. 6, no. 1, pp. 121–145, 2011, doi: 10.1146/annurev-pathol-011110-130203.

[40] X. W., S. Li, S. Pacios, Y. Wang, and D. T. Graves, “Bone remodeling under pathological conditions,” Front Oral Biol, vol. 18, pp. 17–27, 2016.

[41] X. Cao, “RANKL-RANK signaling regulates osteoblast differentiation and bone formation,” Bone Res., no. November, pp. 1–2, 2018, doi: 10.1038/s41413-018-0040-9.

[42] K. S. Houschyar et al., “Wnt Pathway in Bone Repair and Regeneration – What Do We Know So Far,” vol. 6, no. January, pp. 1–13, 2019, doi: 10.3389/fcell.2018.00170.

[43] E. F. Morgan, G. U. Unnikrisnan, and A. I. Hussein, “Bone Mechanical Properties in Healthy and Diseased States,” Annu. Rev. Biomed. Eng., vol. 20, pp. 119–143, 2018, doi: 10.1146/annurev-bioeng-062117-121139.

[44] F. G. Evans, “Factors affecting the mechanical properties of bone,” Bull. N. Y. Acad. Med., vol. 49, no. 9, pp. 751–764, 1973.

[45] J. Currey and G. Butler, “The mechanical properties of bone tissue in children,” JBJS, vol. 57, no. 6, pp. 810–814, 1975.

[46] J. D. Currey, “Effects of differences in mineralization on the mechanical properties of bone,” Philos. Trans. R. Soc. B, vol. 304, no. 1121, pp. 509–518, 1984.

[47] S. Goldstein, “The mechanical properties of trabecular bone: dependence on the anatomic location and function,” J Biomech, vol. 20, pp. 1055–1061, 1987.

[48] A. D. Woolf and K. Åkesson, “Preventing fractures in elderly people,” BMJ, vol. 327, no. 7406, pp. 89–95, 2003.

[49] T. M. Keaveny, E. F. Morgan, G. L. Niebur, and O. C. Yeh, “Biomechanics of trabecular bone,” Annu. Rev. Biomed. Eng., vol. 3, pp. 307–333, 2001.

[50] L.-C. Gerhardt and A. R. Boccaccini, “Bioactive Glass and Glass-Ceramic Scaffolds for Bone Tissue Engineering,” Materials (Basel)., vol. 3, no. 7, pp. 3867–3910, 2010, doi: 10.3390/ma3073867.

[51] D. Carter and W. Hayes, “The compressive behavior of bone as a two-phase porous structure,” J Bone Jt Surg, vol. 59A, pp. 954–962, 1977.

[52] D. Carter, G. Schwab, and D. Spengler, “Tensile fracture of can- cellous bone,” Acta Orthop Scand, vol. 51, pp. 733–741, 1980.

[53] T. Keller, Z. Mao, and D. Spengler, “Young’s modulus, bending strength, and tissue physical properties of human compact bone,” J Orthop Res, vol. 8, pp. 592–603, 1990.

[54] K. Choi and S. Goldstein, “The fatigue properties of bone tissues on a microstructural level.,” Trans. 37th Orthop. Res. Soc, vol. 16, p. 485, 1991.

[55] J. Rho, R. Ashman, and C. Turner, “Young’s modulus of trabecular and cortical bone material,” J Biomech, vol. 26, pp. 111–119, 1993.

[56] A. Ascenzi and E. Bonucci, “The compressive properties of single osteons,” Anat Rec, vol. 161, pp. 377–392, 1968.

[57] A. Ascenzi and E. Bonucci, “The tensile properties of single osteons,” Anat. Rec., vol. 158, pp. 375–386, 1967.

[58] A. Ascenzi, P. Baschieri, and A. Benvenuti, “The bending properties of single osteons,” J. Biomech., vol. 23, pp. 763–771, 1990.

[59] A. Ascenzi, P. Baschieri, and A. Benvenuti, “The torsional properties of single selected osteons,” J. Biomech., vol. 27, pp. 875–884, 1994.

[60] K. Choi, J. L. Kuhn, M. J. Ciarelli, and S. A. Goldstein, “The elastic moduli of human subchondral trabecular, and cortical bone tissue and the size-dependency of cortical bone modulus,” J. Biomech., vol. 23, pp. 1103–1113, 1990.

[61] R. B. Ashman and J. Y. Rho, “Elastic modulus of trabecular bone material,” J. Biomech., vol. 21, pp. 177–181, 1988.

[62] G. H. Bourne, The Biochemistry and physiology of bone, Revised. Elsevier, 2014.

[63] E. Fukada and I. Yasuda, “On the Piezoelectric Effect of Bone,” J. Phys. Soc. Japan, vol. 12, no. 10, pp. 1158–1162, 1957, doi: 10.1143/JPSJ.12.1158.

[64] H. G. Haas and W. Trautwein, “Piezoelectric effect in bone,” Nature, vol. 4862, p. 81, 1963.

[65] A. A. Marino and R. O. Becker, “Origin of the Piezoelectric Effect in Bone,” Calcif. Tissue Res., vol. 8, pp. 177–180, 1971.

[66] H. Athenstaedt, “Pyroelectric and piezoelectric properties of vertebrates,” Ann. N. Y. Acad. Sci., vol. 238, no. 1, 1974.

[67] M. I. Kay, R. A. Young, and A. S. Posner, “Crystal structure of hydroxyapatite,” Nature, vol. 294, pp. 1050–1052, 1964.

[68] A. Gruyerman, D. Wu, B. J. Rodriguez, S. V. Kalinin, and S. Habelitz, “High resolution imaging of proteins in human teeth by scanning probe microscopy,” Biochem. Biophys. Res. Commun., vol. 352, pp. 142–146, 2007.

[69] S. B. Lang et al., “Ferroelectric polarization in nanocrystalline hydroxyapatite thin films on silicon,” Sci. Rep., vol. 3, pp. 1–6, 2013, doi: 10.1038/srep02215.

[70] L. Calderín, M. J. Stott, and A. Rubio, “Electronic and crystallographic structure of apatites,” Phys. Rev. B, vol. 67, p. 134106, 2003.

[71] A. H. Rajabi, M. Jaffe, and T. L. Arinzeh, “Piezoelectric materials for tissue regeneration: A review,” Acta Biomater., vol. 24, pp. 12–23, 2015, doi: 10.1016/j.actbio.2015.07.010.

[72] C. Halperin et al., “Piezoelectric effect in human bones studied in nanometer scale,” Nano Lett., vol. 4, no. 7, pp. 1253–1256, 2004, doi: 10.1021/nl049453i.

[73] H. P. Wiesmann, M. Hartig, U. Stratmann, U. Meyer, and U. Joos, “Electrical stimulation influences mineral formation of osteoblast-like cells in vitro,” Biochim. Biophys. Acta - Mol. Cell Res., vol. 1538, no. 1, pp. 28–37, 2001, doi: 10.1016/S0167-4889(00)00135-X.

[74] C. Y. Su, T. Fang, and H. W. Fang, “Effects of Electrostatic Field on Osteoblast Cells for Bone Regeneration Applications,” Biomed Res. Int., vol. 2017, 2017, doi: 10.1155/2017/7124817.

[75] J. Jacob, N. More, K. Kalia, and G. Kapusetti, “Piezoelectric smart biomaterials for bone and cartilage tissue engineering,” Inflamm. Regen., vol. 38, no. 1, pp. 1–11, 2018, doi: 10.1186/s41232-018-0059-8.

[76] J. A. McAuliffe, “Bone graft substitutes,” J. Hand Ther., vol. 16, no. 2, pp. 180–187, 2003, doi: 10.1016/S0894-1130(03)80013-3.

[77] F. J. O’Brien, “Biomaterials & scaffolds for tissue engineering,” Mater. Today, vol. 14, no. 3, pp. 88–95, 2011, doi: 10.1016/S1369-7021(11)70058-X.

[78] T. Albrektsson and C. Johansson, “Osteoinduction, osteoconduction and osseointegration,” Eur. Spine J., vol. 10, pp. S96–S101, 2001.

[79] H. C. Pape, A. Evans, and P. Kobbe, “Autologous Bone Graft: Properties and Techniques,” vol. 24, no. 3, pp. 36–40, 2010.

[80] N. Shibuya and D. C. Jupiter, “Bone graft substitute: allograft and xenograft,” Clin. Podiatr. Med. Surg., vol. 32, no. 1, pp. 21–34, 2015.

[81] M. Fazlollahi, Y. Pooshidani, and M. Eskandari, “Additive manufacturing in bone tissue engineering,” in 3D Printing in Biomedical Engineering. Materials Horizons: From Nature to Nanomaterials, S. S., P. C., and S. R., Eds. Springer, Singapore, 2020, pp. 95–125.

[82] M. M. Stevens, “Biomaterials for bone tissue engineering,” Mater. Today, vol. 11, no. 5, pp. 18–25, 2008.

[83] Z. Sheikh, S. Najeeb, Z. Khurshid, V. Verma, H. Rashid, and M. Glogauer, “Biodegradable Materials for Bone Repair and Tissue Engineering Applications,” Materials (Basel)., vol. 8, pp. 5744–5794, 2015, doi: 10.3390/ma8095273.

[84] H. Koch, R. Gruberab, B. A. Doll, F. Tegtmeier, and T. A. E. J. O.Hollingerb, “Fracture healing in the elderly patient,” Exp. Gerontol., vol. 41, no. 11, pp. 1080–1093, 2006.

[85] C. H. Turner, M. R. Forwood, and M. W. Otter, “Mechanotransduction in bone: do bone cells act as sensors of fluid flow?,” FASEB J., vol. 8, pp. 875–878, 1994, doi: 10.1096/fasebj.8.11.8070637.

[86] A. R. Amini, C. T. Laurencin, and S. P. Nukavarapu, “Bone tissue engineering: Recent advances and challenges,” Crit Rev Biomed Eng, vol. 40, no. 5, pp. 363–408, 2013.

[87] S. D. Scriven, C. Booth, D. F. M. Thomas, L. K. Trejdosiewicz, and J. Southgate, “Reconstrruction of Human urothelium from monolayer cultures,” J. Urol., vol. 158, no. 3, pp. 1147–1152, 1997.

[88] K. Vig et al., “Advances in skin regeneration using tissue engineering,” Int. J. Mol. Sci., vol. 18, no. 4, 2017, doi: 10.3390/ijms18040789.

[89] H.-C. Chen and Y.-C. Hu, “Bioreactors for tissue engineering,” Biotechnol. Lett., vol. 28, pp. 1415–1423, 2006.

[90] R. F. Canadas, A. P. Marques, R. L. Reis, and J. M. Oliveir, “Bioreactors and microfluidics for osteochondral interface maturation,” in Osteochondral Tissue Engineering. Advances in Experimental Medicine and Biology, J. Oliveira, P. S., R. R., and S. R. J, Eds. Springer, Cham, 2018, pp. 395–420.

[91] S. H. Cartmell and A. J. El Haj, “Mechanical bioreactors for bone tissue engineering,” in Bioreactors for Tissue engineering, C. J. and A.-R. M., Eds. Springer, Dordrecht, 2005, pp. 193–208.

[92] I. Marijanovic, M. Antunovic, I. Matic, M. Panek, and A. Ivkovic, “Bioreactor-Based Bone Tissue Engineering,” in Advanced techniques in Bone Regeneration, A. R. Zorzi and J. B. de Miranda, Eds. IntechOpen, 2016, pp. 223–252.

[93] M. Sladkova and G. M. De Peppo, “Bioreactor systems for human bone tissue angineering,” Processes, vol. 2, pp. 494–525, 2014.

[94] D. A. Gaspar et al., “The role of perfusion bioreactors in bone tissue engineering,” Biomatter, vol. 2, no. 4, pp. 1–9, 2012, doi: 10.4161/biom.22170.

[95] M. Jagodzinski, A. Breitbart, M. Wehmeier, E. Hesse, and C. Haasper, “Influence of perfusion and cyclic compression on proliferation and differentiation of bone marrow stromal cells in 3-dimensional culture,” vol. 41, pp. 1885–1891, 2008, doi: 10.1016/j.jbiomech.2008.04.001.

[96] Gregory N. Bancroft, V. I. Sikavitsas, and A. G. Mikos, “Technical Note: Design of a Flow Perfusion Bioreactor System for Bone Tissue-Engineering Applications,” Tissue Eng., vol. 9, no. 3, pp. 549–554, 2004.

[97] F. Zhao, B. Van Rietbergen, K. Ito, and S. Hofmann, “Flow rates in perfusion bioreactors to maximise mineralisation in bone tissue engineering in vitro,” J. Biomech., vol. 79, pp. 232–237, 2018, doi: 10.1016/j.jbiomech.2018.08.004.

[98] F. W. Janssen, J. Oostra, A. Oorschot, and C. A. Van Blitterswijk, “A perfusion bioreactor system capable of producing clinically relevant volumes of tissue-engineered bone: in vivo bone formation showing proof of concept,” Biomaterials, vol. 27, pp. 315–323, 2006.

[99] A. R. Saatchi, H. Seddiqi, G. Amoabediny, M. N. Helder, B. Zandieh Doulabi, and J. Klein Nulend, “Computational Fluid Dynamics in 3D-Printed Scaffolds with Different Strand-Orientation in Perfusion Bioreactors,” Iran. J. Chem. Chem. Eng., vol. 39, no. 5, pp. 307–320, 2020.

[100] H. Nokhbatolfoghahaei, M. Bohlouli, and K. Adavi, “Computational modeling of media flow through perfusion-based bioreactors for bone tissue engineering,” vol. 234, no. 12, pp. 1397–1408, 2020, doi: 10.1177/0954411920944039.

[101] B. Bhaskar, R. Owen, H. Bahmaee, P. S. Rao, and G. C. Reilly, “Design and Assessment of a Dynamic Perfusion Bioreactor for Large Bone Tissue Engineering Scaffolds,” Appl. Biochem. Biotechnol., vol. 185, pp. 555–563, 2018.

[102] E. Stavenschi, M. Labour, and D. A. Hoey, “Oscillatory fluid flow induces the osteogenic lineage commitment of mesenchymal stem cells: The effect of shear stress magnitude , frequency , and duration,” J. Biomech., vol. 55, pp. 99–106, 2017, doi: 10.1016/j.jbiomech.2017.02.002.

[103] D. Greenspan, “Bioglass at 50-A look at Larry Hench’s legacy and bioactive materials,” Biomed. Glas., vol. 5, no. 1, pp. 178–184, 2019, doi: 10.1515/bglass-2019-0014.

[104] J. V Rau, I. Antoniac, G. Cama, V. S. Komlev, and A. Ravaglioli, “Bioactive Materials for Bone Tissue Engineering,” Biomed Res. Int., vol. 2016, p. 3741428, 2016.

[105] L. L. Hench, “Genetic design of bioactive glasses,” J. Eur. Ceram. Soc., vol. 29, pp. 1257–1265, 2008.

[106] I. D. Xynos, A. J. Edgar, L. D. K. Buttery, L. L. Hench, and J. M. Polak, “Gene-expression profiling of human osteoblasts following treatment with the ionic products of Bioglass® 45S5 dissolution,” J. Biomed. Mater. Res., vol. 55, no. 2, pp. 151–157, 2001, doi: 10.1002/1097-4636(200105)55:2<151: AID-JBM1001>3.0.CO;2-D.

[107] D. C. Greenspan, “Bioactive glass: mechanisms of bone bonding,” Tandläkartidningen Årk, vol. 91, no. 8, pp. 1–32, 1999.

[108] L. L. Hench, D. L. Wheeler, and D. C. Greenspan, “Molecular Control of Bioactivity in sol-gel glasses,” J. Sol-Gel Sci. Technol., vol. 13, pp. 245–250, 1998, doi: 10.1023/A.

[109] L. L. Hench, “The story of Bioglass®,” J. Mater. Sci. Mater. Med., vol. 17, no. 11, pp. 967–978, 2006, doi: 10.1007/s10856-006-0432-z.

[110] A. Yao, D. Wang, W. Huang, Q. Fu, M. N. Rahaman, and D. E. Day, “In vitro bioactive characteristics of borate-based glasses with controllable degradation behavior,” J. Am. Ceram. Soc., vol. 90, no. 1, pp. 303–306, 2007, doi: 10.1111/j.1551-2916.2006.01358. x.

[111] E. A. Abou Neel, D. M. Pickup, S. P. Valappil, R. J. Newport, and J. C. Knowles, “Bioactive functional materials: a perspective on phosphate-based glasses,” J. Mater. Chem., vol. 19, no. 6, pp. 690–701, 2009, doi: 10.1039/B810675D.

[112] P. Balasubramanian, T. Büttner, V. M. Pacheco, and A. R. Boccaccini, “Boron-containing bioactive glasses in bone and soft tissue engineering,” J. Eur. Ceram. Soc., vol. 38, no. 3, pp. 855–869, 2018, doi: 10.1016/j.jeurceramsoc.2017.11.001.

[113] R. Shah, D. Ready, J. C. Knowles, N. P. Hunt, and M. P. Lewis, “Sequential identification of a degradable phosphate glass scaffold for skeletal muscle regeneration,” J. Tissue Eng. Regen. Med., vol. 8, no. 10, pp. 801–810, 2014.

[114] H. R. Fernandes, A. Gaddam, A. Rebelo, D. Brazete, G. E. Stan, and J. M. F. Ferreira, “Bioactive glasses and glass-ceramics for healthcare applications in bone regeneration and tissue engineering,” Materials (Basel)., vol. 11, no. 12, pp. 1–54, 2018, doi: 10.3390/ma11122530.

[115] V. Miguez-pacheco and D. Greenspan, “Bioactive glasses in soft tissue repair,” Am. Ceram. Soc. Bull., vol. 94, no. 6, pp. 27–31, 2015.

[116] F. Baino et al., “Fe-doped sol-gel glasses and glass-ceramics for magnetic hyperthermia,” Materials (Basel)., vol. 11, no. 1, 2018, doi: 10.3390/ma11010173.

[117] S. Kargozar, M. Mozafari, S. Hamzehlou, H. W. Kim, and F. Baino, “Mesoporous bioactive glasses (MBGs) in cancer therapy: Full of hope and promise,” Mater. Lett., vol. 251, pp. 241–246, 2019, doi: 10.1016/j.matlet.2019.05.019.

[118] J. Hum and A. R. Boccaccini, “Bioactive glasses as carriers for bioactive molecules and therapeutic drugs: A review,” J. Mater. Sci. Mater. Med., vol. 23, no. 10, pp. 2317–2333, 2012, doi: 10.1007/s10856-012-4580-z.

[119] S. Kargozar, M. Mozafari, S. Hamzehlou, and F. Baino, “Using bioactive glasses in the management of burns,” Front. Bioeng. Biotechnol., vol. 7, no. MAR, pp. 1–12, 2019, doi: 10.3389/fbioe.2019.00062.

[120] F. Baino, G. Novajra, V. Miguez-pacheco, A. R. Boccaccini, and C. Vitale-Brovarone, “Bioactive glasses: Special applications outside the skeletal system,” J. Non. Cryst. Solids, vol. 432, no. Part A, pp. 15–30, 2016.

[121] Q. Fu, E. Saiz, M. N. Rahaman, and A. P. Tomsia, “Bioactive glass scaffolds for bone tissue engineering: state of the art and future perspectives,” Mater. Sci. Eng. C, vol. 31, no. 7, pp. 1245–1256, 2011, doi: 10.1016/j.msec.2011.04.022.

[122] F. Baino, G. Novajra, and C. Vitale-Brovarone, “Bioceramics and Scaffolds: A Winning Combination for Tissue Engineering,” Front. Bioeng. Biotechnol., vol. 3, no. December, pp. 1–17, 2015, doi: 10.3389/fbioe.2015.00202.

[123] L. L. Hench, “Chronology of Bioactive Glass Development and Clinical Applications,” New J. Glas. Ceram., vol. 03, no. 02, pp. 67–73, 2013, doi: 10.4236/njgc.2013.32011.

[124] J. H. C. Lin, K. H. Kuo, S. J. Ding, and C. P. Ju, “Surface reaction of stoichiometric and calcium-deficient hvdroxyapatite in simulated body fluid,” J. Mater. Sci. Mater. Med., vol. 12, no. 8, pp. 731–741, 2001, doi: 10.1023/A:1011280828663.

[125] J. Serra et al., “Influence of the non-bridging oxygen groups on the bioactivity of silicate glasses,” J. Mater. Sci. Mater. Med., vol. 13, no. 12, pp. 1221–1225, 2002, doi: 10.1023/A:1021174912802.

[126] G. Kaur, G. Pickrell, N. Sriranganathan, V. Kumar, and D. Homa, “Review and the state of the art: Sol–gel and melt quenched bioactive glasses for tissue engineering,” J. Biomed. Mater. Res., vol. 104, no. 6, pp. 1248–1275, 2015.

[127] L. L. Hench and J. K. West, “The sol-gel process,” Chem. Rev., vol. 90, no. 1, pp. 33–72, 1990, doi: 10.1021/cr00099a003.

[128] R. Gupta and A. Kumar, “Bioactive materials for biomedical applications using sol-gel technology,” Biomed. Mater., vol. 3, no. 3, 2008, doi: 10.1088/1748-6041/3/3/034005.

[129] O. P. Filho, G. P. Latorre, and L. L. Hench, “Effect of crystallization on apatite-layer formation of bioactive glass 45S5,” J. Biomed. Mater. Res., vol. 30, no. 4, pp. 509–514, 1996, doi: 10.1002/(SICI)1097-4636(199604)30:4<509: AID-JBM9>3.0.CO;2-T.

[130] J. R. Jones, “Review of bioactive glass: From Hench to hybrids,” Acta Biomater., vol. 9, no. 1, pp. 4457–4486, 2013, doi: 10.1016/j.actbio.2012.08.023.

[131] E. J. A. Pope and J. D. Mackenzie, “Sol-gel processing of silica. II. The role of the catalyst,” J. Non. Cryst. Solids, vol. 87, no. 1–2, pp. 185–198, 1986, doi: 10.1016/S0022-3093(86)80078-3.

[132] T. H. E. Role, O. F. The, C. P. Of, and S. Glass, “H Apter - the Role of the Catalyst in Sol-Gel Processing of Silica.”

[133] Ö. Kesmez, E. Burunkaya, N. Kiraz, H. E. Çamurlu, M. Asiltürk, and E. Arpaç, “Effect of acid, water and alcohol ratios on sol-gel preparation of antireflective amorphous SiO2 coatings,” J. Non. Cryst. Solids, vol. 357, no. 16–17, pp. 3130–3135, 2011, doi: 10.1016/j.jnoncrysol.2011.05.003.

[134] J. R. Jones, “Reprint of: Review of bioactive glass: From Hench to hybrids,” Acta Biomater., vol. 23, no. S, pp. S53–S82, 2015, doi: 10.1016/j.actbio.2015.07.019.

[135] D. Arcos and M. Vallet-Regí, “Sol-gel silica-based biomaterials and bone tissue regeneration,” Acta Biomater., vol. 6, no. 8, pp. 2874–2888, 2010, doi: 10.1016/j.actbio.2010.02.012.

[136] G. J. et al. Owens, “Sol-gel based materials for biomedical applications,” Prog Mater Sci, vol. 77, pp. 1–79, 2016.

[137] I. Izquierdo-Barba and M. Vallet-Regi, “Mesoporous bioactive glasses: relevance of their porous structure compared to that of classical bioglasses.,” Biomed. Glas., vol. 1, pp. 140–150, 2015.

[138] A. López-Noriega, D. Arcos, I. Izquierdo-Barba, Y. Sakamoto, O. Terasaki, and M. Vallet-Regí, “Ordered mesoporous bioactive glasses for bone tissue regeneration,” Chem. Mater., vol. 18, no. 13, pp. 3137–3144, 2006, doi: 10.1021/cm060488o.

[139] I. D. Thompson and L. L. Hcnch, “Mechanical properties of bioactive glasses, glass-ceramics and composites,” Proc. Inst. Mech. Eng. Part H J. Eng. Med., vol. 212, no. 2, pp. 127–136, 1998, doi: 10.1243/0954411981533908.

[140] W. Holand, “Glass-Ceramics,” in Bio-Glasses. An Introduction, 1st ed., J. R. Jones and A. G. Clare, Eds. John Wiley & Sons, Ltd, 2012, pp. 97–105.

[141] E. D. Zanotto, “A bright future for glass-ceramics,” Am. Ceram. Soc. Bull., vol. 89, no. 8, pp. 19–27, 2010.

[142] M. Plewinsky, K. Schickle, M. Lindner, A. Kirsten, M. Weber, and H. Fischer, “The effect of crystallization of bioactive bioglass 45S5 on apatite formation and degradation,” Dent. Mater., vol. 29, no. 12, pp. 1256–1264, 2013.

[143] W. Holand and G. H. Beall, Glass Ceramic Technology, 3rd ed. John Wiley & Sons, 2019.

[144] J. R. Jones, L. M. Ehrenfried, and L. L. Hench, “Optimizing bioactive glass scaffolds for bone tissue engineering,” Biomaterials, vol. 27, no. 7, pp. 964–973, 2006.

[145] F. Baino et al., “Processing methods for making porous bioactive glass-based scaffolds—A state-of-the-art review,” Int. J. Appl. Ceram. Technol., vol. 16, no. 5, pp. 1762–1796, 2019, doi: 10.1111/ijac.13195.

[146] M. O. Prado, E. B. Ferreira, and E. D. Zanotto, “Sintering kinetics of crystallizing glass particles. a review,” Ceram. Trans., vol. 170, no. August 2014, pp. 163–179, 2005, doi: 10.1002/9781118408063.ch13.

[147] S. Wu, H. Hsu, S. Hsiao, and W. Ho, “Preparation of porous 45S5 BioglassVR -derived glass ceramic scaffolds by using rice husk as a porogen additive,” J. Mater. Sci. Mater. Med., vol. 20, pp. 1229–1236, 2009.

[148] C. Vitale-Brovarone, E. Vernè, M. Bosetti, P. Appendino, and M. Cannas, "Microstructural and in vitro characterization of SiO2-Na2O-CaO-MgO glass-ceramic bioactive scaffolds for bone substitutes," J. Mater. Sci. Mater. Med., vol. 16, no. 10, pp. 909–917, 2005.

[149] C. Vitale-Brovarone, E. Verné, and P. Appendino, "Macroporous bioactive glass-ceramic scaffolds for tissue engineering," J. Mater. Sci. Mater. Med., vol. 17, no. 11, pp. 1069–1078, 2006.

[150] Q. Z. Chen, I. D. Thompson, and A. R. Boccaccini, "45S5 Bioglass®-derived glass-ceramic scaffolds for bone tissue engineering," Biomaterials, vol. 27, no. 11, pp. 2414–2425, 2006, doi: 10.1016/j.biomaterials.2005.11.025.

[151] "A. W. Somers, 'Method of Making Ceramic Articles,' 1963."

[152] Y. Park, K. Kim, K. Kim, S. Choi, C. Kim, and R. Legeros, "Feasibility of three-dimensional macroporous scaffold using calcium phosphate glass and polyurethane sponge," J. Mater. Sci., vol. 41, pp. 4357–4364, 2006.

[153] C. J. Brinker, Y. Lu, A. Sellinge, and H. Fan, "Evaporation-Induced Self-Assembly: Nanostructures Made Easy," Adv. Mater., vol. 11, no. 7, pp. 579–585, 1999.

[154] Y. Zhu et al., "Preparation, characterization and in vitro bioactivity of mesoporous bioactive glasses (MBGs) scaffolds for bone tissue engineering," Microporous Mesoporous Mater., vol. 112, pp. 494–503, 2008.

[155] Y. Zhu and S. Kaskel, "Comparison of the in vitro bioactivity and drug release property of mesoporous bioactive glasses (MBGs) and bioactive glasses (BGs) scaffolds," Microporous Mesoporous Mater., vol. 118, no. 1–3, pp. 176–182, 2009.

[156] C. Wu et al., "Multifunctional magnetic mesoporous bioactive glass scaffolds with a hierarchical pore structure," Acta Biomater., vol. 7, no. 10, pp. 3563–3572, 2011, doi: 10.1016/j.actbio.2011.06.028.

[157] P. Jiang, H. Lin, R. Xing, J. Jiang, and F. Qu, "Synthesis of multifunctional macroporous-mesoporous TiO2- bioglasses for bone tissue engineering," J. Sol-Gel Sci. Technol., vol. 61, no. 2, pp. 421–428, 2012.

[158] E. Boccardi, A. Philippart, J. A. Juhasz-Bortuzzo, G. Novajra, C. Vitale-Brovarone, and A. R. Boccaccini, "Characterisation of Bioglass based foams developed via replication of natural marine sponges," Adv. Appl. Ceram., vol. 114, no. sup1, pp. S56–S62, 2015, doi: 10.1179/1743676115Y.0000000036.

[159] J. Ma, H. Lin, X. Li, C. Bian, D. Xiang, and F. Qu, "Synthesis of hierarchical porous bioactive glasses for bone tissue regeneration," IET Nanobiotechnology, vol. 8, pp. 216–221, 2014.

[160] X. Han, X. Li, and H. Lin, "Hierarchical meso – macroporous bioglass for bone tissue engineering," pp. 33–39, 2014, doi: 10.1007/s10971-014-3270-3.

[161] W. Xia and J. Chang, “Bioactive glass scaffold with similar structure and mechanical properties of cancellous bone,” J. Biomed. Mater. Res. - Part B Appl. Biomater., vol. 95 B, no. 2, pp. 449–455, 2010, doi: 10.1002/jbm.b.31736.

[162] Q. Z. Chen, I. D. Thompson, and A. R. Boccaccini, “45S5 Bioglass - derived glass – ceramic scaffolds for bone tissue engineering,” Biomaterials, vol. 27, pp. 2414–2425, 2006, doi: 10.1016/j.biomaterials.2005.11.025.

[163] F. Baino, M. Ferraris, O. Bretcanu, E. Verné, and C. Vitale-Brovarone, “Optimization of composition, structure and mechanical strength of bioactive 3-D glass-ceramic scaffolds for bone substitution,” J. Biomater. Appl., vol. 27, pp. 872–890, 2013.

[164] F. Baino and C. Vitale-Brovarone, “Mechanical properties and reliability of glass-ceramic foam scaffolds for bone repair,” Mater. Lett., vol. 118, pp. 27–30, 2014, doi: 10.1016/j.matlet.2013.12.037.

[165] C. Wu, Y. Zhang, Y. Zhu, T. Friis, and Y. Xiao, “Structure-property relationships of silk-modified mesoporous bioglass scaffolds,” Biomaterials, vol. 31, no. 13, pp. 3429–3438, 2010, doi: 10.1016/j.biomaterials.2010.01.061.

[166] P. Sepulveda, J. R. Jones, and L. L. Hench, “Bioactive sol-gel foams for tissue repair,” J. Biomed. Mater. Res., vol. 59, no. 2, pp. 340–348, 2002, doi: 10.1002/jbm.1250.

[167] J. R. Jones, “Bioactive Glass as Synthetic Bone Grafts and Scaffolds for Tissue Engineering,” in Bio-Glasses: An Introduction, J. R. Jones and A. G. Clare, Eds. Chichester (UK): John Wiley & Sons, Ltd, 2012, pp. 177–201.

[168] M. Navarro et al., “New macroporous calcium phosphate glass ceramic for guided bone regeneration,” Biomaterials, vol. 25, no. 18, pp. 4233–4241, 2004.

[169] Z. Y. Wu, R. G. Hill, S. Yue, D. Nightingale, P. D. Lee, and J. R. Jones, “Melt-derived bioactive glass scaffolds produced by a gel-cast foaming technique,” Acta Biomater., vol. 7, no. 4, pp. 1807–1816, 2011, doi: 10.1016/j.actbio.2010.11.041.

[170] I. Gibson, D. Rosen, and B. Stucker, Additive manufacturing Technologies. New York: Springer, 2014.

[171] O. Ivanova, C. Williams, M. Engineering, V. Tech, and T. Campbell, “Additive manufacturing (AM) and nanotechnology: promises and challenges,” Rapid Prototype J., vol. 19, no. 5, pp. 353–364, 2013.

[172] R. J. Morrison et al., “Regulatory Considerations in the Design and Manufacturing of Implantable 3D-Printed Medical Devices,” Clin. Transl. Sci., vol. 8, no. 5, pp. 594–600, 2015, doi: 10.1111/cts.12315.

[173] Y. Huang, M. C. Leu, J. Mazumder, and A. Donmez, “Additive Manufacturing: Current State, Future Potential, Gaps and Needs, and Recommendations,” J. Manuf. Sci. Eng., vol. 137, no. 1, p. 014001, 2015.

[174] F. Rengier et al., “3D printing based on imaging data: review of medical applications,” Int. J. Comput. Assist. Radiol. Surg., vol. 5, pp. 335–341, 2010.

[175] M. P. Chhaya, P. S. P. Poh, E. R. Balmayor, M. Van Griensven, J.-T. Shantz, and D. W. Hutmacher, “Additive manufacturing in biomedical sciences and the need for definitions and norms,” Expert Rev. Med. Devices, vol. 12, no. 5, pp. 537–543, 2015.

[176] S. Bose, S. Vahabzadeh, and A. Bandyopadhyay, “Bone tissue engineering using 3D printing,” Mater. Today, vol. 16, no. 12, pp. 496–504, 2013, doi: 10.1016/j.mattod.2013.11.017.

[177] J. W. Lee, J. Y. Kim, and D. W. Cho, “Solid free-form fabrication technology and its application to bone tissue engineering,” Int. J. Stem Cells, vol. 3, no. 2, pp. 85–95, 2010, doi: 10.15283/ijsc.2010.3.2.85.

[178] B. Lechner, R. Detsch, and A. R. Boccaccini, “Additive Manufacturing of Bioactive Glasses and Silicate Bioceramics,” no. June, 2015, doi: 10.4416/JCST2015-00001.

[179] Q. Fu, E. Saiz, and A. P. Tomsia, “Direct ink writing of highly porous and strong glass scaffolds for load-bearing bone defects repair and regeneration,” Acta Biomater., vol. 7, no. 10, pp. 3547–3554, 2011.

[180] J. Franco, P. Hunger, M. E. Launey, A. P. Tomsia, and E. Saiz, “Direct write assembly of calcium phosphate scaffolds using a water-based hydrogel,” Acta Biomater., vol. 6, no. 1, pp. 218–228, 2010.

[181] X. Liu, M. N. Rahaman, G. E. Hilmas, and B. S. Bal, “Mechanical properties of bioactive glass (13–93) scaffolds fabricated by robotic deposition for structural bone repair,” Acta Biomater., vol. 9, no. 6, pp. 7025–7034, 2013.

[182] S. Eqtesadi, A. Motealleh, A. Pajares, F. Guiberteau, and P. Miranda, “Improving mechanical properties of 13 – 93 bioactive glass robocast scaffold by poly (lactic acid) and poly (ε -caprolactone) melt in fi ltration,” J. Non. Cryst. Solids, vol. 432, pp. 111–119, 2016, doi: 10.1016/j.jnoncrysol.2015.02.025.

[183] S. Eqtesadi, A. Motealleh, P. Miranda, A. Pajares, A. Lemos, and J. M. F. Ferreira, “Robocasting of 45S5 bioactive glass scaffolds for bone tissue engineering,” J. Eur. Ceram. Soc., vol. 34, no. 1, pp. 107–118, 2014, doi: 10.1016/j.jeurceramsoc.2013.08.003.

[184] A. Motealleh, S. Eqtesadi, A. Civantos, A. Pajares, and P. Miranda, “Robocast 45S5 bioglass scaffolds: in vitro behavior,” J. Mater. Sci., vol. 52, no. 15, pp. 9179–9191, 2017.

[185] A. M. Deliormanli and M. N. Rahaman, “Direct-write assembly of silicate and borate bioactive glass scaffolds for bone repair,” J. Eur. Ceram. Soc., vol. 32, no. 14, pp. 3637–3646, 2012.

[186] J. Cesarano, “Robocasting of ceramics and composites using fine particle suspensions,” University Libraries UNT Digital Library. 1999.

[187] J. A. Lewis, “Direct-write assembly of ceramics from colloidal inks,” Curr. Opin. Solid State Mater. Sci., vol. 6, no. 3, pp. 245–250, 2002.

[188] J. A. Lewis, J. E. Smay, J. Stuecker, and J. Cesarano, “Direct ink writing of three-dimensional ceramic structures, J. Am. Ceram. Soc.,” J. Am. Ceram. Soc., vol. 89, no. 12, pp. 3599–3609, 2006.

[189] E. Fiume and F. Baino, “Robocasting of mesoporous bioactive glasses (MBGs) for bone tissue engineering,” in Bioceramics-From Macro to Nanoscale, A. Osaka and R. Narayan, Eds. Elsevier, 2020, pp. 327–349.

[190] J. Barberi et al., “Robocasting of SiO2-based bioactive glass scaffolds with porosity gradient for bone regeneration and potential load-bearing applications,” Materials (Basel)., vol. 12, no. 7, 2019, doi: 10.3390/ma12172691.

[191] E. Verné et al., “Early Stage Reactivity and In Vitro Behavior of Silica-Based Bioactive Glasses and Glass-Ceramics,” J. Mater. Sci. Med., vol. 20, no. 1, pp. 75–87, 2009.

[192] P. Sepulveda, J. R. Jones, and L. L. Hench, “Characterization of Melt-Derived 45S5 and sol-gel-derived 58S Bioactive Glasses,” J. Biomed. Mater. Res., vol. 58, no. 6, pp. 734–740, 2001, doi: 10.1002/jbm.0000.

[193] M. S. Bahniuk, H. Pirayesh, H. D. Singh, J. A. NychKa, and L. D. Unsworth, “Bioactive Glass 45S5 Powders: Effect of Synthesis Route and Resultant Surface Chemistry and Crystallinity on Protein Adsorption from Human Plasma,” Biointerphases, vol. 4, p. 14, 2012.

[194] T. Kokubo and H. Takadama, “How useful is SBF in predicting in vivo bone bioactivity?,” Biomaterials, vol. 27, no. 15, pp. 2907–2915, 2006, doi: 10.1016/j.biomaterials.2006.01.017.

[195] A. L. B. Macon et al., “A unified in vitro evaluation for apatite-forming ability of bioactive glasses and their variants,” J. Mater. Sci. Mater. Med., vol. 26, no. 2, p. 115, 2015, doi: 10.1007/s10856-015-5403-9.

[196] S. Brunauer, P. H. Emmet, and E. Teller, “Adsorption of gases in multimolecular layers,” J. Am. Ceram. Soc., vol. 60, pp. 309–319, 1938.

[197] M. Avrami, “Kinetics of Phase Change. I General Theory,” J. Chem. Phys., vol. 7, p. 1103, 1939.

[198] J. Malek, “Kinetic analysis of crystallization processes in amorphous materials,” Thermochim. Acta, vol. 355, pp. 239–253, 2000.

[199] T. Ozawa, “Kinetics of Non-Isothermal Crystallization,” Polymers (Basel)., vol. 12, pp. 150–158, 1971.

[200] J. A. Augis and J. E. Bennett, “Calculation of the Avrami parameters for heterogeneous solid-state reactions using a modification of the Kissinger method,” J. Therm. Anal., vol. 13, pp. 283–292, 1978.

[201] H. E. KIssinger, “Variation of peak temperature with heating rate in differential thermal analysis,” J. Res. Nat. Bur. Stand., vol. 57, pp. 217–221, 1956.

[202] K. Matusita, S. Sakka, and Y. Matsui, “Determination of the activation energy for crystal growth by differential thermal analysis,” J. Mater. Sci., vol. 10, pp. 961–966, 1975.

[203] K. Matusita and S. Sakka, “Kinetic Study of Crystallization of Glass by Differential Thermal Analysis - Criterion on Application of Kissinger Plot,” J. Non. Cryst. Solids, vol. 38–39, pp. 471–476, 1980.

[204] K. Matusita, T. Komatsu, and R. Yokota, “Kinetics of non-isothermal crystallization process and activation energy for crystal growth in amorphous materials,” J. Mater. Sci., vol. 19, pp. 291–296, 1984.

[205] A. A. Francis, R. D. Rawlings, and A. R. Sweeney, R.; Boccaccini, “Crystallization Kinetic of Glass Particles Prepared from a Mixture of Coal Ash and Soda-Lime Cullet Glass,” J. Non. Cryst. Solids, vol. 333, pp. 187–193, 2004.

[206] J. Malek and T. Mitsuhashi, “Testing Method for the Johnson–Mehl–Avrami Equation in Kinetic Analysis of Crystallization Processes,” J. Am. Ceram. Soc., vol. 83, pp. 2103–2105, 2000.

[207] D. L. Berlitz, M. Giovenardi, J.-F. Charles, and L. M. Fiúza, “Toxicity intraperitoneal and intragastric route of Bacillus thuringiensis and Melia azedarach in mice,” Arq. Inst. Biol. (Sao. Paulo)., vol. 79, no. 4, pp. 511–517, 2012.

[208] V.-P. R.I., L. Moreno-Fierros, L. Neri-Bazan, A. F. Martínez-Gill, G. De La Riva, and R. Lopéz-Revilla, “Characterization of the mucosal and systemic immune response induced by Cry1Ac protein from Bacillus thuringiensis HD 73 in mice,” Brazilian J. Med. Biol. Res., vol. 33, pp. 147–155, 2000.

[209] O. O. Shevchuk, “Study of some acute toxicity indicators of melphalan in rats,” Med. Clin. Chem., vol. 4, pp. 113–118, 2020.

[210] A. Upadhyay, P. Pandya, and P. Parikh, “Acute exposure of Pyrazosulfuron Ethyl induced Haematological and Blood Biochemical changes in the Freshwater Teleost fish Oreochromis mossambicus,” Int J Adv Res Biol Sci, vol. 1, no. 2, pp. 79–86, 2014.

[211] A. F. F. Camargo, A. M. Baptista, R. Natalino, and O. P. Camargo, “Bioactive glass in cavitary bone defects: a comparative experimental study in rabbits,” Acta Orthop Bras, vol. 23, no. 4, pp. 202–207, 2015.

[212] D. Bellucci et al., “Bone Regeneration by Novel Bioactive Glasses Containing Strontium and/or Magnesium: A Preliminary In-Vivo Study,” Materials (Basel)., vol. 11, p. 2223, 2018.

[213] A. Kharkova and A. M. Grjibovski, “Analysis of two independent samples using stata software: non parametric criteria,” Ekol. cheloveka [Human Ecol., vol. 4, pp. 60–63, 2014.

[214] Q. Z. Chen, I. D. Thompson, and A. R. Boccaccini, “45S5 Bioglass®-derived glass–ceramic scaffolds for bone tissue engineering,” Biomaterials, vol. 27, no. 11, pp. 2414–2425, 2006.

[215] Q. Fu, M. N. Rahaman, H. Fu, and X. Liu, “Silicate, borosilicate, and borate bioactive glass scaffolds with controllable degradation rate for bone tissue engineering applications. I. Preparation and in vitro degradation,” J. Biomed. Mater. Res. - Part A, vol. 95, no. 1, pp. 164–171, 2010, doi: 10.1002/jbm.a.32824.

[216] F. Baino, S. Caddeo, G. Novajra, and C. Vitale-Brovarone, “Using porous bioceramic scaffolds to model healthy and osteoporotic bone,” J. Eur. Ceram. Soc., vol. 36, no. 9, pp. 2175–2182, 2016, doi: 10.1016/j.jeurceramsoc.2016.01.011.

[217] “Attuazione della direttiva 2003713/CE concernente l’etichettatura e la presentazione dei prodotti alimentari, nonchè la relativa pubblicità. Decreto Legislativo 23 giugno 2003, n. 181, Art. 9, Italy.,” vol. n. 181, Ar.

[218] H. R. Fernandes, D. U. Tulyaganov, and J. M. F. Ferreira, “Preparation and characterization of foams from sheet glass and fly ash using carbonates as foaming agents,” Ceram. Int., vol. 35, no. 1, pp. 229–235, 2009, doi: 10.1016/j.ceramint.2007.10.019.

[219] F. Baino, J. Barberi, E. Fiume, G. Orlygsson, J. Massera, and E. Vern, “Robocasting of Bioactive SiO2-P2O5-CaO-MgO-Na2O-K2O Glass Scaffolds,” J. Healthc. Eng., vol. 2019, p. 5153136, 2019.

[220] J. Barberi, A. Nommeots-Nomm, E. Fiume, E. Verné, J. Massera, and F. Baino, “Mechanical characterization of pore-graded bioactive glass scaffolds produced by robocasting,” Biomed. Glas., vol. 5, no. 1, pp. 140–147, 2019, doi: 10.1515/bglass-2019-0012.

[221] V. Karageorgiou and D. Kaplan, “Porosity of 3D biomaterial scaffolds and osteogenesis,” Biomaterials, vol. 26, no. 27, pp. 5474–5491, 2005, doi: 10.1016/j.biomaterials.2005.02.002.

[222] P. Forchheimer, “Wasserbewegung durch boden,” Zeit. Ver. Deut. Ing., vol. 45, pp. 1782–1788, 1901.

[223] S. Ergun, “Fluid flow through packed columns,” Chem. Eng. Prog., vol. 48, pp. 89–94, 1952.

[224] R. K. Niven, “Physical insight into the Ergun and Wen & Yu equations for fluid flow in packed and fluidised beds,” Chem. Eng. Sci., vol. 57, pp. 527–534, 2002.

[225] H. Wadell, “Sphericity and roundness of rock particles,” J. Geol., vol. 41, pp. 310–331, 1933.

[226] J. Zheng and R. D. Hryciw, “Roundness and sphericity of soil particles in assemblies by computational geometry,” J. Comput. Civil. Eng., vol. 30, p. 04016021, 2016.

[227] L. Xianke, Y. Zhao, and D. J. C. Dennis, “Flow measurements in microporous media using micro-particle image velocimetry,” Phys. Rev. Fluids, vol. 3, p. 104202, 2018.

[228] M. V. Chor and W. Li, “A permeability measurement system for tissue engineering scaffolds,” Meas. Sci. Technol., vol. 18, pp. 208–216, 2017.

[229] J. Wu, B. Yu, and M. Yun, “A resistance model for flow through porous media,” Transp. Porous Med., vol. 71, pp. 331–334, 2008.

[230] J. Wu, D. Hu, W. Li, and X. Cai, “A review on non-Darcy flow—Forchheimer equation, hydraulic radius model, fractal model and experiment,” Fractals, vol. 24, no. 02, p. 1630001, 2016.

[231] B. Yu and J. Li, “A geometry model for tortuosity of flow path in porous media,” Chin. Phys. Lett., vol. 21, pp. 1569–1571, 2004.

[232] A. Koponen, M. Kataja, and J. V. Timonen, “Permeability and effective porosity of porous media,” Phys. Rev. E., vol. 56, p. 3319, 1997.

[233] A. Koponen, M. Kataja, and J. V. Timonen, “Tortuous flow in porous media,” Phys. Rev. E., vol. 54, p. 406, 1996.

[234] F. Pennella et al., “A survey of methods for the evaluation of tissue engineering scaffold permeability,” Ann. Biomed. Eng., vol. 41.10, pp. 2027–2041, 2013.

[235] A. Schiavi, C. Guglielmone, F. Pennella, and U. Morbiducci, “Acoustic method for permeability measurement of tissue-engineering scaffold,” Meas. Sci. Technol., vol. 23, p. 105702, 2012.

[236] K. Rasmussen, “Calculation methods for the physical properties of air used in the calibration of microphones,” Report No. PL-11b. Technical University of Den- mark, Lyngby, Denmark, 1997.

[237] D. Brkic and P. Praks, “Unified friction formulation from laminar to fully rough turbulent flow,” Appl. Sci., vol. 8, p. 2036, 2018.

[238] A. Hoppe, N. S. Güldal, and A. R. Boccaccini, “A review of the biological response to ionic dissolution products from bioactive glasses and glass-ceramics,” Biomaterials, vol. 32, no. 11, pp. 2757–2774, 2011.

[239] M. F. Ryan, “The role of magnesium in clinical biochemistry: an overview,” J. Lab. Med., vol. 28, no. 1, pp. 19–26, 1991.

[240] M. Dermience, G. Lognay, F. Mathieu, and P. Goyens, “Effects of thirty elements on bone metabolism,” J. Trace Elem. Med. Biol., vol. 32, pp. 86–106, 2015, doi: 10.1016/j.jtemb.2015.06.005.

[241] A. Bigi, E. Foresti, R. Gregorini, A. Ripamonti, N. Roveri, and J. S. Shah, “the role of magnesium on the structure of biological apatites,” Calcif. Tissue Int., vol. 50, pp. 439–444, 1992.

[242] S. L. Volpe, L. J. Taper, and S. Meacham, “The relationship between boron and magnesium status and bone mineral density in the human: a review.,” Magnes. Res., vol. 6, no. 3, pp. 291–296, 1993.

[243] “Vitamin D and magnesium protect bones from osteoporosis,” Available Online: https://www.woerwagpharma.de/en/health-topics/bone-muscle-joint-health/the-role-of-vitamin-d-and-magnesium-in-bone-

development#:~:text=In%20the%20bones%20the%20stored,therefore%20important%20for%20bone%20cells. (Last accessed 13th June 2021)

[244] N. Sezer, Z. Evis, S. M. Kayhan, A. Tahmasebifar, and M. Koç, "Review of magnesium-based biomaterials and their applications," J. Magnes. Alloy., vol. 6, no. 1, pp. 23–43, 2018, doi: 10.1016/j.jma.2018.02.003.

[245] M. Diba, F. Tapia, A. R. Boccaccini, and L. A. Strobel, "Magnesium-Containing Bioactive Glasses for Biomedical Applications," Int. J. Appl. Glas. Sci., vol. 3, no. 3, pp. 221–253, 2012, doi: 10.1111/j.2041-1294.2012.00095. x.

[246] P. W. McMillan, Glass Ceramics. London: Academic Press, 1979.

[247] S. G. Watts, R. G. Hill, M. D. O'Donnell, and R. V. Law, "Influence of magnesia on the structure and properties of bioctive glasses," J. Non. Cryst. Solids, vol. 356, no. 9, pp. 517–524, 2010.

[248] D. Bellucci, A. Sola, and V. Cannillo, "Low temperature sintering of innovative bioactive glasses," J. Am. Ceram. Soc., vol. 95, no. 4, pp. 1313–1319, 2012, doi: 10.1111/j.1551-2916.2012.05100. x.

[249] H. H. Lu, S. F. El-amin, K. D. Scott, and C. T. Laurencin, "polymer – bioactive glass composite scaffolds with improved mechanical properties support collagen synthesis and mineralization of human osteoblast-like cells in vitro," 2003.

[250] G. Wen, "Effects of P 2 O 5 and sintering temperature on microstructure and mechanical properties of lithium disilicate glass-ceramics," vol. 55, pp. 3583–3591, 2007, doi: 10.1016/j.actamat.2007.02.009.

[251] G. Kaur et al., "Mechanical properties of bioactive glasses, ceramics, glass-ceramics and composites: State-of-the-art review and future challenges," Mater. Sci. Eng. C, vol. 104, no. June, p. 109895, 2019, doi: 10.1016/j.msec.2019.109895.

[252] M. Montazerian and E. D. Zanotto, "Bioactive and inert dental glass-ceramics," J. Biomed. Mater. Res. - Part A, vol. 105, no. 2, pp. 619–639, 2017, doi: 10.1002/jbm.a.35923.

[253] L. Lefebvre et al., "Structural Transformations of Bioactive Glass 45S5 with Thermal Treatments," Acta Mater., vol. 55, pp. 3305–3313, 2007.

[254] A. Tilocca, "Structural models of bioactive glasses from molecular dynamics simulations," Proc. R. Soc., vol. 465, pp. 1003–1027, 2009.

[255] I. B. Leonor et al., "In Situ Study of Partially Crystallized Bioglassr and Hydroxylapatite In Vitro Bioactivity Using Atomic Force Microscopy. J Biomed Mater Res 2002, 62, 82-88.," J. Biomed. Mater. Res., vol. 62, pp. 82–88, 2002.

[256] S. Kashyap, K. Griep, and J. Nychka, "Crystallization Kinetics, Mineralization and Crack Propagation in Partially Crystallized Bioactive Glass 45S5," Mater. Sci. Eng. C, vol. 31, pp. 762–769, 2011.

[257] S. Fagerlund, J. Massera, N. Moritz, L. Hupa, and M. Hupa, "Phase Composition and In Vitro Bioactivity of Porous Implants Made of Bioactive Glass S53P4," Acta Biomater., vol. 8, pp. 2331–2339, 2012.

[258] J. Massera, M. Mayran, J. Rocherullé, and L. Hupa, “Crystallization Behavior of Phosphate Glasses and Its Impact on the Glasses’ Bioactivity, J Mater Sci 2015, 50, 3091-3102.,” J. Mater. Sci., vol. 50, pp. 3091–3102, 2015.

[259] Q. Fu, M. N. Rahaman, B. S. Bal, R. F. Brown, and D. E. Day, “Mechanical and In Vitro Performance of 13–93 Bioactive Glass Scaffolds Prepared by a Polymer Foam Replication Technique,” Acta Biomater., vol. 4, pp. 1854–864, 2008.

[260] C. Renghini et al., “Microstructural Characterization and In Vitro Bioactivity of Porous Glass-ceramic Scaffolds for Bone Regeneration by Synchrotron Radiation X-ray Microtomography, J Eur Ceram Soc 2013, 33, 1553-1565.,” J. Eur. Ceram. Soc., vol. 33, pp. 1553–1565, 2013.

[261] C. Vitale-Brovarone, F. Baino, and E. Verné, “High strength bioactive glass-ceramic scaffolds for bone regeneration,” J. Mater. Sci. Mater. Med., vol. 20, pp. 643–653, 2009.

[262] O. Bretcanu, X. Chatzistavrou, K. Paraskevopoulos, R. Conradt, I. Thompson, and A. R. Boccaccini, “Sintering and crystallisation of 45S5 Bioglass ® powder,” vol. 29, pp. 3299–3306, 2009, doi: 10.1016/j.jeurceramsoc.2009.06.035.

[263] R. Huang, J. Pan, A. R. Boccaccini, and Z. Chen, Q, “A two-scale model for simultaneous sintering and crystallization of glass–ceramic scaffolds for tissue engineering,” Acta Biomater., vol. 4, no. 4, pp. 1095–1103, 2008.

[264] E. P. Erasmus, O. T. Johnson, I. Sigalas, and J. Massera, “Effects of Sintering Temperature on Crystallization and Fabrication of Porous Bioactive Glass Scaffolds for Bone Regeneration,” Sci. Rep., no. July, 2017, doi: 10.1038/s41598-017-06337-2.

[265] M. J. Starink, “The Determination of Activation Energy from Linear Heating Rate Experiments: A Comparison of the Accuracy of Isoconversion Methods,” Thermochim. Acta, vol. 404, pp. 163–176, 2003.

[266] R. Golovchak, P. Thapar, A. Ingram, D. Savytskii, and H. Jain, “Influence of Phase Separation on the Devitrification of 45S5 Bioglass,” Acta Biomater., vol. 10, pp. 4878–4886, 2014.

[267] D. C. Clupper and L. L. Hench, “Crystallization Kinetics of Tape Cast Bioactive Glass 45S5,” J. Non. Cryst. Solids, vol. 318, pp. 43–48, 2003.

[268] F. Smeacetto et al., “Glass-Ceramic Joining Material for Sodium-Based Battery,” Ceram. Int., vol. 43, pp. 8329–8333, 2017.

[269] L. Lilensten, Q. Fu, B. R. Wheaton, A. J. Credle, R. L. Stewart, and J. T. Kohli, “Kinetic study on Lithium-Aluminosilicate (LAS) Glass- Ceramics Containing MgO and ZnO,” Ceram. Int., vol. 40, pp. 11657–11661, 2014.

[270] M. Erol, S. Kucukbayrak, and A. Ersoy-Mericboyu, “The Application of Differential Thermal Analysis to the Study of Isothermal and Non-Isothermal

Crystallization Kinetics of Coal Fly Ash Based Glasses," J. Non. Cryst. Solids, vol. 355, pp. 569–576, 2009.

[271] J. Massera, S. Fagerlund, L. Hupa, and M. Hupa, "Crystallization mechanism of the bioactive glasses, 45S5 and S53P4," J. Am. Ceram. Soc., vol. 95, pp. 603–613, 2012.

[272] X. J. Xu, C. S. Ray, and D. E. Day, "Nucleation and crystallization of Na2O-2CaO-3SiO2 glass by differential thermal analysis," J. Am. Ceram. Soc., vol. 74, pp. 909–914, 1991.

[273] S. Fagerlund and L. Hupa, "Crystallization of 45S5 during isothermal heat treatment," Ceram. Mater., vol. 62, pp. 349–354, 2010.

[274] Y. R. Luo, Comprehensive Handbook of Chemical Bond Energies. Boca Raton, FL(USA): CRC Press, 2007.

[275] D. Bellucci, V. Cannillo, A. Sola, F. Chiellini, M. Gazzarri, and C. Migone, "Macroporous Bioglass derived Scaffolds for Bone Tissue Regeneration," Ceram. Int., vol. 37, pp. 1575–1585, 2011.

[276] C. Lara, M. J. Pascual, and A. Duran, "Glass-Forming Ability, Sinterability and Thermal Properties in the System RO-BaO-SiO2 (R = Mg, Zn)," J. Non. Cryst. Solids, vol. 348, pp. 149–155, 2004.

[277] A. Hruby, "Evaluation of glass-forming tendency by means of DTA," Czech. J. Phys., vol. 22, pp. 1187–1193, 1972.

[278] A. Hodge and B. Sterner, "Toxicity Classes," Canadian Center for Occupational Health and Safety, 2005. .

[279] E. O. Erhirhie, C. P. Ihekwereme, and E. E. Ilodigwe, "Advances in acute toxicity testing: strengths, weaknesses and regulatory acceptance," Iterdisciplinary Toxicol., vol. 11, no. 1, pp. 5–12, 2018.

[280] F. Tulyaganov, D.U., Akbarov, A., Ziyadullaeva, N., Khabilov, B., Baino, "Injectable bioactive glass-based pastes for potential use in bone tissue repair," Biomed. Glas., vol. 6, no. 1, pp. 23–35, 2020.

[281] Q. Z. Chen and G. A. Thouas, "Fabrication and characterization of sol-gel derived 45S5 Bioglass®-ceramic scaffolds," Acta Biomater., vol. 7, pp. 3616–3626, 2011.

[282] I. Cacciotti, M. Lombardi, A. Bianco, A. Ravaglioli, and L. Montanaro, "Sol-gel derived 45S5 bioglass: Synthesis, microstructural evolution and thermal behaviour," J. Mater. Sci. Mater. Med., vol. 23, no. 8, pp. 1849–1866, 2012, doi: 10.1007/s10856-012-4667-6.

[283] K. Zheng et al., "Aging time and temperature effects on the structure and bioactivity of gel-derived 45S5 glass-ceramics," J. Am. Ceram. Soc., vol. 98, no. 1, pp. 30–38, 2015, doi: 10.1111/jace.13258.

[284] J. Faure et al., “A new sol-gel synthesis of 45S5 bioactive glass using an organic acid as catalyst,” Mater. Sci. Eng. C, vol. 47, pp. 407–412, 2015, doi: 10.1016/j.msec.2014.11.045.

[285] D. S. L. Weiss, R. D. Torres, S. Buchner, S. Blunk, and P. Soares, “Effect of Ti and Mg dopants on the mechanical properties, solubility, and bioactivity in vitro of a Sr-containing phosphate-based glass.,” J. Non. Cryst. Solids, vol. 386, pp. 34–38, 2014.

[286] S. M. Rabiee, N. Nazparvar, M. Azizian, D. Vashaee, and L. Tayebi, “Effect of ion substitution on properties of bioactive glasses: A review. Ceram. Int. 2015, 41, 7241–7251.,” Ceram. Int., vol. 41, pp. 7241–7251, 2015.

[287] L. Lefebvre, L. Gremillardm, J. Chevalier, R. Zenati, and D. Bernache-Assolant, “Sintering Behaviour of 45S5 bioactive glass,” Acta Biomater., vol. 4, pp. 1894–1903, 2008.

[288] K. Zheng et al., “Aging time and temperature effects on the structure and bioactivity of gel-derived 45S5 glass-ceramics,” J. Am. Ceram. Soc., vol. 98, pp. 30–38, 2015.

[289] Y. Hoshino, T. Utsunomiya, and O. Abe, “The thermal decomposition of sodium nitrates the effects of several oxides on the decomposition,” Bull. Chem. Soc. Jpn, vol. 54, pp. 1385–1391, 1981.

[290] T. Pradita, S. J. Shih, B. B. Aji, and Sudibyo, “AIP Conference Proceedings,” in Synthesis of MgO powder from magnesium nitrate using spray pyrolysis, 2017, pp. 1823, 020016.

[291] E. S. Freeman, “The kinetics of thermal decomposition of potassium nitrate and of the reaction between potassium nitrate and oxygen,” J. Am. Chem. Soc., vol. 79, no. 4, pp. 838–842, 1957.

[292] J. R. Jones, “Sol-gel derived Glasses for medicine,” in Bio-Glasses. An Introduction, J. R. Jones and S. A. Clarke, Eds. West Sussex, UK: Wiley & Sons, 2012, pp. 29–44.

[293] M. Bohner and J. Lemaitre, “Can bioactivity be tested in vitro with SBF solution?,” Biomaterials, vol. 30, pp. 2175–2179, 2009.

[294] A. M. Galow, A. Rebl, D. Koczan, S. M. Bonk, W. Baumann, and J. Gimsa, “Increased osteoblast viability at alkaline pH in vitro provides a new perspective on bone regeneration. Biochem. Biophys. Rep. 2017, 10, 17–25.,” Biochem. Biophys. Res. Commun., vol. 10, pp. 17–25, 2017.

[295] Q. Z. Chen, Y. Li, L. Y. Jin, J. M. W. Quinn, and P. A. Komesaroff, “A new sol–gel process for producing Na2O-containing bioactive glass ceramics. Acta Biomater. 2010, 6, 4143–4153.,” Acta Biomater., vol. 6, pp. 4143–4153, 2010.

[296] Z. Abbasi, M. E. Bahroloolum, M. H. Shariat, and R. Bagheri, “Bioactive Glasses in Dentistry: A Review,” J. Glas. Dent. A Rev., vol. 2, no. 1, pp. 1–9, 2015.

[297] F. Baino and E. Verné, “Glass-based coatings on biomedical implants: a state-of-the-art review,” Biomed. Glas., vol. 3, no. 1, pp. 1–17, 2017, doi: 10.1515/bglass-2017-0001.

[298] J. N. Oliver, D. Zhu, Y. Su, X. Lu, P. Kuo, and J. Du, “Bioactive glass coatings on metallic implants for biomedical applications,” Bioact. Mater., vol. 4, pp. 261–270, 2019, doi: 10.1016/j.bioactmat.2019.09.002.

[299] R. Sergi, D. Bellucci, and V. Cannillo, “A Comprehensive Review of Bioactive Glass Coatings: State of the Art , Challenges and Future Perspectives,” Coatings, vol. 10, no. 757, 2020.

[300] G. Brunello and H. Elsayed, “Bioactive Glass and Silicate-Based Ceramic Coatings on Metallic Implants: Open Challenge or Outdated topic?,” Materials (Basel)., vol. 12, no. 2929, 2019.

[301] S. J. Hollister, “Scaffold design and manufacturing: From concept to clinic,” Adv. Mater., vol. 21, no. 32–33, pp. 3330–3342, 2009, doi: 10.1002/adma.200802977.

[302] S. G. Hollister, E. E. Liao, E. N. Moffit, C. G. Jeong, and J. M. Kemppainen, “Defining design targets for tissue engineering scaffolds,” in Fundamentals of Tissue Engineering and Regenerative medicine, U. Meyer, Ed. Berlin, 2009, pp. 521–538.

[303] S. Roosa, J. Kemppainen, E. Moffitt, P. Krebsbach, and S. Hollister, “The pore size of polycaprolactone scaffolds has limited influence on bone regeneration in an in vivo model,” J. Biomed. Mater. Res., vol. 92A, pp. 359–368, 2009.

[304] M. Bohner, Y. Loosli, G. Baroud, and D. Lacroix, “Commentary: deciphering the link between architecture and biological response of a bone graft substitute,” Acta Biomater., vol. 7, pp. 478–484, 2011.

[305] G. Falvo D’Urso Labate, G. Catapano, C. Vitale-Brovarone, and F. Baino, “Quantifying the micro-architectural similarity of bioceramic scaffolds to bone,” Ceram. Int., vol. 43, no. 12, pp. 9443–9450, 2017, doi: 10.1016/j.ceramint.2017.04.121.

[306] “ASTM F2952 – 14. Standard Guide for Determining the Mean Darcy Permeability Coefficient for a Porous Tissue Scaffold.” .

[307] K. Prashant and F. Topin, “Influence of Morphology on Flow Law Characteristics in Open-Cell Foams: An Overview of Usual Approaches and Correlations,” J Fluids Eng, vol. 139, p. 071301, 2017.

[308] P. Kumar and F. Topin, “State-of-the-art of pressure drop in open-cell porous foams: review of experiments and correlations,” J Fluids Eng, vol. 139, pp. 111401–111413, 2017.

[309] A. Inayat, M. Klumpp, M. Lämmermann, H. Freund, and W. Schwieger, “Development of a new pressure drop correlation for open-cell foams based completely on theoretical grounds: Taking into account strut shape and geometric tortuosity,” Chem Eng J, vol. 287, pp. 704-719., 2016.

[310] D. Edouard, M. Lacroix, C. P. Huu, and F. Luck, “Pressure drop modeling on SOLID foam: State-of-the art correlation,” Chem Eng J, vol. 144, pp. 299–311, 2008.

[311] L. Shijie and J. H. Masliyah, “Principles of single-phase flow through porous media,” Adv Chem, vol. 251, pp. 227–286, 1996.

[312] P. Sridhar and S. Aliabadi, “Computational study of no-slip and rarefied slip flows in infinite structured porous media,” Comput Fluids, vol. 136, pp. 485–496, 2016.

[313] D. Brkić and P. Praks, “Unified friction formulation from laminar to fully rough turbulent flow,” Appl. Sci., vol. 8, no. 11, p. 2036, 2018.

[314] J. Henkel et al., “Bone Regeneration Based on Tissue Engineering Conceptions – A 21st Century Perspective,” Bone Res., vol. 3, pp. 216–248, 2013.

[315] F. S. Kaplan, W. C. Hayes, T. M. Keaveny, A. Boskey, T. A. Einhorn, and J. P. Iannotti, “Form and function of bone,” in Orthopaedic basic science, S. R. Simon, Ed. Rosemont: American Academy of Orthopaedic Surgeons, 1994, pp. 128–184.

[316] C. Navalón, P. Ros-Tárraga, A. Murciano, P. Velasquez, P. Mazón, and P. N. De Aza, “Easy manufacturing of 3D ceramic scaffolds by the foam replica technique combined with sol-gel or ceramic slurry,” Ceram Inter, vol. 45, pp. 18338–18346, 2019.

[317] J. A. Hipp, A. Jansujwicz, C. A. Simmons, and B. D. Snyder, “Trabecular bone morphology from micro-magnetic resonance imaging,” J Bone Min. Res, vol. 11, pp. 286–292, 1996.

[318] I. Ochoa, J. A. Sanz-herrera, J. M. Garcia-Aznar, M. Doblaré, D. M. Yunos, and A. R. Boccaccini, “Permeability evaluation of 45S5 Bioglass-based scaffolds for bone tissue engineering,” J. Biomech., vol. 42, pp. 257–260, 2009.

[319] S. Li, J. R. De Wijn, J. Li, P. Layrolle, and K. De Groot, “Macroporous biphasic calcium phosphate scaffolds with high permeability/porosity ratio,” Tissue Eng., vol. 9, pp. 535–546, 2003.

[320] M. J. Grimm and J. L. Williams, “Measurements of permeability in human calcaneal trabecular bone,” J. Biomech., vol. 30, pp. 743–745, 1997.

[321] E. A. Nauman, K. E. Fong, and T. M. Keaveny, “Dependence of Intertrabecular Permeability on Flow Direction and Anatomic Site,” Ann. Biomed. Eng., vol. 27, no. 4, pp. 517–524, 1999, doi: 10.1114/1.195.

[322] S. Yang, K. F. Leong, Z. Du, and C. K. Chua, “The design of scaffolds for use in tissue engineering. Part I. Traditional factors,” Tissue Eng., vol. 7, pp. 679–689, 2001.

[323] J. P. Du Plessis, “Analytical quantification of coefficients in the Ergun equation for fluid friction in a packed bed,” Trans Porous Media, vol. 16, pp. 189–207, 1994.

[324] J. R. Jones, L. M. Ehrenfried, and L. L. Hench, “Optimising bioactive glass scaffolds for bone tissue engineering,” Biomaterials, vol. 27, no. 7, pp. 964–973, 2006, doi: 10.1016/j.biomaterials.2005.07.017.

[325] K. Anselme, P. Davidson, A. Popa, M. Giazzon, M. Liley, and L. Ploux, “The interactions of cells and bacteria with surfaces structured at the nanometre scale,” Acta Biomater., vol. 6, pp. 3824–3846, 2010.

[326] I. Review, “Modelling the Mechanical Behavior of Cellular Materials,” vol. 110, 1989.

[327] Z. Zhang et al., “Acidic pH environment induces autophagy in osteoblasts,” Sci. Rep., vol. 7, no. November 2016, pp. 1–9, 2017, doi: 10.1038/srep46161.

[328] S. Gunasekaran and G. Anbalagan, “Thermal decomposition of natural dolomite,” vol. 30, no. 4, pp. 339–344, 2007.

[329] H. Tripathi, S. K. Hira, A. S. Kumar, U. Gupta, P. P. Manna, and S. P. Singh, “Structural characterization and in vitro bioactivity assessment of SiO2–CaO–P2O5–K2O–Al2O3 glass as bioactive ceramic material,” Ceram. Int., vol. 41, no. 9B, pp. 11756–11769, 2015.

[330] H. Tripathi, C. Rath, A. S. Kumar, P. P. Manna, and S. P. Singh, “Structural, physico-mechanical and in-vitro bioactivity studies on SiO2–CaO–P2O5–SrO–Al2O3 bioactive glasses,” Mater. Sci. Eng. C, vol. 94, pp. 279–290, 2019.

[331] A. A. El-Kheshen, F. A. Khaliafa, E. A. Saad, and R. L. Elwan, “Effect of Al2O3 addition on bioactivity, thermal and mechanical properties of some bioactive glasses,” Ceram. Int., vol. 34, no. 7, p. 1667.1673, 2008.

[332] F. Lüthen, U. Bulnheim, P. D. Müller, J. Rychly, H. Jesswein, and J. G. Nebe, “Influence of manganese ions on cellular behavior of human osteoblasts in vitro,” Biomol. Eng., vol. 24, no. 5, pp. 531–536, 2007.

[333] M. Miola et al., “In vitro study of manganese-doped bioactive glasses for bone regeneration,” Mater. Sci. Eng. C, vol. 38, pp. 107–118, 2014.

[334] N. Brown and S. Revankar, “A review of catalytic sulfur (VI) oxide decomposition experiments,” Int. J. Hydrogen Energy, vol. 37, p. 2685.2698, 2011.

[335] E. Moreschi et al., “Effect of dolomite on the repair of bone defects in rats: histological study,” pp. 1547–1556, 2010.

[336] L. J. Gibson and M. F. Ashby, Cellular solids: structure and properties, Second Edi. Cambridge University Press, 1999.

[337] E. Morgan, H. Bayractar, and T. Keaveny, “Trabecular bone modulus–density relationships depend on anatomic site,” J. Biomech., vol. 36, pp. 897–904, 2003.

[338] D. Kohn, M. Sarmadi, J. Helman, and P. Krebsbach, “Effects of pH on human bone marrow stromal cells in vitro: Implications for tissue engineering of bone,” J. Biomed. Mater. Res., vol. 60, no. 2, pp. 2–9, 2002.

[339] D. A. N. N. Ungureanu, N. Angelescu, R. M. Ion, E. V. Stoian, and C. Z. Rizescu, “Synthesis and Characterization of Hydroxyapatite Nanopowders by Chemical Precipitation,” pp. 296–301.

[340] B. A. E. Ben-Arfa, A. S. Neto, I. E. Palamá, I. M. Miranda Salvado, R. C. Pullar, and J. M. F. Ferreira, “Robocasting of ceramic glass scaffolds: Sol–gel glass, new horizons,” J. Eur. Ceram. Soc., vol. 39, no. 4, pp. 1625–1634, 2019, doi: 10.1016/j.jeurceramsoc.2018.11.019.

[341] B. A. E. Ben-Arfa and R. C. Pullar, “A comparison of bioactive glass scaffolds fabricated by robocasting from powders made by sol-gel and melt-quenching methods,” Processes, vol. 8, no. 5, 2020, doi: 10.3390/PR8050615.

[342] B. A. E. Ben-Arfa, I. M. Miranda Salvado, J. M. F. Ferreira, and R. C. Pullar, “A hundred times faster: Novel, rapid sol-gel synthesis of bio-glass nanopowders (Si-Na-Ca-P system, Ca:P = 1.67) without aging,” Int. J. Appl. Glas. Sci., vol. 8, no. 3, pp. 337–343, 2017, doi: 10.1111/ijag.12255.

[343] Q. Dou, A. A. Karim, and X. J. Loh, “Modification of thermal and mechanical properties of PEG-PPG-PEG copolymer (F127) with MA-POSS,” Polymers (Basel)., vol. 8, p. 341, 2016.

[344] E. García-Gareta, J. Hua, and G. W. Blunn, “Osseointegration of acellular and cellularized osteoconductive scaffolds: Is tissue engineering using mesenchymal stem cells necessary for implant fixation?,” J. Biomed. Mater. Res. - Part A, vol. 103, no. 3, pp. 1067–1076, 2015, doi: 10.1002/jbm.a.35256.

[345] G. Caetano et al., “Cellularized versus decellularized scaffolds for bone regeneration,” Mater. Lett., vol. 182, pp. 318–322, 2016, doi: 10.1016/j.matlet.2016.05.152.

[346] L. Fassina et al., “Effects of Electromagnetic Stimulation on Calcified Matrix Production by SAOS-2 Cells over a Polyurethane Porous Scaffold,” Tissue Eng., vol. 12, no. 7, pp. 1985–1999, 2006.

[347] M.-T. Tsai, W. H.-S. Chang, K. Chang, R.-J. Hou, and T.-W. Wu, “Pulsed electromagnetic fields affect osteoblast proliferation and differentiation in bone tissue engineering,” Bioelectromagnetics, vol. 28, no. 7, pp. 519–528, 2007.

[348] M. Hronik-Tupaj, W. L. Rice, M. Cronin-Golomb, D. L. Kaplan, and I. Georgakoudi, “Osteoblastic differentiation and stress response of human mesenchimal stem cells exposed to alternating current electric fields,” Biomed. Eng. Online, vol. 10, p. 9, 2011.

[349] “Chiusura a baionetta - Fulgosi Srl,” https://www.fulgosi.com/index.php/it/prodotti/chiusure-rapide/fulg-o-tooth#:~:text=La%20chiusura%20Fulg%2Do%2Dtooth,contatto%20con%20i%20%22denti%22. (Last accessed 13th June 2021)

[350] “Form 3 SLA 3D Printer - Formlabs Official Website,” https://formlabs.com/eu/3d-printers/form-3/?&utm_source=google&utm_medium=cpc&utm_campaign=EX-EMEA-Prospecting-Search_Brand-Form_3-Brand-EN-Exact-Paid-

Adwords&utm_term=form%203%20formlabs&utm_content=Form_3_formlabs&utm_device=c&_bt=345160474787&_bk=form%. (Last accessed 13th 2021)

[351] "Formlabs Dental SG Resin - Solid Print3D - No.1 In The UK," https://www.solidprint3d.co.uk/product/dental-sg-resin/?ppc_keyword=formlabs%20dental%20sg%20resin&gclid=Cj0KCQjw38-DBhDpARIsADJ3kjlH8mu2Y6Eva5ZUVhPb4em27j76lnsAuTJkxJLE0aC4i1ZGFTYuFocaAjEFEALw_wcB. (Last accessed 13th June 2021)

[352] G. Lutišanoá, E. Kuzielová, M. Palou, and J. Kozánkoá, "Static and dynamic in vitro test of bioactivity of glass ceramics," Ceram. - Silikaty, vol. 55, no. 2, pp. 106–113, 2011.

[353] A. Ramila and M. Vallet-Regí, "Static and dynamic in vitro study of a sol-gel glass bioactivity," Biomaterials, vol. 22, pp. 2301–2306, 2000.

[354] I. Izquierdo-Barba, A. J. Salinas, and M. Vallet-Regí, "Effect of the continuous solution exchange on the in vitro reactivity of a CaO-SiO2 sol-gel glass," J. Biomed. Mater. Res., vol. 51, p. 2, 2000.

[355] J. R. Jones, P. Sepulveda, and L. L. Hench, "Dose-dependent behavior of bioactive glass dissolution," J. Biomed. Mater. Res., vol. 58, pp. 720–726, 2001.

[356] M. Arango-Ospina, L. Hupa, and A. R. Boccaccini, "Bioactivity and dissolution behavior of boron-containing bioactive glasses under static and dynamic conditions in different media," Biomed. Glas., vol. 5, no. 1, pp. 124–139, 2019, doi: 10.1515/bglass-2019-0011.

[357] M. Höner, F. Böke, M. Weber, and H. Fischer, "Mimicking physiological flow conditions to study alterations of bioactive glass surfaces in vitro," J. Biomed. Mater. Res. Part B, vol. 106, no. 1, pp. 228–236, 2017.

Appendix A

Publication list resulting from the work presented in this thesis

Publications

[1] **Fiume, E.**; Schiavi, A.; Orlygsson, G.; Bignardi, C.; Verné, E.; Baino, F., Comprehensive assessment of bioactive glass and glass-ceramic scaffold permeability: experimental measurements by pressure wave drop, modelling and computed tomography-based analysis, Acta Biomaterialia 2021, 119: 405-418.

[2] **Fiume, E.**; Serino, G.; Bignardi, C.; Verné, E.; Baino, F., Sintering behavior of a six-oxide bioactive glass for scaffold manufacturing, Applied Sciences 2020, 10(22):8279.

[3] **Fiume, E.**; Tulyaganov, D.; Ubertalli, G.; Verne, E.; Baino, F., Dolomite-foamed bioactive silicate scaffolds for bone tissue repair, Materials 2020, 13(3): 628, DOI: 10.3390/ma13030628.

[4] **Fiume, E.**; Migneco, C.; Verne, E.; Baino, F., Comparison between bioactive sol-gel and melt-derived glasses/glass-ceramics based on the multicomponent SiO2-P2O5-CaO-MgO-Na2O-K2O System, Materials 2020, 13(3):540, DOI: 10.3390/ma13030540.

[5] **Fiume, E.**; Verne, E.; Baino, F., Crystallization behaviour of SiO2-P2O5-CaO-MgO-Na2O-K2O bioactive glass powder, Biomedical Glasses 2019, 5(1): 46-52, DOI: 10.1515/bglass-2019-0004.

[6] **Fiume, E.**; Serino, G.; Bignardi, C.; Verne, E.; Baino, F., Bread-derived bioactive porous scaffolds: An innovative and sustainable approach to bone tissue engineering, Molecules 2019, 24 (16): 2954, DOI: 10.3390/molecules24162954

[7] Baino, F.; **Fiume, E.**, Quantifying the effect of particle size on the crystallization of 45S5 bioactive glass, Materials Letters 2018, 224: 54-58, DOI: 10.1016/j.matlet.2018.04.073

Proceedings

[1] Massai, D.; Gabetti, S.; Putame, G.; Armando, I.; **Fiume, E.**; Sanginario, A.; Carbonaro, D.; Baino, F.; Audenino, A.L.; Verné, E.; Bignardi, C., Versatile perfusion and electrical stimulation bioreactor for bone tissue engineering, In: VII Congresso Nazionale di Bioingegneria (GNB 2020), Trieste (Italy) 10th-12th June 2020, pp.1, 2020.

[2] **Fiume, E.**; Baino, F.; Massera, J.; Massai, D.; Bignardi, C.; Verne', E., 3D printing of sol-gel and melt-derived glass-ceramics for bone regeneration, In: 44th International Conference & Exposition on Advanced Ceramics & Composites - Abstract Book, American Ceramic Society (United States of America), 44th International Conference & Exposition on Advanced Ceramics & Composites (ICACC 2020), Daytona Beach (FL, USA) 26th-31st Jenuary, 2020, pp. 1, 2020, Vol. 1

[3] **Fiume, E.**; Massera, J.; Baino, F.; Verné, E., Robocasting of sol-gel glasses and glass-ceramics: a facile approach for bone scaffold manufacturing, In: 30th Conference of the European Society for Biomaterials (ESB 2019), ESB, 30th Conference of the European Society for Biomaterials (ESB 2019), Dresden (Germany) 9th-13th September 2019, 2019

[4] Baino, F.; **Fiume, E.**; Schiavi, A.; Massai, D.; Bignardi, C.; Verné, E., Acoustic method for evaluating the permeability of bone-like bioactive glass-ceramic scaffolds, In: Book of Abstract of the XVI Conference of the European Ceramic Society (ECersS), Società Ceramica Italiana (ITALIA), XVI Conference of the European Ceramic Society (ECersS), Torino 17th-20th June 2019, pp. 1, 2019

[5] **Fiume, E.**; Baino, F.; Verné, E., Innovative and highly-sustainable bread-derived bioactive glass scaffolds for bone tissue engineering, In: Book of Abstracts - MSE 2018, Congress press (Germany), Materials Science and Engineering (MSE) 2018 Congress, Darmstadt 26th-28th September, 2018, pp. 1, 2018

Appendix B

Publication List: supplementary works

Publications

[1] Migneco, C.; **Fiume, E.**; Verné, E.; Baino, F., A guided walk through the world of mesoporous bioactive glasses (MBGs): Fundamentals, processing and applications, *Nanomaterials* 2020, 10(12):2571.

[2] Kargozar, S.; Mozafari, M.; Ghodrat, S.; **Fiume, E.**; Baino, F., Copper-containing bioactive glasses and glass-ceramics: From tissue regeneration to cancer therapeutic strategies, *Materials Science and Engineering C* 2020, In Press.

[3] Baino, F.; **Fiume, E.**, 3D printing of hierarchical scaffolds based on mesoporous bioactive glasses (MBGs)-fundamentals and applications, *Materials* 2020, 13(7):1688, DOI: 10.3390/ma13071688.

[4] Baino, F.; Fiume, E., Mechanical characterization of 45S5 bioactive glass-derived scaffolds, MATERIALS LETTERS 2019, 245: 14-17, DOI: 10.1016/j.matlet.2019.02.086

[5] Baino, F.; Barberi, J.; **Fiume, E.**; Orlygsson, G.; Massera, J.; Verne, E., Robocasting of Bioactive SiO 2 -P 2 O 5 -CaO-MgO-Na 2 O-K 2 O Glass Scaffolds, *Journal of Healthcare Engineering* 2019, 2019, 2019: 5153136, DOI: 10.1155/2019/5153136..

[6] Baino, F.; **Fiume, E.**; Miola, M.; Leone, F.; Onida, B.; Verné, Enrica, Fe-doped bioactive glass-derived scaffolds produced by sol-gel foaming, *Materials Letters* 2019, 235: 207-211, DOI: 10.1016/j.matlet.2018.10.042.

[7] Kargozar, S.; Montazerian, M.; **Fiume, E.**; Baino, F., Multiple and promising applications of strontium (Sr)-containing bioactive glasses in bone tissue engineering, *Frontiers in Bioengineering and Biotechnology* 2019, 7: 161, DOI: 10.3389/fbioe.2019.00161

[8] Barberi, J.; Baino, F.; **Fiume, E.**; Orlygsson, G.; Nommeots-Nomm, A.; Massera, J.; Verné, E., Robocasting of SiO2-based bioactive glass scaffolds with porosity gradient for bone regeneration and potential load-bearing applications, *Materials* 2019, 12 (17): 2691, DOI: 10.3390/ma12172691.

[9] Baino, F.; **Fiume, E.**; Barberi, J.; Kargozar, S.; Marchi, J.; Massera, J.; Verne, E., Processing methods for making porous bioactive glass-based scaffolds—A state-of-the-art review, *International Journal of Applied Ceramic Technology* 2019, 16: 1762-1796, DOI: 10.1111/ijac.13195.

[10] Baino, F.; Verne, E.; **Fiume, E.**; Peitl, O.; Zanotto, E. D.; Brandao, S. M.; Schellini, S. A., Bioactive glass and glass-ceramic orbital implants, *International Journal of Applied Ceramic Technology* 2019, 16: 1850-1863, DOI: 10.1111/ijac.13236

[11] Baino, F.; **Fiume, E.**, Elastic mechanical properties of 45S5-based bioactive glass-ceramic scaffolds, *Materials* 2019, 12: 3244, DOI: 10.3390/ma12193244

[12] Barberi, J.; Nommeots-Nomm, A.; **Fiume, E.**; Verné, E.; Massera, J.; Baino, F., Mechanical characterization of pore-graded bioactive glass scaffolds produced by robocasting, *Biomedical Glasses* 2019,5(1): 140-147, DOI: 10.1515/bglass-2019-0012.

[13] Baino, F.; **Fiume, E.**; Miola, M.; Leone, F.; Onida, B.; Laviano, F.; Gerbaldo, R.; Verné, E., Fe-doped sol-gel glasses and glass-ceramics for magnetic hyperthermia, *Materials* 2018, 11: 173, DOI: 10.3390/ma11010173.

[14] **Fiume, E.**; Barberi, J.; Verné, E.; Baino, F., Bioactive glasses: from parent 45S5 composition to scaffold-assisted tissue-healing therapies, *Journal of Functional Biomaterials* 2018, 9(1): 24, DOI: 10.3390/jfb9010024.

[15] Baino, F.; **Fiume, E.**; Miola, M.; Verné, E., Bioactive sol-gel glasses: Processing, properties, and applications, *International Journal of Applied Ceramic Technology* 2018, 15: 841-860, DOI: 10.1111/ijac.12873

[16] Yu, M.; **Fiume, E.**; Verné, E.; Saunders, T.; Reece, M. J.; Baino, F., Bioactive sol-gel glass-coated wood-derived biocarbon scaffolds, *Materials Letters*, Elsevier B.V., pp. 4, 2018, Vol. 232, ISSN: 0167-577X, DOI: 10.1016/j.matlet.2018.08.067.

[17] **Fiume, E.**; Baino, F. (2021), Robocasting of mesoporous bioactive glasses (MBGs) for bone tissue engineering. In: A. Osaka and R. Narayan, Bioceramics: from Macro to Nanoscale (pp: 327-249), Elsevier.

Proceedings

[1] Baino, F.; **Fiume, E.**; Verné, E.; Kargozar, S., Bioactive glasses for tissue engineering: where are we and where are we going? In: Book of Abstracts of the 7th International Congress on Ceramics (ICC7), Congress press (Brazil), 7th International Congress on Ceramics (ICC7), Foz de Iguacu (Brazil) 17th-21st June, 2018, pp. 1, 2018

[2] **Fiume, E.**; Baino, F.; Miola, M.; Leone, F.; Onida, B.; Laviano, F.; Gerbaldo, R.; Verné, E., Multifunctional Fe-doped sol-gel bioactive scaffolds for bone tissue engineering and cancer treatment, In: Poster, GNB press, VI Congresso Gruppo Nazionale di Bioingegneria (GNB 2018), Milan 25th-27th June, 2018, pp. 1, 2018

[3] **Fiume, E.**; Baino, F.; Barberi, J.; Massera, J.; Verné, E., 3D-printed grid-like bioactive glass scaffolds for bone tissue engineering, In: Book of Abstracts, Congress press, II Congresso Nazionale IDBN "3D Printing and Biomechanics" and III Thematic Conference ESB-ITA, Pavia (Italy) 5th-7th September, 2018, pp. 1, 2018

[4] **Fiume, E.**; Baino, F.; Verné, E., Innovative and highly-sustainable bread-derived bioactive glass scaffolds for bone tissue engineering, In: Book of Abstracts - MSE 2018, Congress press (Germany), Materials Science and Engineering (MSE) 2018 Congress, Darmstadt 26th-28th September, 2018, pp. 1, 2018

[5] **Fiume, E.**; Baino, F.; Verné, E., Bread-templating scaffolds: an innovative bone tissue engineering approach, In: Coach Industrial Workshop "Advanced materials for high-growth industries", Workshop press, Coach Industrial Workshop "Advanced materials for high-growth industries", Torino (Italy), 3rd-4th October 2018, 2018.

Appendix C

List of Acronyms

2D	Two-dimensional
3D	Three-dimensional
3DP	Three-dimensional Printing
ABS	Acrylonitrile Butadiene Styrene
AC	Alternating Current
AFM	Atomic Force Microscopy
ALP	Alkaline Phosphatase
AMTs	Additive Manufacturing Technologies
ATCC	American Type Colture Collection
ATF4	Activating Transcription Factor 4
BDS	Bread-Derived Scaffolds
BET	Brunauer-Emmett-Teller Theory

BGCs	Bioactive Glass-Ceramics
BGs	Bioactive Glasses
BMSCs, ATCC PCS500012	Human Mesenchimal Stem Cells
BMU	Basic Multicellular Unit
BTE	Bone Tissue Engineering
C	Compression Bioreactor
CAD	Computer-Aided Design
CFD	Computational Fluid Dynamic
CNC	Computerized Numerical Control
CT	Computed Tomography
DFS	Dolomite Foamed Scaffolds
DH	Dentinal Hypersensitivity
DMEM	Dulbecco's Modified Eagle Medium
DMP1	Dentine Matrix Acidic Phosphoprotein 1
DTA	Differential Thermal Analysis
EA.hy926, ATCC CRL-2922	Human Endothelial Cells
ECM	Extracellular Matrix
EDS	Energy Dispersion Spectrometry
EISA	Evaporation Induced Self-Assembly
EtOH	Ethanol
FBS	Fetal Bovine Serum
FDA	Food And Drug Administration

FDM	Fused Deposition Modelling
FRM	Foam Replica Method
FRS	Foam-Replicated Scaffolds
FS	Foaming Strategies
GLP	Good Laboratory Practice
H&E	Haematoxylin and Eosine
HA	Hydroxyapatite
HCA	Hydroxycarbonate Apatite
hES-MP	Human Embrionic-Derived Mesenchimal Progenitor Cells
HPBG	Hierarchically Porous Bioactive Glass
HSM	Hot Stage Microscopy
HTT	Heat Treatment Temperature
ICG	International Commission On Glass
ICP-OES	Inductively Coupled Plasma Optical Emission Spectroscopy
IGF-I	Insuline Growth Factor I
IGF-II	Insuline Growth Factor II
JMA	Johnson-Mehl-Avrami
LD50	Median Lethal Dose
MBGs	Mesoporous Bioactive Glasses
MR	Magnetic Resonance
MSC	Mesenchimal Stem Cells
NASA	National Aeronautics And Space Administration

OFF	Oscillatory Fluid Flow
OIM	Osteogenesis Induction Media
P	Perfusion Bioreactor
PCL	Polycaprolactone
PDMS	Polydimethylsiloxane
PE	Polyethylene
PEF	Pulsed Electric Fields
PFM	Piezoresponse Force Microscopy
PS	Pore Size
PSD	Pore Size Distribution
PU	Polyurethane
PVA	Polyvinyl Alcohol
RC	Robocasting
RCS	Robocasted Scaffolds
RWV	Rotating Wall Vessels Bioreactor
SBF	Simulated Body Fluids
SEM	Scanning Electron Microscopy
SF	Spinner Flasks Bioreactor
SFF	Solid Free-Form Fabrication
SL	Stereolithography
SLS	Selective Laser Sintering
SSA	Specific Surface Area

TC04	Technical Committee 4
TE	Tissue Engineering
TEOS	Tetraethyl Orthosilicate
TG/TGA	Thermogravimetry/ Thermogravimetric Analysis
TMOS	Tetramethyl Orthosilicate
U2OS, ATCC HTB-96	Human Mature Osteoblasts
XRD	X-Ray Diffraction
β-TCP	B-Tricalcium Phosphate
μ-CT	Micro Computed Tomography

Appendix D

Nomenclature of physical and mathematical constants and variables

A_k	Piston surface area	/m^2
A_p	Pore surface area	/mm^2
A_s	Scaffold cross sectional area	/mm^2
D	Diffusion coefficient	m^2/s
d_g	Glass particles diameter	/μm
d_p	Pore diameter	mm
D_s	Scaffold diameter	/mm
d_t	Throat diameter	/mm
E	Elastic modulus (Young's modulus)	Gpa
E_c	Activation energy for crystallization	/kJ/mol

$E_{c,K}$	Activation energy for crystallization according to Kissinger's model	/kJ/mol
E_{vf}	Activation energy for viscous flow	/kJ/mol
F	Applied force	N
f	Piston oscillation frequency	/Hz
f_c	Friction factor	/dimensionless
F_{max}	Maximum load	/N
h/h_0	Normalized sample height	/dimensionless
h	Piston stroke (peak to peak)	/m
J	Diffusive flux	/mol·m^{-2}·s^{-1}
k	Intrinsic permeability	/m^2
kB	Boltzmann constant	/m^{2}·kg·s^{-2}·K^{-1}
Kc	Fracture toughness	/MPa·m$^{1/2}$
Kh	Hruby parameter	/dimensionless
L_p	Pore length	/mm
L_s	Scaffold length	/mm
m	Numerical factor describing the dimensionality of crystal growth	/dimesionless
m_s	Scaffold mass	/g
n	Johnson-Mehl-Avrami (JMA) coefficient	/dimensionless
PM	Molecular weight	g/mol

p_{rms}	r.m.s. pressure	/Pa
Q_v	Volumetric flow rate	/$m^3 \cdot s^{-1}$
$q_{v,rms}$	r.m.s volumetric airflow	/$m^3 \cdot s^{-1}$
R	Ideal gas constant	/J/(mol·K)
r	Open-to-close ratio	/dimensionless
RH	Relative humidity	/dimensionless
R_i	Interstitial Reynolds number	/dimensionless
R_p	Radius of diffusing particles	/m
T	Temperature	/°C
T_{air}	Air temperature	/°C
Tp	Temperature of maximum crystallization rate	/°C
T_f	Temperature of crystallization end	/°C
T_g	Temperature of glass transition	/°C
t	Time	/h
T_m	Temperature of glass melting	/°C
T_s	Sintering temperature	/°C
T_x	Temperature of crystallization onset	/°C
U	Linear flow velocity	/$m \cdot s^{-1}$
v	Fluid velocity	/$m \cdot s^{-1}$

Vf	Final ink volume	/ml
V_p	Pore volume	/mm^3
x	Position/flow direction	/m
ΔT_{FWHM}	Half maximum full width of the DTA exothermic peak	/°C
ΔP	Pressure differential	/Pa
∂P	Pressure gradient	/Pa
β *(Chapter 3,5)*	Heating rate	/°C/min
β *(Chapter 4,6)*	Pore diameter/throat ratio	/dimensionless
ε	Scaffold effective porosity	/dimensionless
ε_0	Scaffold total porosity	/dimensionless
φ	Concentration of ideal mixture	/mol/m^3
Φ	Specific heat flow	/W/m^2
φ_p	Pore sphericity	/dimensionless
ε_c	Scaffold closed porosity	/dimensionless
μ	Fluid dynamic viscosity	/Pa · s
λ	Mean free path of air	/mm
ρ	Generic density (specified by the subscript)	/kg · m^{-3}
σ_c	Compressive strength	/MPa
σ_t	Tensile strength	/MPa

τ	Tortuosity	/dimensionless
χ	Volume fraction of crystallized phase	/dimensionless